Accurate treatment of the electronic structure of atoms and molecules in strong magnetic fields

Dissertation
zur Erlangung des Grades
„Doktor der Naturwissenschaften“
im Promotionsfach Chemie

am Fachbereich Chemie, Pharmazie, Geographie
und Geowissenschaften der
Johannes Gutenberg-Universität Mainz

von
Florian Hampe
geboren in Mainz

Mainz, 2019

1. Berichterstatter: [redacted]

2. Berichterstatter: [redacted]

3. Berichterstatter: [redacted]

Tag der mündlichen Prüfung: 30.09.2019

Auch Weiße Zwerge haben einmal klein angefangen.

Die vorliegende Arbeit wurde im Zeitraum vom 16. September 2015 bis zum 25. August 2019 am Institut für Physikalische Chemie der Johannes Gutenberg-Universität Mainz im Arbeitskreis von [redacted] erstellt.

Danksagung
Mein besonderer Dank gilt [redacted] und [redacted] für die spannende Aufgabenstellung sowie für das Führen hilfreicher Diskussionen während meiner Promotion. Des Weiteren möchte ich mich herzlich für die vielen ermöglichten Gelegenheiten bedanken, bei denen ich im Ausland neue Kontakte knüpfen konnte. In diesem Kontext möchte ich dem Centre for Advanced Study der Norwegian Academy of Science and Letters danken, das mich bei mehreren kleinen Forschungsaufenthalten beherbergt hat und so erst einige Kooperationen initiiert hat, von der diese Arbeit profitieren konnte. Außerdem möchte ich [redacted] für die Finanzierung der Teilnahme an drei Workshops in den USA herzlich danken.
Bedanken möchte ich mich auch bei allen Mitgliedern des Arbeitskreises, die meine Promotionszeit entscheidend geprägt haben. Insbesondere gilt dies für meinen Bürokollegen [redacted], den ich schmerzlich als solchen vermissen werde, und [redacted], mit der ich gerne noch weitere Sommerschulen, Workshops und Konferenzen gemeinsam besucht hätte.
Schließlich möchte ich mich bei meinen Eltern [redacted], meinem Bruder [redacted], meiner Mitbewohnerin [redacted] sowie all meinen weiteren Freunden für ihre unermüdliche Unterstützung danken.

Contents

1 Introduction

Ever since the big bang happened more than 13.5 billion years ago, myriad stars have been born and decayed again. Mankind is fascinated by the thought of stars dying in an unimaginably powerful explosion, a supernova, leaving behind either a neutron star or a black hole. Both these remnants feature their own properties that are hardly conceivable by the human brain. For example, the diameter of a neutron star is only several kilometers but at the same time the star is heavier than the Sun. A black hole possesses a gravitational field so strong that even light cannot escape. However, the vast majority of stars end in a much less dramatical manner as white dwarfs [1] after having their outer layer ejected into space which results in objects with the size of the Earth and the mass of the Sun. In order to better understand the details of stellar evolution, astrophysicists are particularly interested in knowing the exact composition of stars and their remnants. For common white dwarfs, this has been extensively investigated. Besides hydrogen and helium, also heavier elements (C, O, Na, Mg, Al, S, Ca, Fe, ...) [2–5] have been found in their atmospheres. Even molecular hydrogen has been detected. [6] Such detections are carried out by the use of observational spectra exhibiting the corresponding absorption lines. The latter occur when light of a particular wavelength and, thus, with a specific energy is absorbed by an atom or molecule which in turn gets electronically excited. As all chemical species exhibit a unique set of such absorption features, spectra of, e.g., white dwarfs can be compared to spectra from laboratories on Earth enabling the assignment of signals to certain atoms and molecules. However, about 10% of all white dwarfs are magnetic and exhibit field strengths of up to 100000 T. [7,8] For comparison, Earth's magnetic field is of the order of 10^{-5} T, a conventional horseshoe magnet supplies about 10^{-2} T, a magnetic resonance tomograph used in human medicine utilizes magnets with up to 10 T, and the strongest non-destructive magnets on Earth can reach field strengths of 100 T. Magnetic white dwarfs with fields that are even 2-3 orders of magnitude larger than this, therefore, pose a challenge. Strong magnetic fields alter the electronic structure of atoms and molecules dramatically and, thus, their corresponding absorption features. Experimental spectra for comparison are, hence, not available as such high field strengths cannot be produced in any laboratory. Therefore, theoretical quantum-chemical predictions become indispensible for the proper assignment of observational spectra of magnetic white dwarfs.

In order to predict spectra, the electronic Schrödinger equation (SE) for the respective system has to be solved yielding the wave function of the system as well as the total energy of the electronic ground and the different excited states, thus, giving the excitation energies. However, the SE cannot be solved exactly for systems with more than one electron. Therefore, approximations have to be introduced and algorithms have to be developed that, then, determine an approximative solution. Naturally, there already exist many quantum-chemical program packages featuring a variety of approximative schemes to solve the SE. Magnetic fields are usually treated using perturbative approaches. However, in the so-called intermediate regime [1] where $B > 10000$ T, Coulomb and Lorentz interactions become equally imporant, thus, necessitating a non-perturbative treatment of the magnetic field. Such a treatment, however, comes along with additional complications [9] such as, among other things, complex wave-function parameters which require new software implementations. So far, hydrogen [10,11] and helium [12–14] have been proven to exist in the atmospheres of magnetic white dwarfs by using predictions based on Hartree-Fock (HF) calculations on the hydrogen atom [15–18] and full configuration interaction (FCI) calculations on the helium atom, [19–21] respectively. The assignment was realized by generating a so-called $B - \lambda$ diagram which describes the change of excitation energies with the magnetic field strength. Typically, on magnetic white dwarfs, the magnetic field is not static. Hence, for clear signals to appear in the spectrum, the excitation energy must not change significantly within a given range of magnetic field strengths. $B - \lambda$ diagrams reveal stationary points and indicate which signals can be expected to be seen for a given field strength. Thereby, they can be used to assign absorption lines. The suggestion for this procedure goes back to Greenstein [10] and led to the breakthrough in assigning the first hydrogen absorption lines for a magnetic white dwarf. However, sufficiently accurate theoretical predictions for species other than hydrogen and helium have not been available due to the limited applicability of FCI to systems with more than only a few electrons. So far, for strong magnetic fields, atoms like boron, [22] carbon, [23] and sodium [24] have only been treated using numerical Hartree-Fock (HF) procedures. Since HF neglects electron-correlation effects, it lacks the required accuracy necessary for the assignment of spectra. Therefore, the interpretation of observable spectra of magnetic white dwarfs in the intermediate regime has not kept advancing.

Besides the astrophysical context, there has been a growing interest to understand the induced fundamental changes in physics and chemistry in the intermediate regime. Hence, several non-perturbative finite field *ab-initio* programs have been developed over the past years. In the beginning, calculations on molecules suffered from limitations concerning the orientation of the magnetic field. Molecular orbitals were constructed from atomic orbitals obtained for the individual atoms in strong magnetic fields, e.g., for the H_2^+ molecule. [25] Therefore, early calculations were limited to linear molecules with a parallely oriented magnetic field vector. Additionally, the results were dependent on the chosen gauge origin of the vector potential of the magnetic field. These limitations were first tackled by Schmelcher *et al.* in 1988 by introducing a special basis set within a FCI implementation allowing for nearly gauge-origin independent results and the choice of an arbitrarily oriented magnetic field vector.[26] Several HF-based property investigations have been reported since for larger systems (see, e.g., Refs. [27] and [28]). However, these implementations still suffered from severe convergence problems caused by the gauge-origin dependence of the utilized basis sets. Huge progress was made in 2008, when Tellgren *et al.* presented the LONDON program package[29] with the first HF program utilizing gauge-including atomic orbitals (GIAOs)[30,31] allowing for calculations with arbitrarily oriented magnetic field vectors yielding gauge-origin independent results. The FCI development incorporated into the LONDON package by Lange *et al.* enabled the discovery of a new type of bonding mechanism only occuring in strong magnetic fields: perpendicular paramagnetic bonding.[32] Progress accelerated and a first non-perturbative current-density functional theory (CDFT) implementation[33] aiming at producing improved magnetic properties within the DFT framework was reported in 2014. Broadening the field, Shiozaki and coworkers implemented a fully-relativistic HF[34] and complete active space self-consistent field (CASSCF)[35] code for the investigation of heavy elements in magnetic fields. In 2015, Stopkowicz *et al.* presented the first implementation of a complex-valued coupled-cluster (CC) code within the LONDON program.[36] This marked a first step toward the prediction of spectra for many-electron species in strong magnetic fields since CC methods can yield ground state energies that are accurate enough for such an endeavor and yet can be applied to larger systems.

However, further development is needed in order to treat excited states and, hence, to be able to predict spectra. For the latter, highly accurate transition wavelengths have to be provided with error bars smaller than 100 Å. Equation-of-motion (EOM) CC methods[37] are a powerful extension of CC theory offering similar high accuracy as the parent CC methods for ground-state energies but at a much lower cost than FCI. Therefore, the implementation of a complex-valued EOM-CC code has been pursued in this work in order to pave the way to predict accurate spectra for atoms and molecules.

In this thesis, a quantum-chemical program package has been developed whose infrastructure allows for a fast and simple implementation of new CC methods. Within the package, a toolbox of several complex-valued CC and EOM-CC methods has been implemented. At the EOM-CCSD level, these are the variant for electronically excited states (EE),[38] the spin-flip (SF) variant,[39–41] as well as EOM for ionization potential (IP)[42] and electron attachment (EA).[43] Furthermore, the first CCSDT and EOM-EE-CCSDT implementations for the application in strong magnetic fields are reported. The applicability and accuracy of these methods in the context of strong magnetic fields is tested and compared to the field-free case. With this toolbox of highly accurate methods, for the first time, the whole landscape of electronic states including excited states of systems in strong magnetic fields can be explored. This allows for a thorough investigation of how the electronic structure is altered by a magnetic field. Additionally, curious field-induced effects as the perpendicular paramagnetic bonding mechanism mentioned above are explored further and first attempts to assign distinct absorption features in spectra from potentially magnetic white dwarfs are made.

After a thorough introduction to the theoretical fundamentals in Chpt. 2, Chpt. 3 explains all details on the implementation of the new program package QCUMBRE. Chpt. 4 covers the performance assessment while Chpt. 5 comprises the applications mentioned before. Last, a conclusion and an outlook are given in the final Chpt. 6.

2 Theory

All methods that are used in this thesis are so-called post-Hartree-Fock (HF) methods [44] aiming at solving the electronic Schrödinger equation (SE) [45]

$$\hat{H} |\Psi\rangle = E |\Psi\rangle \tag{2.1}$$

within the Born-Oppenheimer (BO) approximation [46] for systems exposed to a static homogeneous magnetic field. In Eq. (2.1), $\hat{H}$ is the electronic Hamiltonian and $|\Psi\rangle$ the electronic wave function. In the following section, first, the magnetic-field dependent Hamiltonian is derived from the Dirac equation. A discussion of the effects of a magnetic field on the energy and their consequences for actual calculations follows. The HF theory [47] is briefly summarized and the formalism of second quantization [45] is explained. Thereafter, the quantum-chemical methods relevant for this thesis are discussed, backed by an introduction to diagrammatic techniques.

2.1 Magnetic fields

The fundamental equations of classical electromagnetism are Maxwell's equations [48]

$$\boldsymbol{\nabla} \cdot \boldsymbol{E} = \frac{\rho}{\varepsilon_0}, \tag{2.2}$$

$$\boldsymbol{\nabla} \cdot \boldsymbol{B} = 0, \tag{2.3}$$

$$\boldsymbol{\nabla} \times \boldsymbol{E} = -\frac{\partial \boldsymbol{B}}{\partial t}, \tag{2.4}$$

$$\boldsymbol{\nabla} \times \boldsymbol{B} = \mu_0 \left(\boldsymbol{j} + \varepsilon_0 \frac{\partial \boldsymbol{E}}{\partial t} \right), \tag{2.5}$$

as well as the Lorentz force law [48]

$$\boldsymbol{F} = q \left(\boldsymbol{E} + \boldsymbol{v} \times \boldsymbol{B} \right). \tag{2.6}$$

$\boldsymbol{E}$ and $\boldsymbol{B}$ are the vectors of the electric and magnetic field, respectively. ρ and $\boldsymbol{j}$ are the charge and current density, ε_0 and μ_0 are the vacuum permittivity and permeability, respectively. $\boldsymbol{F}$ is the Lorentz force acting on a particle of charge q moving through an electromagnetic field with a velocity $\boldsymbol{v}$. Considering the homogeneous system of equations spanned by Eqs. (2.3) and (2.4) shows that $\boldsymbol{E}$ and $\boldsymbol{B}$ may be expressed in terms of a vector potential $\boldsymbol{A}$ and a scalar potential ϕ. [48] Thus, the same physical situation can be defined in a simplified manner such that it depends on fewer parameters

$(A_x,\ A_y,\ A_z,\ \phi)$:

$$\boldsymbol{E} = -\boldsymbol{\nabla}\phi - \frac{\partial \boldsymbol{A}}{\partial t}, \tag{2.7}$$

$$\boldsymbol{B} = \boldsymbol{\nabla} \times \boldsymbol{A}. \tag{2.8}$$

$\boldsymbol{A}$ and ϕ are not unique and may be subjected to a gauge transformation

$$\phi' = \phi - \frac{\partial f}{\partial t}, \tag{2.9}$$

$$\boldsymbol{A}' = \boldsymbol{A} + \boldsymbol{\nabla} f, \tag{2.10}$$

with the gauge function f while leaving the physical situation unaffected:

$$\boldsymbol{E}' = -\boldsymbol{\nabla}\phi' - \frac{\partial \boldsymbol{A}'}{\partial t} = -\boldsymbol{\nabla}\phi + \boldsymbol{\nabla}\frac{\partial f}{\partial t} - \frac{\partial \boldsymbol{A}}{\partial t} - \frac{\partial \boldsymbol{\nabla} f}{\partial t} = \boldsymbol{E}, \tag{2.11}$$

$$\boldsymbol{B}' = \boldsymbol{\nabla} \times \boldsymbol{A}' = \boldsymbol{\nabla} \times (\boldsymbol{A} + \boldsymbol{\nabla} f) = \boldsymbol{B} + \underbrace{\boldsymbol{\nabla} \times \boldsymbol{\nabla} f}_{=0} = \boldsymbol{B}. \tag{2.12}$$

Hence, we may choose $\boldsymbol{A}$ to fulfill the Coulomb gauge, i.e., $\boldsymbol{A}$ becomes divergenceless: [48]

$$\boldsymbol{\nabla} \cdot \boldsymbol{A} = 0. \tag{2.13}$$

For a uniform magnetic field, the vector potential fulfills the Coulomb gauge if, e.g., expressed by

$$\boldsymbol{A}_{\boldsymbol{O}}(\boldsymbol{r}) = \frac{1}{2}\boldsymbol{B} \times \boldsymbol{r}^{\boldsymbol{O}} \tag{2.14}$$

with the gauge origin $\boldsymbol{O}$ for which $\boldsymbol{A}_{\boldsymbol{O}}(\boldsymbol{O}) = 0$ and $\boldsymbol{r}^{\boldsymbol{O}} = \boldsymbol{r} - \boldsymbol{O}$ the position relative to $\boldsymbol{O}$. However, it has to be noted that the gauge is not uniquely fixed and the gauge origin can still be chosen arbitrarily for a static homogeneous magnetic field.

The Hamiltonian in a static homogeneous magnetic field

In order to derive the non-relativistic Hamiltonian for an N-electron system, first, the Hamiltonian for a single electron is derived. We will start from the Dirac equation [49] (2.15) from relativistic quantum chemistry, thereby incorporating spin in a natural manner:

$$\begin{pmatrix} \hat{V}_{\mathrm{ne}} & c\boldsymbol{\sigma}\hat{\boldsymbol{\pi}} \\ c\boldsymbol{\sigma}\hat{\boldsymbol{\pi}} & \hat{V}_{\mathrm{ne}} - 2m_{\mathrm{e}}c^2 \end{pmatrix} \begin{pmatrix} \varphi \\ \chi \end{pmatrix} = E \begin{pmatrix} \varphi \\ \chi \end{pmatrix}. \tag{2.15}$$

Due to the appearance of the velocity $\boldsymbol{v}$ in (2.6), a moving particle in an electromagnetic field is not a conservative system. Hence, instead of the canonical momentum operator $\hat{\boldsymbol{p}}$ the kinetic momentum operator $\hat{\boldsymbol{\pi}} = \hat{\boldsymbol{p}} + \mathrm{e}\boldsymbol{A}$ needs to be used with e as the elementary electric charge. $\hat{V}_{\mathrm{ne}}$ is the external potential defined by the Coulomb interaction between the electron and the nuclei, $m_{\mathrm{e}}c^2$ is the rest energy with m_{e} the electron mass, and c the speed of light while $\boldsymbol{\sigma}$ is the vector of the Pauli spin matrices. In this notation, the four-component wave function is represented via the two-component functions φ and χ which are named large and small component, respectively. Expanding the second equation in (2.15) yields the following proportionality relation with respect to c:

$$\chi \sim \frac{1}{c}\varphi. \tag{2.16}$$

This motivates the introduction of a new metric [49] to obtain quantities of the same order in c. With $\bar{\chi} = c\chi$ and $\bar{\varphi} = \varphi$, Eq. (2.15) may be rewritten as

$$\begin{pmatrix} \hat{V}_{\mathrm{ne}} & \boldsymbol{\sigma}\hat{\boldsymbol{\pi}} \\ \boldsymbol{\sigma}\hat{\boldsymbol{\pi}} & \dfrac{\hat{V}_{\mathrm{ne}}}{c^2} - 2m_{\mathrm{e}} \end{pmatrix} \begin{pmatrix} \bar{\varphi} \\ \bar{\chi} \end{pmatrix} = E \begin{pmatrix} 1 & 0 \\ 0 & \dfrac{1}{c^2} \end{pmatrix} \begin{pmatrix} \bar{\varphi} \\ \bar{\chi} \end{pmatrix}. \tag{2.17}$$

For $c \to \infty$, the Lévy-Leblond equation [50] (2.18) is obtained, representing the proper non-relativistic limit of the Dirac equation:

$$\begin{pmatrix} \hat{V}_{\mathrm{ne}} & \boldsymbol{\sigma}\hat{\boldsymbol{\pi}} \\ \boldsymbol{\sigma}\hat{\boldsymbol{\pi}} & -2m_{\mathrm{e}} \end{pmatrix} \begin{pmatrix} \bar{\varphi} \\ \bar{\chi} \end{pmatrix} = E \begin{pmatrix} 1 & 0 \\ 0 & 0 \end{pmatrix} \begin{pmatrix} \bar{\varphi} \\ \bar{\chi} \end{pmatrix}. \tag{2.18}$$

Solving the second equation of Eq. (2.18) for $\bar{\chi}$ and inserting the result into the first equation yields a two-component SE with

$$\underbrace{\left(\frac{(\boldsymbol{\sigma}\hat{\boldsymbol{\pi}})^2}{2m_{\mathrm{e}}} + \hat{V}_{\mathrm{ne}} \right)}_{=\hat{h}} \bar{\varphi} = E\bar{\varphi}. \tag{2.19}$$

The expression in brackets constitutes the Hamiltonian $\hat{h}$ for a single electron. With the magnetic field vector defining the spin-quantization axis, each component of the wave function can be interpreted as the wave function of an electron with parallel or antiparallel spin which are referred to as α- or β-spin, respectively. To obtain a Hamiltonian depending on $\boldsymbol{B}$, $(\boldsymbol{\sigma}\hat{\boldsymbol{\pi}})^2$ has to be expanded assuming the Coulomb gauge giving

$$
\begin{aligned}
(\boldsymbol{\sigma}\hat{\boldsymbol{\pi}})^2 &= \hat{\boldsymbol{\pi}}^2 + \mathrm{i}\boldsymbol{\sigma}\left(\hat{\boldsymbol{\pi}} \times \hat{\boldsymbol{\pi}}\right) \\
&= \hat{\boldsymbol{\pi}}^2 + \mathrm{i}\boldsymbol{\sigma}\,(\underbrace{\hat{\boldsymbol{p}} \times \hat{\boldsymbol{p}}}_{=0} + \underbrace{\mathrm{e}^2\left(\boldsymbol{A} \times \boldsymbol{A}\right)}_{=0} + \mathrm{e}\left(\boldsymbol{A} \times \hat{\boldsymbol{p}} + \hat{\boldsymbol{p}} \times \boldsymbol{A}\right)) \\
&= \hat{\boldsymbol{\pi}}^2 + \mathrm{e}\hbar\boldsymbol{\sigma}\underbrace{\left(\boldsymbol{\nabla} \times \boldsymbol{A}\right)}_{=\boldsymbol{B}}.
\end{aligned}
\tag{2.20}
$$

Further expanding $\hat{\boldsymbol{\pi}}^2$ and introducing the spin operator $\hat{\boldsymbol{s}}$ yields

$$
\hat{h} = \frac{\hat{\boldsymbol{p}}^2}{2m_\mathrm{e}} + \frac{\mathrm{e}}{m_\mathrm{e}}\underbrace{\frac{\hbar}{2}\boldsymbol{\sigma}}_{=\hat{\boldsymbol{s}}}\,\boldsymbol{B} + \frac{\mathrm{e}}{m_\mathrm{e}}\boldsymbol{A}\hat{\boldsymbol{p}} + \frac{\mathrm{e}^2}{2m_\mathrm{e}}A^2 + \hat{V}_\mathrm{ne}. \tag{2.21}
$$

Inserting expression (2.14) for the vector potential into Eq. (2.21) yields the Hamiltonian expressed in terms of $\boldsymbol{B}$:

$$
\begin{aligned}
\hat{h} &= \frac{\hat{\boldsymbol{p}}^2}{2m_\mathrm{e}} + \frac{\mathrm{e}}{m_\mathrm{e}}\boldsymbol{B}\hat{\boldsymbol{s}} + \frac{\mathrm{e}}{2m_\mathrm{e}}\underbrace{\left(\boldsymbol{B} \times \boldsymbol{r}^{\boldsymbol{O}}\right)\hat{\boldsymbol{p}}}_{=\hat{\boldsymbol{l}}^{\boldsymbol{O}}\boldsymbol{B}} + \frac{\mathrm{e}^2}{8m_\mathrm{e}}\left(\boldsymbol{B} \times \boldsymbol{r}^{\boldsymbol{O}}\right)^2 + \hat{V}_\mathrm{ne} \\
&= \frac{\hat{\boldsymbol{p}}^2}{2m_\mathrm{e}} + \frac{\mathrm{e}}{m_\mathrm{e}}\boldsymbol{B}\hat{\boldsymbol{s}} + \frac{\mathrm{e}}{2m_\mathrm{e}}\boldsymbol{B}\hat{\boldsymbol{l}}^{\boldsymbol{O}} + \frac{\mathrm{e}^2}{8m_\mathrm{e}}\left(B^2 r^{\boldsymbol{O}2} - \left(\boldsymbol{B}\boldsymbol{r}^{\boldsymbol{O}}\right)^2\right) + \hat{V}_\mathrm{ne}.
\end{aligned}
\tag{2.22}
$$

Using that the scalar triple product is unchanged under a cyclic permutation of its three operands to obtain $\left(\boldsymbol{B} \times \boldsymbol{r}^{\boldsymbol{O}}\right)\hat{\boldsymbol{p}} = \left(\boldsymbol{r}^{\boldsymbol{O}} \times \hat{\boldsymbol{p}}\right)\boldsymbol{B}$, the canonical angular momentum operator $\hat{\boldsymbol{l}}^{\boldsymbol{O}}$ has been introduced. Due to the presence of this operator in the Hamiltonian, the wave function, in general, may become complex-valued. Assuming a magnetic field in z-direction and introducing atomic units[1] simplifies Eq. (2.22) further:

$$
\hat{h} = \frac{\hat{\boldsymbol{p}}^2}{2} + B_z\hat{s}_z + B_z\hat{l}^{\boldsymbol{O}}_z + \frac{1}{8}B_z^2\left(x^{\boldsymbol{O}2} + y^{\boldsymbol{O}2}\right) + \hat{V}_\mathrm{ne}. \tag{2.23}
$$

For a free electron without longitudinal translational motion, the solutions to the corresponding SE

$$
\hat{h}\bar{\varphi}(n, l, m_l) = E^\mathrm{Landau}_{n,m_l,m_s}\bar{\varphi}(n, l, m_l) \tag{2.24}
$$

are the so-called Landau levels [51]

$$
E^\mathrm{Landau}_{n,m_l,m_s} = \left(n + \frac{1}{2}\left(1 + m_l + |m_l| + 2m_s\right)\right)B_z, \qquad n \in \mathbb{N}_0. \tag{2.25}
$$

---

[1] $m_\mathrm{e} = \mathrm{e} = \hbar = {}^{1}/_{4\pi\epsilon_0} = 1$ a.u.

In Eqs. (2.24)-(2.25), n is the main quantum number, l the azimuthal quantum number, m_l the magnetic quantum number, and m_s the spin quantum number. In order to obtain the electronic Hamiltonian for an N-electron molecule consisting of M nuclei in a magnetic field in z-direction, one has to sum over all $\hat{h}(\alpha)$ and add the instantaneous Coulomb interactions:

$$\begin{aligned}\hat{H} &= \sum_{\alpha} \hat{h}(\alpha) + \sum_{\alpha<\beta} \frac{1}{|\boldsymbol{r}_\alpha - \boldsymbol{r}_\beta|} \\ &= \overbrace{\sum_{\alpha}^{N} \frac{\hat{\boldsymbol{p}}_\alpha^2}{2} - \sum_{\alpha}^{N}\sum_{A}^{M} \frac{Z_A}{|\boldsymbol{R}_A - \boldsymbol{r}_\alpha|} + \sum_{\alpha<\beta}^{N} \frac{1}{|\boldsymbol{r}_\alpha - \boldsymbol{r}_\beta|}}^{\hat{H}_0} \\ &\quad \underbrace{+ \sum_{\alpha}^{N} B_z \hat{s}_{z,\alpha}}_{\text{spin-Zeeman}} + \underbrace{\frac{1}{2}\sum_{\alpha}^{N} B_z \hat{l}^{\boldsymbol{O}}_{z,\alpha}}_{\text{orbital-Zeeman}} + \frac{1}{8} B_z^2 \sum_{\alpha}^{N} \left(x_\alpha^{\boldsymbol{O}2} + y_\alpha^{\boldsymbol{O}2} \right) \\ &= \hat{H}_0 + \underbrace{B_z \hat{S}_z + \frac{1}{2} B_z \hat{L}^{\boldsymbol{O}}_z}_{\text{paramagnetic}} + \underbrace{\frac{1}{8} B_z^2 \sum_{\alpha}^{N} \left(x_\alpha^{\boldsymbol{O}2} + y_\alpha^{\boldsymbol{O}2} \right)}_{\text{diamagnetic}} . \end{aligned} \tag{2.26}$$

$\hat{H}_0$ is the many-body Hamiltonian for the field-free case and the magnetic-field dependent terms are characterized as 'paramagnetic' and 'diamagnetic' contributions. The former contain the spin- as well as the orbital-Zeeman terms, which are linear in $\boldsymbol{B}$ and may raise or lower the total energy of the system. Since antiparallel spin-orientation leads to a lower energy, high-spin open-shell states become favored with increasing field strength. Furthermore, the occupation of orbitals resulting in a large negative expectation value of $\hat{L}_z$ is preferred. The diamagnetic term on the other hand is quadratic in $\boldsymbol{B}$ and always raises the energy acting as a confining harmonic potential in the directions perpendicular to the magnetic field. For sufficiently large field strengths, the diamagnetic term, thus, becomes dominant. It is this interplay between the paramagnetic and diamagnetic contributions that leads to the complex behavior of electronic energies as a function of the magnetic field strength and, hence, the absorption spectra of atoms and molecules that depend on the energy differences between electronic states for a given $\boldsymbol{B}$.

London orbitals

It is obvious from Eq. (2.26) that the Hamiltonian depends on the arbitrary choice of the gauge origin $\boldsymbol{O}$ for which the vector potential vanishes. Changing $\boldsymbol{O}$ to another point in space $\boldsymbol{X}$ corresponds to a gauge transformation

$$\boldsymbol{A_X}(\boldsymbol{r}) = \boldsymbol{A_O}(\boldsymbol{r}) + \boldsymbol{\nabla} f(\boldsymbol{r}) \tag{2.27}$$

with the gauge function $f(\boldsymbol{r}) = -\boldsymbol{A_O}(\boldsymbol{X}) \cdot \boldsymbol{r}$. Using such a transformed vector potential to build up a Hamiltonian $\hat{H}_{\boldsymbol{X}}$ is equivalent to a unitary transformation of the original Hamiltonian

$$\hat{H}_{\boldsymbol{X}} = \mathrm{e}^{-\mathrm{i}f} \hat{H}_{\boldsymbol{O}} \mathrm{e}^{\mathrm{i}f}. \tag{2.28}$$

Accordingly, the wave function must undergo the unitary transformation

$$\Psi_{\boldsymbol{X}} = \mathrm{e}^{-\mathrm{i}f} \Psi_{\boldsymbol{O}} : \tag{2.29}$$

$$\Psi_{\boldsymbol{X}} = \exp\left(\frac{\mathrm{i}}{2} \boldsymbol{B} \times (\boldsymbol{X} - \boldsymbol{O}) \cdot \boldsymbol{r}\right) \Psi_{\boldsymbol{O}}. \tag{2.30}$$

In general, the phase factor in Eq. (2.30) will introduce oscillations in the exact wave function that cannot be mimicked properly by standard Gaussian functions in a finite basis set. [52] Therefore, results become gauge-origin dependent in actual calculations which is unphysical. In order to resolve this problem, gauge-including atomic orbitals [53] (GIAOs, also called London orbitals) ω_{l,m_l} can be used. They move the global gauge origin $\boldsymbol{X}$ for each AO χ_{l,m_l} into its center $\boldsymbol{C}$:

$$\omega_{l,m_l}(\boldsymbol{r_C}, \boldsymbol{B}, \boldsymbol{C}) = \exp\left(\frac{\mathrm{i}}{2} \boldsymbol{B} \times (\boldsymbol{X} - \boldsymbol{C}) \cdot \boldsymbol{r}\right) \chi_{l,m_l}(\boldsymbol{r_C}). \tag{2.31}$$

The atomic orbitals $\chi_{l,m_l}(\boldsymbol{r_C})$ as well as the GIAOs $\omega_{l,m_l}(\boldsymbol{r_C}, \boldsymbol{B}, \boldsymbol{C})$ are eigenfunctions to the one-electron Hamiltonian $\hat{h}_{\boldsymbol{C}}$ for which the gauge origin is in the center of the atomic orbital. In order to show the advantages of GIAOs, it can, for example, be proven that a GIAO $\omega_{l,m_l}(\boldsymbol{r_C}, \boldsymbol{B}, \boldsymbol{C})$ is also an eigenfunction to $\hat{h}_{\boldsymbol{X}} = \mathrm{e}^{-\mathrm{i}f} \hat{h}_{\boldsymbol{C}} \mathrm{e}^{\mathrm{i}f}$ for any gauge origin $\boldsymbol{X}$:

$$\begin{aligned} \hat{h}_{\boldsymbol{X}} \omega_{l,m_l} &= \hat{h}_{\boldsymbol{X}} \ \exp(\mathrm{i}\boldsymbol{A_C}(\boldsymbol{X}))\chi_{l,m_l} \\ &= \exp(\mathrm{i}\boldsymbol{A_C}(\boldsymbol{X})) \ \hat{h}_{\boldsymbol{C}} \chi_{l,m_l} \\ &= \epsilon \ \exp(\mathrm{i}\boldsymbol{A_C}(\boldsymbol{X}))\chi_{l,m_l} = \epsilon \ \omega_{l,m_l}, \end{aligned} \tag{2.32}$$

where ϵ is a corresponding eigenvalue of $\hat{h}_{\boldsymbol{C}}$. The right-hand side in Eq. (2.32) is independent of $\boldsymbol{X}$. As the first-order response of the London orbitals to a gauge-transformation is exact, fast basis set convergence is implied. [54]

Eq. (2.32) holds, because the action of the gauge-transformed operator $\hat{\boldsymbol{\pi}}^2_{\boldsymbol{X}}$ upon the corresponding phase factor appearing in the GIAO yields

$$\begin{aligned}
&\hat{\boldsymbol{\pi}}_{\boldsymbol{X}}^2 \exp(\mathrm{i}\boldsymbol{A}_{\boldsymbol{C}}(\boldsymbol{X})) \\
=&\hat{\boldsymbol{\pi}}_{\boldsymbol{X}} \left[\exp(\mathrm{i}\boldsymbol{A}_{\boldsymbol{C}}(\boldsymbol{X})) \cdot \underbrace{(\hat{\boldsymbol{\pi}}_{\boldsymbol{X}} + \boldsymbol{A}_{\boldsymbol{C}}(\boldsymbol{X}))}_{=\hat{\boldsymbol{\pi}}_{\boldsymbol{C}}}\right] \\
=&\hat{\boldsymbol{\pi}}_{\boldsymbol{X}} \exp(\mathrm{i}\boldsymbol{A}_{\boldsymbol{C}}(\boldsymbol{X}))\ \hat{\boldsymbol{\pi}}_{\boldsymbol{C}} = \exp(\mathrm{i}\boldsymbol{A}_{\boldsymbol{C}}(\boldsymbol{X}))\ \hat{\boldsymbol{\pi}}_{\boldsymbol{C}}^2.
\end{aligned} \tag{2.33}$$

Therefore,

$$\hat{h}_{\boldsymbol{X}} \exp(\mathrm{i}\boldsymbol{A}_{\boldsymbol{C}}(\boldsymbol{X})) = \exp(\mathrm{i}\boldsymbol{A}_{\boldsymbol{C}}(\boldsymbol{X}))\ \hat{h}_{\boldsymbol{C}}. \tag{2.34}$$

Symmetry

In order to determine the symmetry of a molecule in a homogeneous magnetic field, one has to take into account that the field vector $\boldsymbol{B}$ is a pseudovector. It is defined by the cross product of two polar vectors, i.e., $\boldsymbol{B} = \boldsymbol{\nabla} \times \boldsymbol{A}$. This means that its components transform like yz, xz, and xy, respectively. As a consequence, the point-group symmetry of a molecule in a magnetic field is in general lower than in the field-free case. This even gives rise to symmetry classes that do not occur for molecules in the field-free case (see Chpt. 12 in Ref. [51]). Tab. 2.1 illustrates this by the example of a hydrogen molecule in a magnetic field. [55] Without a field, the molecule is of $D_{\infty h}$ symmetry.

Table 2.1: Symmetry elements in H_2 in the absence and presence of a magnetic field with parallel ($\parallel$), perpendicular ($\perp$), or arbitrary orientation ($\diagdown$) with respect to the molecular axis (z-direction).

$\boldsymbol{B}$	Symmetry elements							Point group
$\mathbf{0}$	E	C_∞	σ_v	i	σ_h	S_∞	C_2	$D_{\infty h}$
	✓	✓ (z)	✓ $\forall\sigma \supset z\ (\infty)$	✓	✓ (σ_{xy})	✓ (z)	✓ $\forall C_2 \perp z\ (\infty)$	
$\parallel$	E	C_∞	σ_v	i	σ_h	S_∞	C_2	$C_{\infty h}$
	✓	✓ (z)	✗	✓	✓ (σ_{xy})	✓ (z)	✗	
$\perp$	E	C_∞	σ_h	i	σ_v	S_∞	C_2	C_{2h}
	✓	✗	✓ $\sigma \perp \boldsymbol{B}$	✓	✗	✗	✓ $C_2 \parallel \boldsymbol{B}$	
$\diagdown$	E	C_∞	σ_h	i	σ_v	S_∞	C_2	C_i
	✓	✗	✗	✓	✗	✗	✗	

Applying a field parallel to the molecular axis preserves the identity, the inversion center, the perpendicular mirror plane, as well as the infinite rotation and rotation reflection axes. However, the infinitely many mirror planes containing the molecular axis as well as all C_2 rotation axes perpendicular to it are no longer symmetry elements. These transformations invert the direction of the magnetic field vector. The point-group symmetry is, therefore, lowered to $C_{\infty h}$. When a perpendicular field is applied, all axial symmetry elements along the molecular axis are removed since the principal axis is now perpendicular to it. On the other hand, the C_2 rotation axis parallel to the field vector becomes a valid symmetry element again. For the mirror planes, similar observations can be made. The former σ_h plane - now referred to as σ_v as the principal axis is determined by the field vector - is no longer existent. However, the former σ_v plane perpendicular to $\boldsymbol{B}$ becomes a new σ_h mirror plane. In total, the point-group symmetry is now C_{2h}. For any other orientation of the molecule in a magnetic field, only the identity and the inversion symmetry are retained resulting in the point-group symmetry C_i.

2.2 Hartree-Fock theory

The simplest physically sound ansatz for an N-electron wave function is given by a single Slater determinant

$$|\Phi_0\rangle = \frac{1}{\sqrt{N!}} \left| \varphi_1(1) \quad \varphi_2(2) \quad \dots \quad \varphi_N(N) \right| \tag{2.35}$$

composed of N orthonormal spin orbitals φ_i. In non-relativistic theories, a spin orbital $\varphi_i(\boldsymbol{\tau}_\alpha) = \phi_i(\boldsymbol{r}_{\boldsymbol{\alpha}})\sigma_i(s_\alpha)$ can usually be written as the product of a spatial orbital $\phi_i(\boldsymbol{r}_\alpha)$ and a spin function $\sigma_i(s_\alpha)$ which is either α or β. $\boldsymbol{\tau}_\alpha$ merges the spatial coordinate $\boldsymbol{r}_\alpha$ and the artificial spin coordinate s_α. The energy expectation value for the ansatz in Eq. (2.35) defines the HF energy and is given by:

$$\begin{aligned} E_{\mathrm{HF}} &= \frac{\langle\Phi_0|\,\hat{H}\,|\Phi_0\rangle}{\langle\Phi_0|\Phi_0\rangle} \\ &= \sum_i^N \underbrace{\langle\varphi_i|\,\hat{h}\,|\varphi_i\rangle}_{=h_{ii}} + \frac{1}{2}\sum_{i,j}^N \Big(\langle\varphi_i|\,\hat{J}_j - \hat{K}_j\,|\varphi_i\rangle\Big) \\ &= \sum_i^N h_{ii} + \frac{1}{2}\sum_{i,j}^N \Big(\underbrace{\langle\varphi_i(1)\varphi_j(2)|\,\frac{1}{r_{12}}\,|\varphi_i(1)\varphi_j(2)\rangle}_{=\langle ij|ij\rangle = J_{ij}} - \underbrace{\langle\varphi_i(1)\varphi_j(2)|\,\frac{1}{r_{12}}\,|\varphi_j(1)\varphi_i(2)\rangle}_{=\langle ij|ji\rangle = K_{ij}}\Big) \\ &= \sum_i^N h_{ii} + \frac{1}{2}\sum_{i,j}^N \langle ij|\,|ij\rangle\,. \end{aligned} \tag{2.36}$$

$\hat{J}_j$ is the Coulomb operator

$$\hat{J}_j \varphi_i(1) = \int \mathrm{d}\boldsymbol{\tau}_2 \varphi_j^*(2) \frac{1}{r_{12}} \varphi_i(1) \varphi_j(2) \tag{2.37}$$

with r_{12} as the interelectronic distance. J_{ij} is the corresponding Coulomb integral describing the Coulomb interaction of the electrons represented by the spin orbitals i and j via their charge densities. Hence, HF theory describes the Coulomb interaction only in a mean-field manner. $\hat{K}_j$ is the exchange operator

$$\hat{K}_j \varphi_i(1) = \int \mathrm{d}\boldsymbol{\tau}_2 \varphi_j^*(2) \frac{1}{r_{12}} \varphi_j(1) \varphi_i(2). \tag{2.38}$$

K_{ij} is the corresponding exchange integral arising due to the antisymmetry of the Slater determinant and is solely a quantum-mechanical effect. In order to determine the optimal spin orbitals $\{\varphi_i\}$, the variational principal is applied and the HF energy is minimized with respect to the spin orbitals. The latter are constrained to be orthonormal. The canonical HF equations

$$\hat{F} \varphi_i = \varepsilon_i \varphi_i \tag{2.39}$$

are obtained with

$$\hat{F} = \hat{h} + \sum_j^N \left(\hat{J}_j - \hat{K}_j \right) \tag{2.40}$$

as the Fock operator and the orbital energies ε_i. Within restricted HF (RHF) theory [47] which is only applicable to closed-shell systems, electrons that only differ in m_s are placed in the same spatial orbital. For RHF, the canonical HF equations

$$\hat{F}^{\mathrm{RHF}} \phi_i = \varepsilon_i \phi_i \tag{2.41}$$

are obtained with the spatial Fock operator

$$\hat{F}^{\mathrm{RHF}} = \hat{h} + \sum_j^{\frac{N}{2}} \left(2\hat{J}_j^{\mathrm{RHF}} - \hat{K}_j^{\mathrm{RHF}} \right) \tag{2.42}$$

including now a sum over spatial orbitals ϕ_j and the RHF Coulomb and exchange operators

$$\hat{J}_j^{\mathrm{RHF}} \phi_i(1) = \int \mathrm{d}\boldsymbol{r}_2 \phi_j^*(2) \frac{1}{r_{12}} \phi_i(1) \phi_j(2), \tag{2.43}$$

$$\hat{K}_j^{\mathrm{RHF}} \phi_i(1) = \int \mathrm{d}\boldsymbol{r}_2 \phi_j^*(2) \frac{1}{r_{12}} \phi_j(1) \phi_i(2). \tag{2.44}$$

In actual calculations, the spatial orbitals are represented as a linear combination of M atomic orbital [46] (LCAO) basis functions

$$|\phi_i\rangle = \sum_{\mu}^{M} c_{\mu i} |\chi_\mu\rangle . \tag{2.45}$$

Inserting (2.45) into (2.41) and projecting upon basis functions $\langle\chi_\nu|$ gives the Roothaan-Hall equations [47]

$$\sum_{\mu}^{M} \underbrace{\langle\chi_\nu| \hat{F}^{\mathrm{RHF}} |\chi_\mu\rangle}_{=F_{\nu\mu}} c_{\mu i} = \underbrace{\langle\chi_\nu|\chi_\mu\rangle}_{=S_{\nu\mu}} c_{\mu i}\varepsilon_i \tag{2.46}$$

which can be recast in their algebraic form

$$\boldsymbol{Fc} = \boldsymbol{Sc\varepsilon}. \tag{2.47}$$

$\boldsymbol{F}$ is the Fock matrix, $\boldsymbol{c}$ the coefficient matrix, $\boldsymbol{S}$ the overlap matrix, and $\boldsymbol{\varepsilon}$ the matrix of the orbital energies.

For open-shell systems, unrestricted HF (UHF) [47] may be used allowing for the use of different spatial orbitals for electrons of α and β spin:

$$\varphi_i(\boldsymbol{\tau}_\alpha) = \begin{cases} \phi_i^\alpha(\boldsymbol{r}_\alpha)\alpha(s_\alpha) \\ \phi_i^\beta(\boldsymbol{r}_\alpha)\beta(s_\alpha) \end{cases} . \tag{2.48}$$

For UHF, a set of canonical HF equations is obtained:

$$\begin{aligned} \hat{F}^\alpha \phi_i^\alpha &= \varepsilon_i^\alpha \phi_i^\alpha, \\ \hat{F}^\beta \phi_i^\beta &= \varepsilon_i^\beta \phi_i^\beta. \end{aligned} \tag{2.49}$$

The spatial Fock operators $\hat{F}^\alpha$ and $\hat{F}^\beta$ are defined as

$$\begin{aligned} \hat{F}^\alpha &= \int \mathrm{d}s_\gamma \alpha^*(s_\gamma)\hat{F}\alpha(s_\gamma) \\ &= \hat{h} + \sum_{j}^{N_\alpha} \left[\hat{J}_j^\alpha - \hat{K}_j^\alpha\right] + \sum_{j}^{N_\beta} \hat{J}_j^\beta, \end{aligned} \tag{2.50}$$

$$\begin{aligned} \hat{F}^\beta &= \int \mathrm{d}s_\gamma \beta^*(s_\gamma)\hat{F}\beta(s_\gamma) \\ &= \hat{h} + \sum_{j}^{N_\beta} \left[\hat{J}_j^\beta - \hat{K}_j^\beta\right] + \sum_{j}^{N_\alpha} \hat{J}_j^\alpha \end{aligned} \tag{2.51}$$

with the numbers of α and β electrons N_α and N_β, respectively. The unrestricted Coulomb and exchange operators are defined as

$$\hat{J}_j^\alpha \phi_i^\sigma(1) = \int \mathrm{d}\boldsymbol{r}_2 \phi_j^{\alpha *}(2) \frac{1}{r_{12}} \phi_i^\sigma(1) \phi_j^\alpha(2), \tag{2.52}$$

$$\hat{J}_j^\beta \phi_i^\sigma(1) = \int \mathrm{d}\boldsymbol{r}_2 \phi_j^{\beta *}(2) \frac{1}{r_{12}} \phi_i^\sigma(1) \phi_j^\beta(2), \tag{2.53}$$

$$\hat{K}_j^\alpha \phi_i^\sigma(1) = \int \mathrm{d}\boldsymbol{r}_2 \phi_j^{\alpha *}(2) \frac{1}{r_{12}} \phi_j^\alpha(1) \phi_i^\sigma(2), \tag{2.54}$$

$$\hat{K}_j^\beta \phi_i^\sigma(1) = \int \mathrm{d}\boldsymbol{r}_2 \phi_j^{\beta *}(2) \frac{1}{r_{12}} \phi_j^\beta(1) \phi_i^\sigma(2). \tag{2.55}$$

By applying the LCAO ansatz for each set of $\{\phi_i^{\alpha/\beta}\}$, the Pople-Nesbet equations [47] are obtained:

$$\boldsymbol{F}^\alpha \boldsymbol{c}^\alpha = \boldsymbol{S} \boldsymbol{c}^\alpha \boldsymbol{\varepsilon}^\alpha, \tag{2.56}$$

$$\boldsymbol{F}^\beta \boldsymbol{c}^\beta = \boldsymbol{S} \boldsymbol{c}^\beta \boldsymbol{\varepsilon}^\beta. \tag{2.57}$$

The Roothaan-Hall or Pople-Nesbet equations are typically solved by the self-consistent field (SCF) procedure [47] providing $2M$ spin orbitals. The N spin orbitals

$$\{|\varphi_i\rangle, |\varphi_j\rangle, |\varphi_k\rangle, \dots\} \subset \{|\varphi_p\rangle\}$$

with the lowest orbital energies constitute $|\Phi_0\rangle$ and are called occupied, while the remaining $2M - N$ spin orbitals

$$\{|\varphi_a\rangle, |\varphi_b\rangle, |\varphi_c\rangle, \dots\} \subset \{|\varphi_p\rangle\}$$

are referred to as virtual. As the HF method is a mean-field approach and no direct correlation between two electrons' positions is considered, the correlation energy [47] can be defined as the difference between the HF energy and the exact non-relativistic solution of the SE:

$$\Delta E_{\mathrm{corr}} = E_{\mathrm{exact}}^{\mathrm{nrel}} - E_{\mathrm{HF}}. \tag{2.58}$$

It can be approximated by applying so-called post-HF methods.

2.3 Second quantization and normal ordering

For post-HF methods, the wave function is represented by the HF determinant and a subset of all other determinants that can be constructed using the $\{|\varphi_p\rangle\}$. [44] It is convenient to classify the additional determinants in terms of excitations with respect to $|\Phi_0\rangle$. They can be constructed by replacing one, two, three, ... occupied orbitals by virtual ones and are referred to as singly, doubly, triply, ... excited determinants $|\Phi_{ijk...}^{abc...}\rangle$.

A useful formalism when working in a determinantal basis is second quantization.[56] Here, any determinant can be represented apart from the sign by a vector of size $2M$ containing occupation numbers n_i in a canoncial order, i.e., i starts with 1 and goes to $2M$:

$$|\Phi_I\rangle = \frac{1}{\sqrt{N!}} \begin{vmatrix} \varphi_{I_1} & \dots & \varphi_{I_N} \end{vmatrix} \equiv |n_1 \dots n_{2M}\rangle \,. \tag{2.59}$$

For the N spin orbitals φ_p contained in the determinant, the corresponding occupation numbers equal one while the other $2M-N$ occupation numbers are zero. The occupation number vectors can be manipulated by creation and annihilation operators $\hat{a}_i^\dagger$ and $\hat{a}_i$, respectively:[56]

$$\hat{a}_i^\dagger |n_1 \dots n_i \dots n_{2M}\rangle = \delta_{n_i 0} \Gamma_i^N |n_1 \dots n_i + 1 \dots n_{2M}\rangle \,, \tag{2.60}$$

$$\hat{a}_i |n_1 \dots n_i \dots n_{2M}\rangle = \delta_{n_i 1} \Gamma_i^N |n_1 \dots n_i - 1 \dots n_{2M}\rangle \,. \tag{2.61}$$

The pre-factor $\Gamma_p^N = \prod_{r=1}^{p-1} (-1)^{n_r}$ ensures the correct overall sign by accounting for the change of sign when permuting two columns or rows in the Slater determinant. The Kronecker delta ensures the limitation of $n_i \in \{0, 1\}$. Specifically, any determinant can be represented by a string of creation operators acting upon the vacuum state which is an occupation number vector with $n_i = 0 \; \forall \; i$:

$$\frac{1}{\sqrt{2}} \begin{vmatrix} \varphi_1(1) \varphi_3(2) \end{vmatrix} \equiv \hat{a}_1^\dagger \hat{a}_3^\dagger |\mathrm{VAC}\rangle \,, \tag{2.62}$$

$$\frac{1}{\sqrt{2}} \begin{vmatrix} \varphi_1^*(1) \varphi_3^*(2) \end{vmatrix} \equiv \langle \mathrm{VAC}| \hat{a}_3 \hat{a}_1 . \tag{2.63}$$

It can be shown that the annihilation and creation operators for fermions obey the following anticommutator relations:[56]

$$\left[\hat{a}_p^\dagger, \hat{a}_q^\dagger\right]_+ = 0, \tag{2.64}$$

$$\left[\hat{a}_p, \hat{a}_q\right]_+ = 0, \tag{2.65}$$

$$\left[\hat{a}_p^\dagger, \hat{a}_q\right]_+ = \delta_{pq}. \tag{2.66}$$

Operators in second quantization are composed of integrals and strings of creation and annihilation operators such that the Slater-Condon rules[47] are satisfied. One- and two-electron operators of the form $\hat{O}_1 = \sum_\alpha \hat{o}_1(\alpha)$ and $\hat{O}_2 = \frac{1}{2} \sum_{\alpha,\beta} \hat{o}_2(\alpha, \beta)$ in first quantization are expressed in second quantization as:

$$\hat{O}_1 = \sum_{p,q} \underbrace{\langle \varphi_p | \hat{o}_1 | \varphi_q \rangle}_{o_{1_{pq}}} \hat{a}_p^\dagger \hat{a}_q, \tag{2.67}$$

$$\hat{O}_2 = \frac{1}{4} \sum_{p,q,r,s} \underbrace{\langle \varphi_p \varphi_q | \hat{o}_2 | \varphi_r \varphi_s \rangle - \langle \varphi_p \varphi_q | \hat{o}_2 | \varphi_s \varphi_r \rangle}_{\langle pq || rs \rangle} \hat{a}_p^\dagger \hat{a}_q^\dagger \hat{a}_s \hat{a}_r. \tag{2.68}$$

To simplify the evaluation of expectation values $\langle \Phi_I | \hat{O} | \Phi_I \rangle$, the concept of normal ordering is introduced. [56] An operator is normal ordered when all creation operators are left of all annihilation operators. The vacuum expectation value of a normal ordered operator is always zero as long as any creation or annihilation operator is present:

$$\begin{aligned} \mathrm{N}(\dots \hat{a}_p^\dagger \dots \hat{a}_q \dots)\, |\mathrm{VAC}\rangle &= 0, \\ \langle \mathrm{VAC}|\, \mathrm{N}(\dots \hat{a}_p^\dagger \dots \hat{a}_q \dots) &= 0, \\ \Rightarrow \langle \mathrm{VAC} | \mathrm{N}(\dots \hat{a}_p^\dagger \dots \hat{a}_q \dots) | \mathrm{VAC} \rangle &= 0. \end{aligned} \tag{2.69}$$

$\mathrm{N}(\dots)$ denotes the normal order of an operator string that is obtained by antisymmetric pairwise interchanging of the single creation and annihilation operators. Wick's theorem [56] (2.70) provides instructions to rewrite a string of creation and annihilation operators $\hat{A} = \dots \hat{a}_p^\dagger \hat{a}_q \hat{a}_r \dots$ using so-called contractions such that it is given in normal-ordered form:

$$\hat{A} = \mathrm{N}(\hat{A}) + \sum_{\text{1-fold}} \mathrm{N}(\overbracket{\hat{A}}) + \sum_{\text{2-fold}} \mathrm{N}(\overbracket{\overbracket{\hat{A}}}) + \dots \tag{2.70}$$

A contraction between two operators $\hat{A}$ and $\hat{B}$ is defined as the difference between their product and its normal-ordered form:

$$\overbracket{\hat{A}\hat{B}} = \hat{A}\hat{B} - \mathrm{N}(\hat{A}\hat{B}). \tag{2.71}$$

In post-HF methods, a more suitable starting point than the vacuum state $|\mathrm{VAC}\rangle$ is the HF determinant. In order to define the latter as a vacuum, meaning that all respective occupation numbers are zero, occupied and virtual spin orbitals need to be treated differently. In the so-called particle-hole-formalism, occupied spin orbitals are now referred to as holes whereas virtual spin orbitals are denoted as particles. Therefore, the new quasiparticle creation operators are the $\{\hat{a}_i\}$ (create holes) and $\{\hat{a}_a^\dagger\}$ (create particles) while the quasiparticle annihilation operators are given by $\{\hat{a}_i^\dagger\}$ (annihilate holes) and $\{\hat{a}_a\}$ (annihilate particles). Normal ordering with respect to the HF reference (the so-called Fermi vacuum) is denoted by $\{\dots\}$ instead of $\mathrm{N}(\dots)$. Thereby, the

Hamiltonian in its normal-ordered form in second quantization is given by

$$\hat{H} = E_{\mathrm{HF}} + \sum_{p,q} f_{pq} \left\{\hat{a}_p^\dagger \hat{a}_q\right\} + \frac{1}{4} \sum_{p,q,r,s} \langle pq||rs\rangle \left\{\hat{a}_p^\dagger \hat{a}_q^\dagger \hat{a}_s \hat{a}_r\right\} \tag{2.72}$$

with the Fock matrix elements

$$f_{pq} = \langle \varphi_p | \hat{F} | \varphi_q \rangle . \tag{2.73}$$

2.4 Configuration interaction

A formally exact solution of the SE is obtained by parametrizing the wave function $|\Psi\rangle$ as a linear combination of N-electron Slater determinants forming a complete basis $\{|\Phi_I\rangle\}$

$$|\Psi\rangle = \sum_I c_I |\Phi_I\rangle \tag{2.74}$$

and optimizing the coefficients c_I by using the variational method. This is called the configuration interaction (CI) approach. [45] The CI coefficients are determined by minimizing the energy expression

$$\tilde{E} = \langle \Psi | \hat{H} | \Psi \rangle - \lambda \left(\sum_J |c_I|^2 - 1 \right) . \tag{2.75}$$

Here, the normalization of the CI wave function

$$\langle \Psi | \Psi \rangle = \sum_I |c_I|^2 = 1 \tag{2.76}$$

is considered via the method of Lagrange multipliers (here: λ). The minimization yields

$$\delta\tilde{E} = \sum_I \delta c_I^* \left(\sum_J \langle \Phi_I | \hat{H} | \Phi_J \rangle c_J - \lambda c_I \right) + \text{complex conj.} \overset{!}{=} 0. \tag{2.77}$$

Eq. (2.77) only holds if the term in brackets is zero. Recasting it in a matrix equation and realizing that $\lambda = E$ yields

$$\sum_J \underbrace{\langle \Phi_I | \hat{H} | \Phi_J \rangle}_{H_{IJ}} c_J = E c_I$$

$$\boldsymbol{H}\boldsymbol{c} = E\boldsymbol{c}. \tag{2.78}$$

Accordingly, using Eq. (2.74) as an ansatz and invoking the variational principle is equivalent to diagonalizing the N-electron Hamiltonian in the determinantal basis

$\{|\Phi_I\rangle\}$. This yields energy eigenvalues E and corresponding eigenvectors $\boldsymbol{c}$ that contain the wave-function coefficients c_I. In an actual calculation, several roots of $\boldsymbol{H}$ may be determined by the iterative Davidson procedure [57] (see Chpt. 3.3.2).

In practice, the $|\Phi_I\rangle$ are constructed from only a limited set of $2M$ spin orbitals. Consequently, for a closed-shell system, $\binom{M}{N/2}^2$ Slater determinants can be formed which makes the diagonalization space finite and, therefore, incomplete. However, diagonalization in the full space of a given finite basis (the so-called full CI (FCI) approach [45]) provides the exact solution within the respective basis-set approximation.

Rewriting Eq. (2.74) using the classification of determinants by their degree of excitation with respect to the HF determinant gives

$$|\Psi\rangle = c_0 \, |\Phi_0\rangle + \sum_i \sum_a c_i^a \, |\Phi_i^a\rangle + \sum_{i<j} \sum_{a<b} c_{ij}^{ab} \, |\Phi_{ij}^{ab}\rangle + \ldots \tag{2.79}$$

This can be re-expressed by introducing excitation operators

$$\hat{C}_{ijk\ldots}^{abc\ldots} = c_0^{-1} \cdot c_{ijk\ldots}^{abc\ldots} \hat{\tau}_{ijk\ldots}^{abc\ldots} = c_0^{-1} \cdot c_{ijk\ldots}^{abc\ldots} \hat{a}_a^\dagger \hat{a}_b^\dagger \hat{a}_c^\dagger \ldots \hat{a}_k \hat{a}_j \hat{a}_i \tag{2.80}$$

that generate the excited determinants $|\Phi_{ijk\ldots}^{abc\ldots}\rangle$ when acting upon the HF reference wave function:

$$|\Psi\rangle = \left(1 + \sum_i \sum_a \hat{C}_i^a + \sum_{i<j} \sum_{a<b} \hat{C}_{ij}^{ab} + \ldots \right) |\Phi_0\rangle \, . \tag{2.81}$$

This FCI approach is only practical for small systems with few electrons and using comparatively small basis sets. The number of possible Slater determinants grows factorially with the number of basis functions and so does the computing time for solving the eigenvalue problem. Hence, the wave function may be approximated by including only certain classes of excitations. E.g., including the HF as well as all singly excited determinants yields the CI singles (CIS) method (see, e.g., Ref. [58]). However, the CIS method does not account for any correlation effects and can be viewed as a HF method for excited states. Additionally including double excitations yields the (CISD) method [45]. Here, correlation effects are described to some extent and computing times are greatly decreased ($\mathcal{O}(N^6)$) with respect to the FCI approach. The additional consideration of triple excitations yields the CISDT method [45] ($\mathcal{O}(N^8)$) that recovers a larger part of the FCI energy as compared to CISD, etc. However, truncated CI approaches go along with the loss of size-extensivity. [45] This means that these methods do not show the proper linear scaling behavior of the energy with respect to the size of the system. An illustrative model system to show this is the supermolecule of two infinitely seperated H_2 molecules in a minimal basis. [59] For each H_2 molecule, the CI doubles

(CID) wave function is exact.[2] As the two molecules do not interact, the energy of the supermolecule is equal to the sum of the single molecules' energies. In accordance with the superposition principle, the wave function of the supermolecule $|\Psi_{\mathrm{A+B}}\rangle$ is obtained by taking the antisymmetrized product of the wave functions of the subsystems A and B that are given as $|\Psi^{\mathrm{CID}}_{\mathrm{A/B}}\rangle = (1+\hat{C}^{\mathrm{A/B}}_{\mathrm{D}})\,|\Phi^{\mathrm{A/B}}_0\rangle$:

$$\begin{aligned}|\Psi_{\mathrm{A+B}}\rangle &= (1+\hat{C}^{\mathrm{A}}_{\mathrm{D}})\,|\Phi^{\mathrm{A}}_0\rangle \cdot (1+\hat{C}^{\mathrm{B}}_{\mathrm{D}})\,|\Phi^{\mathrm{B}}_0\rangle \\ &= (1+\hat{C}^{\mathrm{A}}_{\mathrm{D}}+\hat{C}^{\mathrm{B}}_{\mathrm{D}}+\hat{C}^{\mathrm{A}}_{\mathrm{D}}\hat{C}^{\mathrm{B}}_{\mathrm{D}})\,|\Phi^{\mathrm{A}}_0\Phi^{\mathrm{B}}_0\rangle \neq |\Psi^{\mathrm{CID}}_{\mathrm{A+B}}\rangle\,. \end{aligned} \tag{2.82}$$

However, the CID wave function of the supermolecule misses by definition the quadruply excited determinant which leads to the lack of size-extensivity in approximated CI expansions. But since size-extensivity is a highly desirable property of a quantum-chemical method, nowadays, truncated CI calculations are rarely used due to better alternatives.

2.5 Coupled-cluster theory

In Eq. (2.82), it was shown that the lack of size-extensivity for CID (and all other truncated CI methods) arises from the representation of the combined system's wave function as a *sum* of the different excitation operators

$$|\Psi^{\mathrm{CID}}_{\mathrm{A+B+\ldots}}\rangle = \left(1+\sum_{i=\mathrm{A,B,\ldots}}\hat{C}_{D,i}\right)|\Phi_0\rangle\,. \tag{2.83}$$

However, the exact wave function demands a *product* form:

$$|\Psi^{\mathrm{correct}}_{\mathrm{A+B+\ldots}}\rangle = \prod_{i=A,B,\ldots}\left(1+\hat{C}_{D,i}\right)|\Phi_0\rangle\,. \tag{2.84}$$

It can be recast in an exponential form:

$$|\Psi^{\mathrm{correct}}_{\mathrm{A+B+\ldots}}\rangle = \exp\left(\sum_{i=\mathrm{A,B,\ldots}}\hat{C}_{D,i}\right)|\Phi_0\rangle\,. \tag{2.85}$$

The exponential function of an operator is defined via the series expansion

$$\mathrm{e}^{\hat{A}} = 1+\hat{A}+\frac{1}{2!}\hat{A}^2+\frac{1}{3!}\hat{A}^3+\ldots \tag{2.86}$$

---

[2] Single excitations do not contribute to the final wave function due to symmetry reasons.

The wave-function ansatz (2.85) shows the correct separability into the wave functions of the subsystems. Consequently, the additivity of the total energy is ensured which is a weak condition for size-extensivity. [59] This motivates the exponential ansatz for the wave function of the coupled-cluster (CC) method: [59–61]

$$|\Psi\rangle = \mathrm{e}^{\hat{T}} |\Phi_0\rangle \,. \tag{2.87}$$

$\hat{T}$ is the cluster operator and $|\Phi_0\rangle$ is the reference wave function which is usually the HF determinant. The cluster operator

$$\hat{T} = \hat{T}_1 + \hat{T}_2 + \hat{T}_3 + \cdots + \hat{T}_N \tag{2.88}$$

generates singly, doubly, ..., N-foldly excited determinants when acting on the reference. The $\hat{T}_n$ are defined analogously to the excitation operators used for the CI methods shown in Eq. (2.80)

$$\hat{T}_1 = \sum_i \sum_a t_i^a \; \hat{a}_a^\dagger \hat{a}_i, \tag{2.89}$$

$$\hat{T}_2 = \frac{1}{4} \sum_{i,j} \sum_{a,b} t_{ij}^{ab} \; \hat{a}_a^\dagger \hat{a}_b^\dagger \hat{a}_j \hat{a}_i, \tag{2.90}$$

$$\hat{T}_3 = \frac{1}{36} \sum_{i,j,k} \sum_{a,b,c} t_{ijk}^{abc} \; \hat{a}_a^\dagger \hat{a}_b^\dagger \hat{a}_c^\dagger \hat{a}_k \hat{a}_j \hat{a}_i, \tag{2.91}$$

$$\ldots$$

with strings of quasiparticle creation operators and weighting factors $t_{ijk\ldots}^{abc\ldots}$ called amplitudes. Note that the series expansion (2.86) for $\mathrm{e}^{\hat{T}}$ terminates naturally after the term of power N. The FCI wave function is retrieved for $\hat{T} = \sum\limits_{n=1}^{N} \hat{T}_n$. However, $\hat{T}$ is truncated to reduce the computational effort but, in contrast to truncated CI methods, the resulting CC schemes are size-extensive. A hierarchy of CC methods with different accuracy and computational scaling can be defined:

- $\hat{T} = \hat{T}_2$: CC doubles (CCD), [60, 62, 63] $\mathcal{O}(N^6)$
- $\hat{T} = \hat{T}_1 + \hat{T}_2$: CC singles doubles (CCSD), [64] $\mathcal{O}(N^6)$
- $\hat{T} = \hat{T}_1 + \hat{T}_2 + \hat{T}_3$: CC singles doubles triples (CCSDT), [65–67] $\mathcal{O}(N^8)$
- $\ldots$

A popular scheme is given by the CCSD(T) method [68] in which a CCSD result is refined by adding a correction accounting for a perturbative treatment of triple excitations. The

advantage lies in reduced computational cost of $\mathcal{O}(N^7)$ as compared to that of CCSDT, i.e., $\mathcal{O}(N^8)$. Since the quality of the results is as good or often even better as compared to CCSDT, CCSD(T) is frequently referred to as the 'gold standard' of quantum chemistry producing an accuracy of often < 1 $^{\text{kcal}}/_{\text{mol}}$ for the correlation energy. [69]
Given the same truncation level, CC results are superior to their CI counterparts due to the disconnected terms in the wave function that ensure size-extensivity and because of the implicit consideration of higher excitations. E.g., for CCD:

$$\mathrm{e}^{\hat{T}_2} = 1 + \underbrace{\overbrace{\hat{T}_2}^{\text{connected}}}_{\text{2-fold}} + \frac{1}{2}\underbrace{\overbrace{\hat{T}_2^2}^{\text{disconnected}}}_{\text{4-fold}} + \dots \tag{2.92}$$

In order to obtain expressions for the energy and the wave-function parameters, the SE $\hat{H}\left|\Psi_{\text{CC}}\right\rangle = E_{\text{CC}}\left|\Psi_{\text{CC}}\right\rangle$ is premultiplied by $\mathrm{e}^{-\hat{T}}$. Projection onto the reference determinant yields the energy equation

$$\left\langle\Phi_0\right| \mathrm{e}^{-\hat{T}}\hat{H}_{\text{N}}\mathrm{e}^{\hat{T}}\left|\Phi_0\right\rangle = \Delta E_{\text{corr}}. \tag{2.93}$$

Projection onto all excited determinants $\left|\Phi_I\right\rangle$ that can be produced by $\hat{T}$ generates a set of non-linear so-called amplitude equations

$$\left\langle\Phi_I\right| \mathrm{e}^{-\hat{T}}\hat{H}_{\text{N}}\mathrm{e}^{\hat{T}}\left|\Phi_0\right\rangle = 0. \tag{2.94}$$

$\Delta E_{\text{corr}} = E_{\text{CC}} - E_{\text{HF}}$ is the correlation energy and $\hat{H}_{\text{N}}$ is the normal ordered Hamiltonian subtracted by the HF energy:

$$\hat{H}_{\text{N}} = \sum_{p,q} f_{pq}\left\{\hat{a}_p^\dagger\hat{a}_q\right\} + \frac{1}{4}\sum_{p,q,r,s}\langle pq||rs\rangle\left\{\hat{a}_p^\dagger\hat{a}_q^\dagger\hat{a}_s\hat{a}_r\right\} = \hat{F} + \hat{W}. \tag{2.95}$$

The similarity transformed Hamiltonian $\mathrm{e}^{-\hat{T}}\hat{H}_{\text{N}}\mathrm{e}^{\hat{T}}$ can be rewritten using the Baker-Campbell-Hausdorff (BCH) expansion in order to obtain algebraic expressions. This yields the bare Hamiltonian and commutators with the cluster operator: [59]

$$\mathrm{e}^{-\hat{T}}\hat{H}_{\text{N}}\mathrm{e}^{\hat{T}} = \hat{H}_{\text{N}} + \left[\hat{H}_{\text{N}}, \hat{T}\right] + \frac{1}{2!}\left[\left[\hat{H}_{\text{N}}, \hat{T}\right], \hat{T}\right] + \dots \tag{2.96}$$

For further simplifications, the commutators can be evaluated using an extension to Wick's theorem [56] (2.97) that states how to bring the product of two already normal ordered operators into normal-ordered form:

$$\hat{A}\hat{B} = \{\hat{A}\hat{B}\} + \sum_{\text{1-fold}}\{\overline{\hat{A}\hat{B}}\} + \sum_{\text{2-fold}}\{\overline{\overline{\hat{A}\hat{B}}}\} + \dots \tag{2.97}$$

Evaluating the first commutator in (2.96) then gives: [56]

$$\begin{aligned}
\left[\hat{H}_{\mathrm{N}},\hat{T}\right] = \hat{H}_{\mathrm{N}}\hat{T}-\hat{T}\hat{H}_{\mathrm{N}} = & \overbrace{\left\{\hat{H}_{\mathrm{N}}\hat{T}\right\}-\left\{\hat{T}\hat{H}_{\mathrm{N}}\right\}}^{=0} \\
& + \sum_{\text{1-fold}}\left\{\overset{\sqcap}{\hat{H}_{\mathrm{N}}\hat{T}}\right\} - \sum_{\text{1-fold}}\overbrace{\left\{\overset{\sqcap}{\hat{T}\hat{H}_{\mathrm{N}}}\right\}}^{=0} \\
& + \sum_{\text{2-fold}}\left\{\overset{\overline{\sqcap}}{\hat{H}_{\mathrm{N}}\hat{T}}\right\} - \sum_{\text{2-fold}}\overbrace{\left\{\overset{\overline{\sqcap}}{\hat{T}\hat{H}_{\mathrm{N}}}\right\}}^{=0} + \dots \\
& \equiv \left(\hat{H}_{\mathrm{N}}\hat{T}\right)_{\mathrm{c}}\,. \qquad (2.98)
\end{aligned}$$

The index 'c' implies that the expression only includes so-called connected terms in which $\hat{H}_{\mathrm{N}}$ is at least singly contracted with a $\hat{T}$-operator to its right. All terms that exhibit contractions within the product $\hat{T}\hat{H}_{\mathrm{N}}$ vanish since $\hat{T}$ solely consists of quasiparticle creation operators which makes the product already normal ordered. As a result, the full series expansion is given by:

$$\begin{aligned}
\mathrm{e}^{-\hat{T}}\hat{H}_{\mathrm{N}}\mathrm{e}^{\hat{T}} = & \hat{H}_{\mathrm{N}} + (\hat{H}_{\mathrm{N}}\hat{T})_{\mathrm{c}} + \frac{1}{2!}((\hat{H}_{\mathrm{N}}\hat{T})_{\mathrm{c}}\hat{T})_{\mathrm{c}} + \frac{1}{3!}(((\hat{H}_{\mathrm{N}}\hat{T})_{\mathrm{c}}\hat{T})_{\mathrm{c}}\hat{T})_{\mathrm{c}} \\
& + \frac{1}{4!}((((\hat{H}_{\mathrm{N}}\hat{T})_{\mathrm{c}}\hat{T})_{\mathrm{c}}\hat{T})_{\mathrm{c}}\hat{T})_{\mathrm{c}} \equiv \left(\hat{H}_{\mathrm{N}}\mathrm{e}^{\hat{T}}\right)_{\mathrm{c}} \qquad (2.99)
\end{aligned}$$

The expansion terminates after the fourfold connected term as $\hat{H}_{\mathrm{N}}$ contains operator strings of four operators at most that can be contracted with the cluster operator.

2.5.1 A diagrammatic approach

The evaluation of the CC expressions

$$\langle\Phi_0|\,\hat{H}_{\mathrm{N}} + (\hat{H}_{\mathrm{N}}\hat{T})_{\mathrm{c}} + \frac{1}{2!}((\hat{H}_{\mathrm{N}}\hat{T})_{\mathrm{c}}\hat{T})_{\mathrm{c}} + \dots\;|\Phi_0\rangle = \Delta E_{\mathrm{corr}}, \qquad (2.100)$$

$$\langle\Phi_I|\,\hat{H}_{\mathrm{N}} + (\hat{H}_{\mathrm{N}}\hat{T})_{\mathrm{c}} + \frac{1}{2!}((\hat{H}_{\mathrm{N}}\hat{T})_{\mathrm{c}}\hat{T})_{\mathrm{c}} + \dots\;|\Phi_0\rangle = 0 \qquad (2.101)$$

to obtain algebraic expressions is greatly facilitated by using antisymmetrized Brandow-type diagrams. [70] As seen before in Eqs. (2.67) and (2.68), every operator in second quantization is represented by a matrix element and a string of quasiparticle creation and annihilation operators. A graphic equivalent can be defined for each operator by using the following set of rules: [59]

1. An individual symbol is assigned to each type of operator. E.g., the elements of

the cluster operator $\hat{T}$ are represented by a solid line whereas dashed lines are chosen for the Fock matrix elements and the two-electron integrals. The former are marked by an additional cross.

2. Each symbol is provided with as many vertices as there are pairs of creation and annihilation operators. E.g., the $\hat{T}_1$-operator has one vertex, the $\hat{T}_2$-operator has two, etc.

3. Every quasiparticle operator is depicted by a line starting from one vertex. There is a maximum of two lines located at one vertex. Annihilation operators are located below a vertex, creation operators above.

4. An arrow is assigned to each line. Arrows pointing downward represent hole lines (occupied orbitals) while particle lines (virtual orbitals) come with an upward pointing arrow. Not more than one arrow can point to or away from a vertex.

The same rules can in principle be applied to determinants since they can be represented by a string of quasiparticle operators acting upon a vacuum reference according to Eqs. (2.62) and (2.63). However, they are usually left out in diagrams for the sake of clarity. The graphic counterparts to the first elements of $\hat{T}$ and all elements of $\hat{H} = \hat{F} + \hat{W}$ are shown in Fig. 2.1.

Any matrix element $\langle \Phi_I | \dots \hat{A}\hat{B} \dots | \Phi_J \rangle$ can now be depicted by drawing the diagrams of the corresponding operators. In doing so, operators on the left are placed at the top of the new diagram and operators on the right at the bottom. Consistent with Wick's theorem, two operators can now graphically be contracted: The different operator diagrams are connected by direct linking of lines with their arrows pointing into the same direction. In order for the diagram to be valid for the considered matrix element, the lines that are left after the linking process have to match those representing the determinants $\langle \Phi_I |$ and $| \Phi_J \rangle$, respectively. As an example, Fig. 2.2 lists all contributions to the CC (except for CCD) energy (2.100). As both the bra and ket determinant are the HF reference, all energy diagrams need to be closed, meaning that after the contractions no open lines should remain. As all CC equations only exhibit connected terms, every T_n-operator has to be connected to the Hamiltonian. In the diagrammatic context, this means that every $\hat{T}_n$-diagram has to share at least one line with the respective $\hat{H}$-diagram. When assembled, every diagram can be converted into an algebraic expression by applying the following rules: [59]

1. Open lines are pairwise marked with their corresponding target indices representing the indices of the determinants $\langle \Phi_{ij\dots}^{ab\dots} |$ and $| \Phi_{kl\dots}^{cd\dots} \rangle$, respectively. Connecting

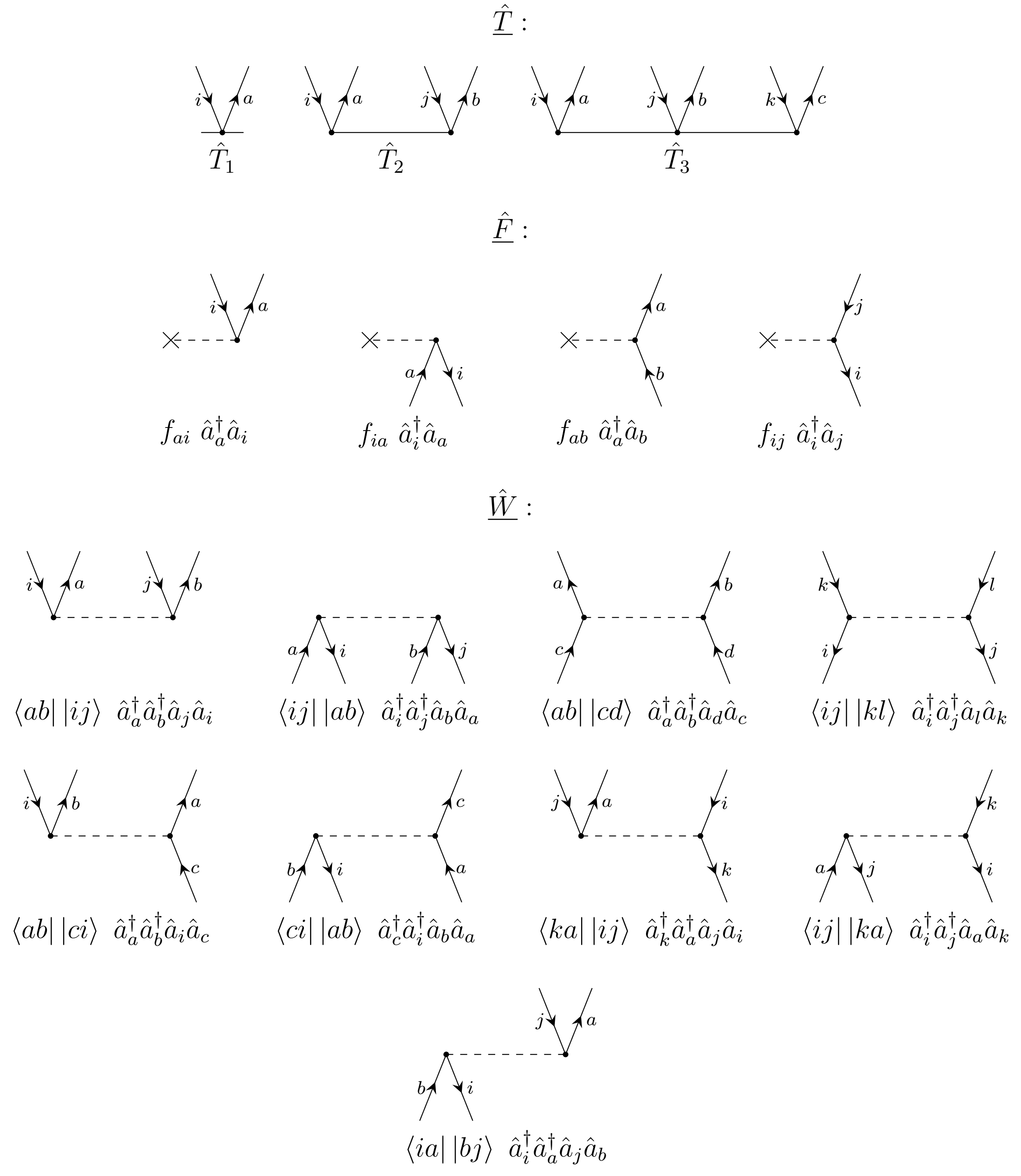

Figure 2.1: Diagrammatic representation of the excitation operators $\hat{T}_1$ to $\hat{T}_3$ as well as all elements of the Hamiltonian.

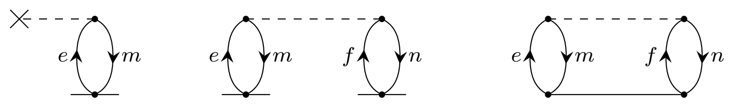

Figure 2.2: Diagrammatic representation of the energy equations for CCSD and higher levels of theory.

lines are called internal. Internal hole lines are labeled with m, n, ... whereas internal particle lines are denoted by e, f, ... Internal indices make up the summation indices.

2. Every operator contributes a matrix element:
    - One-particle vertices $\hat{F}$ (see Eq. (2.95)) are associated with a Fock matrix element $f_{\text{out},\text{in}}$ with the indices of the out- and in-going arrow.
    - Two-particle vertices $\hat{W}$ (see Eq. (2.95)) contribute an antisymmetrized two-electron integral $\langle$left-out right-out$|\,|$left-in right-in$\rangle$.
    - $\hat{T}_i$-vertices are associated with an amplitude $t_{ij\cdots}^{ab\cdots}$. Here, i and a as well as j and b are positioned pairwise at the same vertex.
3. n internal lines are equivalent to each other if they identically connect vertices of the same two operators. Each n-tuple of equivalent internal lines gives a factor of $1/n!$.
4. Each n-tuple of $\hat{T}_i$-operators that are identically connected to the same operator gives a factor of $1/n!$.
5. The sign of the term is determined by $(-1)^{l+h}$. h is the number of internal hole lines while l is the number of loops. A loop is defined as a closed arrow path between the vertices of at least two operators.
6. For target hole and particle lines x and y of the bra or ket state, respectively, emerging from vertices of different operator diagrams, antisymmetric permutations $P_{-}(xy)$ have to be taken into account.

Applying these rules to the diagrams given in Fig. 2.2 yields:

$$\Delta E_{\text{corr}} = \sum_{e}\sum_{m} f_{me}\ t_m^e + \frac{1}{2}\sum_{e,f}\sum_{m,n} \langle mn|\,|ef\rangle\ t_m^e\ t_n^f + \frac{1}{4}\sum_{e,f}\sum_{m,n} \langle mn|\,|ef\rangle\ t_{mn}^{ef}. \quad (2.102)$$

The diagrams and algebraic expressions for the CCSD and CCSDT amplitude equations as well as the perturbative triples correction are given in Appendix A.

2.6 Equation-of-motion coupled-cluster theory

CC is essentially a ground state method which makes targeting excited states difficult. [71] Additionally, it demands the HF reference determinant to be a good approximation to the exact wave function in order to give sound results. [38] The so-called equation-of-motion (EOM) CC methods [37,72] extend CC theory to the treatment of excited, ionized, and electron-attached states. They also allow for targeting states with multiconfigurational character within a single reference framework. [37,73,74] The EOM wave function

$|\Psi_{\mathrm{EOM}}\rangle$ is parametrized in a linear CI-like fashion with respect to the CC reference wave function $|\Psi_{\mathrm{CC}}\rangle$:

$$|\Psi_{\mathrm{EOM}}\rangle = \hat{\mathcal{R}}\,|\Psi_{\mathrm{CC}}\rangle\,, \tag{2.103}$$

$$\hat{\mathcal{R}} = \hat{\mathcal{R}}_0 + \hat{\mathcal{R}}_1 + \hat{\mathcal{R}}_2 + \ldots \tag{2.104}$$

The operators $\hat{\mathcal{R}}_n$ are defined as

$$\hat{\mathcal{R}}_n = \sum_{\mu} r_{\mu}^{(n)}\,\hat{\Omega}_{\mu}^{(n)}, \tag{2.105}$$

where the weigthing factors $r_{\mu}^{(n)}$ are the $\hat{\mathcal{R}}$-amplitudes and $\hat{\Omega}_{\mu}^{(n)}$ are strings of quasiparticle creation operators $\{\hat{a}_a^{\dagger}\}$ and $\{\hat{a}_i\}$. While the definition of the $\hat{\Omega}_{\mu}^{(n)}$ is different for the various EOM methods, the general EOM-CC equations are the same. Inserting the ansatz (2.103) into the SE and subtracting the reference energy E_{CC} gives

$$(\hat{H} - E_{\mathrm{CC}})\hat{\mathcal{R}}\mathrm{e}^{\hat{T}}\,|\Phi_0\rangle = \Delta E_{\mathrm{exc}}\hat{\mathcal{R}}\mathrm{e}^{\hat{T}}\,|\Phi_0\rangle\,. \tag{2.106}$$

As $\hat{\mathcal{R}}$ and $\mathrm{e}^{\hat{T}}$ commute, inserting a resolution of the identity and projection onto all $|\Phi_I\rangle$ that can be produced by letting $\hat{\mathcal{R}}$ act upon $|\Phi_0\rangle$ gives

$$\begin{aligned}\sum_J \langle\Phi_I|\underbrace{\mathrm{e}^{-\hat{T}}(\hat{H} - E_{\mathrm{CC}})\mathrm{e}^{\hat{T}}}_{\bar{H}}|\Phi_J\rangle\,\langle\Phi_J|\,\hat{\mathcal{R}}\,|\Phi_0\rangle &= \Delta E_{\mathrm{exc}}\,\langle\Phi_I|\,\hat{\mathcal{R}}\,|\Phi_0\rangle \\ \sum_J \bar{H}_{IJ} r_J &= \Delta E_{\mathrm{exc}} r_I.\end{aligned} \tag{2.107}$$

$\bar{H}_{IJ}$ are the elements of the non-Hermitian matrix $\bar{\boldsymbol{H}}$ and r_J are the $\hat{\mathcal{R}}$-amplitudes. The equation can be recast in its algebraic form:

$$\bar{\boldsymbol{H}}\boldsymbol{r} = \Delta E_{\mathrm{exc}}\boldsymbol{r}. \tag{2.108}$$

Due to the fact that the similarity transformed Hamiltonian $\bar{\boldsymbol{H}}$ is not Hermitian, there exists a set of different left eigenvectors to the same spectrum of eigenvalues. They satisfy the eigenvalue problem

$$\boldsymbol{l}\bar{\boldsymbol{H}} = \Delta E_{\mathrm{exc}}\boldsymbol{l} \tag{2.109}$$

and correspond to the weighting factors $l_{\mu}^{(n)}$ of a de-excitation operator $\hat{\mathcal{L}}$ with

$$\hat{\mathcal{L}} = \hat{\mathcal{L}}_0 + \hat{\mathcal{L}}_1 + \hat{\mathcal{L}}_2 + \ldots, \tag{2.110}$$

$$\hat{\mathcal{L}}_n = \sum_{\mu} l_{\mu}^{(n)}\,\hat{\Omega}_{\mu}^{\dagger(n)}. \tag{2.111}$$

In contrast to the eigenvectors of a Hermitian matrix, $\boldsymbol{l}_K$ and $\boldsymbol{r}_K$ to an eigenvalue $\Delta E_{\text{exc}}^{(K)}$ are not Hermitian transposes with respect to each other. In addition, the sets $\{\boldsymbol{l}_K\}$ and $\{\boldsymbol{r}_K\}$ are not orthogonal among themselves but biorthogonal among each other and can be chosen such that

$$\boldsymbol{l}_K \boldsymbol{r}_L = \langle \Phi_0 | \hat{\mathcal{L}}_K \hat{\mathcal{R}}_L | \Phi_0 \rangle = \delta_{KL}. \tag{2.112}$$

However, the EOM eigenvalue problem is similar to the CI eigenvalue problem and the EOM energy can be determined in an analog way by diagonalizing the $\bar{\boldsymbol{H}}$ matrix using a modified Davidson procedure. [75] Considering the complete EOM operator $\hat{\mathcal{R}}$ gives the FCI wave function for any choice of $\hat{T}$. For actual calculations, it has to be truncated due to the limitation of computational resources. With the same truncation level for $\hat{T}$ and $\hat{\mathcal{R}}$, the standard hierarchy [76] of EOM methods is obtained: EOM-CCSD, EOM-CCSDT, ... It is important to note that in contrast to truncated CI methods EOM excitation energies are size-intensive[3] even if the $\hat{\mathcal{R}}$-operator is truncated.

2.6.1 Variants of EOM-CC theory

The equations defining the matrix-vector product $\bar{\boldsymbol{H}}\boldsymbol{r}$ depend on the choice of the $\hat{\Omega}_\mu^{(n)}$. They can be characterized in terms of particle and spin conservation and give rise to a variety of EOM variants. Four methods have been implemented within the scope of this work: EOM-CC for electronically excited states (EE), [38] spin-flip (SF), [39–41] ionization potential (IP), [42] and electron attachment (EA) [43] (see Fig. 2.3 for an overview). They are introduced in the following paragraphs in detail. The working equations in spin-orbital basis used for the implementation are given in Appendix B.2-B.4 for all EOM variants with further remarks on factorizations where necessary.

EOM-CC for electronically excited states

The EOM-EE method is defined by $\hat{\mathcal{R}}$ being both particle and M_S-conserving. This means that all $\hat{\mathcal{R}}_n$ consist of strings of pairs of quasiparticle creation operators $\hat{a}_a^\dagger \hat{a}_i$ and that each pair acts upon orbitals of the same spin. Using the convention to denote β-spin orbitals with an overbarred index, the spin-integrated EOM-EE operator is given

---

[3] A property is referred to as size-intensive if its value is independent of the size of the system. [77]

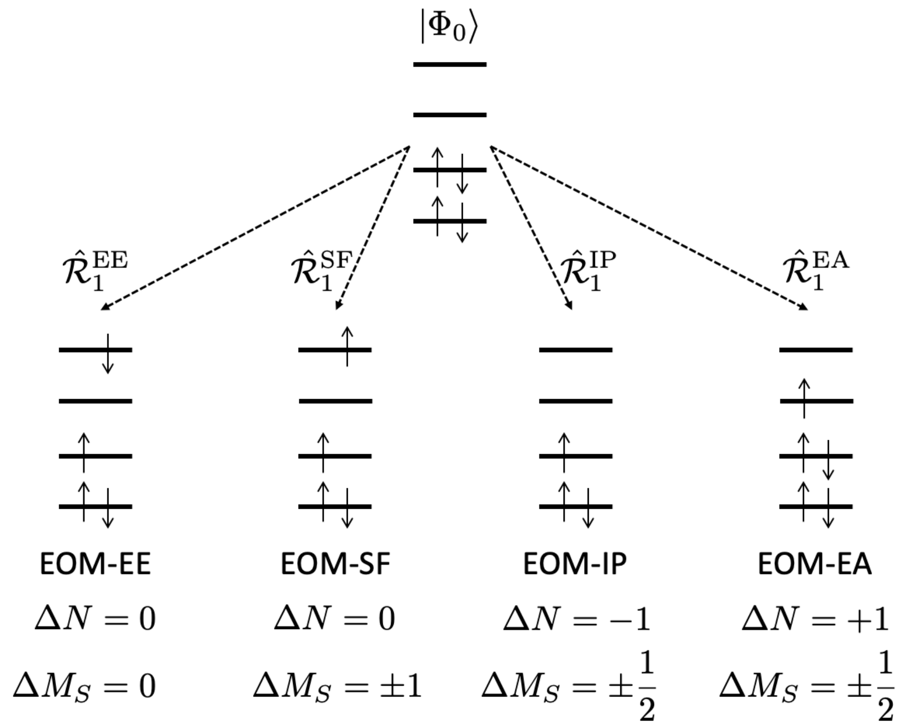

Figure 2.3: Illustration of the action of an $\hat{\mathcal{R}}_1$-operator upon a reference determinant for the different EOM-CC variants.

as

$$\begin{aligned}\hat{\mathcal{R}}_{\mathrm{EE}} = r_0 &+ \sum_i \sum_a r_i^a\ \hat{a}_a^\dagger \hat{a}_i + \sum_{\bar{i}} \sum_{\bar{a}} r_{\bar{i}}^{\bar{a}}\ \hat{a}_{\bar{a}}^\dagger \hat{a}_{\bar{i}} \\ &+ \frac{1}{4} \sum_{i,j} \sum_{a,b} r_{ij}^{ab}\ \hat{a}_a^\dagger \hat{a}_b^\dagger \hat{a}_j \hat{a}_i + \frac{1}{4} \sum_{\bar{i},\bar{j}} \sum_{\bar{a},\bar{b}} r_{\bar{i}\bar{j}}^{\bar{a}\bar{b}}\ \hat{a}_{\bar{a}}^\dagger \hat{a}_{\bar{b}}^\dagger \hat{a}_{\bar{j}} \hat{a}_{\bar{i}} \\ &+ \sum_i \sum_{\bar{j}} \sum_a \sum_{\bar{b}} r_{i\bar{j}}^{a\bar{b}}\ \hat{a}_a^\dagger \hat{a}_{\bar{b}}^\dagger \hat{a}_{\bar{j}} \hat{a}_i + \ldots \end{aligned} \tag{2.113}$$

The spectrum of target systems for EOM-EE is rather broad. Most prominently, it is the method of choice to calculate excitation energies and transition probabilities needed to predict electronic absorption spectra. [76] Starting with a well-behaved reference wave function describing the electronic ground state of a system, an in principle arbitrary number of electronically excited states can be modeled and their corresponding excitation energies determined within a single EOM-EE calculation. Moreover, EOM-EE allows for the description of open-shell singlets within a single-reference formalism, [37] while targeting such states directly requires more involved approaches, e.g., those from multireference (MR) CC theory. [59] Additionally, calculations on closed-shell reference wave functions give access to triplet states with $M_S = 0$ where due to symmetry reasons the r_i^a and $r_{\bar{i}}^{\bar{a}}$ are of equal value but of opposite sign.

For EOM-EE, excited states of the same spatial and spin symmetry as the reference state can be targeted. Therefore, the constant value r_0 appears which formally adds the reference wave function to the diagonalization space. Fig. 2.4 shows schematically how the similarity transformed Hamiltonian matrix is built up in EOM-EE-CCSD theory. The many-body elements of $\bar{H}$ - $\mathcal{F}$, $\mathcal{W}$, and $\mathcal{X}$ - are defined in Appendix B.1. Notably,

$$\begin{array}{c|ccc|}
 & |\Phi_0\rangle & |\Phi_\mathrm{S}\rangle & |\Phi_\mathrm{D}\rangle \\
\langle\Phi_0| & 0 & \mathcal{F}_{ia} & \mathcal{W}_{ijab} \\
\langle\Phi_\mathrm{S}| & 0 & \mathcal{F}_{ij} + \mathcal{F}_{ab} + \mathcal{W}_{iabj} & \mathcal{F}_{ia} + \mathcal{W}_{ijka} + \mathcal{W}_{ciab} \\
\langle\Phi_\mathrm{D}| & 0 & \mathcal{W}_{kaij} + \mathcal{W}_{abci} + \mathcal{X}_{abkijc} & \begin{array}{c} \mathcal{F}_{ij} + \mathcal{F}_{ab} + \mathcal{W}_{iabj} + \mathcal{W}_{ijkl} \\ +\mathcal{W}_{abcd} + \mathcal{X}_{ajcibd} + \mathcal{X}_{ajkibl} \end{array}
\end{array}$$

Figure 2.4: Schematic representation of the $\bar{\boldsymbol{H}}$-matrix within EOM-EE-CCSD theory. Shown are all terms that can contribute to entries in the respective matrix blocks.

the first column of $\bar{\boldsymbol{H}}$ only contains 0 as the CC amplitude equations hold. Therefore, r_0 has no contribution to the matrix-vector product $\bar{\boldsymbol{H}}\boldsymbol{r}$ and in particular does not contribute to the energy eigenvalue. Thus, the reference determinant does not have to be contained in the diagonalization space. However, if desired,[4] r_0 can be calculated for each converged eigenvector $\boldsymbol{r}_K$ by using

$$r_0^{(K)} = \sum_{i=1} \bar{H}_{0i}\, r_i^{(K)} \cdot \Delta E_\mathrm{exc}^{(K)^{-1}}. \tag{2.114}$$

Notably, the CC reference wave function itself is a solution to the EOM-EE eigenvalue problem with $r_0 = 1$ and all $r_{ij\ldots}^{ab\ldots} = 0$. To obtain biorthonormality, the corresponding constant of $\hat{\mathcal{L}}$ is $l_0 = 1$ while the $l_{ab\ldots}^{ij\ldots}$ equal the amplitudes of the Λ-operator known from CC derivative theory. [59] For all excited states, l_0 equals zero. The calculation of each root scales like the underlying level of CC theory. For EOM-EE-CCSD, the computational effort scales with $\mathcal{O}(N^6)$.

EOM-CC spin-flip

The EOM-SF variant is obtained by choosing $\hat{\mathcal{R}}$ to be particle conserving but to change the spin of one electron. Therefore, one pair of quasiparticle creation operators in the $\hat{\Omega}_n$ acts upon orbitals of different spin resulting in EOM operators targeting states with $\Delta M_S = \pm 1$ as compared to the reference. Therefore, r_0 is always zero as the reference determinant cannot contribute to the target wave function. The spin-integrated

---

[4] r_0 is needed for the calculation of properties.

operator for the case with $\Delta M_S = +1$ is given by

$$\begin{aligned}\hat{\mathcal{R}}_{\mathrm{SF},\Delta M_S=+1} &= \sum_{\bar{i}} \sum_{a} r_{\bar{i}}^{a}\ \hat{a}_a^\dagger \hat{a}_{\bar{i}} \\ &+ \frac{1}{2} \sum_{\bar{i}} \sum_{j} \sum_{a,b} r_{\bar{i}j}^{ab}\ \hat{a}_a^\dagger \hat{a}_b^\dagger \hat{a}_j \hat{a}_{\bar{i}} + \frac{1}{2} \sum_{\bar{i},\bar{j}} \sum_{a} \sum_{\bar{b}} r_{\bar{i}\bar{j}}^{a\bar{b}}\ \hat{a}_a^\dagger \hat{a}_{\bar{b}}^\dagger \hat{a}_{\bar{j}} \hat{a}_{\bar{i}} + \ldots \end{aligned} \tag{2.115}$$

$\hat{\mathcal{R}}_{\mathrm{SF},\Delta M_S=-1}$ is obtained by exchanging α- and β-spins. The EOM-SF approach can, i.a., be used to adequately describe the energetic evolution of electronic states during bond breaking and torsion [40] as well as ground and excited states of di- and triradicals. [40,78] These applications have in common that several exactly or nearly degenerate configurations contribute to the wave function. These configurations have then to be treated on an equal footing. This can often be achieved by using the EOM-SF method based on a well-behaved reference wave function of higher or lower multiplicity than the target states. The cost of the EOM-SF methods scale analogously to their EOM-EE counterparts.

EOM-CC for ionization potential and electron attachment

Abandoning the requirement for particle conservation leads to the EOM-IP- and -EA-CC variants. Again, the multiplicity of any target state is different from the reference state as an electron is removed from or attached to the system resulting in $r_0 = 0$. The EOM-IP operator can be obtained from the EOM-EE operator by leaving out one particle creation operator $\hat{a}_a^\dagger$ in each $\hat{\Omega}_n$. Similarly, removing a hole creation operator $\hat{a}_i$ leads to the EOM-EA operator. For $\Delta M_S = +{}^1\!/\!_2$, the spin-integrated $\hat{\mathcal{R}}$-operators are:

$$\begin{aligned}\hat{\mathcal{R}}_{\mathrm{IP},\Delta M_S=+1/2} &= \sum_{\bar{i}} r_{\bar{i}}\ \hat{a}_{\bar{i}} \\ &+ \sum_{\bar{i}} \sum_{j} \sum_{b} r_{j\bar{i}}^{b}\ \hat{a}_b^\dagger \hat{a}_j \hat{a}_{\bar{i}} + \frac{1}{2} \sum_{\bar{i},\bar{j}} \sum_{\bar{b}} r_{\bar{j}\bar{i}}^{\bar{b}}\ \hat{a}_{\bar{b}}^\dagger \hat{a}_{\bar{j}} \hat{a}_{\bar{i}} + \ldots\ , \end{aligned} \tag{2.116}$$

$$\begin{aligned}\hat{\mathcal{R}}_{\mathrm{EA},\Delta M_S=+1/2} &= \sum_{a} r^{a}\ \hat{a}_a^\dagger \\ &+ \frac{1}{2} \sum_{j} \sum_{a,b} r_{j}^{ba}\ \hat{a}_a^\dagger \hat{a}_b^\dagger \hat{a}_j + \sum_{\bar{j}} \sum_{a} \sum_{\bar{b}} r_{\bar{j}}^{\bar{b}a}\ \hat{a}_a^\dagger \hat{a}_{\bar{b}}^\dagger \hat{a}_{\bar{j}} + \ldots \end{aligned} \tag{2.117}$$

Exchanging α- and β-spins gives the corresponding operators for target states with $\Delta M_S = -{}^1\!/\!_2$. The appeal of these two methods is the capability to calculate several vertical ionization energies and electron affinities directly within a single calculation instead of performing seperate CC calculations on all target systems.[43] Additionally, EOM-IP- and EOM-EA-CC calculations have a lower scaling in N and are, therefore, favored from a computational point of view. For EOM-IP/EA-CCSD, the scaling is $\mathcal{O}(N^5)$. Furthermore, EOM-IP and EOM-EA methods can be used to easily describe doublet radical wave functions using the closed-shell reference wave function of a corresponding charged system and, thereby, avoid symmetry breaking.[43]

2.6.2 Calculation of one-electron single-state and transition properties

EOM expectation value

The generalized expectation value of an operator $\hat{O}$ within the EOM framework is defined as

$$\langle\Psi^{(I)}_{\mathrm{EOM}}|\,\hat{O}\,|\Psi^{(J)}_{\mathrm{EOM}}\rangle = \langle\Phi_0|\,\hat{\mathcal{L}}^{(I)}\,\underbrace{\mathrm{e}^{-\hat{T}}\hat{O}\mathrm{e}^{\hat{T}}}_{\bar{O}}\,\hat{\mathcal{R}}^{(J)}\,|\Phi_0\rangle \tag{2.118}$$

yielding single-state properties for $I = J$ and transition properties for $I \neq J$. The calculation of the expectation value is rather straightforward but the additional determination of the left eigenvectors of $\bar{\boldsymbol{H}}$ is required. An important property in the context of, e.g., UV/VIS-spectroscopy is the transition dipole moment as it determines the intensity of a certain transition. EOM transition dipole moments are obtained by evaluating

$$\boldsymbol{\mu}_{I\to J} = \langle\Phi_0|\,\hat{\mathcal{L}}^{(I)}\bar{\boldsymbol{\mu}}\hat{\mathcal{R}}^{(J)}\,|\Phi_0\rangle = \mathrm{Tr}\left(\boldsymbol{\rho}_{I\to J}\boldsymbol{\mu}\right). \tag{2.119}$$

Hence, the transition dipole moments are determined by tracing the reduced one-particle transition density matrix[5] $\boldsymbol{\rho}_{I\to J}$ defined by

$$[\boldsymbol{\rho}_{I\to J}]_{pq} = \langle\Phi_0|\,\hat{\mathcal{L}}^{(I)}\left(\hat{a}^\dagger_p\hat{a}_q\mathrm{e}^{\hat{T}}\right)_{\mathrm{c}}\hat{\mathcal{R}}^{(J)}\,|\Phi_0\rangle \tag{2.120}$$

with the dipole moment integrals $\boldsymbol{\mu}$.[76] The defining equations for the one-particle density matrices for all presented EOM variants can be found in Appendix B.5. The intensity of bands in absorption spectra is proportional to the oscillator strength $f_{I\to J}$[76] with

$$f_{I\to J} = \frac{2}{3}(E_J - E_I)|\boldsymbol{\mu}_{I\to J}|^2 \tag{2.121}$$

and, therefore, to the square of the absolute value of the transition moment. It is important to note that due to the non-Hermiticity of the EOM-CC theory the desired quantity is the product of a 'left' and a 'right' transition moment

$$|\boldsymbol{\mu}_{I\to J}|^2 = \boldsymbol{\mu}_{I\to J}\cdot\boldsymbol{\mu}_{J\to I}. \tag{2.122}$$

---

[5] For single-state properties, the corresponding one-particle density matrix $\boldsymbol{\rho}_I$ is used and for many-particle operators a many-particle density matrix has to be set up.

In this thesis, $|\boldsymbol{\mu}_{I\to J}|^2$ is referred to as the squared transition moment (STM). However, EOM properties calculated via an expectation value are not size-intensive. Recasting Eq. (2.118) gives

$$\begin{aligned}\langle\Phi_0|\,\hat{\mathcal{L}}^{(I)}\mathrm{e}^{-\hat{T}}\hat{O}\mathrm{e}^{\hat{T}}\hat{\mathcal{R}}^{(I)}\,|\Phi_0\rangle &= \langle\Phi_0|\,\hat{\mathcal{L}}^{(I)}\left[\bar{O},\hat{\mathcal{R}}^{(I)}\right]|\Phi_0\rangle + \underbrace{\langle\Phi_0|\,\hat{\mathcal{L}}^{(I)}\hat{\mathcal{R}}^{(I)}\bar{O}\,|\Phi_0\rangle}_{=\Theta} \\ &= \langle\Phi_0|\,\hat{\mathcal{L}}^{(I)}\left(\bar{O}\hat{\mathcal{R}}^{(I)}\right)_{\mathrm{c}}|\Phi_0\rangle + \Theta. \end{aligned} \tag{2.123}$$

Θ is a disconnected term and, thus, responsible for the lack of size-intensivity. It only vanishes for the determination of the energy with $\hat{O} = \hat{H} - E_{\mathrm{CC}}$. Defining $\{\Phi_P\} \subset \{\Phi_Q\}$ as the determinants spanning the diagonalization space and $\{\Phi_R\} \subset \{\Phi_Q\}$ as the set of all other determinants spanning the complementary space, it can be shown that, in this case, $\Theta = 0$:

$$\begin{aligned}\Theta = \langle\Phi_0|\,\hat{\mathcal{L}}^{(I)}\hat{\mathcal{R}}^{(I)}\bar{H}\,|\Phi_0\rangle &= \sum_Q \langle\Phi_0|\,\hat{\mathcal{L}}^{(I)}\hat{\mathcal{R}}^{(I)}\,|\Phi_Q\rangle\,\langle\Phi_Q|\,\bar{H}\,|\Phi_0\rangle \\ = \langle\Phi_0|\,\hat{\mathcal{L}}^{(I)}\hat{\mathcal{R}}^{(I)}\,|\Phi_0\rangle\,&\underbrace{(E_{\mathrm{CC}} - E_{\mathrm{CC}})}_{=0} \\ + \sum_P \langle\Phi_0|\,\hat{\mathcal{L}}^{(I)}\hat{\mathcal{R}}^{(I)}\,|\Phi_P\rangle\,&\underbrace{\langle\Phi_P|\,\bar{H}\,|\Phi_0\rangle}_{=0} \\ + \sum_R \underbrace{\langle\Phi_0|\,\hat{\mathcal{L}}^{(I)}\hat{\mathcal{R}}^{(I)}\,|\Phi_R\rangle}_{=0}\,&\langle\Phi_R|\,\bar{H}\,|\Phi_0\rangle = 0. \end{aligned} \tag{2.124}$$

Therefore, only a connected term is left in Eq. (2.123) which makes the EOM excitation energy a size-intensive quantity.

Size-intensive properties (CC linear response)

To obtain size-intensive results for properties, the disconnected term in Eq. (2.123) has to be eliminated. Hence, Eq. (2.123) may be reformulated by adding the following terms of similar structure that add up to zero: [79, 80]

$$\begin{aligned}0 &= \langle\Phi_0|\,\hat{\mathcal{L}}^{(I)}\left[\bar{H},\hat{A}\right]\hat{\mathcal{R}}^{(J)}\,|\Phi_0\rangle - \omega_{IJ}\,\langle\Phi_0|\,\hat{\mathcal{L}}^{(I)}\hat{A}\hat{\mathcal{R}}^{(J)}\,|\Phi_0\rangle \\ &= \langle\Phi_0|\,\hat{\mathcal{L}}^{(I)}\left(\left[\bar{H},\hat{A}\right]\hat{\mathcal{R}}^{(J)}\right)_{\mathrm{c}}|\Phi_0\rangle + \langle\Phi_0|\,\hat{\mathcal{L}}^{(I)}\hat{\mathcal{R}}^{(J)}\left[\bar{H},\hat{A}\right]|\Phi_0\rangle \\ &\quad - \omega_{IJ}\,\langle\Phi_0|\,\hat{\mathcal{L}}^{(I)}\hat{A}\hat{\mathcal{R}}^{(J)}\,|\Phi_0\rangle \end{aligned} \tag{2.125}$$

In order to show that Eq. (2.125) yields zero, one may evaluate the first term:

$$\begin{aligned}\langle\Phi_0|\,\hat{\mathcal{L}}^{(I)}\left[\bar{H},\hat{A}\right]\hat{\mathcal{R}}^{(J)}\,|\Phi_0\rangle &= \underbrace{\langle\Phi_0|\,\hat{\mathcal{L}}^{(I)}\bar{H}}_{\Delta E^{(I)}_{\text{exc}}\langle\Phi_0|\hat{\mathcal{L}}^{(I)}}\,\hat{A}\hat{\mathcal{R}}^{(J)}\,|\Phi_0\rangle - \langle\Phi_0|\,\hat{\mathcal{L}}^{(I)}\hat{A}\,\underbrace{\bar{H}\hat{\mathcal{R}}^{(J)}\,|\Phi_0\rangle}_{\Delta E^{(J)}_{\text{exc}}\hat{\mathcal{R}}^{(J)}|\Phi_0\rangle} \\ &= \omega_{IJ}\,\langle\Phi_0|\,\hat{\mathcal{L}}^{(I)}\hat{A}\hat{\mathcal{R}}^{(J)}\,|\Phi_0\rangle\,.\end{aligned}\tag{2.126}$$

Eq. (2.125) holds for an arbitrary operator $\hat{A}$ and $\omega_{IJ} = \Delta E^{(I)}_{\text{exc}} - \Delta E^{(J)}_{\text{exc}}$ is the energy difference between the states I and J. Inserting the formal zero, Eq. (2.123) becomes for transition dipole moments:

$$\begin{aligned}\boldsymbol{\mu}_{I\to J} &= \langle\Phi_0|\,\hat{\mathcal{L}}^{(I)}\left(\bar{\boldsymbol{\mu}}\hat{\mathcal{R}}^{(J)}\right)_{\text{c}}|\Phi_0\rangle + \langle\Phi_0|\,\hat{\mathcal{L}}^{(I)}\hat{\mathcal{R}}^{(J)}\bar{\boldsymbol{\mu}}\,|\Phi_0\rangle \\ &\left.\begin{aligned}&+\langle\Phi_0|\,\hat{\mathcal{L}}^{(I)}\left(\left[\bar{H},\hat{A}\right]\hat{\mathcal{R}}^{(J)}\right)_{\text{c}}|\Phi_0\rangle \\ &+\langle\Phi_0|\,\hat{\mathcal{L}}^{(I)}\hat{\mathcal{R}}^{(J)}\left[\bar{H},\hat{A}\right]|\Phi_0\rangle \\ &-\omega_{IJ}\,\langle\Phi_0|\,\hat{\mathcal{L}}^{(I)}\hat{A}\hat{\mathcal{R}}^{(J)}\,|\Phi_0\rangle\,.\end{aligned}\right\}=0\end{aligned}\tag{2.127}$$

Analyzing the terms with respect to their connectedness shows that the first and third term are connected while the three other ones are disconnected. For a size-intensive theory, the latter should vanish:[6]

$$\begin{aligned}0 &\overset{!}{=} \langle\Phi_0|\,\hat{\mathcal{L}}^{(I)}\hat{\mathcal{R}}^{(J)}\bar{\boldsymbol{\mu}}\,|\Phi_0\rangle + \langle\Phi_0|\,\hat{\mathcal{L}}^{(I)}\hat{\mathcal{R}}^{(J)}\left[\bar{H},\hat{A}\right]|\Phi_0\rangle - \omega_{IJ}\,\langle\Phi_0|\,\hat{\mathcal{L}}^{(I)}\hat{A}\hat{\mathcal{R}}^{(J)}\,|\Phi_0\rangle \\ &= \sum_Q \langle\Phi_0|\,\hat{\mathcal{L}}^{(I)}\hat{\mathcal{R}}^{(J)}\,|\Phi_Q\rangle\cdot\Big(\langle\Phi_Q|\,\bar{\boldsymbol{\mu}}\,|\Phi_0\rangle + \langle\Phi_Q|\left[\bar{H},\hat{A}\right]|\Phi_0\rangle \\ &\qquad\qquad -\omega_{IJ}\,\langle\Phi_Q|\,\hat{A}\,|\Phi_0\rangle\Big)\,.\end{aligned}\tag{2.128}$$

Eq. (2.128) holds for all Φ_Q within the complementary space $\{\Phi_R\}$ due to the vanishing prefactor (see Eq. (2.124)). For all other determinants Φ_Q within the diagonalization space $\{\Phi_P\}$, the term in brackets in Eq. (2.128) has to be zero. This gives an equation for $\hat{A}$ and it turns out that these equations correspond to the perturbed frequency-dependent CC amplitude equations [77,81] and, therefore, $\hat{A} = \hat{T}^{\varepsilon}(\omega_{IJ})$:

$$\omega_{IJ}t^{\varepsilon}_Q(\omega_{IJ}) = \langle\Phi_Q|\,\bar{\boldsymbol{\mu}}\,|\Phi_0\rangle + \langle\Phi_Q|\left[\bar{H},\hat{T}^{\varepsilon}(\omega_{IJ})\right]|\Phi_0\rangle\,.\tag{2.129}$$

Size-intensive transition moments are, hence, obtained by

$$\boldsymbol{\mu}^{\text{c}}_{I\to J} = \langle\Phi_0|\,\hat{\mathcal{L}}^{(I)}\left(\bar{\boldsymbol{\mu}}\hat{\mathcal{R}}^{(J)}\right)_{\text{c}}|\Phi_0\rangle + \langle\Phi_0|\,\hat{\mathcal{L}}^{(I)}\left(\left[\bar{H},\hat{T}^{\varepsilon}(\omega_{IJ})\right]\hat{\mathcal{R}}^{(J)}\right)_{\text{c}}|\Phi_0\rangle\,.\tag{2.130}$$

---

[6] Here, $\hat{A}$ is assumed to be an excitation operator and, hence, $\left[\hat{\mathcal{R}}^{(J)},\hat{A}\right] = 0$.

Transition moments defined by Eq. (2.130) are identical to the ones obtained from CC linear response (LR) theory.[82] The difference to Eq. (2.119) is given by considering the response of the amplitudes to the frequency-dependent perturbation.

Lagrangian formalism

In order to avoid solving the perturbed CC equations, the Lagrangian formalism can be applied. First, Eq. (2.130) may also be derived by taking the derivative of a Lagrangian[79,80]

$$L_{IJ} = \langle\Phi_0|\,\hat{\mathcal{L}}^{(I)}\left(\bar{H}\hat{\mathcal{R}}^{(J)}\right)_{\mathrm{c}}|\Phi_0\rangle + \langle\Phi_0|\,\hat{\mathcal{L}}^{(I)}\sum_R \hat{P}_R\Delta E_{\mathrm{exc}}^{(R)}\hat{\mathcal{R}}^{(J)}\,|\Phi_0\rangle \tag{2.131}$$

with respect to the electric field $\boldsymbol{\varepsilon}$. While the first term in Eq. (2.131) equals the connected EOM energy expression (2.123), the second term is necessary to ensure stationarity with respect to the $\hat{\mathcal{R}}$- and $\hat{\mathcal{L}}$-amplitudes. Here, $\hat{P}_R$ is a perturbation-independent projection operator with

$$\hat{P}_R = \hat{\mathcal{R}}^{(R)}\,|\Phi_0\rangle\,\langle\Phi_0|\,\hat{\mathcal{L}}^{(R)}. \tag{2.132}$$

The determination of the perturbed $\hat{T}$-amplitudes for each component ε_i $(i = x, y, z)$ of $\boldsymbol{\varepsilon}$ can be avoided by taking advantage of the $(2n+1)$-rule[45] from analytic derivative theory. Another profound advantage of this formulation is that it establishes a starting point for the determination of higher-order transition moments.[83] To proceed along the route, the Lagrangian in Eq. (2.131) is modified such that its stationarity with respect to the CC amplitudes is ensured:

$$\tilde{L}_{IJ} = L_{IJ} + \langle\Phi_0|\,\hat{\mathcal{Z}}(\omega_{IJ})\left(\bar{H} - \omega_{IJ}\hat{T}\right)|\Phi_0\rangle\,. \tag{2.133}$$

$\hat{\mathcal{Z}}$ is a de-excitation operator defined analogously to $\hat{\mathcal{L}}$ with the Lagrange multipliers $\zeta_{ab\ldots}^{ij\ldots}$ as amplitudes:

$$\hat{\mathcal{Z}} = \hat{\mathcal{Z}}_1 + \hat{\mathcal{Z}}_2 + \ldots, \tag{2.134}$$

$$\hat{\mathcal{Z}}_n = \frac{1}{(n!)^2}\sum_{ij\ldots}\sum_{ab\ldots}\zeta_{ab\ldots}^{ij\ldots}\;\hat{a}_i^\dagger\hat{a}_j^\dagger\ldots\hat{a}_b\hat{a}_a. \tag{2.135}$$

The additional term in Eq. (2.133) consists of the CC amplitude equations extended by a frequency-dependent term arising due to the time derivative appearing in the time-dependent SE.[46] Size-intensive transition moments may be obtained by taking the derivative of the Lagrangian with respect to $\boldsymbol{\varepsilon}$:[79,80]

$$\boldsymbol{\mu}_{I\to J}^{\mathrm{c}} = \frac{\mathrm{d}\tilde{L}_{IJ}}{\mathrm{d}\boldsymbol{\varepsilon}} = \langle\Phi_0|\,\hat{\mathcal{L}}^{(I)}\left(\bar{\boldsymbol{\mu}}\hat{\mathcal{R}}^{(J)}\right)_{\mathrm{c}}|\Phi_0\rangle + \langle\Phi_0|\,\hat{\mathcal{Z}}(\omega_{IJ})\bar{\boldsymbol{\mu}}\,|\Phi_0\rangle\,. \tag{2.136}$$

The first term can be evaluated by using the one-particle density matrices from Eq. (2.120) and leaving out all terms where $\hat{\mathcal{R}}^{(J)}$ is not connected to $\bar{\boldsymbol{\mu}}$. For the second term, only one set of $\hat{\mathcal{Z}}$-amplitudes has to be determined by solving the linear equation system in Eq. (2.137):

$$\begin{aligned} 0 \overset{!}{=} \frac{\partial \tilde{L}_{IJ}}{\partial t_p} &= \langle \Phi_0 | \hat{\mathcal{L}}^{(I)} \left[\left[\bar{H}, \hat{\tau}_p \right], \hat{\mathcal{R}}^{(J)} \right] | \Phi_0 \rangle \\ &+ \langle \Phi_0 | \hat{\mathcal{Z}}(\omega_{IJ}) \left[\bar{H}, \hat{\tau}_p \right] | \Phi_0 \rangle \\ &- \omega_{IJ} \langle \Phi_0 | \hat{\mathcal{Z}}(\omega_{IJ}) | \Phi_p \rangle \, . \end{aligned} \tag{2.137}$$

Thus, the perturbed CC amplitudes that are necessary to solve Eq. (2.130) do not have to be determined. Hence, computation time is reduced as only one set of equations has to be solved instead of one for every component of $\boldsymbol{\varepsilon}$. The corresponding $\hat{\mathcal{Z}}$-equations are given in Appendix B.5.

3 Implementational and computational details

In the course of this thesis, the complex-valued CC and EOM-CC program package Qcumbre (***Q**uantum **C**hemical **U**tility enabling **M**agnetic-field dependent investigations **B**enefitting from **R**igorous **E**lectron-correlation treatment*) has been written using the programming language C++ [84] in order to study the electronic structure of atoms and molecules exposed to homogeneous strong magnetic fields. Tab. 3.1 gives an overview of all methods that have been implemented.

Table 3.1: Implemented components of the Qcumbre program package. [85–88]

	CIS	CCSD				CCSD(T)	CCSDT
Energy	✓	✓				✓	✓[a]
EOM energies	-	EE	SF	IP	EA	✗	EE[a]
$1e^-$-properties							
Expectation value	✓	✓	✓	✓	✓	✗	✗
Linear response	-	✓	✗	✗	✗	✗	✗

[a] These methods have been implemented by N. Gross in the context of his master's thesis. [89]

In the presence of a magnetic field, the wave function and, hence, the integrals and wave-function parameters become complex. A respective quantum-chemical program, therefore, needs to work with complex quantities which has the following consequences:

1. The memory requirements are increased due to two factors:
    - The storage of any quantity takes twice the amount of memory as compared to a real-valued implementation.
    - The two-electron integrals exhibit less permutational symmetry:

$$\begin{aligned} \langle pq|rs\rangle = \langle qp|sr\rangle = \langle rs|pq\rangle^* &= \langle sr|qp\rangle^* \\ &\neq \\ \langle ps|rq\rangle = \langle sp|qr\rangle = \langle rq|ps\rangle^* &= \langle qr|sp\rangle^* \end{aligned} \tag{3.1}$$

2. The computational cost is higher since the addition of two numbers requires two floating-point operations instead of only one. For multiplications, the ratio is formally (see Chpt. 3.2) four to one.

So far, no complex-valued quantum-chemical program package has been available that allows for performing EOM-CC calculations. Hence, Qcumbre has been developed which renders accurate calculations of excited states in strong magnetic fields possible. In the design of the program package, the following goals have been pursued:

1. Coding of working equations shall be simple also for the developers. Therefore, the respective code should resemble the equations on paper.
2. Equations shall be evaluated efficiently.
   All equations underlying the presented methods within this thesis consist of tensor contractions that can be internally recast as matrix multiplications. This is a standard procedure of efficient tensor libraries, see, for example, Refs. [90–92]. In order to fulfill both demands listed above, a black-box *contraction routine* with an appropriate input format is warranted.
3. The implementation of future performance improvements shall not affect exisiting code, in particular equations.
   A special hierarchic *data-type structure* based on a 'self-aware' data type needs to ensure that all performance improvements can be implemented on a level that does not affect working equations. Yet, it has to allow for the programmer-friendly *and* efficient functionality of the program.
4. A modular structure shall facilitate the fast implementation of program extensions. In an ideal program, the implementation of a new method should only necessitate the coding of the respective equations. Therefore, the program at hand should feature a set of *general solver routines* and independent *main routines* for each kind of methodology. Thereby, extensions can be included by only specifying which set of equations has to be solved within the respective solver routine. The program's general framework should remain unaltered.
5. The program shall be easily migratable to other underlying program packages.
   As input, the QCUMBRE program requires integrals in the MO basis. Hence, an *interface* has to provide that external data is properly read. Migration to other underlying integral-providing program packages should only necessitate the adaptation of the reading process.

The following chapters explain in detail how these challenges are tackled within the QCUMBRE program package and how the individual routines work. First, the topic of data-type structure and management is elucidated. Subsequently, the contraction routine - effectively the heart of the program - is explained, focusing on its functionality and how it simplifies the implementation of equations. Following, the solver routines and their functionality are discussed before the main routines and exemplary program code are presented. Last, all validation tests performed to verify the implementation are specified. A list of all keywords available in the input file as well as an exemplary input file for a QCUMBRE calculation are given in Appendix C including detailed explanations.

3.1 Data-type structure and management

The data-type structure used in the present program package is designed in such a way that it features two important aspects. First, the implementation of equations of the form as they appear in CC and EOM-CC theory is rather simple. Indices are rearranged *internally* in order to group them to superindices for matrix multiplications. Secondly, the latter are carried out efficiently avoiding nested loop structures. In order to motivate the choice of data-type structure, the following contribution to the EOM-EE equations

$$\sigma_i^a = \ldots + \sum_e \sum_m \mathcal{W}_{maei}\, b_m^e + \ldots \tag{3.2}$$

may be considered as a showcase which stems from the entries of the $\boldsymbol{\sigma}$-vector (see Chpt. 3.3) defined by

$$\sigma_i^a = \sum_I \langle \Phi_i^a | \, \bar{H} \, | \Phi_I \rangle \, r_I . \tag{3.3}$$

b_m^e are the singles amplitudes of the basis vector $\boldsymbol{b}$ and $\mathcal{W}_{maei}$ is a two-body term of $\bar{H}$. After spin integration,[7]

$$\sigma_i^a = \ldots + \sum_e \sum_m \mathcal{W}_{maei}\, b_m^e + \sum_{\bar{e}} \sum_{\bar{m}} \mathcal{W}_{\bar{m}a\bar{e}i}\, b_{\bar{m}}^{\bar{e}} + \ldots , \tag{3.4}$$

$$\sigma_{\bar{i}}^{\bar{a}} = \ldots + \sum_e \sum_m \mathcal{W}_{m\bar{a}e\bar{i}}\, b_m^e + \sum_{\bar{e}} \sum_{\bar{m}} \mathcal{W}_{\bar{m}\bar{a}\bar{e}\bar{i}}\, b_{\bar{m}}^{\bar{e}} + \ldots \tag{3.5}$$

is obtained. As each quantity is composed of a set of non-redundant spin cases, the choice of a hierarchic data-type structure is natural.[8] From this example, the idea of using three different data types becomes plausible:

1. The smallest data unit named `flex` is an n-dimensional tensor. It comprises a non-redundant spin case of a quantity. Thus, it contains the values which are actually needed to evaluate a single contribution to any working equation, i.e., to perform a single matrix multiplication. E.g., for the second contribution in Eq. (3.4), the $\beta\alpha\beta\alpha$-spin case of the two-body term $\mathcal{W}_{maei}$ and the $\beta\beta$-spin case of the $\boldsymbol{b}_1$-amplitudes are represented by one `flex` object each.

---

[7] For efficiency reasons, all working equations within QCUMBRE are spin integrated.

[8] Additionally, considering spatial symmetry allows for subdividing tensors into symmetry blocks. This can more easily be incorporated into a program infrastructure that offers access to a hierarchic class structure.

2. The next larger data unit named `group` is a vector of `flex` objects. Therefore, it incorporates all spin cases of a given n-index quantity. In the example above, the two-body term $\mathcal{W}_{maei}$ is represented by an object of the data type `group` collecting all six non-redundant spin cases that exist for this quantity (see Tab. 3.4 in Chpt. 3.1.2).

3. The third data unit is called `complete` and is another vector of `flex` objects. In contrast to a `group` object, it combines all `flex` objects that assemble a solution vector. E.g., this applies to the basis or sigma vectors $\boldsymbol{b}$ and $\boldsymbol{\sigma}$, respectively, that, for EOM-CCSD, are composed of the corresponding singles and doubles amplitudes with their appropriate spin cases (see Tab. 3.6 in Chpt. 3.1.3).

In the following, each data type is presented in detail focusing on its structure, utilization, and construction.

3.1.1 `flex` data type

The `flex` data type is the basis data type utilized in a matrix multiplication in Qcumbre. Objects of this type contain all entries of a tensor of a certain spin case. They serve both as input and as output data of contractions. Additional information which is stored within the `flex` type is given in Tab. 3.2. The values of the multidimensional tensor are stored independently of the actual dimension in a one-dimensional array. Hereby, the hindmost index is the fastest defining a row-major order which is the usual way of data storage in C++. Besides the actual values, a `flex` object carries information on the dimensionality of the corresponding quantity and on the size of each dimension. This information is needed as input for the matrix multiplication routine. Additionally, the indices of the tensor are stored where upper case letters are

Table 3.2: The object structure of the data type `flex`. As a showcase, the information on the $\beta\alpha\beta\alpha$-spin case of a tensor $\mathcal{W}_{iabj}$ is given.

Information	Data type	Example: $\mathcal{W}_{\bar{i}a\bar{b}j}$
Values	`std::vector<std::complex<double> >`	(...)
Dimensionality	`int`	4
Dimensions	`std::vector<int64_t>`	(`nbo`,`nav`,`nbv`,`nao`)[a]
Indices	`std::string`	"iAbJ"
Represented quasiparticles	`std::string`	"hpph"

[a] See Chpt. 3.1.4 for definitions.

used for α-spin and lower case letters for β-spin orbitals. As each index stands for a quasiparticle, information on those is saved in an additional string with `"h"` and `"p"` abbreviating hole and particle, respectively. This is solely used for consistency checks in the coded equations. A `flex` object cannot be constructed individually and is not directly manipulable by the programmer. Instead, objects of this data type are always constructed in conjunction with an object of type `group` or `complete` as explained in the following paragraphs and are only accessible through methods belonging to these collecting data types.

3.1.2 `group` data type

Objects of the type `group` collect all `flex` objects that belong to a quantity with a certain index order. This means that a `group` object covers all spin cases of a certain n-dimensional quantity with a given quasiparticle string. The one- and two-electron integrals, the N-body terms of $\bar{H}$, as well as all intermediates that have to be defined in order to implement the working equations in CC and EOM-CC theory are saved each as a `group` object. In addition to the vector of `flex` objects, the following information is stored within the `group` class as shown in Tab. 3.3. The dimensionality and the represented quasiparticles serve for consistency check purposes. A vector of strings keeps hold of the order in which the `flex` objects for the different spin cases are saved. This enables choosing the correct `flex` object demanded for a certain contraction. `"a"` and `"b"` are used to abbreviate α- and β-spin, respectively. A `group` object of name `"object_name"` is created by attributing certain indices to it, e.g.,

Table 3.3: The object structure of the data type `group`. As a showcase, the information on the $\mathcal{W}_{\text{hpph}}$ component of $\bar{\boldsymbol{H}}$ is given.

Information	Data type	Example: $\mathcal{W}_{\text{hpph}}$
Values	`std::vector<flex>`	(...)
Dimensionality	`int`	4
Represented quasiparticles	`std::string`	"hpph"
Spin cases	`std::vector<std::string>`	("aaaa","bbbb","abab", "baba","abba","baab")

```
group object_name("IABJ"); .
```

The string `"IABJ"` represents these indices which are analyzed with respect to the quasiparticles they represent. Letters `"a"`-`"h"` are reserved for particle indices and letters `"i"`-`"p"` for hole indices. The indices themselves are not attributed to the created object. Instead, for each quasiparticle string, the existing spin cases are tabulated and the corresponding `flex` objects are created while fixed index strings are assigned. Tab. 3.4 shows which quasiparticle strings have been implemented and which spin cases are associated with the corresponding quantities. In addition, the index strings that `group` objects are assigned with are listed. The actual values and, thus, the single `flex` objects can be manipulated by methods of the respective `group` object. The following Chpt. 3.2 covers this topic in more detail.

Table 3.4: Possible quasiparticle strings for `group` objects in Qcumbre. The corresponding non-redundant spin cases and the fixed index strings of the associated `flex` objects are listed (disregarding the spin case).

Quasiparticle string	Spin cases	Default index string
p / h	α, β	a / i
pp / hh / ph / hp	$\alpha\alpha$, $\beta\beta$ (or $\alpha\beta$ or $\beta\alpha$)[a]	ab / ij / ai / ia
pppp / hhhh / pphh / hhpp	$\alpha\alpha\alpha\alpha$, $\beta\beta\beta\beta$, $\alpha\beta\alpha\beta$	abcd / ijkl / abij / ijab
ppph / hhhp / phpp / hphh	$\alpha\alpha\alpha\alpha$, $\beta\beta\beta\beta$, $\alpha\beta\alpha\beta$, $\beta\alpha\beta\alpha$	abci / ijka / ciab / kaij
hpph	$\alpha\alpha\alpha\alpha$, $\beta\beta\beta\beta$, $\alpha\beta\alpha\beta$, $\beta\alpha\beta\alpha$, $\alpha\beta\beta\alpha$, $\beta\alpha\alpha\beta$	iabj
pphhhh	$\alpha\alpha\alpha\alpha\alpha\alpha$, $\beta\beta\beta\beta\beta\beta$, $\alpha\alpha\beta\alpha\alpha\beta$, $\alpha\beta\beta\alpha\beta\beta$, $\alpha\beta\alpha\alpha\beta\alpha$, $\beta\beta\alpha\beta\beta\alpha$	ablijk
phhhhh	$\alpha\alpha\alpha\alpha\alpha\alpha$, $\beta\beta\beta\beta\beta\beta$, $\alpha\alpha\beta\alpha\alpha\beta$, $\alpha\beta\beta\alpha\beta\beta$, $\beta\alpha\alpha\beta\alpha\alpha$, $\beta\alpha\beta\beta\alpha\beta$	almijk

[a] For EOM-SF, intermediates including the spin flipping EOM operator are constructed. For these, the $\alpha\alpha$- and $\beta\beta$-spin cases do not occur but rather one of the spin cases listed in parentheses. Such intermediates are constructed by using a case sensitive index string in its constructor, e.g., via `group object_name("Ia");` .

3.1.3 `complete` data type

The `complete` data type resembles the `group` data type as it is likewise collecting several `flex` objects. However, it comprises all `flex` objects that together correspond to a solution vector to a (linear) equation system, namely the CC and the EOM-CC equations. This means, that all $\hat{T}$-, $\hat{\mathcal{R}}$-, $\hat{\mathcal{L}}$-, and $\hat{\mathcal{Z}}$-amplitudes (see Eqs. (2.89)-(2.91), (2.105), (2.111), and (2.135)) as well as the basis and sigma vectors appearing in the Davidson method (see Chpt. 3.3) are saved as `complete` objects. As is shown in Tab. 3.5, `complete` objetcs are built up analogously to `group` objects apart from the fact that `flex` objects of different dimensionality and therefore quasiparticle strings are collected. Hence, information about the latter becomes gratuitous. The construction of a `complete` object is independent of any additional information and, therefore, very simple. When instancing a `complete` object by

Table 3.5: The object structure of the data type `complete`. As a showcase, the information on the basis vector $\boldsymbol{b}$ in an EOM-EE-CCSD calculation is given.

Information	Data type	Example: $\boldsymbol{b}$
Values	`std::vector<flex>`	(...)
Spin cases	`std::vector<std::string>`	("aa","bb", "aaaa","bbbb","abab")

`complete object_name`; ,

the comprised `flex` objects are constructed automatically. For each implemented method, the associated `flex` objects constructing a solution vector are tabulated. This is shown in Tab. 3.6 together with additional information on the fixed index strings for each `flex` object.

3.1.4 Interface

In principle, QCUMBRE is a complex-valued CC and EOM-CC program package that is not limited to the application of finite magnetic field calculations. It is solely dependent on spin-integrated integrals in the MO basis. To simplify migration to various integral-providing program packages, it is supposed to be largely independent of external data types. Currently, integrals are obtained via an interface to the LONDON program package [29] which first performs a HF-SCF calculation using GIAOs and then transforms the integrals into the MO basis. In particular, the interface reads the Fock matrix elements f_{ij}, f_{ab}, f_{ia}, and f_{ai} for each non-recurrent and non-vanishing spin case

Table 3.6: For all implemented methods, the non-redundant spin cases of the `flex` objects that correspond to a `complete` object are listed. The fixed index strings of the associated `flex` objects are listed (disregarding the spin case).

Method	Spin cases	Default index string
(EOM-EE-)CCSD	$\alpha\alpha$, $\beta\beta$	ai
	$\alpha\alpha\alpha\alpha$, $\beta\beta\beta\beta$, $\alpha\beta\alpha\beta$	abij
additionally for CCSDT	$\alpha\alpha\alpha\alpha\alpha\alpha$, $\beta\beta\beta\beta\beta\beta$, $\alpha\alpha\beta\alpha\alpha\beta$, $\alpha\beta\beta\alpha\beta\beta$	abcijk
EOM-SF-CCSD	$\alpha\beta$	ai
$\Delta M_S = +1$	$\alpha\alpha\beta\alpha$, $\alpha\beta\beta\beta$	abij
EOM-SF-CCSD	$\beta\alpha$	ai
$\Delta M_S = -1$	$\beta\alpha\alpha\alpha$, $\beta\beta\alpha\beta$	abij
EOM-IP-CCSD	β	i
$\Delta M_S = +\frac{1}{2}$	$\alpha\alpha\beta$, $\beta\beta\beta$	bji
EOM-IP-CCSD	α	i
$\Delta M_S = -\frac{1}{2}$	$\alpha\alpha\alpha$, $\beta\beta\alpha$	bji
EOM-EA-CCSD	α	a
$\Delta M_S = +\frac{1}{2}$	$\alpha\alpha\alpha$, $\alpha\beta\beta$	abj
EOM-EA-CCSD	β	a
$\Delta M_S = -\frac{1}{2}$	$\beta\alpha\alpha$, $\beta\beta\beta$	abj

as well as the antisymmetrized two-electron integrals $\langle ab||cd\rangle$, $\langle ij||kl\rangle$, $\langle ij||ab\rangle$, $\langle ab||ci\rangle$, $\langle ij||ka\rangle$, and $\langle ia||bj\rangle$. If necessary, the dipole moment integrals μ^w_{ij}, μ^w_{ab}, μ^w_{ia}, and μ^w_{ai} ($w = x, y, z$) are transferred as well. Tensors are saved in binary code in row-major order with preceding information on the number and extent of dimensions. Values are directly saved in their corresponding `flex` objects. Therefore, program migration only requires adjustments in the reading process if the ordering of the tensors' values differs from the described pattern. During the reading process, the information about the number of electrons with α- and β-spin (occupation numbers `nao` and `nbo`, respectively) as well as the number of virtual orbitals (`nav` and `nbv`) is extracted from the bounds of the $\langle i\bar{j}||a\bar{b}\rangle$ submatrix. Optionally, converged $\hat{T}$-amplitudes that have been generated in a CCSD calculation within London can be read.

3.2 Contraction routine - Implementing equations

While integrals are read in from disk via an appropriate function, other quantities like the many-body terms of $\bar{\boldsymbol{H}}$ and the $\hat{T}$- or $\hat{\mathcal{R}}$-amplitudes have to be determined by evaluating corresponding working equations. As shown, these equations consist of sums of contractions between multidimensional quantities. Any such operation

$$C_{ab\ldots ij\ldots} = \sum_{mn\ldots} A_{ab\ldots mn\ldots} B_{mn\ldots ij\ldots} \tag{3.6}$$

can be understood as a matrix multiplication

$$\boldsymbol{AB} = \boldsymbol{C} \qquad \text{with elements} \qquad C_{pr} = \sum_{q} A_{pq} B_{qr} \tag{3.7}$$

where $mn\ldots = q$ is the superindex that both quantities have in common and $ab\ldots = p$ and $ij\ldots = r$ are the two dimensions of the resulting matrix. Hence, for each term appearing in the working equations, a matrix multiplication can be performed. The resulting tensor can be scaled by a potential prefactor and added to existing values. As these are saved in `flex` objects for each spin case, `flex` objects, therefore, feature a contraction method to manipulate the quantity's entries. The essential requirements for such a routine are:

1. Programming the individual terms should be simple. This means that coded equations should resemble their written form on paper. This implies that the routine is capable of internally performing any index permutations necessary for a matrix multiplication.

2. The numerical evaluation should be fast and, hence, take advantage of the BLAS complex-valued matrix multiplication routine *zgemm3m*. [93, 94][9]

The actual contraction routine call is mediated by a method of the `group` or `complete` object for that values are to be calculated:

`object_name.contract(`spin case, prefactor, quantity 1, indices 1,
quantity 2, indices 2`);` .

It contains the spin case of the resulting quantity which is the spin case of the `flex` object whose values are modified, the term's prefactor, as well as the two `group` or `complete` objects and their respective index strings. Hence, going back to the second term in Eq. (3.4) as a showcase, the corresponding contraction reads:

```
sigma.contract("aa", 1., W_iabj, "mAeI", b, "em"); .
```

---

[9] It reduces the number of formally necessary multiplications of real matrices from four to three coming at the cost of performing five instead of two matrix additions which saves up to 25% computation time. [94]

In a first step, a consistency check is performed on the indices.[10] The first entry `"aa"` determines that the `flex` object used for the $\alpha\alpha$-spin case of the $\boldsymbol{\sigma}$-vector's singles amplitudes is to be manipulated. The actual contraction routine is a method of the class `flex` and is called automatically. The routine's structure is depicted in Fig. 3.1 and illustrated by the mentioned showcase. Initially, the two index strings are checked for redundant characters. Those are recognized as the summation indices from which the superindex is constructed. If for one quantity the summation indices are already in the correct position,[11] this order is chosen as superindex. Assembling the superindex that way minimizes the number of permutations and, thereby, the computational cost. Following, the requested spin case of each input quantity is determined by analyzing the case sensitive index strings. If the index order of any input quantity has to be changed, the required `flex` object is duplicated and its values are swapped in a one-step process to match the desired index order. For quantities already exhibiting the appropriate index order, the original `flex` object is used directly as input for the matrix multiplication. The matrix multiplication is performed using the BLAS routine *zgemm3m* [93, 94] that multiplies arbitrary complex-valued matrices. The dimensions of the input matrices are given by the product of the dimensions of the target indices and the summation indices, respectively. The resulting matrix represents a multidimensional quantity with as many dimensions as target indices. Its index order arises from combining the target indices of the first and the second contracted quantity. A last consistency check is performed by comparing the remaining indices to the index string of the target `flex` object. Last, the obtained values are scaled by the prefactor and added upon the values of the `flex` object that called the contraction method. If the index order does not yet equal the one of the target quantity, swapping and adding of the values are taken care of in another one-step process.

3.3 Solver routines

All quantum-chemical methods presented in this thesis formally necessitate the handling of matrices with a dimensionality d of potentially several millions. For both a system of linear equations (SLE) or an eigenvalue problem (EVP), hence, a direct solving approach poses major difficulties. All entries of the respective matrix have to be kept in the virtual memory at the same time. For a matrix with $d = 100000$ containing real double-precision floating-point numbers, this would already correspond to 75 GB and twice as much for complex values. Therefore, iterative solving techniques have to be applied.

---

[10] All consistency checks are available for debugging and can be dropped for production runs.

[11] This means all summation indices make up the last indices of the first quantity or the first indices of the second quantity, respectively.

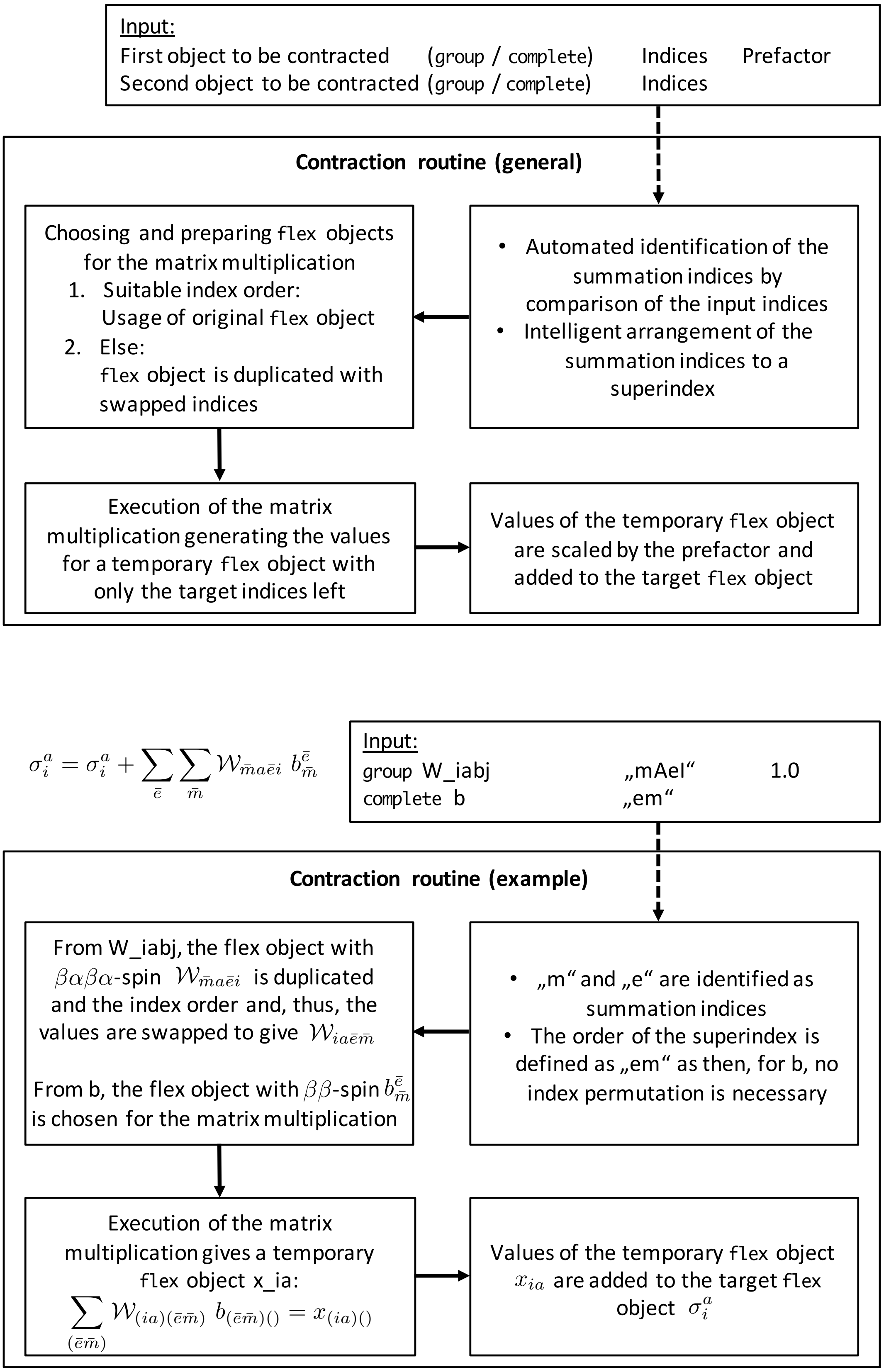

Input:
First object to be contracted (`group` / `complete`) Indices Prefactor
Second object to be contracted (`group` / `complete`) Indices

Contraction routine (general)

- Automated identification of the summation indices by comparison of the input indices
- Intelligent arrangement of the summation indices to a superindex

Choosing and preparing `flex` objects for the matrix multiplication
1. Suitable index order: Usage of original `flex` object
2. Else: `flex` object is duplicated with swapped indices

Execution of the matrix multiplication generating the values for a temporary `flex` object with only the target indices left

Values of the temporary `flex` object are scaled by the prefactor and added to the target `flex` object

$$\sigma_i^a = \sigma_i^a + \sum_{\bar{e}} \sum_{\bar{m}} \mathcal{W}_{\bar{m}a\bar{e}i}\, b_{\bar{m}}^{\bar{e}}$$

Input:
`group` W_iabj „mAel“ 1.0
`complete` b „em“

Contraction routine (example)

- „m“ and „e“ are identified as summation indices
- The order of the superindex is defined as „em“ as then, for b, no index permutation is necessary

From W_iabj, the flex object with $\beta\alpha\beta\alpha$-spin $\mathcal{W}_{\bar{m}a\bar{e}i}$ is duplicated and the index order and, thus, the values are swapped to give $\mathcal{W}_{ia\bar{e}\bar{m}}$

From b, the flex object with $\beta\beta$-spin $b_{\bar{m}}^{\bar{e}}$ is chosen for the matrix multiplication

Execution of the matrix multiplication gives a temporary `flex` object x_ia:

$$\sum_{(\bar{e}\bar{m})} \mathcal{W}_{(ia)(\bar{e}\bar{m})}\; b_{(\bar{e}\bar{m})()} = x_{(ia)()}$$

Values of the temporary `flex` object x_{ia} are added to the target `flex` object σ_i^a

Figure 3.1: Flow chart illustrating the structure of the contraction routine.

The solver routines in QCUMBRE comprise an iterative linear solver including the DIIS (*direct inversion of the iterative subspace*) extrapolation technique [95] as well as a generalized Davidson routine. [57,75] The former is used to solve the CC amplitude equations, to obtain the left eigenvectors for EOM-CC states, and to evaluate the $\hat{\mathcal{Z}}$-equations for CCSD-LR calculations. The generalized Davidson routine solves for a set of roots and corresponding (right) eigenvectors of the $\bar{\boldsymbol{H}}$-matrix within EOM-CC calculations. Both solver routines are presented in the following.

3.3.1 Iterative linear solver and DIIS

An SLE as well as an EVP may be expressed by

$$\boldsymbol{At} + \boldsymbol{b} = \omega \boldsymbol{t}. \tag{3.8}$$

$\boldsymbol{A}$ is a matrix, $\boldsymbol{t}$ a solution vector, $\boldsymbol{b}$ an inhomogeneity ($= \boldsymbol{0}$ for EVP), and ω an eigenvalue ($= 0$ for SLE). In both cases, an iterative linear solver can provide solutions for $\boldsymbol{t}$ if all other components are known. In order to obtain an expression that allows for an iterative procedure, a formal zero is added introducing a diagonal matrix $\boldsymbol{D}$ that is a good approximation to $\boldsymbol{A}$:

$$\boldsymbol{At} + \boldsymbol{Dt} - \boldsymbol{Dt} + \boldsymbol{b} = \omega \boldsymbol{t}. \tag{3.9}$$

$\boldsymbol{t}$ may then be determined iteratively by solving

$$\boldsymbol{t}^{(n+1)} = (\boldsymbol{At}^{(n)} - \boldsymbol{Dt}^{(n)} + \boldsymbol{b}) \cdot (\mathbb{1}\omega - \boldsymbol{D})^{-1}. \tag{3.10}$$

In this way, the matrix $\boldsymbol{A}$ does not have to be assembled. Instead, only instructions on how to evaluate the product $\boldsymbol{At}$ have to be available. These are given by, e.g., the EOM working equations or the $\hat{\mathcal{Z}}$-equations.[12]

As depicted in Fig. 3.2, all additional steps per iteration are trivial and non-expensive as they only comprise vector addition as well as scalar multiplication. In case of the CC amplitude equations, only a division by the denominator given in Eq. (3.19) occurs additionally. Two different convergence criterion checks have been implemented. For the CC amplitude equations, convergence is reached when the largest difference of elements of the solution vector $|t_k'^{(n+1)} - t_k^{(n)}|$ does not exceed the convergence criterion. For general SLEs, the norm of the difference vector $|\boldsymbol{t}'^{(n+1)} - \boldsymbol{t}^{(n)}|$ is used. Each iteration provides a trial vector $\boldsymbol{t}^{(n)}$ and a difference vector $\boldsymbol{e}^{(n)} = \boldsymbol{t}'^{(n+1)} - \boldsymbol{t}^{(n)}$. The aim of the optional DIIS approach is now to not only consider the current iteration's correction

---

[12] For the CC amplitude equations, see the numerator in Eq. (3.19) in Chpt. 3.4.1).

but all corrections of the i previous iterations. An error vector $\boldsymbol{E}$ may be defined as a linear combination of the last i difference vectors $\boldsymbol{e}_i$ with

$$\boldsymbol{E} = \sum_i c_i \boldsymbol{e}_i \qquad , \qquad \sum_i c_i = \sum_i c_i^\dagger = 1. \tag{3.11}$$

The norm of this error vector has to be minimized. Hence, a Lagrangian can be set up as

$$L = |\boldsymbol{E}|^2 + \lambda \sum_i (c_i^\dagger - 1) = \sum_{ij} c_i^\dagger \boldsymbol{e}_i^\dagger c_j \boldsymbol{e}_j + \lambda \sum_i (c_i^\dagger - 1) \tag{3.12}$$

resulting in the conditional equations (3.13) and (3.14):

$$\frac{\partial L}{\partial c_k^\dagger} = \sum_j \boldsymbol{e}_i^\dagger \boldsymbol{e}_j c_j + \lambda = \sum_j B'_{ij} c_j + \lambda \overset{!}{=} 0, \tag{3.13}$$

$$\frac{\partial L}{\partial \lambda} = \sum_i (c_i^\dagger - 1) = \sum_i (c_i - 1) \overset{!}{=} 0. \tag{3.14}$$

They can be combined in an SLE containing the DIIS matrix $\boldsymbol{B}$ and a solution vector with the desired coefficients c_i:

$$\begin{pmatrix} 0 & 1 & 1 & 1 & \cdots \\ 1 & B'_{11} & B'_{12} & B'_{13} & \cdots \\ 1 & B'_{21} & B'_{22} & B'_{23} & \cdots \\ 1 & B'_{31} & B'_{32} & B'_{33} & \cdots \\ \vdots & \vdots & \vdots & \vdots & \ddots \end{pmatrix} \begin{pmatrix} \lambda \\ c_1 \\ c_2 \\ c_3 \\ \vdots \end{pmatrix} = \begin{pmatrix} 1 \\ 0 \\ 0 \\ 0 \\ \vdots \end{pmatrix}. \tag{3.15}$$

This small SLE is directly solved with the standard LAPACK *zgesv*-solver for complex-valued problems. [96] With the optimized coefficients obtained, the new trial vector can be assembled not only as a linear combination of the trial and difference vector of the current iteration but is rather extrapolated by a linear combination of those of the last i iterations:

$$\boldsymbol{t}'^{(n+1)} = \sum_i^n c_i \left(\boldsymbol{t}^{(i)} + \boldsymbol{e}^{(i)} \right). \tag{3.16}$$

Thus, convergence may be accelerated.

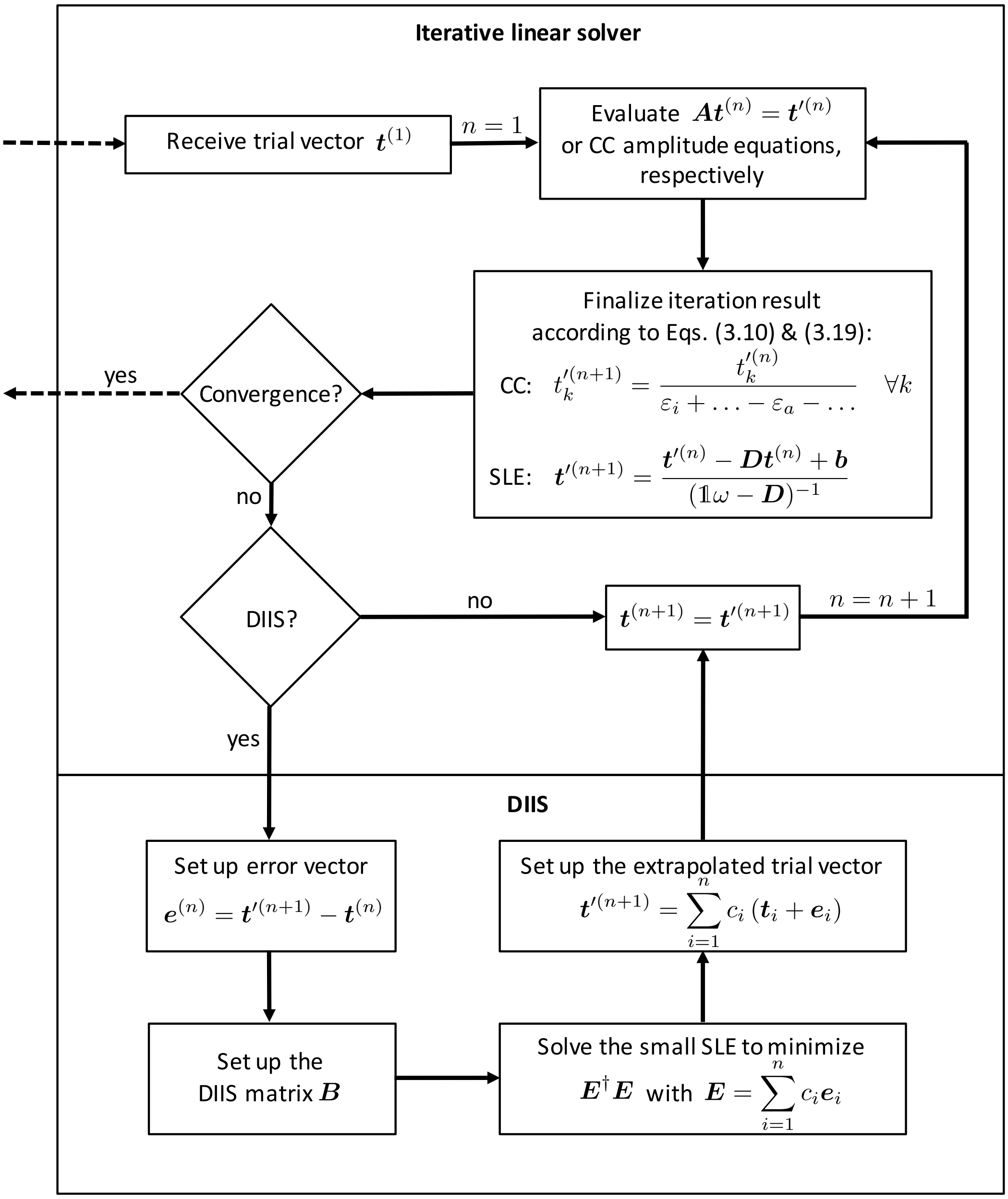

Figure 3.2: Flow chart illustrating the structure of the iterative linear solver including the DIIS extrapolation technique.

3.3.2 Davidson procedure

Solving the CI or EOM-CC problem requires the diagonalization of the CI-matrix $\boldsymbol{H}$ or the EOM-matrix $\bar{\boldsymbol{H}}$. A direct solving approach not only exhibits an enormous virtual-memory demand but also loses a lot of computing time. In most cases, only the lowest eigenvalues and their eigenvectors are of interest. However, a direct diagonalization yields all solutions simultaneously. These issues can be alleviated by applying an iterative strategy. The Davidson procedure [57] has originally been developed to iteratively calculate the lowest eigenvalues of large Hermitian matrices. To do so, the eigenvalue problem is solved in a low-dimensional subspace yielding an approximate solution when transformed into the full space. The subspace is enlarged with each iteration until the solution is sufficiently accurate. Fig. 3.3 illustrates the steps involved for the case of a non-Hermitian matrix $\bar{\boldsymbol{H}}$.

In the beginning, a first basis vector $\boldsymbol{b}^{(1)}$ for spanning the subspace is chosen (**1**). Following, the matrix-vector product of $\bar{\boldsymbol{H}}$ with the basis vector $\boldsymbol{b}^{(n)}$ is calculated and the so-called sigma vector $\boldsymbol{\sigma}^{(n)}$ is obtained (**2**). Subsequently, the Hamiltonian matrix is projected onto the subspace by calculating the entries $\tilde{H}_{ij}$ via the dot product between the corresponding basis and sigma vectors (**3**). Standard routines [96] can diagonalize $\tilde{\boldsymbol{H}}$ (**4**) and the desired eigenvalue $\lambda^{(n)}$ and subspace eigenvector $\tilde{\boldsymbol{r}}^{(n)}$ can be chosen (**5**) from the provided set. $\tilde{\boldsymbol{r}}^{(n)}$ is transformed into the full space vector $\boldsymbol{r}^{(n)}$ (**6**) and the deviation of the approximate solution is quantified by calculating the residual vector $\boldsymbol{k}^{(n)} = \bar{\boldsymbol{H}}\boldsymbol{r}^{(n)} - \lambda^{(n)}\boldsymbol{r}^{(n)}$ (**7**) and determining its norm (**8**). If this is smaller than a certain threshold ε (**9**), the procedure has converged. Otherwise, a new basis vector $\boldsymbol{b}^{'}$ is defined by scaling the entries of the residual vector individually according to (**10**). In the following, it is orthonormalized against the existing set of basis vectors $\{\boldsymbol{b}^{(i)}\}$ and the procedure enters the next iteration.

The Davidson method does not require the calculation of $\bar{\boldsymbol{H}}$ in any step as only the matrix-vector multiplication $\bar{\boldsymbol{H}}\boldsymbol{b} = \boldsymbol{\sigma}$ is needed. As the number of iterations is by far smaller than the dimensionality of $\bar{\boldsymbol{H}}$, virtual memory is saved as compared to a direct diagonalization. Such a generalized Davidson routine [75] has been implemented in the QCUMBRE program package in order to solve the EOM-CC equations (2.108). In the case of EOM-CC for finite magnetic fields, the usage of the LAPACK *zgeev*-solver [96] for diagonalizing the general complex-valued matrix $\tilde{\boldsymbol{H}}$ is required.

The tracking of roots (**5**) when diagonalizing $\tilde{\boldsymbol{H}}$ throughout the iterations is handled in the following way: For $||\boldsymbol{k}^{(n)}|| > 10^{-1}$, the eigenvector yielding the largest overlap with the initial guess vector is chosen. If $||\boldsymbol{k}^{(n)}||$ is smaller, the eigenvector with the largest overlap with the previous iteration's eigenvector is selected.

In order to reduce memory requirements, an optional user-defined upper limit to the number of basis and sigma vectors $\boldsymbol{b}^{(n)}$ and $\boldsymbol{\sigma}^{(n)}$ has been implemented. Whenever adding another basis vector would exceed this limit in iteration n, all current basis and sigma vectors are deleted. The basis vectors are then replaced by the current eigenvector $\boldsymbol{b}^{(1)} = \boldsymbol{r}^{(n)}$ while the corresponding sigma vector is obtained by

$$\boldsymbol{\sigma}^{(1)} = \sum_{i=1}^{n} \tilde{r}_i \cdot \boldsymbol{\sigma}^{(i)} \text{ (see } (\mathbf{6})\text{)}. \tag{3.17}$$

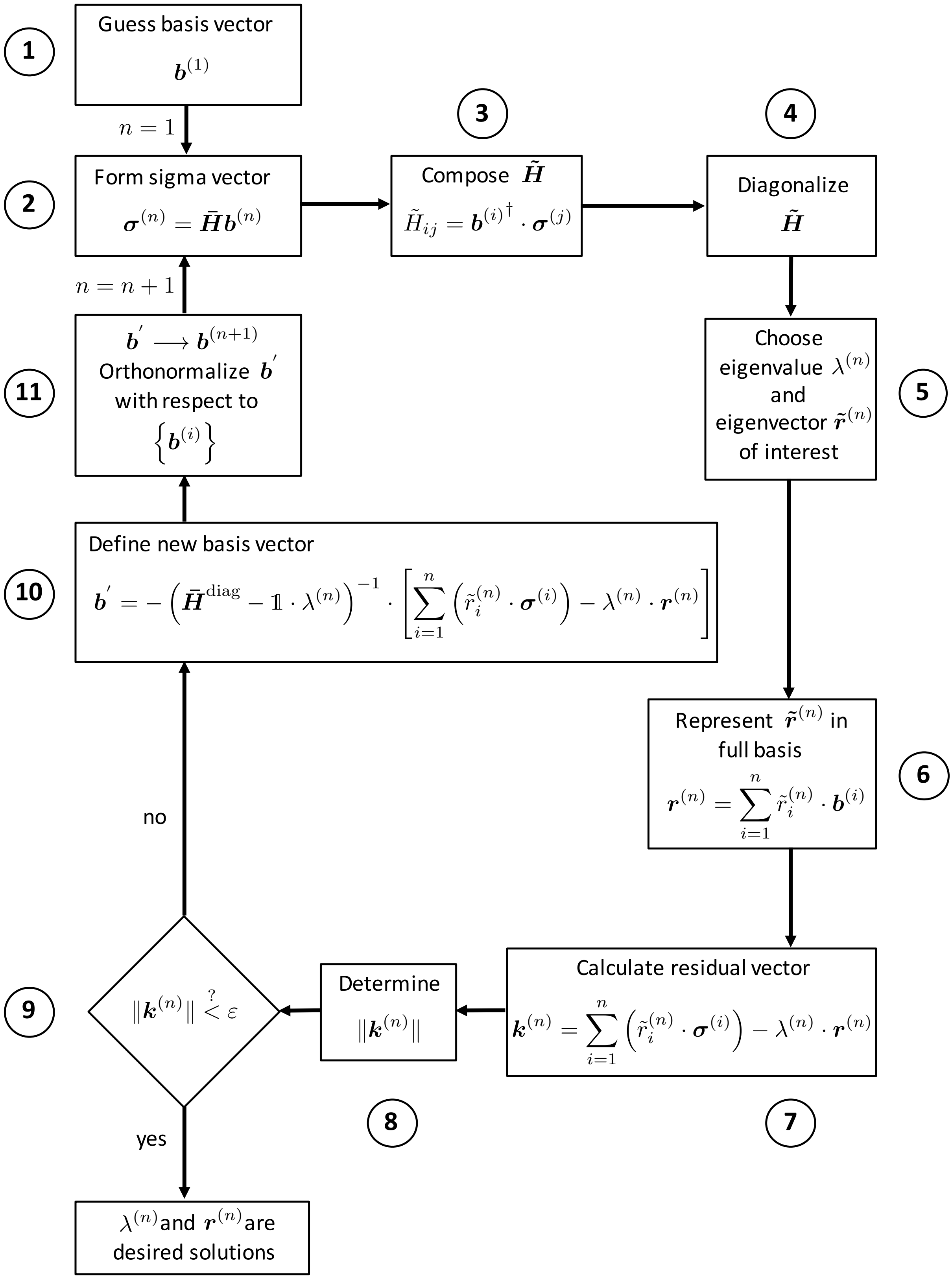

Figure 3.3: Flow chart illustrating the modified Davidson method [57,75] for the diagonalization of a non-Hermitian matrix $\bar{\boldsymbol{H}}$. In the case of EOM-CC for finite magnetic fields, step **4** requires a diagonalization routine for a general complex-valued matrix.

Thus, memory requirements are reduced at the cost of slowed convergence.

3.4 Method routines

With the solver routines at hand, the actual method routines merely have to serve preparative and administrative functions as is shown in the following.

3.4.1 CC program

If no $\hat{T}$-amplitudes are provided by a preceding calculation of an underlying program package, the CC program is called in order to determine them as well as the correlation energy. As a starting point, the $\hat{T}_2$-amplitudes from second-order Møller-Plesset perturbation theory (MP2) are calculated:

$$t_{ij}^{ab(1)} = \frac{\langle ab| |ij\rangle}{\varepsilon_i + \varepsilon_j - \varepsilon_a - \varepsilon_b}. \tag{3.18}$$

They are used as the initial vector for the linear solver. Note that the CC amplitude equations are not a linear equation system but are treated as such. It is assumed that the coupling between the amplitudes is small and, therefore, convergence can be reached (see, e.g., Ref. [97]). In order to obtain expressions enabling iterative solving approaches, the CC amplitude equations are recast. In each amplitude equation, the terms $P_-(a/b\ldots)\sum_e t_{ij\ldots}^{eb\ldots} f_{ae}$ and $-P_-(i/j\ldots)\sum_m t_{mj\ldots}^{ab\ldots} f_{mi}$ appear which simplify to $t_{ij\ldots}^{ab\ldots}(\varepsilon_a + \varepsilon_b + \ldots)$ and $-t_{ij\ldots}^{ab\ldots}(\varepsilon_i + \varepsilon_j + \ldots)$, respectively, where the ε_p are the diagonal elements of the Fock matrix. Recasting gives

$$t_{ij\ldots}^{ab\ldots(n+1)} = \frac{\langle \Phi_{ij\ldots}^{ab\ldots}| (\hat{H}\mathrm{e}^{\hat{T}^{(n)}})_\mathrm{c} |\Phi_0\rangle - t_{ij\ldots}^{ab\ldots(n)}(\varepsilon_a + \varepsilon_b + \ldots) + t_{ij\ldots}^{ab\ldots(n)}(\varepsilon_i + \varepsilon_j + \ldots)}{\varepsilon_i + \varepsilon_j + \ldots - \varepsilon_a - \varepsilon_b - \ldots}, \tag{3.19}$$

and, therefore, allows for an iterative approach. Currently, the CCSD, CCSD(T), and CCSDT schemes are implemented.

After convergence, the final CC correlation energy is calculated using Eq. (2.102) and the perturbative triples correction is evaluated if demanded. The largest $\hat{T}_2$-amplitudes are printed to allow for an assessment of the multireference character of the investigated state.

3.4.2 EOM-CC program

Each EOM-CC calculation is preceded by a CIS calculation. For the different variants of the EOM method, this means that the bare Hamiltonian is directly diagonalized in the basis of all determinants that can be produced by letting $\hat{\mathcal{R}}_1$ act upon the reference determinant $|\Phi_0\rangle$. The CIS eigenvalues are ordered in ascending order. For the requested number of roots, the corresponding eigenvectors are used each as an initial basis vector in the Davidson routine. In this process, the CIS coefficients match the corresponding $\hat{\mathcal{R}}_1$-amplitudes while all other amplitudes are chosen to be zero. The program offers the option to skip selected CIS roots and additionally allows for user-defined guess vectors. After convergence is reached for all desired roots, the excitation energies are printed. In addition, the leading excitations, i.e., the largest entries in the corresponding eigenvector, are listed. For EOM-EE, -SF, -IP, and -EA, the methods have been implemented within the CCSD approximation. Additionally, the EOM-EE-CCSDT scheme is available.

3.4.3 EOM-CC properties program

If the calculation of (transition) dipole moments is requested, the program for determining one-electron properties is called. Fig. 3.4 illustrates its algorithmic structure. In a first step in the case of EOM-EE, the converged right eigenvectors are completed by calculating the r_0-values using Eq. (2.114). Subsequently, the left eigenvectors corresponding to the converged right eigenvectors $\boldsymbol{r}_K$ are determined. As the eigenvalues $\Delta E_{\text{exc}}^{(K)}$ are already known, $\boldsymbol{l}_K\bar{\boldsymbol{H}} = \Delta E_{\text{exc}}^{(K)}\boldsymbol{l}_K$ can be solved with a linear solver taking

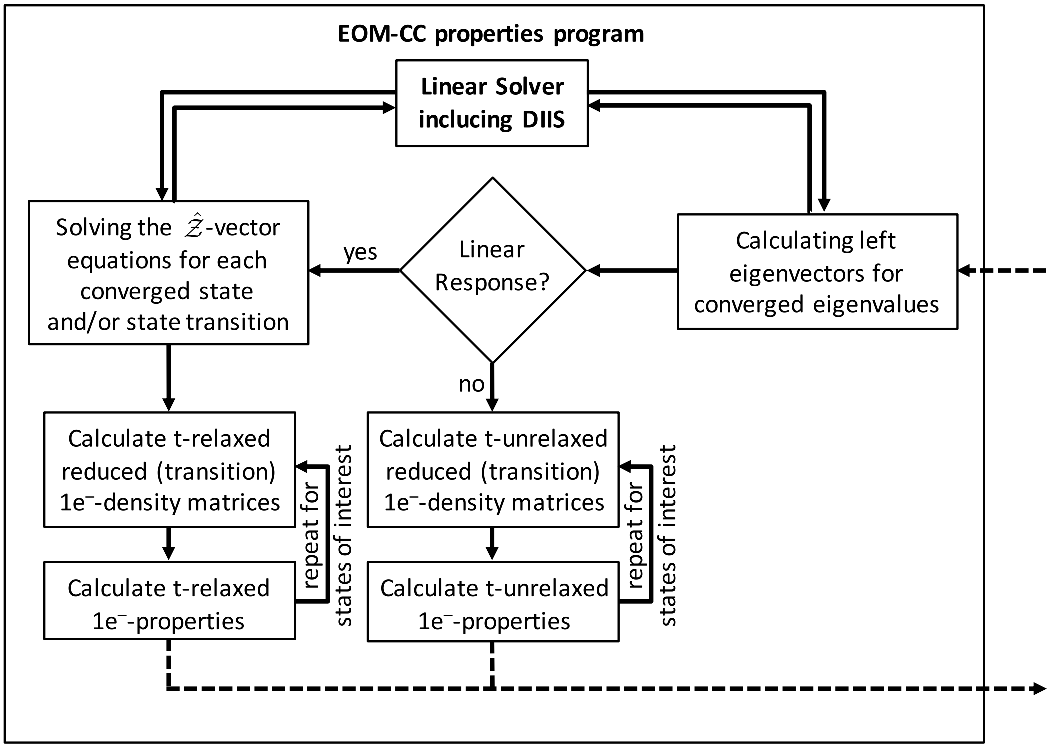

Figure 3.4: Flow chart illustrating the structure of the EOM-CC properties program.

advantage of the DIIS technique.[13] The $\boldsymbol{r}_K^\dagger$ are used as the corresponding guess vectors. If properties are to be calculated at the EOM level of theory following Eq. (2.119), the corresponding reduced one-electron density matrix is set up from a pair of $\boldsymbol{r}_K$ and $\boldsymbol{l}_L$ and contracted with the dipole moment integrals which are read in via the interface. Thus, the desired EOM property is obtained. The procedure is repeated for all states ($K = L$: dipole moment) or pair of states ($K \neq L$: transition dipole moment) before the final output is produced.

For a size-intensive evaluation of properties, the procedure is altered in the way that the calculation of the modified (connected) one-electron matrix is preceded by solving the corresponding $\hat{\mathcal{Z}}$-equations (2.137). For the linear solver, a zero vector is used as a guess vector. The final property is calculated by following Eq. (2.136) which involves contractions between the dipole integrals and the one-electron density matrix as well as additional contractions containing the $\hat{\mathcal{Z}}$-amplitudes.

3.5 Compact program code

A CC and EOM-CC program package based upon the presented routines consists of a managable number of code lines. Figure 3.5 illustrates their interplay and, hence, the general structure of the QCUMBRE program package. In a first step, the interface routine is called, reading the necessary integrals for the calculation. If no $\hat{T}$-amplitudes are provided, the CC program is invoked and a CC calculation is performed. Consecutively, the EOM-CC program is executed determining respective excitation energies and corresponding right eigenvectors. In a last step, the EOM-CC properties program manages the calculation of one-electron properties if requested.

As intended, program extensions merely require the implementation of the additional equations (contractions) that are called by the respective solver routines. In fact, the modular program structure and user-friendly contraction-routine input enabled the implementation, verification, and application of both the CCSDT and EOM-EE-CCSDT method in the context of a master's thesis by N. Gross. [89] For illustrative purposes, Fig. 3.6 displays the program code that constitutes the spin-integrated singles amplitude equations within the CCSD and CCSDT method. Each contributing term is represented by a single short line of code. It consists of hardly more information than the respective algebraic expression itself features. The code merely includes a prefactor, the name of two quantities and their index strings.[14] In this way, all major equations can be represented by a couple of simple lines of code.

---

[13] Since for the CC ground state $\Delta E_{\text{exc}}^{(0)} = 0$, the same procedure can be used to evaluate the Λ-equations.

[14] Note that a preceding `"X"` in the index string indicates that the complex-conjugate of the corresponding quantity is used.

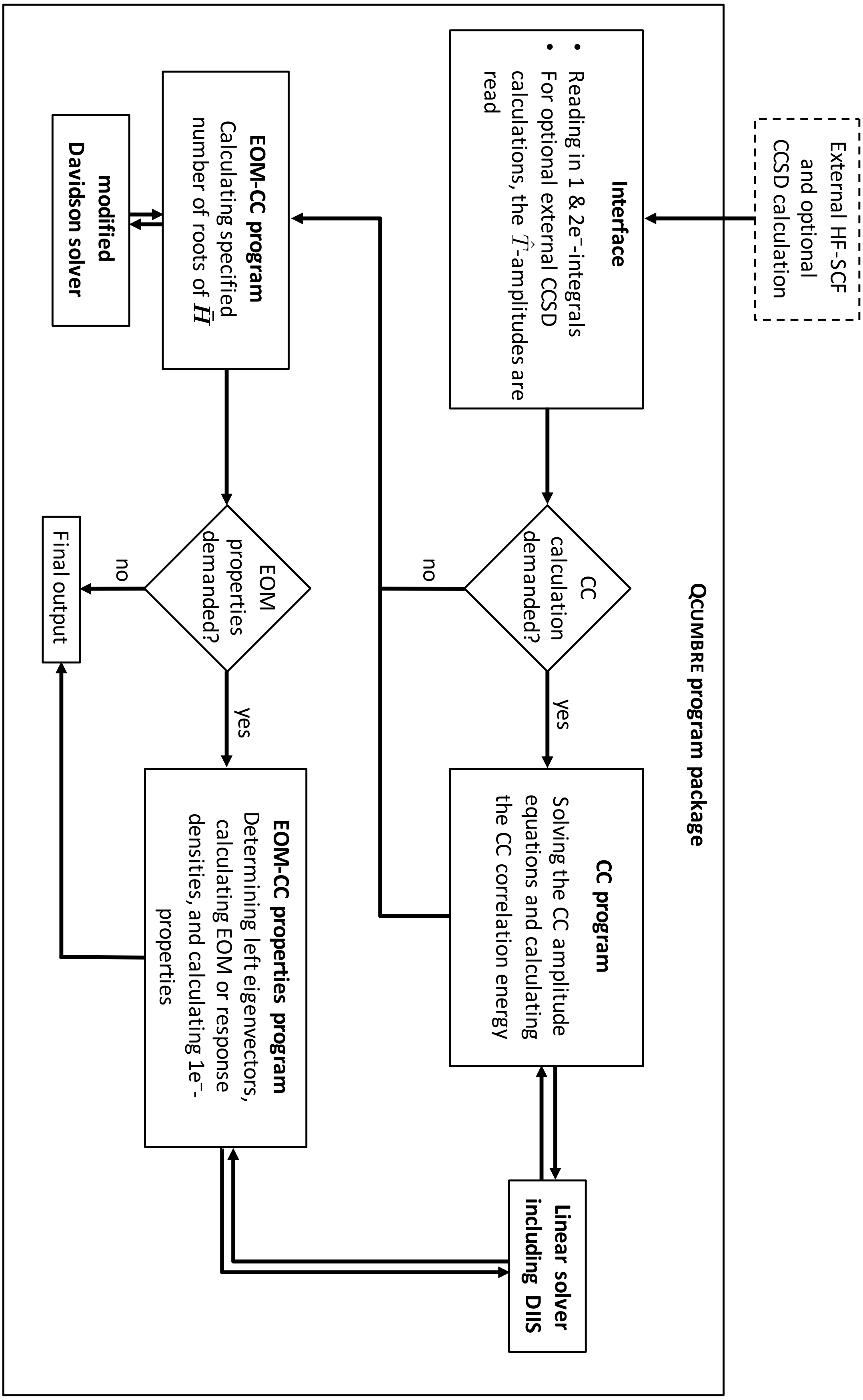

Figure 3.5: Flow chart illustrating the structure of the QCUMBRE program package.

```
sigma.contract(1., "aa", f_ai);
sigma.contract("aa", 1., F_ab, "AE", t, "EI");
sigma.contract("aa", -1., f_ab, "AE", t, "EI");
sigma.contract("aa", -1., F_ij, "MI", t, "AM");
sigma.contract("aa", 1., f_ij, "MI", t, "AM");
sigma.contract("aa", 1., F_ia, "ME", t, "AEIM");
sigma.contract("aa", 1., F_ia, "me", t, "AeIm");
sigma.contract("aa", 1., I_iabj, "MAEI", t, "EM");
sigma.contract("aa", 1., I_iabj, "mAeI", t, "em");
sigma.contract("aa", -0.5, I_ijka, "MNIE", t, "AEMN");
sigma.contract("aa", -1., I_ijka, "MnIe", t, "AeMn");
sigma.contract("aa", 0.5, I_abci, "XEFAM", t, "EFIM");
sigma.contract("aa", 1., I_abci, "XEfAm", t, "EfIm");

if (CC=="ccsdt") {
    sigma.contract("aa", 0.25, I_ijab, "MNEF", t, "AEFIMN");
    sigma.contract("aa", 1., I_ijab, "MnEf", t, "AEfIMn");
    sigma.contract("aa", 0.25, I_ijab, "mnef", t, "AefImn");
}


sigma.contract(1., "bb", f_ai);
sigma.contract("bb", 1., F_ab, "ae", t, "ei");
sigma.contract("bb", -1., f_ab, "ae", t, "ei");
sigma.contract("bb", -1., F_ij, "mi", t, "am");
sigma.contract("bb", 1., f_ij, "mi", t, "am");
sigma.contract("bb", 1., F_ia, "me", t, "aeim");
sigma.contract("bb", 1., F_ia, "ME", t, "EaMi");
sigma.contract("bb", 1., I_iabj, "maei", t, "em");
sigma.contract("bb", 1., I_iabj, "MaEi", t, "EM");
sigma.contract("bb", -0.5, I_ijka, "mnie", t, "aemn");
sigma.contract("bb", -1., I_ijka, "mNiE", t, "EaNm");
sigma.contract("bb", 0.5, I_abci, "Xefam", t, "efim");
sigma.contract("bb", 1., I_abci, "XEfAm", t, "EfMi");

if (CC=="ccsdt") {
    sigma.contract("bb", 0.25, I_ijab, "MNEF", t, "EFaMNi");
    sigma.contract("bb", 1., I_ijab, "MnEf", t, "EafMin");
    sigma.contract("bb", 0.25, I_ijab, "mnef", t, "aefimn");
}
```

Figure 3.6: Code for the spin-integrated singles amplitude equations for CCSD/CCSDT within QCUMBRE.

3.6 Validation

In the following, the validation of the code is described for each methodology. For all methods,[15] the following tests have been performed:

- In the field-free case, total energies, (transition) dipole moments, and reduced one-electron (transition) density matrices (where available) have been compared to results obtained by the use of the program package CFOUR [98] for open- and closed-shell systems with varying multiplicity.
- For cases where FCI equals the respective method, total energies, (transition) dipole moments, and reduced one-electron (transition) density matrices (where available) have been compared to results obtained by the use of the FCI implementation within the program package LONDON [29] for open- and closed-shell systems with varying multiplicity in a magnetic field.

CC:

- For arbitrary systems in the presence of a magnetic field, CCSD and CCSD(T) total energies have been compared to results obtained by the use of the program package LONDON.

EOM-EE-CC:

- Cases for which the paramagnetic contribution vanishes ($L = S = 0$) can be treated within the standard EOM-EE-CCSD implementation in the program package CFOUR. For this, the diamagnetic term is included as a harmonic potential. Total energies for these cases have been compared.
- For arbitrary systems in a magnetic field, the full $\bar{\boldsymbol{H}}$-matrix has been set up for EOM-EE-CCSD and diagonalized in order to compare the resulting eigenvalues to those obtained within the Davidson procedure. Setting up the full $\bar{\boldsymbol{H}}$-matrix has been accomplished by both using the many-body terms of $\bar{\boldsymbol{H}}$ directly and setting up the $\boldsymbol{H}$-matrix followed by manually performing the similarity transformation.

EOM-SF-CC:

- For triplet states of the same L value, the total energies of the states with $M_S = 0$ and $M_S = \pm 1$ differ only by the trivial spin-Zeeman term. The respective dipole moments are equivalent. With the same singlet reference wave function, the total energies as well as dipole moments of triplets states with $M_S = 0$ have been

---

[15] There is no EOM-SF-CCSD implementation available within CFOUR.

calculated using EOM-EE-CCSD. The corresponding triplet states with $M_S = \pm 1$ have been targeted using EOM-SF-CCSD in the presence of a magnetic field. The energy differences have been verified to only consist in the spin-Zeeman term while the dipole moments have been checked to be identical.

EOM-IP/EA-CCSD:

- For arbitrary systems in a magnetic field, EOM-IP/EA-CCSD-calculations can be mimicked using the EOM-EE-CCSD code. Ionization from an occupied orbital corresponds to the excitation of an electron from an occupied into a non-interacting virtual orbital of zero energy. Electron attachment into a virtual orbital corresponds to the excitation of an electron from a non-interacting occupied orbital of zero energy into a virtual orbital. In order to verify the EOM-IP/EA-CCSD total energies starting from an N-electron system, the following steps have been taken to accordingly modify the EOM-EE-CCSD calculation:
  For the IP case, an EOM-EE-CCSD calculation is performed on the N-electron system. After convergence of the HF-SCF program and the transformation of the integrals to the MO basis, an artificial virtual orbital is added. All additional entries in the one- and two-electron integrals are zero. The total energies obtained with the EOM-EE-CCSD calculation on those states with a dominant excitation into the artificial virtual orbital have been compared to the corresponding EOM-IP-CCSD total energies.
  For the EA case, an EOM-EE-CCSD calculation is performed on the N-electron system. After convergence of the HF-SCF program and the transformation of the integrals to the MO basis, an artificial occupied orbital is added. Again, all additional entries in the one- and two-electron integrals are zero. The total energies obtained with the EOM-EE-CCSD calculation on those states with a dominant excitation from the artificial occupied orbital have been compared to the corresponding EOM-EA-CCSD total energies.

3.7 Computational details and notation conventions

For all calculations presented in this thesis, Cartesian Gaussian basis functions have been used. If not stated otherwise, uncontracted Dunning's correlation-consistent basis sets [99–101] have been utilized (see Chpt. 4.3). To avoid linear dependencies, basis functions have been removed on the basis of a linear-dependence tolerance of 10^{-8}. Tab. 3.7 lists the used basis sets and how they are abbreviated within this thesis. The level of a calculation is specified by the expression 'method/basis set'.

Throughout this thesis, electronic states are labeled as A/B. A refers to the field-free

Table 3.7: Basis sets and their corresponding abbreviations as used within this thesis (X=D,T,Q,5).

Basis set	Abbreviation
cc-pVXZ [99]	X
aug-cc-pVXZ [100]	aX
aug-cc-pCVXZ [101]	aCX

symmetry and B represents the respective symmetry within the magnetic field. For simplicity, orbital occupations are given with respect to the field-free symmetry. For open-shell systems, unpaired electrons are implied to exhibit antiparallel (β-)spin with respect to the orientation of the magnetic field vector's orientation which is defining the spin-quantization axis. Corresponding states with unpaired α-spin electrons are higher in energy due to the spin-Zeeman term and, therefore, not considered.

4 Assessment

With the Qcumbre program package at hand, EOM-CC calculations can now be performed for atoms and molecules in strong magnetic fields. Before delving into the new chemistry and physics that is investigated in Chpt. 5, the performance of the respective methods is assessed. First, the power and flexibility of EOM methods in performing calculations in strong magnetic fields is demonstrated. For most quantum-chemical problems, it is possible to find a suitable EOM method such that the reference wave function is well-behaved and relevant states are treated on the same footing where required. This will be illustrated in the following. The performance of EOM-CC methods in terms of accuracy is investigated by discussing the influence of the truncation level and the choice of basis set. Last, the effects of seeming drawbacks such as the non-Hermiticity of CC and EOM-CC methods as well as the lack of a size-intensive evaluation of properties by EOM-CC methods are quantified.

4.1 Versatility of EOM-CC methods in strong magnetic fields

4.1.1 Accessing excited states - EOM-EE and EOM-SF

In this chapter, the accuracy of EOM-CC methods is emphasized by investigating total energies of the carbon atom [85] and comparing them to results from ground-state CC theory. The survey is confined to electronic states that become the ground state of the carbon atom for a certain range of field strengths (see Chpt. 5.1.1). These states are to some extent accessible via both EOM-CC as well as ground-state CC methods. The magnetic field is varied between $B = 0$-$1\ \mathrm{B}_0$ (with $1\ \mathrm{B}_0 \approx 235000$ T) and the energies have been calculated at the (EOM-EE/SF)-CCSD/aCQ levels of theory. In addition to the deviations in the total energies, the magnetic field strength for which these states cross is compared for the different methods.

Fig. 4.1a shows the total electronic energies of the $1^3\mathrm{P}_g/1^3\Pi_{-1,g}$ (black), the $1^5\mathrm{S}_u/1^5\Sigma_u$ (blue), and the $1^5\mathrm{F}_g/1^5\Phi_{-3,g}$ states (red) of the carbon atom obtained at the CCSD level of theory.[16] The CC energies for all considered states have been obtained in the following way: A HF calculation is performed for a field strength for that the desired state is the ground state. The converged HF density from this calculation is then used as a starting guess for the HF calculation for another field strength of interest. In doing so, convergence into the desired state is possible to some extent even for field strengths for which this is an excited state. For the $1^5\mathrm{F}_g/1^5\Phi_{-3,g}$ state, this procedure meets its limits for small field strengths and the calculation converges into the $1^5\mathrm{S}_u/1^5\Sigma_u$

---

[16] A corresponding discussion of energies obtained at the CCSD(T)/aC5 and CCSDT/aQ levels of theory can be found in the bachelor's and master's theses [89, 102] of Gross. The respective calculations have been performed by N. Gross under my guidance.

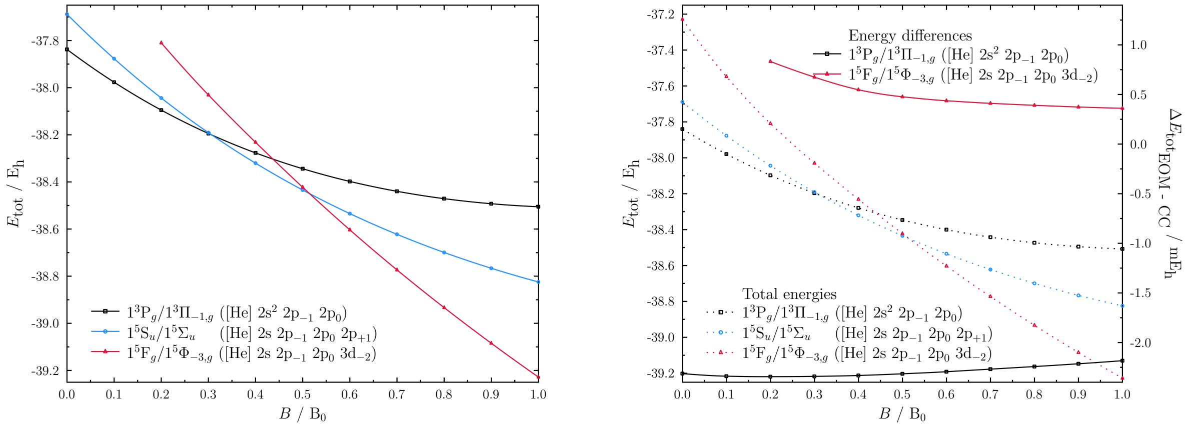

(a) E_{tot} (CCSD)

(b) E_{tot} (EOM-CCSD) & $\Delta E_{\mathrm{tot}_{\mathrm{EOM\,-\,CC}}}$

Figure 4.1: Total electronic energies of selected states of the carbon atom in a magnetic field between 0-1 B$_0$ obtained at the (a) CCSD/aCQ and (b) EOM-EE/SF-CCSD/aCQ levels of theory including energy differences.

state. Such problems do not occur when using the EOM-CC methods and such a rather cumbersome approach can be avoided. In the EOM calculations, the 1^5S$_u$/$1^5\Sigma_u$ state has been chosen as a reference wave function. In the latter, all p orbitals are singly occupied by electrons of the same spin and, hence, breaking the symmetry of the p orbitals is avoided. The 1^5F$_g$/$1^5\Phi_{-3,g}$ state can be reached via the EOM-EE variant by exciting the electron from the $2\mathrm{p}_{+1}^{\beta}$ into the $3\mathrm{d}_{-2}^{\beta}$ spin orbital. The 1^3P$_g$/$1^3\Pi_{-1,g}$ state can be described using the EOM-SF variant and transferring the $2\mathrm{p}_{+1}^{\beta}$ electron into the $2\mathrm{s}^{\alpha}$ orbital. Fig. 4.1b shows both the obtained total energies (dotted lines) as well as the deviation with respect to the CCSD results.

For the 1^3P$_g$/$1^3\Pi_{-1,g}$ state, total energies are lowered by 2.1-2.4 mE$_\mathrm{h}$ compared to CCSD. On the other hand, the total energies of the 1^5F$_g$/$1^5\Phi_{-3,g}$ state are higher by 0.3-0.9 mE$_\mathrm{h}$. The deviation with respect to CCSD, thereby, is smaller than 0.07 eV. A second criterion to assess the quality of the EOM-CC results is the field strength for which two states cross. Tab. 4.1 compares the crossing field strengths obtained at the different levels of theory including CCSD(T) results. Comparing EOM-CCSD to CCSD results, the first crossing point is shifted from $B \approx 0.3075$ B$_0$ by about 1200 T to a higher field strength of $B \approx 0.3124$ B$_0$. This coincides with the CCSD(T) result. However, this is put into perspective when consulting Ref. [89]. There, CCSD(T) crossing field strengths are compared to CCSDT results using the aQ basis set. There, an additional shift by approximately 700 T to higher field strengths is found for the first crossing. For EOM-CCSD, the second crossing point is shifted to a higher field strength of $B \approx 0.5165$ B$_0$ which differs from the CCSD, CCSD(T), and CCSDT results by approximately 600 T. However, unlike for the CC results, the EOM-CC approach

Table 4.1: Transition field strengths at which selected states of the carbon atom cross in a magnetic field between 0-1 B_0 calculated at different levels of theory.

	$\mathbf{1^3P_g/1^3\Pi_{-1,g}}$ **to** $\mathbf{1^5S_u/1^5\Sigma_u}$		$\mathbf{1^5S_u/1^5\Sigma_u}$ **to** $\mathbf{1^5F_g/1^5\Phi_{-3,g}}$	
Method	B / B_0	B / T	B / B_0	B / T
CCSD	0.3075	$\approx$ 72300	0.5140	$\approx$ 120800
CCSD(T)	0.3125	$\approx$ 73500	0.5141	$\approx$ 120800
EOM-CCSD	0.3124	$\approx$ 73400	0.5165	$\approx$ 121400

offers access to the evolution of the $1^5F_g/1^5\Phi_{-3,g}$ state for $B < 0.2$ B_0 and the initial slope of $-7/2$ E_h/B_0 can now be observed.[17] Considering the large discrepancies between total energies for different basis sets for the $1^5F_g/1^5\Phi_{-3,g}$ state (see also Chpt. 4.3), both the EOM-EE and EOM-SF variant offer very similar results compared to the CC approach.

4.1.2 Splitting of $^2\Pi$-states - EOM-IP and EOM-EA I

An illustrative showcase for the power of the EOM variants is the description of the energy landscape of excited states including spatially degenerate electronic states in open-shell systems. The carbyne radical (CH) is a molecule that exhibits a degenerate $1^2\Pi$ ground state ($1\sigma^2$ $2\sigma^2$ $3\sigma^2$ π) in the field-free case. It might well be present on magnetic white dwarfs since CH absorption bands occur in spectra from non-magnetic white dwarfs [103] and is, therefore, investigated in the following. The best-suited EOM variant for such systems is identified and the drawbacks and errors of the methods are discussed.

In a magnetic field parallel to the molecular axis, the degeneracy of the π orbitals is lifted[18] by the orbital-Zeeman term and the $1^2\Pi/1^2\Pi_{-1}$ as well as the $1^2\Pi/1^2\Pi_{+1}$ states emerge. The former is energetically stabilized in a magnetic field, the latter destabilized by the same amount. Their energy difference is, hence, solely determined by the orbital-Zeeman term and should, therefore, amount exactly to $|B|$ E_h. Hence, to test the performance of different EOM methods, FCI as well as different EOM-CCSD calculations have been performed to obtain total energies of the two states. The deviation from the FCI results as well as the energy difference between the states have been quantified. Fig. 4.2a shows the total energies of the two states as well as their energy difference calculated at the FCI/D level of theory. As the FCI wave function

---

[17] For a discussion of the general behavior of electronic states in a magnetic field, see Chpts. 2.1 and 5.1.1.

[18] A similiar discussion on the splitting of $^2\Pi$ states is also relevant in the context of spin-orbit coupling and the same arguments for choosing a certain EOM method can be made (see, e.g., Ref. [104]).

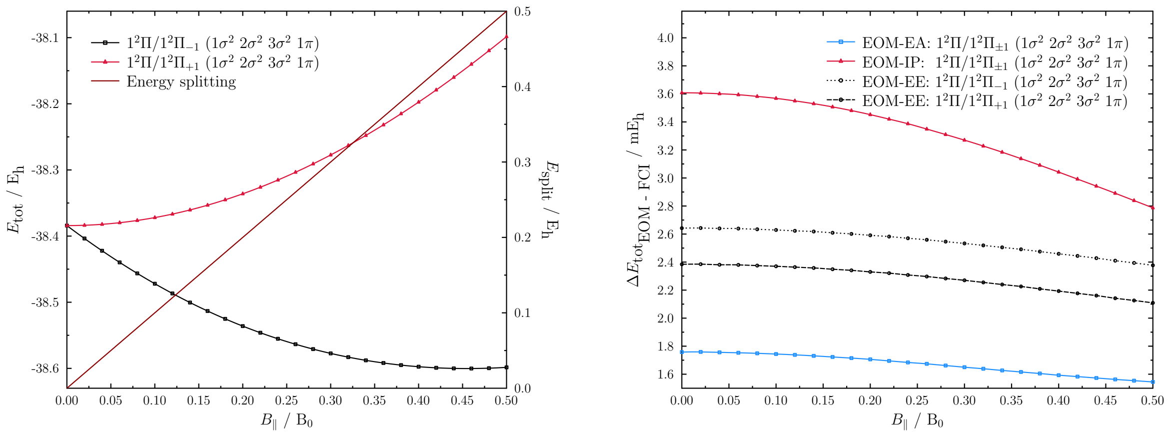

(a) E_{tot} (FCI)

(b) ΔE_{tot} (EOM-CC methods)

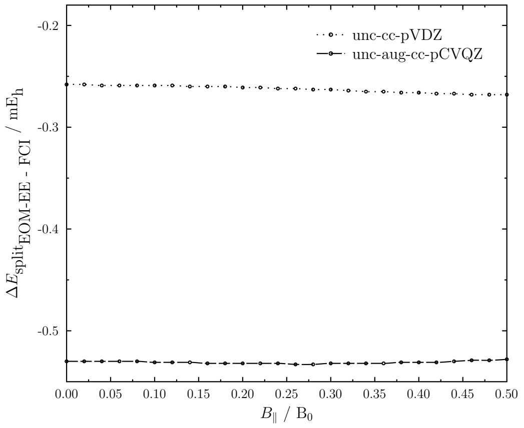

(c) ΔE_{split} (EOM-EE-CC)

Figure 4.2: (a) Total energy and energy splitting of the lowest $1^2\Pi/1^2\Pi_{\pm1}$ states of carbyne in a magnetic field between 0-0.5 B$_0$, (b) deviation from FCI for calculations at different levels of theory, and (c) deviation of the energy splitting for EOM-EE-CCSD.

is exact within the given MO basis, the energy splitting behaves in the correct way. As described, e.g., in Ref. [105], there are three EOM approaches that can be applied in order to model the desired states: First, the $1^2\Pi/1^2\Pi_{-1}$ state can described by a CCSD wave function which acts as a reference state for a subsequent EOM-EE-CC calculation of the $1^2\Pi/1^2\Pi_{+1}$ state by exciting the electron from one π orbital into the other. When using this approach, however, the π orbitals are treated unequally in the HF reference wave function such that the splitting is not expected to match the physical reality. Indeed, when comparing the deviation of the total energies obtained by using EOM methods from the FCI results, it is found that they differ for the two Π states. This is illustrated in Fig. 4.2b. In contrast, the EOM-EA and EOM-IP approaches both treat the two states on equal footing as the same model Hamiltonian is used for their description. For EOM-EA, the closed-shell wave function of the cation is chosen as a reference, while for EOM-IP, the high-spin open-shell wave function of the respective anion is used. Hence, in both HF reference wave functions the occupation of the π orbitals is kept symmetric. Therefore, the deviation for the two states is identical. However, the absolute deviation from the FCI total energy is largest for EOM-IP. Since for the EOM-IP approach a UHF reference is necessary,[19] this approach introduces spin contamination. However, the spin contamination in CC wave functions with a high-spin HF reference is usually rather small [44, 63, 106] while the substantial deviation of 2.8-3.6 mE$_\mathrm{h}$ from the FCI results is twice as large as for the EOM-EA approach. Hence, the spin contamination might not be the origin of the rather large deviation. In fact, one may have expected for the EOM-IP results to perform best, since the approach is based on a reference for which the correlation effects for the π electron are treated within the exponential ansatz of the CC wave function. For the EOM-EA approach, they are solely described by the linear EOM-operator. A possible explanation could be the comparatively small basis set since the EOM-IP calculation relies on a more diffuse reference with two occupied π orbitals as compared to the EOM-EA calculations. This would also explain the stronger decrease in the deviation from the FCI results with increasing field strength since a stronger field leads to more compact orbitals. Coming back to the comparison to FCI, it is found that the EOM-EA approach gives the smallest error with a deviation from the FCI energies of 1.8-1.5 mE$_\mathrm{h}$. The CCSD/EOM-EE route yields energies that differ by 2.1-2.8 mE$_\mathrm{h}$. Here, the description of the $1^2\Pi/1^2\Pi_{+1}$ state by EOM-EE leads to even smaller errors as compared to FCI than modeling the $1^2\Pi/1^2\Pi_{-1}$ state using CCSD. In Fig. 4.2c, it is shown that the energy splitting is underestimated by 0.26-0.27 mE$_\mathrm{h}$ for the D basis set. To quantify the deviation for the use of a physically more reasonable basis set, respective EOM-EE-CCSD calculations using the aCQ basis set have been performed. The deviation from the correct splitting even increases to 0.52-0.53 mE$_\mathrm{h}$.

It becomes apparent from this example how important the availability of the EOM-IP and EOM-EA approaches is to describe the energetical landscape of doublet radicals in a physically sound manner. Furthermore, the use of a well-behaved reference determinant is underlined. With the available toolbox of EOM methods it becomes possible to find the best-suited method for each application.

---

[19] For the time being, a restricted open-shell HF (ROHF) implementation is not available.

4.1.3 Direct access to ionization potentials and electron affinities - EOM-IP and EOM-EA II

The field of possible applications for the different EOM methods is exceptionally broad. In the preceding Chpt. 4.1.2, the EOM-IP- and EOM-EA-CCSD methods have been applied to target a certain set of electronic states and describe them on an equal footing. As the names imply, they are also ideal candidates for the investigation of ionization potentials and electron affinities. Within one calculation, a complete set of ionized states can be accessed. However, when first presented, Nooijen and Bartlett put the EOM-EA approach to a test and, i.a., compared it to the ΔCCSD approach. [43] EOM-IP and EOM-EA methods benefit from a reduced computational cost as compared to two subsequent CCSD calculations. However, one may suspect that the latter lead to better results since one ensures an optimal description of both the orbitals and the amplitudes for the neutral and ionic species. In Ref. [43], however, no significant differences in the performance of the methods are found, i.e., the deviations are smaller than 0.02 eV. Before applying the EOM methods in this context, the performance of EOM-IP and EOM-EA is investigated in a magnetic field. Same as in Ref. [43], the investigation is performed on the electron affinity of lithium ($1^2\mathrm{S}_g/1^2\Sigma_g \rightarrow 1^1\mathrm{S}_g/1^1\Sigma_g$) but the magnetic field is varied between 0-0.5 B_0. Tab. 4.2 shows the energy differences between the total energies of the lithium atom in the $1^2\mathrm{S}_g/1^2\Sigma_g$ state and the lithium anion in the $1^1\mathrm{S}_g/1^1\Sigma_g$ state. The corresponding calculations have been performed at the aCQ level of theory. The field-free electron affinity is in excellent agreement with

Table 4.2: Differences between the total energies of the lithium atom in the $1^2\mathrm{S}_g/1^2\Sigma_g$ state and the lithium anion in the $1^1\mathrm{S}_g/1^1\Sigma_g$ state given in eV in a magnetic field between 0-0.5 B_0 obtained via ΔCCSD, EOM-IP-CCSD, and EOM-EA-CCSD.

B / B_0	$\Delta E_{\Delta\mathrm{CCSD}}$	$\Delta E_{\text{EOM-IP-CCSD}}$	$\Delta E_{\text{EOM-EA-CCSD}}$
Ref. [43]	−0.608	−0.626	−0.606
0.00	−0.608	−0.629	−0.606
0.05	0.325	0.305	0.324
0.10	1.532	1.513	1.529
0.15	2.851	2.832	2.848
0.20	4.222	4.202	4.217
0.25	5.612	5.591	5.607
0.30	7.004	6.981	6.998
0.35	8.390	8.365	8.383
0.40	9.766	9.740	9.760
0.45	11.135	11.106	11.128
0.50	12.497	12.467	12.490

Ref. [43] and the EOM-IP and EOM-EA results are essentially identical. They exhibit a difference of 0.021 eV and 0.002 eV, respectively. In the field, the magnitude of these deviations hardly changes amounting to a maximum of 0.030 eV for EOM-IP and 0.007 eV for EOM-EA at $B = 0.5\ \mathrm{B}_0$. Hence, the conclusion that the computationally less expensive EOM methods yield a similar accuracy compared to ΔCCSD still holds when a magnetic field of up to $B = 0.5\ \mathrm{B}_0$ is applied.

4.2 Importance of triple excitations for doubly excited states

So far, applications for the EOM-CCSD schemes have been presented. In the following, the impact of considering triple excitations within $\hat{T}$ and $\hat{\mathcal{R}}$ on the accuracy is quantified. The four lowest singlet states of the methylidinium cation (CH^+) in a parallel magnetic field are investigated. Notably, the HF determinants for the three lowest states (in the field-free case) differ only in one orbital: $1^1\Sigma^+/1^1\Sigma$ state ($1\sigma^{+2}\ 2\sigma^{+2}\ 3\sigma^{+2}$, black), $1^1\Pi/1^1\Pi_{-1}$ state ($1\sigma^{+2}\ 2\sigma^{+2}\ 3\sigma^{+}\ 1\pi$, green), and $1^1\Pi/1^1\Pi_{+1}$ state ($1\sigma^{+2}\ 2\sigma^{+2}\ 3\sigma^{+}\ 1\pi$, red). As the $1^1\Sigma^+/1^1\Sigma$ state is a closed-shell system and well-behaved, it is a useful reference for EOM-EE calculations. However, in order to reach the $1^1\Delta$ state ($1\sigma^{+2}\ 2\sigma^{+2}\ 1\pi^2$, yellow), a double excitation from the $3\sigma^+$ orbital into the energetically lowest of the 1π orbitals is required. Hence, EOM-EE-CCSD fails to provide an equally good description of electron correlation effects for all considered states. This raises the question how severe the consequences are on the accuracy of the obtained energies. As triple excitations in $\hat{T}$ and $\hat{\mathcal{R}}$ are required to give results of comparable accuracy as obtained for singly excited states with EOM-CCSD, their effect is quantified in the following. For the parallel orientation, the total energies of the four states of interest have been caluclated using FCI, EOM-EE-CCSD, and EOM-EE-CCSDT with the comparatively small D basis set. The results are shown in Fig. 4.3a. The $1^1\Delta/1^1\Delta_{-1}$ state (yellow) exhibits a much larger discrepancy between the EOM-EE-CCSD and the FCI result than all other states. This becomes even more apparent when considering Fig. 4.3b which shows the energy differences between the EOM and the FCI results. For the $1^1\Sigma^+/1^1\Sigma$ (black) and the $1^1\Pi/1^1\Pi_{\pm 1}$ states (brown), the EOM-CCSD deviation amounts to 2-3 $\mathrm{mE_h}$ while for the same level of theory the energy of the $1^1\Delta/1^1\Delta_{-2}$ state (yellow) is higher by 36-38 $\mathrm{mE_h}$. In comparison, the respective deviations for EOM-CCSDT are smaller than 0.04 $\mathrm{mE_h}$ for the singly excited states and 1.5-2.0 $\mathrm{mE_h}$ for the $1^1\Delta/1^1\Delta_{-2}$ state giving an error margin comparable to the EOM-CCSD performance for the other states. Notably, the deviations for the singly excited states are nearly constant for the considered range of field strengths. For the $1^1\Delta/1^1\Delta_{-2}$ state (yellow), a clear dependence of the error on the magnetic field can be observed which

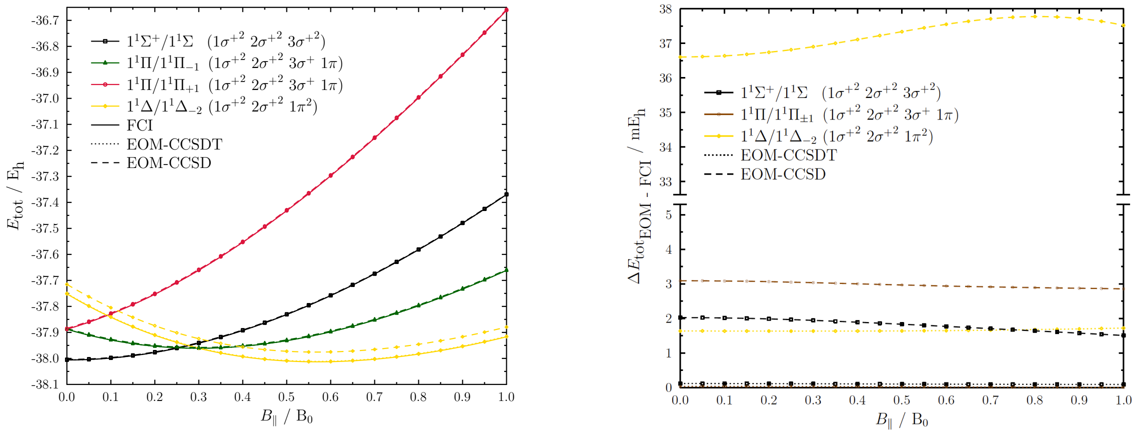

(a) E_{tot}

(b) ΔE_{tot}

Figure 4.3: (a) Total energies of low-lying singlet states of the methylidinium cation in a magnetic field between 0-1 B_0 with parallel orientation to the molecular axis calculated at the FCI/, EOM-EE-CCSD/, and EOM-EE-CCSDT/D levels of theory and (b) respective energy differences.

might hint at a multireference character of this state.

In order to quantify the effect of triple excitations when using larger basis sets, respective calculations at the EOM-EE-CCSD and EOM-EE-CCSDT/aCQ levels of theory have been conducted. Fig. 4.4a shows the total energies of the previously presented states. In order to emphasize the consequences of the insufficient description of the

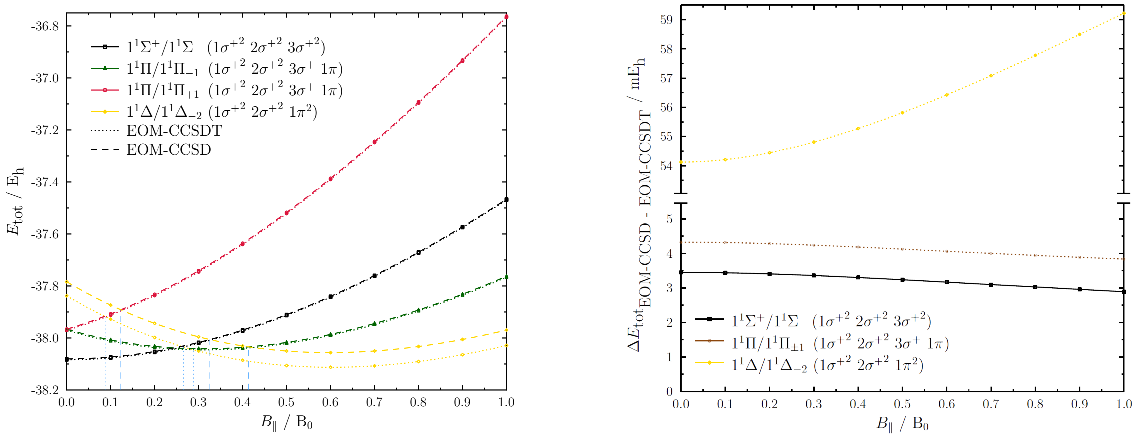

(a) E_{tot}

(b) ΔE_{tot}

Figure 4.4: (a) Total energies of low-lying singlet states of the methylidinium cation in a magnetic field between 0-1 B_0 with parallel orientation to the molecular axis calculated at the EOM-CCSD/-CCSDT/aCQ levels of theory and (b) respective energy differences.

$1^1\Delta/1^1\Delta_{-2}$ state (yellow), its respective field strengths for the crossings with all other states are marked by blue lines.[20] At the EOM-CCSDT level, they are all shifted to smaller values as the $1^1\Delta/1^1\Delta_{-2}$ state (yellow) is shifted to lower energies as has been observed for the small basis. The crossing with the $1^1\Sigma^+/1^1\Sigma$ state (black) occurs at 0.2651 B_0 instead of 0.3256 B_0 ($\Delta B \approx 14200$ T), the one with the $1^1\Pi/1^1\Pi_{-1}$ state (green) is shifted from 0.4139 B_0 to 0.2889 B_0 ($\Delta B \approx 29400$ T), and for the $1^1\Pi/1^1\Pi_{+1}$ state the crossing occurs at 0.0892 B_0 instead of 0.1232 B_0 ($\Delta B \approx 8000$ T). Additionally, the differences between the EOM-CCSD and EOM-CCSDT results are larger as compared to the D results amounting to 3.0-4.5 $\mathrm{mE_h}$ for the $1^1\Sigma^+/1^1\Sigma$ (black) and the $1^1\Pi/1^1\Pi_{\pm1}$ states (brown) while it is 54-58 $\mathrm{mE_h}$ for the doubly excited $1^1\Delta/1^1\Delta_{-2}$ state (yellow). The field-dependence of the deviation for this state becomes more pronounced for a larger one-particle basis set. Concluding, the consideration of triple excitations for the description of doubly excited states in a magnetic field is indispensable as it is in the field-free case. For highly accurate results as EOM-CCSDT provides for singly excited states, further steps have to be taken.

4.3 Basis-set convergence in a strong magnetic field

Besides the choice of truncation level, the chosen basis set has great impact on the accuracy. The application of isotropic GTOs in finite magnetic-field calculations in the context of CC theory has been discussed in Ref. [36]. As a result, quadruple-zeta Dunning basis sets with augmented and additional core functions aCQ have been evaluated to be reliable for field strengths of up to about 1 B_0. In the following, it is investigated whether this also applies for calculations on the electronic states of the carbon atom considered in Chpt. 4.1.1. In Ref. [102], magnetic-field dependent CCSD(T)/aC5 calculations have been performed for the same states. This allows for a discussion of the basis set influence on the accuracy in strong magnetic fields. Fig. 4.5 shows the energy differences obtained when using the two different basis sets. For the total energy differences shown in Fig. 4.5c, the $1^3\mathrm{P}_g/1^3\Pi_{-1,g}$ and $1^5\mathrm{S}_u/1^5\Sigma_u$ states show a similar behavior with the energy difference amounting to less than 3 $\mathrm{mE_h}$ for the considered field range. Thereby, the error is comparable to the effect of triple excitations on singly excited states. The differences in the HF energy of these two states is less than 0.5 $\mathrm{mE_h}$ indicating a good convergence already with the quadruple-zeta basis set. For field strengths of $B > 0.8$ B_0, a slight increase can be noticed hinting at the fact that for higher field strengths the basis set starts lacking sufficient flexibility to properly mimic the orbital distortion induced by the diamagnetic confinement. As in the field-free case, the HF energy converges faster than the correlation energy. [107] For the latter, deviations of 1.4-2.3 $\mathrm{mE_h}$ are obtained for the $1^3\mathrm{P}_g/1^3\Pi_{-1,g}$ and $1^5\mathrm{S}_u/1^5\Sigma_u$ states. A very differ-

---

[20] The significance of these crossing points is subject of Chpt. 5.2.2.

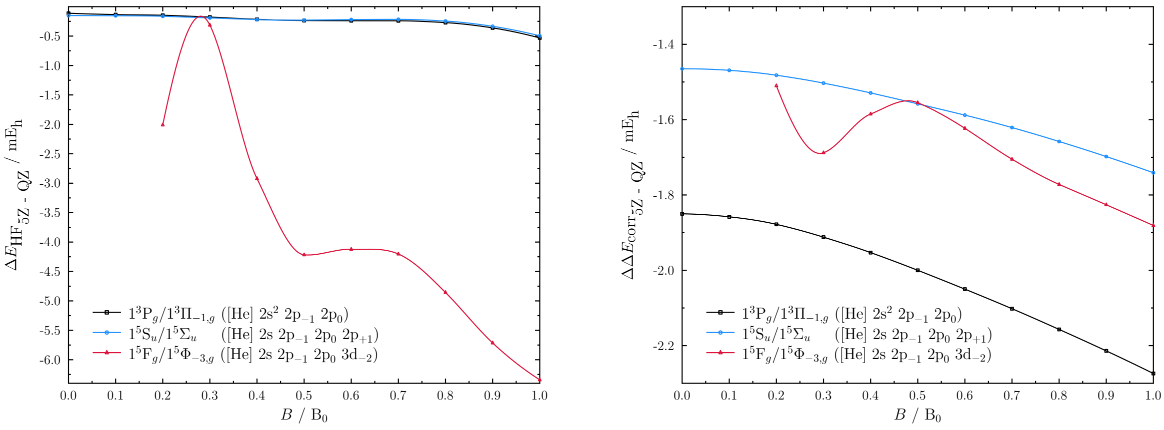

(a) ΔE_{HF} (b) $\Delta\Delta E_{\mathrm{corr}}$

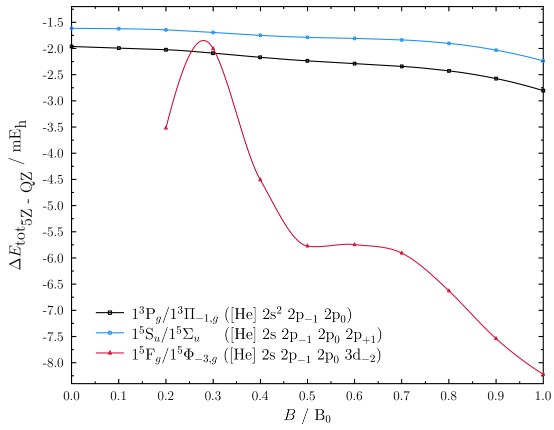

(c) ΔE_{tot}

Figure 4.5: Energy differences ((a) HF energy, (b) correlation energy, (c) total energy) for the respective ground states occuring for the carbon atom in a magnetic field between 0-1 B$_0$ calculated at the CCSD/aCQ and aC5 [102] levels of theory.

ent picture can be observed for the 1^5F$_g$/$1^5\Phi_{-3,g}$ state. For both the HF as well as the correlation energy, no consistent trend is observable indicating a basis set insufficiency in properly describing a state with an occupied d orbital at the aCQ level. This is also indicated when comparing the crossing field strengths for the respective ground states. While for CCSD(T) the first crossing is shifted by only about 500 T to a higher field strength of $B \approx 0.3145$ B$_0$, [102] the second crossing is shifted to a lower field strength of $B \approx 0.5088$ B$_0$ [102] by more than 1200 T. However, the correlation energy for the 1^5S$_u$/$1^5\Sigma_u$ is larger than for the 1^5F$_g$/$1^5\Phi_{-3,g}$ state. Therefore, its correction should be larger as well when using larger basis sets. Hence, only high-field shifts should be observed as the displacement to lower energies for the 1^5S$_u$/$1^5\Sigma_u$ state should be more pronounced. However, deviations of more than 8 mE$_h$ are obtained for the 1^5F$_g$/$1^5\Phi_{-3,g}$

state with the larger basis set. This suggests that for such high angular-momentum states basis sets with high cardinal numbers or, even more importantly, additional augmentation is necessary as has also been discussed in Ref. [108]. In general, the use of anisotropic basis functions would be preferable as the basis set convergence is a serious issue for high-accuracy results. While they are not at hand, the use of uncontracted basis sets is required to ensure enough flexibility to allow for orbital distortions in the magnetic field. Additionally, extrapolation toward the basis set limit should be pursued.

4.4 Influence of non-Hermiticity

In the case of finite magnetic fields, for CC and EOM-CC methods, $\bar{\boldsymbol{H}}$ is a complex non-Hermitian matrix. In general, such matrices can have complex eigenvalues. In the field-free case where the $\bar{\boldsymbol{H}}$ matrix is non-Hermitian but real, pairwise complex eigenvalues may occur only for excitation energies at conical intersections as has been discussed in Refs. [109–112]. However, when considering finite magnetic fields, it is possible to obtain complex correlation and excitation energies for truncated CC and EOM-CC schemes in general. Therefore, it is of great interest to investigate these complex energies and quantify the effect on the accuracy of the real part.

In Ref. [113], an artifical model system that consists of four electrons and six possible electronic states yielding complex CCSD energies has been studied. There, FCI[21] and CCSD results have been compared. The absolute value of the imaginary part of the CCSD energies has been found to be of the same order of magnitude as the deviation between the corresponding real part and the FCI energy. [113] Here, a real molecular system, i.e., the water molecule in an arbitrarily oriented magnetic field is studied. The field strength is chosen to be $B = 0.5\ \mathrm{B}_0$ and the calculations are performed at the (EOM-EE-)CCSD/aT level of theory. Fig. 4.6 shows the real and imaginary parts of the CCSD ground state energy E_{CCSD} as a function of the orientation of the magnetic field vector with respect to the z-axis of the water molecule. Additionally, the real and imaginary parts of the excitation energy ΔE_{exc} into the lowest triplet state with $M_S = 0$ are shown. The molecule is placed in the yz-plane with the C_2 rotational axis in z-direction. For each point on the energy surface, the magnetic field vector has been rotated away from the C_2 axis by β between the z- and x-axis and by α between the z- and $-y$-axis. Fig. 4.7 illustrates the setup.

It becomes apparent that complex-valued energies are obtained both for the CCSD correlation as well as the EOM-EE-CCSD excitation energy. However, for some orien-

---

[21] Note that in a magnetic field $\boldsymbol{H}$ is complex-valued but Hermitian and, therefore, real energies are obtained.

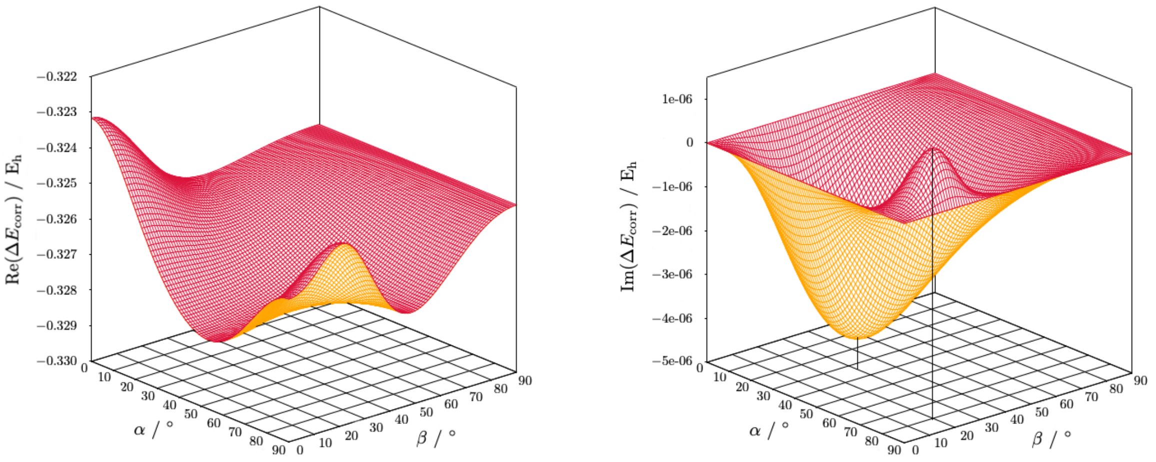

(a) Re(ΔE_{corr})

(b) Im(ΔE_{corr})

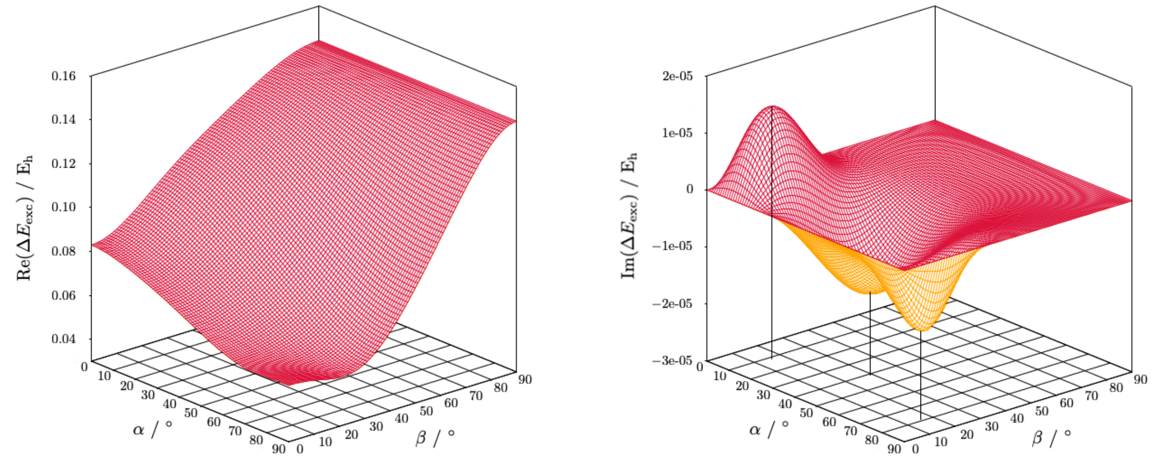

(c) Re(ΔE_{exc})

(d) Im(ΔE_{exc})

Figure 4.6: Real and imaginary part (a,b) of the CCSD correlation energy of the 1^1A_1 ground state and (c,d) of the EOM-EE-CCSD excitation energy of the 1^3B_1 triplet state with $M_S = 0$ of water in a magnetic field of $B = 0.5$ B$_0$ with arbitrary orientation.

tations, real energies are obtained for both the correlation and the excitation energy. This applies for all orientations with either α or β equal to 0° or 90° (on the corners in the plot). If the field vector is parallel to the z-axis, the point-group symmetry is C_2. If the field vector is parallel to either the x- or y-axis, the point-group symmetry is C_s. The appearance of real energies for these constellations is consistent with the findings of the CC and EOM-CC calculations performed so far for systems in strong magnetic fields.[36,85,86] There, the investigated systems exhibit point-group symmetries different

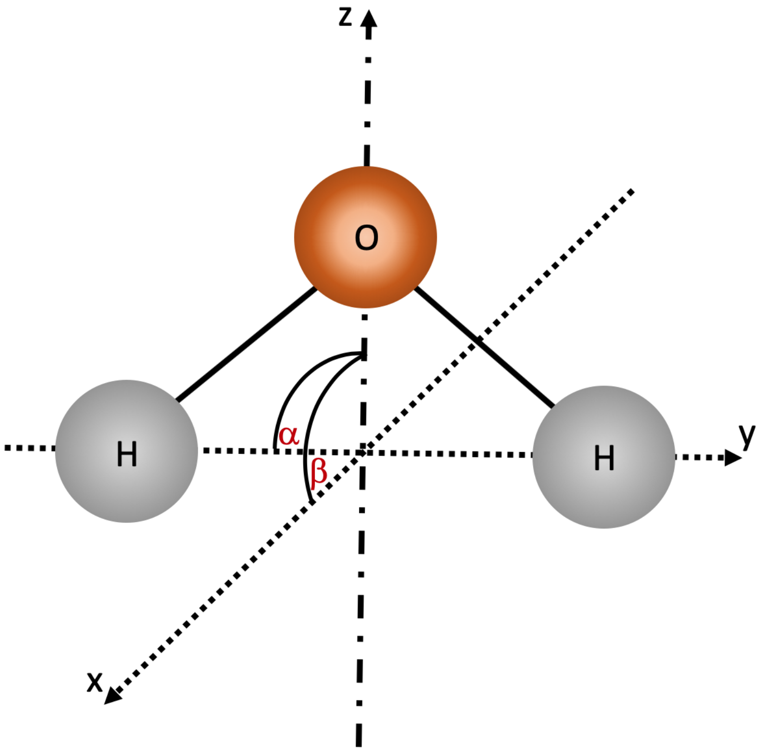

Figure 4.7: Orientation of the water molecule in the 3D-space and the rotation angles α and β defining the deflection of the magnetic field vector away from the z-axis.

from C_1 and no imaginary energies were found. Interestingly, when considering Fig. 4.6 again, it can be observed that the imaginary part also vanishes if the field vector lies in either the xz- or xy-plane (on the edges in the plot). Here, the resulting point-group symmetry is C_1. In this thesis, real energies are also obtained for another system with C_1 symmetry: For diatomic heteronuclear molecules within a magnetic field whose orientation is varied between a parallel and perpendicular alignment with the molecular bond axis, no complex-valued energies emerge.

However, complex energies are obtained for the water molecule for most orientations of the magnetic field vector. This is somewhat dissatisfactory from a formal standpoint as a complex number for an observable is physically unsound. Interestingly, the imaginary part exhibits extrema that are different for the correlation and the excitation energy. For the CCSD correlation energy, the imaginary part exhibits extrema at $(\alpha = 34^{\circ}, \beta = 30^{\circ})$ with an absolute value of $4.27 \cdot 10^{-6}$ $\mathrm{E_h}$ and at $(\alpha = 81^{\circ}, \beta = 19^{\circ})$ with an absolute value of $1.19 \cdot 10^{-6}$ $\mathrm{E_h}$. Considering accuracy, we note that the imaginary part is five orders of magnitude smaller as compared to the real part of the energy where the latter varies between -0.33 and -0.32 $\mathrm{E_h}$. In this example, for the excited 1^3B_1 state, the imaginary part of the EOM-EE-CCSD excitation energy is about one order of magnitude larger than it is for the CCSD correlation energy. Its largest absolute value amounts to

$1.542 \cdot 10^{-5}$ $\mathrm{E_h}$. Note that the imaginary part of the excitation energy is four orders of magnitude smaller than the real part where the latter amounts to 0.05-0.15 $\mathrm{E_h}$.

It should be noted that for all other applications within this thesis no complex energies were encountered. Still, the subject of complex energies has to be dealt with. For applications like the prediction of spectra for larger molecules, all orientations need to be accounted for. Two ways to proceed are possible. The first option is the use of alternative methods that yield real energies. However, for this to be useful, the results provided by these methods have to be at least as accurate as the real part of comparable CC and EOM-CC energies. Thus, for FCI with its limited applicability, no such method has been presented in the context of finite magnetic fields. Ref. [113] discusses several alternative approaches that could be pursued. They can be divided into two groups:

The first category of methods aims at eliminating the imaginary part within truncated CC theory in order to provide real ground state energies. For example, in linear CC (LCC), all terms non-linear in the amplitude equations are left out as those cause the complex-valued energy. However, for the six-state model in Ref. [113], the real part of the CCSD energy is much closer to the FCI results than the LCCSD energy.

The second category comprises Hermitian approaches. These include truncated CI methods which, however, lack size-consistency. Alternatively, unitary coupled-cluster (UCC) methods [114] could be applied. The ansatz for UCC methods [114] is given by $|\Psi_{\mathrm{UCC}}\rangle = \mathrm{e}^{\hat{\tau}} |\Phi_0\rangle$ with $\hat{\tau} = \hat{T} - \hat{T}^{\dagger}$. $\mathrm{e}^{-\hat{\tau}} \hat{H}_{\mathrm{N}} \mathrm{e}^{\hat{\tau}}$ therefore becomes a unitary transformation and the effective Hamiltonian is still Hermitian. While the obtained energies are ensured to be real, there are major disadvantages arising with these methods. [115] For $\hat{\tau}$, the BCH expansion does not terminate. This raises the question not only on how to truncate $\hat{T}$ but also the expansion in a reasonable and systematic way. Additionally, these equations quickly become far more complex than the common CC equations and the effort to obtain results of similar quality rises. Furthermore, truncated variants like UCCSD(4) [114,115] or UCC(4) [116] tend to overshoot correlation energies. [116] In order to judge their performance for systems in strong magnetic fields on a sound standing, a complex-valued implementation of UCCSD(4) and an adaption to EOM-UCCSD(4)[22] would need to be implemented.

Alternatively, the imaginary part of the CC energies may simply be ignored, thereby only considering the real part of the energy as the error is very small. In the example given above, the imaginary part of the selected excitation energy for the water molecule is two orders of magnitude smaller than then conservatively estimated error of EOM-CCSD methods [37,43] and, hence, negligible.

---

[22] Thus far, no generalized EOM-UCCSD implementation has been realized even for the field-free case.

4.5 On the lack of size-intensivity

As explained in the theory in Chpt. 2.6.2, in the general case, the evaluation of properties via truncated EOM-CC approaches is not size-intensive. Contrary to CC-LR, the amplitude response is ignored. For the field-free case, it is known that CCSD-LR transition moments differ only marginally from their EOM counterparts for single small molecules.[117] To test whether this also holds in increasing magnetic fields, EOM-EE-CCSD and CCSD-LR STMs have been calculated and their differences have been quantified. Fig. 4.8 shows the relative error of EOM STMs compared to the size-intensive CCSD-LR STMs as a function of the magnetic field strength. The survey covers electronic transitions from the $1^1\Sigma^+/1^1A'$ reference state into the three lowest excited singlet states for the LiH molecule and the CH$^+$ cation, respectively, in a perpendicular magnetic field.

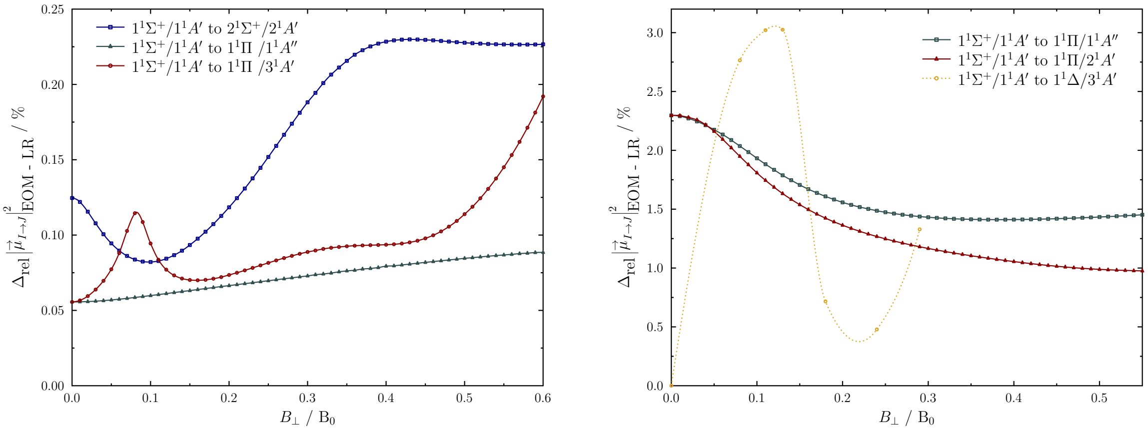

(a) LiH

(b) CH$^+$

Figure 4.8: Error of the EOM-CCSD STMs relative to CCSD-LR for electronic transitions between the $1^1\Sigma^+/1^1A'$ state and the three lowest excited singlet states of the (a) LiH molecule and (b) methylidinium cation in a magnetic field between 0-0.6/0.55 B$_0$ with perpendicular orientation to the molecular axis.

For LiH, the deviation of the EOM STMs from their CCSD-LR counterparts for the considered transitions is always smaller than 0.25% of the corresponding CCSD-LR STMs. Interestingly, the relative discrepancy also reflects avoided crossings that is reflected in the energies of the involved states.[23] The deviation for the transition between the $1^1\Sigma^+/1^1A'$ and the $1^1\Pi/1^1A''$ state (dark-green) smoothly increases, thus, showing that amplitude relaxation becomes somewhat more important for higher field strengths. The other two examples (darkblue and darkred) show distinct bends in the range of occuring

---

[23] For both the discussion of the magnitude and behavior of STMs as a function of the magnetic field strength as well as the topic of avoided crossings in magnetic fields and their connection to STMs, see Chpt. 5.2.4.

avoided crossings. This implies that the effect of amplitude relaxation is not equally large for different states. Hence, the change of character of a state can be observed in the difference between EOM and CCSD-LR STMs. A similar picture is obtained for the CH^+ cation. The overall deviations are a bit larger than for LiH possibly implying a greater importance of amplitude relaxation effects for a system with more electrons, but hardly ever exceed 3% for the considered transitions. However, this slightly larger deviation is only to be observed for an excitation into a doubly excited state.

In the context of astrophysical applications it should be considered that accurate theoretical data from calculations is used as input for atmospheric models in order to predict the actual observational spectra. In this process, broadening of bands and a change of intensities is observed. Additionally, observational spectra do not exhibit a perfect resolution. Therefore, deviations of 3% in the STMs at the EOM-CCSD level are entirely irrelevant. Thus, the influence of amplitude relaxation is negligible for this purpose. Hence, the increased computational effort of calculating STMs at the CC-LR rather than the EOM-CC level can safely be avoided.

4.6 Conclusion on applying EOM-CC methods on systems in strong magnetic fields

In the preceding chapters, the following conclusions for the application of EOM-CC methods on systems in strong magnetic fields are drawn:

1. A broad variety of electronic states can be targeted in a physically sound manner by the combination of a well-suited reference wave function and one of the available EOM-CC methods.

2. Total energies obtained by EOM-CCSD calculations are of comparable accuracy as the corresponding CCSD energies with deviations smaller than the estimated overall error of EOM-CC methods of 0.1-0.3 eV. [37,43]

3. The inclusion of triple excitations within the EOM-EE scheme yields total energies with very high accuracy for singly excited states (deviation from FCI results are smaller than 0.1 $\mathrm{mE_h}$) independent of the applied field strength (for $B < 1\ \mathrm{B_0}$). For doubly excited states, the accuracy of EOM-CCSD methods for singly excited states is recovered.

4. The use of an aCQ basis set is sufficient for treating states of low angular momentum. The deviation of total energies obtained at the EOM-CCSD/aCQ level of theory compared to the basis set limit is similar to the error of the method.

5. Investigations show that - if not zero anyway - the imaginary part of energies obtained within the CC and EOM-CC framework is four to six orders of magnitude smaller than the respective real part. It may, therefore, be safely chosen to be ignored.
6. If small molecules are investigated, the difference between transition moments obtained via EOM-CC and CC-LR is negligible.

5 Applications

In the previous chapter, technical considerations of the application of EOM-CC methods in the context of strong magnetic fields have been discussed. This chapter focuses on the question how chemistry and physics are affected by the presence of strong magnetic fields. In particular, the investigation covers the change in the electronic energies of ground and excited states as well as the dependence of STMs on the magnetic field strength. A broad understanding of both aspects is vital for the prediction of spectra, e.g., of strongly magnetized white dwarfs. Apart from the astrophysical motivation, curious field-induced phenomena such as the perpendicular paramagnetic bonding mechanism [32] and the paramagnetic behavior of closed-shell molecules [118] are further analyzed. Especially for the latter, the power of EOM-CC methods to target excited states provides the key to new insights.

In the first part, this chapter investigates presumably simple systems, namely atoms. The focus lies on the energetics of ground as well as ionized states in strong magnetic fields. Subsequently, the landscape of ground and excited electronic states as well as STMs for electronic transitions between them is studied for molecules. In particular, the influence of their orientation with respect to the magnetic field vector is discussed. The center of attention lies on the effect of symmetry-lowering by an applied magnetic field. Thereby, the consequences of this effect on chemistry and physics are highlighted. Closing, first steps toward the actual prediction of spectra in the astrophysical context are presented.

5.1 Atoms in strong magnetic fields

5.1.1 Electronic ground-state of the carbon atom

It is well-known that carbon is abundant on several non-magnetic white dwarfs. [119] However, astrophysicists so far have not been able to prove its existence on strongly magnetized white dwarfs. In general, the energy of electronic states of systems changes significantly as a function of the magnetic field strength. One of the basic questions is, therefore, which state becomes the ground state for a certain range of magnetic field strengths. Given that knowledge, the main spectral features can be assigned to excitations between states of the same multiplicity as the ground state.

In this chapter, the respective ground states of the carbon atom are discussed. The respective calculations have been performed at the EOM-CCSD/aCQ level of theory (see Chpt. 4.1.1). Results are compared to previous numerical HF results by Ivanov and Schmelcher. [23] However, at the HF level of theory, the influence of electron correlation is neglected. This first chapter serves as an introduction on how electronic states evolve as a function of the magnetic field strength and why methods that account for electron correlation are indispensable for their accurate description.

In the field-free case, the $1^3\mathrm{P}_g/1^3\Pi_{-1,g}$ state ([He] $2\mathrm{s}^2$ $2\mathrm{p}_{-1}$ $2\mathrm{p}_0$) is the ground state of the carbon atom. As shown in Fig. 5.1, the $1^3\mathrm{P}_g/1^3\Pi_{-1,g}$ state (black) is energetically stabilized with increasing field strength in the considered range. The initial

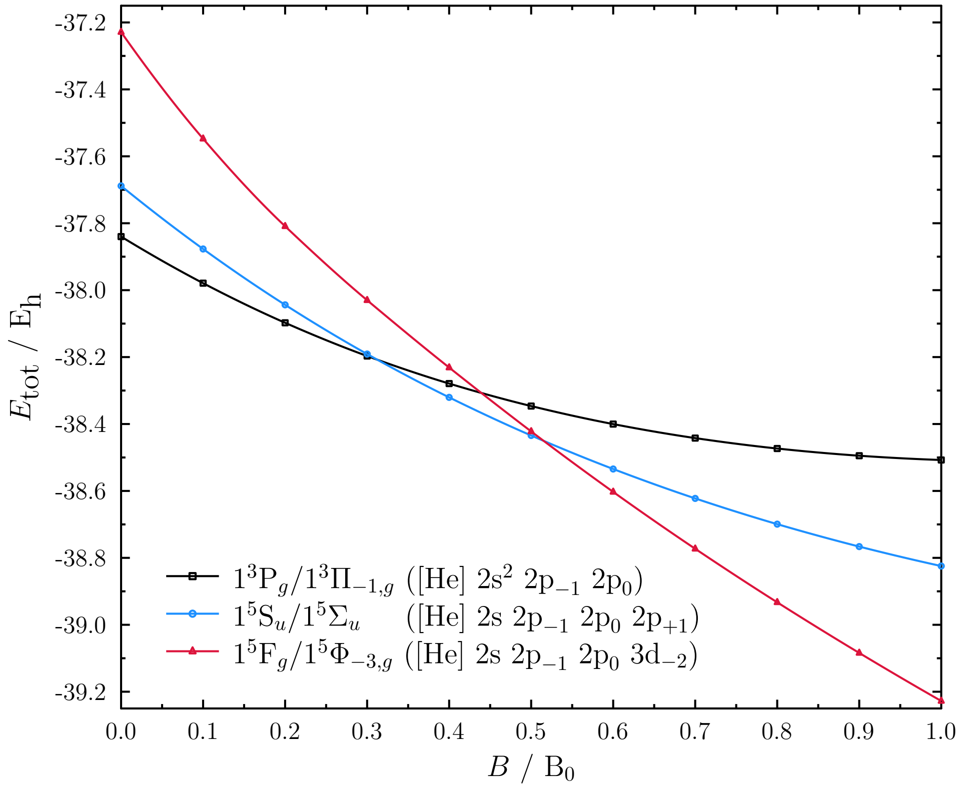

Figure 5.1: Total electronic energies of the respective ground states occuring for the carbon atom in a magnetic field between 0-1 $\mathrm{B_0}$ obtained at the EOM-EE/SF-CCSD/aCQ levels of theory.

slope amounts to $-{}^{3}\!/_{2}\ {}^{\mathrm{E_h}}\!/_{\mathrm{B_0}}$ adding up from the stabilizing spin-Zeeman ($-1\ {}^{\mathrm{E_h}}\!/_{\mathrm{B_0}}$ for $M_S = -1$) and orbital-Zeeman ($-{}^{1}\!/_{2}\ {}^{\mathrm{E_h}}\!/_{\mathrm{B_0}}$ for $M_L = -1$) term. The paramagnetic contributions are counterbalanced by the diamagnetic term at around $B \approx 1$ $\mathrm{B_0}$, The latter will dominate for higher field strengths due to its quadratic dependence on the magnetic field strength. However, at $B \approx 0.3075$ $\mathrm{B_0} \approx 72300$ T, the $1^5\mathrm{S}_u/1^5\Sigma_u$ state ([He] 2s $2\mathrm{p}_{-1}$ $2\mathrm{p}_0$ $2\mathrm{p}_{+1}$, blue) becomes the ground state. In the HF picture, it relates to the $1^3\mathrm{P}_g/1^3\Pi_{-1,g}$ state by promoting the electron from the $2\mathrm{s}^\alpha$ into the $2\mathrm{p}_{+1}^\beta$ spin orbital. Hence, the orbital-Zeeman term vanishes. Yet, the initial slope amounts to $-2\ {}^{\mathrm{E_h}}\!/_{\mathrm{B_0}}$ due to the increased multiplicity ($M_S = -2$). Since the p_{+1} orbital is occupied, the extent of the electron-density distribution in the plane perpendicular to the magnetic field increases, thereby also increasing the diamagnetic contribution. However, this effect is not large enough to prevent the $1^5\mathrm{S}_u/1^5\Sigma_u$ state from crossing the $1^3\mathrm{P}_g/1^3\Pi_{-1,g}$ state. For field strengths larger than $B \approx 0.5140$ B$_0 \approx 120800$ T, the $1^5\mathrm{F}_g/1^5\Phi_{-3,g}$ state ([He] 2s $2\mathrm{p}_{-1}$ $2\mathrm{p}_0$ $3\mathrm{d}_{-2}$, red) is energetically lowest. In comparison to the $1^5\mathrm{S}_u/1^5\Sigma_u$ state, the electron from the $2\mathrm{p}_{+1}^{\beta}$ spin orbital is promoted to the $3\mathrm{d}_{-2}^{\beta}$ spin orbital for which the orbital-Zeeman term is energetically stabilizing rather than destabilizing. The total orbital-Zeeman contribution amounts to $-3/2$ E$_\mathrm{h}$/B$_0$ while the spin-Zeeman term is again -2 E$_\mathrm{h}$/B$_0$ causing an initial steep slope of $-7/2$ E$_\mathrm{h}$/B$_0$. Therefore, the $1^5\mathrm{F}_g/1^5\Phi_{-3,g}$ state crosses both states that are the respective ground states for lower field strengths. Consequently, the carbon atom exhibits three different ground states already for field strengths that might well be present on white dwarfs.

Comparing the obtained crossing field strengths to the HF results from Ref. [23] exhibits significant deviations as is illustrated in Tab. 5.1. For HF, the first crossing field strength is $B \approx 0.1862$ B$_0$ (about 29700 T lower than for EOM-CCSD) and amounts to $B \approx 0.4903$ B$_0$ (about 6200 T lower than for EOM-CCSD) for the second crossing field strength. These differences can be understood by looking at the correlation energies of the involved states. They have been calculated at the CCSD/aCQ level of theory and are depicted in Fig. 5.2. The correlation energies of the different states differ both in evolution and magnitude. The reasons for the differing behavior are explained in detail in Ref. [36]. However, the main reason for the large deviations in crossing field strengths is the difference in magnitude of the correlation energy which is about 60 mE$_\mathrm{h}$ between the $1^3\mathrm{P}_g/1^3\Pi_{-1,g}$ and the $1^5\mathrm{S}_u/1^5\Sigma_u$ states (black/blue). This difference arises from the different multiplicities of the states: For a given number of electrons, the correlation energy for high-spin systems is smaller than for corresponding lower-spin systems as electrons of the same spin already avoid each other by the Pauli exclusion principle. Compared to HF, the $1^3\mathrm{P}_g/1^3\Pi_{-1,g}$ state is, therefore, shifted more strongly to lower energies than the $1^5\mathrm{S}_u/1^5\Sigma_u$ state which leads to a large shift of the crossing field strength toward higher values. For the crossing between the $1^5\mathrm{S}_u/1^5\Sigma_u$ and

Table 5.1: Comparison of the crossing field strengths for the respective ground states of the carbon atom calculated at the numerical HF level [23] and the EOM-EE/SF-CCSD/aCQ levels of theory.

	$\mathbf{1^3P_g/1^3\Pi_{-1,g}}$ **to** $\mathbf{1^5S_u/1^5\Sigma_u}$		$\mathbf{1^5S_u/1^5\Sigma_u}$ **to** $\mathbf{1^5F_g/1^5\Phi_{-3,g}}$	
Method	B / B$_0$	B / T	B / B$_0$	B / T
HF	0.1862	≈ 43800	0.4903	≈ 115200
EOM-CCSD	0.3124	≈ 73400	0.5165	≈ 121400
$\Delta_{\text{HF − EOM-CCSD}}$	0.1262	≈ 29700	0.0262	≈ 6200

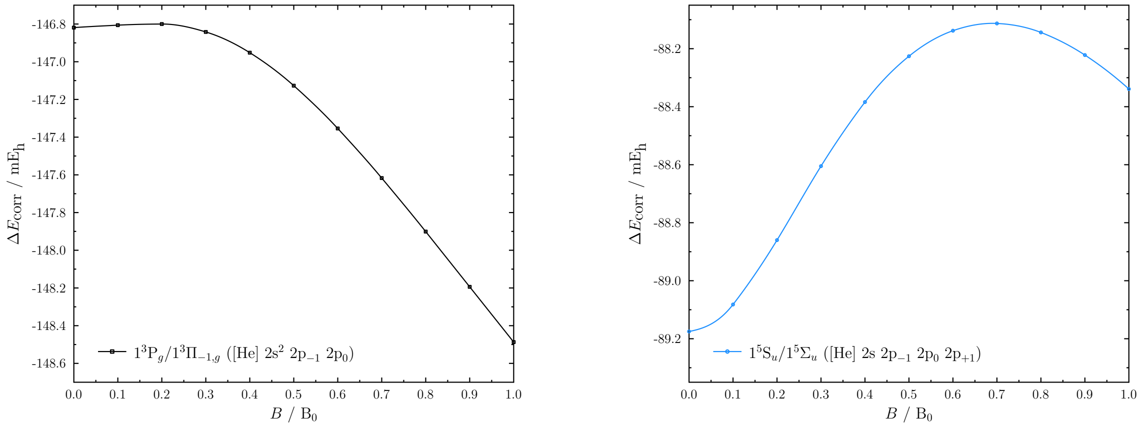

(a) $1^3\mathrm{P}_g/1^3\Pi_{-1,g}$

(b) $1^5\mathrm{S}_u/1^5\Sigma_u$

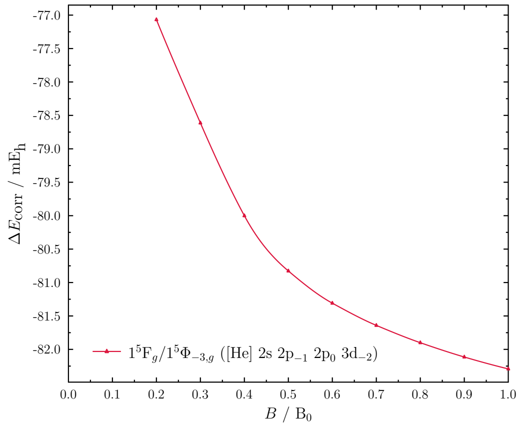

(c) $1^5\mathrm{F}_g/1^5\Phi_{-3,g}$

Figure 5.2: Correlation energies for the respective ground states occuring for the carbon atom in a magnetic field between 0-1 B$_0$.

$1^5\mathrm{F}_g/1^5\Phi_{-3,g}$ states (blue/red), the difference in the correlation energy is about one order of magnitude smaller. While both states have the same multiplicity, the latter is more diffuse and, therefore, exhibits a somewhat smaller correlation energy. This leads to the still considerable but less pronounced high-field shift in the crossing field strength. It becomes apparent that the consideration of electron correlation is indispensable for the accurate determination of the presented crossing field strengths.

5.1.2 Ionization energies for first and second row elements

Sticking to astrophysical applications, it can be noted that white dwarfs have surface temperatures ranging from far more than 150000 K to less than 4000 K. [120,121] It goes without saying that this allows for ionization processes. Electrons may be freed and eventually even recombine with other ions or neutral species. This raises the general question of how ionization energies (*IE*s) and electron affinities (*EA*s)[24] are affected by the presence of a magnetic field and how they change as a function of the magnetic field strength. The ionization energies and electron affinities for the first ten elements of the periodic table are studied for $B \leq 0.25$ B$_0$. For the chapter on IEs, results are presented which have been used as benchmark data in Ref. [122]. The same basis sets as the ones in Ref. [122] are used in Chpts. 5.1.2-5.1.3. A straightforward approach to determine ionization energies of selected atoms is to perform two sets of EOM-IP-CCSD calculations ($\Delta M_S = +1/2$ and $\Delta M_S = -1/2$) on the respective ground state reference wave function and pick the lowest energy obtained. For the carbon atom with the $1^3\mathrm{P}_g/1^3\Pi_{-1,g}$ ground state, the resulting EOM-IP energies are plotted as a function of the magnetic field strength in Fig. 5.3 together with the orbital energies of the orbitals that are to be depopulated. Up to $B = 0.191$ B$_0$, the EOM-IP energy is rising as the electron to be removed comes from the $2\mathrm{p}_0^\beta$ orbital which gets stabilized in the field due to the spin-Zeeman term. For higher field strengths, ionization occurs from the $2\mathrm{s}^\alpha$ orbital which in contrast is energetically destabilized. The corresponding orbital energies already cross for $B \approx 0.14$ B$_0$ which, however, does not entirely coincide with the kink in the EOM-IP energy. This means that Koopmans' picture is off by more than 11750 T and should not be consulted for systems in finite magnetic fields.

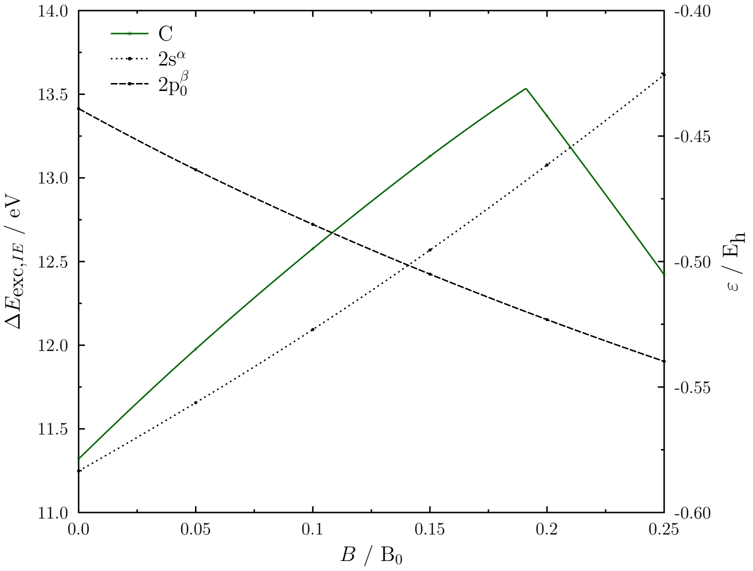

Figure 5.3: Lowest EOM-IP energy for the carbon atom in the $1^3\mathrm{P}_g/1^3\Pi_{-1,g}$ state in a magnetic field between 0-0.25 B$_0$ involving ionization from the $2\mathrm{p}_0^\beta$ and the $2\mathrm{s}^\alpha$ spin orbital, respectively. For comparison, the corresponding orbital energies are plotted as a function of the magnetic field strength.

---

[24] Note that in this thesis the denotation *EA* is used for the energy difference $E_{\mathrm{anionic}} - E_{\mathrm{neutral}}$ and the usual sign convention does not apply.

While the interpretation of EOM-IP energies as *IE*s is correct in the field-free case, the same does not apply in the presence of a magnetic field because the energy of the ionized electron is different from zero. This is not considered within the EOM framework since the electron is removed entirely from the system and, hence, is no longer subjected to the magnetic field. With the lowest Landau energy E^L (see Eq. (2.25)), the *IE* for the ionization process generating a state $S2$ from a state $S1$ can, therefore, be calculated as

$$IE = E(S2) - E(S1) + E^L. \tag{5.1}$$

Taking the corresponding corrections into account, the *IE*s depicted in Fig. 5.4 are obtained for the atoms H-Ne. The most striking feature to be observed is the fact that

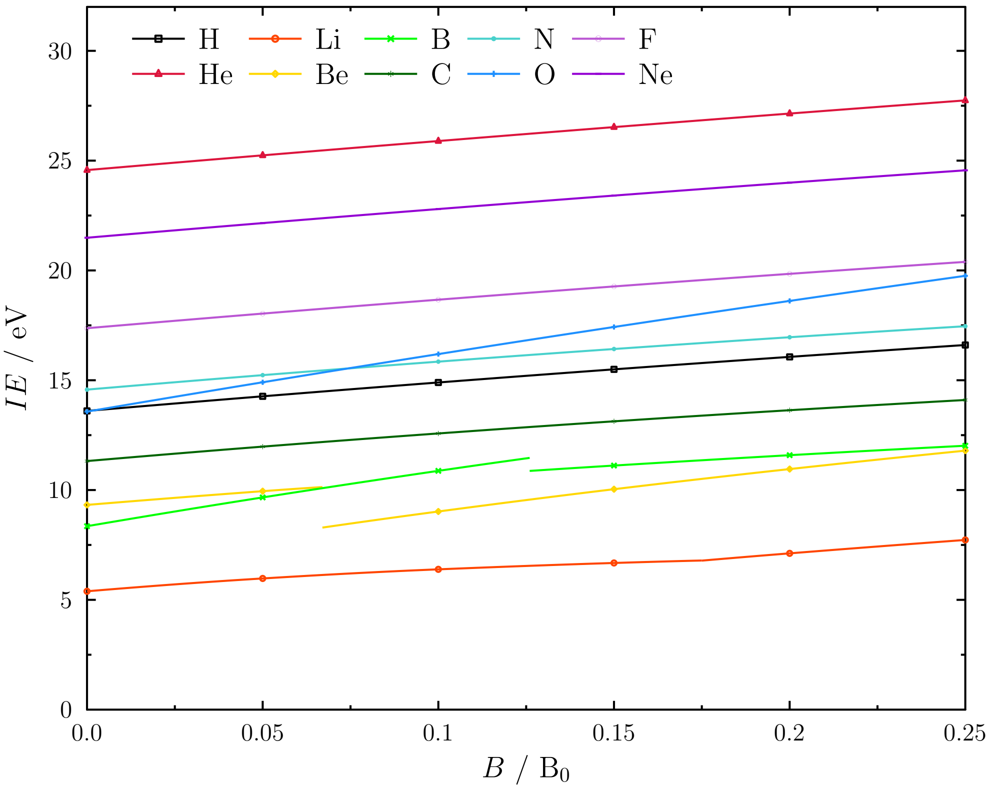

Figure 5.4: Landau-corrected physical ionization energies of the atoms H-Ne in a magnetic field between 0-0.25 B_0.

for the considered range all *IE*s are rising with increasing field strength in a concave manner as assessed in Ref. [122]. This can be understood by inquiring Eq. (5.1) again:

$$\begin{aligned} IE &= E(S2) - E(S1) + E^L \\ &= \Delta E_0^{S2-S1} + \Delta E_{\text{para}}^{S2-S1} + \Delta E_{\text{dia}}^{S2-S1} + \underbrace{\left(\frac{1}{2}m_l + m_s\right) \cdot B}_{E_{\text{para}}^L} + \underbrace{\frac{1}{2}\left(1 + |m_l|\right) \cdot B}_{E_{\text{dia}}^L} \\ &= \Delta E_0^{S2-S1} + \Delta E_{\text{dia}}^{S2-S1} + E_{\text{dia}}^L + \underbrace{\Delta E_{\text{para}}^{S2-S1} + E_{\text{para}}^L}_{=0^*} \\ &= \underbrace{\Delta E_0^{S2-S1}}_{\mathcal{O}(B^0)} + \underbrace{E_{\text{dia}}^L}_{\mathcal{O}(B^1)} + \underbrace{\Delta E_{\text{dia}}^{S2-S1}}_{\mathcal{O}(B^2)} . \end{aligned} \tag{5.2}$$

*only if M_L is a good quantum number

First, the energy difference between the initial and final state is split up in the field-independent contribution as well as the differences in the paramagnetic and diamagnetic energy terms. As noted in Ref. [122], the Landau energy can also be viewed as being composed of a paramagnetic and a diamagnetic contribution. In Eq. (5.2), all paramagnetic contributions cancel out exactly. ΔE_0^{S2-S1} does not scale with B. However, it should be noted that this term is not constant for different magnetic field strengths because the orbitals as well as the corresponding amplitudes are optimized for a given B. In any case, this term defines the origin of all *IE* curves at $B = 0\ \mathrm{B}_0$. The diamagnetic term $1/2 \cdot (1 + |m_l|) \cdot B$ of the Landau energy is linear in B and always greater than/equal to zero. Therefore, the initial slope is always positive. The difference in the diamagnetic contribution for the states $S1$ and $S2$ scales with B^2. As the diamagnetic contribution for the $(N-1)$-electron system is expected to be smaller than it is for the corresponding N-electron system, $|\Delta E_{\text{dia}}^{S2-S1}/B^2| < 0$. Hence, the magnitude of the initial slope is decreased with increasing field strength and the observed concave functions are obtained. This means that, in the field range considered here, ionization is less favorable with increasing field strength as compared to the field-free case. For stronger magnetic fields, however, it should become easier. The extent to which ionization is more hindered varies for the different atoms. Considering Fig. 5.4, for all *IE*s included, only two different initial slopes m can be observed. As the latter soleley depend on $E_{\text{dia}}^L = 1/2 \cdot (1 + |m_l|) \cdot B$, ionizations from s and p_0 orbitals ($m_l = 0$) exhibit an initial slope of $m = 1/2$ and for ionizations from a $\mathrm{p}_{\pm 1}$ orbital is $m = 1$. The initial slopes are tabulated in the last column of Tab. 5.2. In this context, it should be emphasized that this can lead to preferred ionization from orbitals different from the HOMO. For Ne, the ionization occurs from the $2\mathrm{p}_0^\alpha$ or $2\mathrm{p}_0^\beta$ orbital rather than from the $2\mathrm{p}_{+1}^\alpha$ orbital which is the HOMO. In fact, as the paramagnetic contributions have no effect on the *IE*s, ionizations from corresponding α and β orbitals as well as orbitals with the same

Table 5.2: Details on the ionization processes of the atoms H-Ne occuring in a magnetic field between 0-0.25 $\mathrm{B_0}$. The respective ground states are given with their magnetic-field range in $\mathrm{B_0}$. Additionally, the ionized spin orbital (ISO), its order number n in HOMO$-n$ with applied field, the Landau energy E^{L} of the detached electron in $\mathrm{E_h}$, and the resulting initial slope m of the *IE* curve in $^{\mathrm{E_h}}/_{\mathrm{B_0}}$ are listed. If relevant, degenerate ionization processes are considered.

Atom	Field	Ground state	ISO	HOMO-n[a]	E^{L}	m
H		$^2\mathrm{S}_g/^2\Sigma_g$ ($1\mathrm{s}^\beta$)	$1\mathrm{s}^\beta$	0	0	½
He		$^1\mathrm{S}_g/^1\Sigma_g$ ($1\mathrm{s}^2$)	$1\mathrm{s}^\beta$	1	0	½
			$1\mathrm{s}^\alpha$	0	$\|B\|$	½
Li	≤ 0.175	$^2\mathrm{S}_g/^2\Sigma_g$ ($1\mathrm{s}^2\ 2\mathrm{s}^\beta$)	$2\mathrm{s}^\beta$	0	0	½
	≥ 0.175	$^2\mathrm{P}_u/^2\Pi_{-1,u}$ ($1\mathrm{s}^2\ 2\mathrm{p}^\beta_{-1}$)	$2\mathrm{p}^\beta_{-1}$	0	0	1
Be	≤ 0.067	$^1\mathrm{S}_g/^1\Sigma_g$ ($1\mathrm{s}^2\ 2\mathrm{s}^2$)	$2\mathrm{s}^\beta$	1	0	½
			$2\mathrm{s}^\alpha$	0	$\|B\|$	½
	≥ 0.067	$^3\mathrm{P}_u/^3\Pi_{-1,u}$ ($1\mathrm{s}^2\ 2\mathrm{s}^\beta\ 2\mathrm{p}^\beta_{-1}$)	$2\mathrm{p}^\beta_{-1}$	0	0	1
B	≤ 0.126	$^2\mathrm{P}_u/^2\Pi_{-1,u}$ ($1\mathrm{s}^2\ 2\mathrm{s}^2\ 2\mathrm{p}^\beta_{-1}$)	$2\mathrm{p}^\beta_{-1}$	0	0	1
	≥ 0.126	$^4\mathrm{P}_g/^4\Pi_{-1,g}$ ($1\mathrm{s}^2\ 2\mathrm{s}^\beta\ 2\mathrm{p}^\beta_{-1}\ 2\mathrm{p}^\beta_0$)	$2\mathrm{p}^\beta_0$	0	0	½
C		$^3\mathrm{P}_g/^3\Pi_{-1,g}$ ($1\mathrm{s}^2\ 2\mathrm{s}^2\ 2\mathrm{p}^\beta_{-1}\ 2\mathrm{p}^\beta_0$)	$2\mathrm{p}^\beta_0$	0-1	0	½
N		$^4\mathrm{S}_u/^4\Sigma_u$ ($1\mathrm{s}^2\ 2\mathrm{s}^2\ 2\mathrm{p}^\beta_{-1}\ 2\mathrm{p}^\beta_0\ 2\mathrm{p}^\beta_{+1}$)	$2\mathrm{p}^\beta_0$	1-2	0	½
O		$^3\mathrm{P}_g/^3\Pi_{-1,g}$ ($1\mathrm{s}^2\ 2\mathrm{s}^2\ 2\mathrm{p}^2_{-1}\ 2\mathrm{p}^\beta_0\ 2\mathrm{p}^\beta_{+1}$)	$2\mathrm{p}^\alpha_{-1}$	0	$\|B\|$	1
F		$^2\mathrm{P}_u/^2\Pi_{-1,u}$ ($1\mathrm{s}^2\ 2\mathrm{s}^2\ 2\mathrm{p}^2_{-1}\ 2\mathrm{p}^2_0\ 2\mathrm{p}^\beta_{+1}$)	$2\mathrm{p}^\alpha_0$	0	$\|B\|$	½
Ne		$^2\mathrm{S}_g/^2\Sigma_g$ ($1\mathrm{s}^2\ 2\mathrm{s}^2\ 2\mathrm{p}^2_{-1}\ 2\mathrm{p}^2_0\ 2\mathrm{p}^2_{+1}$)	$2\mathrm{p}^\beta_0$	4	0	½
			$2\mathrm{p}^\alpha_0$	1	$\|B\|$	½

[a] Spin orbitals are numbered with integers n (order number) in ascending order with respect to their orbital energy. The energetically highest occupied spin orbital defines $n = 0$. If the order number changes within a given range of magnetic field strengths (see second column), the range of order numbers of that spin orbital is listed.

$|m_l|$ for given n and l are degenerate if ΔE_0^{S2-S1} is equal for both cases. Therefore, an *IE* diagram for the 2p orbitals of Ne would only give two signals. The second striking feature in Fig. 5.4 are the discontinuities in the *IE* curves for Li, B, and Be. They stem solely from a change of the ground state for the respective atoms at a certain magnetic field strength. For Li, the different *IE*s are very similar making the discontinuity less pronounced. For higher field strengths than the ones considered here, kinks in the evolution of the *IE*s due to a change in the preferred ionization process are to be expected. For example, while the *IE* for ionizing the $2\mathrm{p}^\beta_0$ orbital in the oxygen atom is higher than for the $2\mathrm{p}^\alpha_{-1}$ orbital in the field-free case, the slope of the *IE* for the former process is smaller compared to the one for the latter. Hence, the respective *IE* curves will eventually cross and ionization from the $2p_0^\beta$ orbital will become energetically favorable. Concluding, the evolution of *IE*s for the first and second row atoms as a function of the magnetic field is essentially governed by the diamagnetic contribution of the freed electron's energy. [122] It increases the energy necessary to ionize an atom in a magnetic field. Only for higher field strengths than the ones considered in this study, a decrease of *IE*s is to be expected as has been seen for indicative calculations for field strengths > 1 B$_0$.

5.1.3 Electron affinities for first and second row elements

Similar considerations as for *IE*s are also possible for electron affinities. Again, consideration of the Landau correction on the EOM-EA energies is required. However, there are differences leading to a higher complexity of the final $EA(B)$ curves than has been observed for the *IE*s. The EA describing the energy difference between an $(N+1)$-system in state $S2$ and the preceding N-electron system in state $S1$ is

$$EA = E(S2) - E(S1) - E^L. \tag{5.3}$$

To emphasize the importance of the Landau correction, the situation for the fluorine atom, first, is examined without considering the Landau energy. Fig. 5.5 shows the lowest EOM-EA energy obtained for the fluorine atom in the $1^2\mathrm{P}_u/1^2\Pi_{-1,u}$ ground state up to a field strength of $B = 0.25$ B$_0$. The EOM-EA energy for the attachment of an electron in the $2p_{+1}^\alpha$ orbital is increasing steeply up to $B \approx 0.13$ B$_0$ implying that attaching an electron to fluorine to yield fluoride is harder in a magnetic field. The increase flattens when capturing a $3p_{-1}^\beta$ electron becomes preferred and even turns into a decrease for $B \gtrapprox 0.2$ B$_0$ for which attaching a $3d_{-2}^\beta$ electron becomes energetically favorable. While the second kink in the EOM-EA energy curve almost coincides with the crossing of the orbital energies of the $3p_{-1}^\beta$ and $3d_{-2}^\beta$ orbital, the first sudden change in slope occurs for much higher field strengths than the corresponding orbital energies suggest. This can be understood in the following way: By capturing a $2p_{+1}^\alpha$ electron, a stable noble gas configuration is obtained. This process is preferred over capturing a $3p_{-1}^\beta$ electron even for field strengths for which the energy of the $3p_{-1}^\beta$ orbital is already lower than the $2p_{+1}^\beta$ orbital. As shown for *IE*s, Koopmans' picture is off by more than 29000 T. However, comparing these results to the physical *EA*s shown in Fig. 5.6 that include the Landau corrections reveals that attaching an electron to fluorine to yield fluoride is actually easier in a magnetic field. The first impression is that the *EA*s evolve less smoothly with increasing magnetic field strength compared to the corresponding *IE*s. Most of them are decreasing while some increase parabolically. All curves exhibit

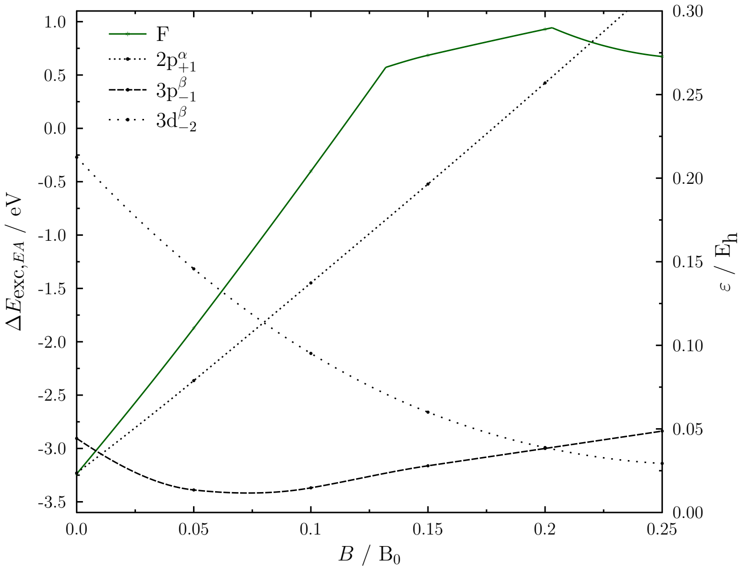

Figure 5.5: Lowest EOM-EA energy for the fluorine atom in the $1^2\mathrm{P}_u/1^2\Pi_{-1,u}$ state in a magnetic field between 0-0.25 B$_0$ involving electron attachment in the $2\mathrm{p}^{\alpha}_{+1}$, $3\mathrm{p}^{\beta}_{-1}$, and the $3\mathrm{d}^{\beta}_{-2}$ spin orbital, respectively. For comparison, the corresponding orbital energies are plotted as a function of the magnetic field strength.

concave behavior which can be explained by rewriting Eq. (5.3) in an analogous way as has been done for the IEs:

$$EA = \underbrace{\Delta E_0^{S2-S1}}_{\mathcal{O}(B^0)} - \underbrace{E^L_{\mathrm{dia}}}_{\mathcal{O}(B^1)} + \underbrace{\Delta E^{S2-S1}_{\mathrm{dia}}}_{\mathcal{O}(B^2)} . \tag{5.4}$$

The inital slope is always negative as the Landau energy has to be subtracted in order to obtain EAs. However, $|{}^{\Delta E^{S2-S1}_{\mathrm{dia}}}/_{B^2}| > 0$ for the electron attachment and, thus, the quadratic term is positive with increasing field strength leading to concave functions. As the Landau energy is stabilizing the electron attached system, capturing electrons with a large $|m_l|$ is desirable. Hence, for the nitrogen atom, it is more beneficial to capture a $2p^{\alpha}_{\pm 1}$ than a $2p^{\alpha}_0$ electron. This and the fact that electron spin has no influence on the most favorable attachment process through the paramagnetic contribution means that the LUMO will usually not be populated. For example, the boron atom in the $^2\mathrm{P}_u/^2\Pi_{-1,u}$ state ($1\mathrm{s}^2$ $2\mathrm{s}^2$ $2\mathrm{p}^{\beta}_{-1}$) preferably captures a $2p^{\beta}_{+1}$ rather than a $2p^{\beta}_0$ electron. All details on the electron attachment processes for the first ten elements of the periodic table in strong magnetic fields are listed in Tab. 5.3.

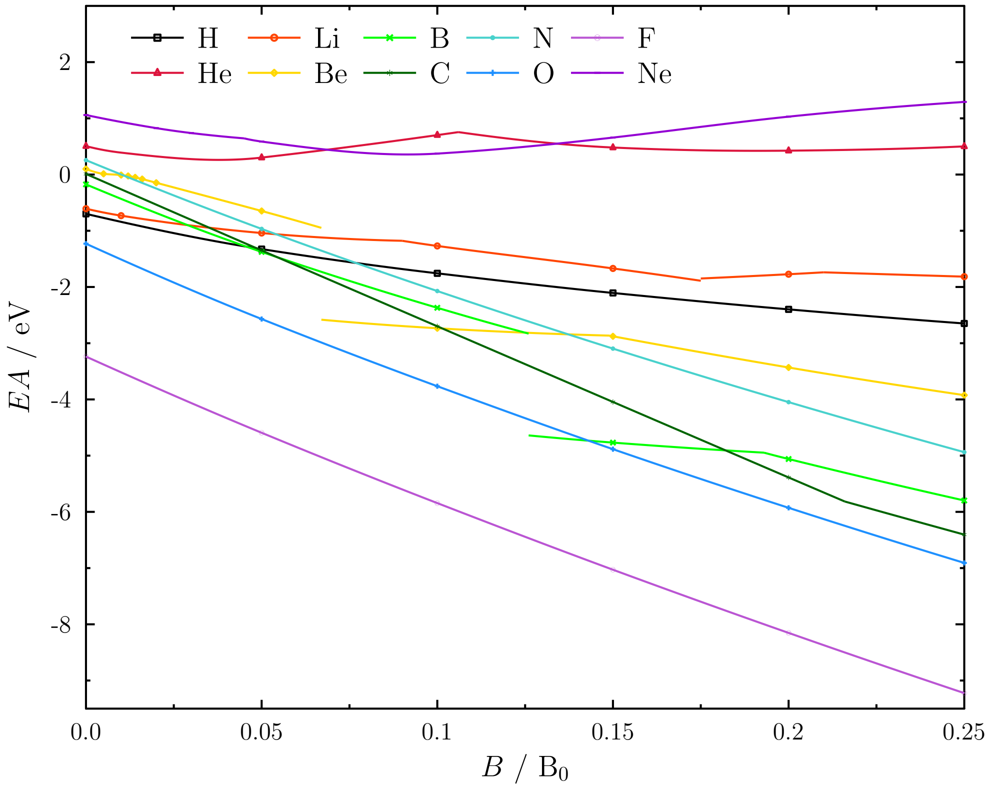

Figure 5.6: Landau-corrected physical electron affinities of the atoms H-Ne in a magnetic field between 0-0.25 $\mathrm{B_0}$.

Table 5.3: Details on the electron attachment processes of the atoms H-Ne occuring in a magnetic field between 0-0.25 $\mathrm{B_0}$. The respective ground states are given with their magnetic-field range in $\mathrm{B_0}$. Additionally, the newly occupied spin orbital (OSO), its order number n in LUMO+n with applied field, the Landau energy E^{L} of the attached electron in $\mathrm{E_h}$, and the resulting initial slope m of the EA curve in $^{\mathrm{E_h}}/_{\mathrm{B_0}}$ are listed. If relevant, degenerate electron attachment processes are considered.

Atom	Field	Ground state	OSO	LUMO+n$^{\mathrm{c}}$	E^{L}	m
H		$^2\mathrm{S}_g/^2\Sigma_g$ $(1\mathrm{s}^\beta)$	$1\mathrm{s}^\alpha$	0-7	$\lvert B\rvert$	$-^1/_2$
He		$^1\mathrm{S}_g/^1\Sigma_g$ $(1\mathrm{s}^2)$				
	≤ 0.106		$2\mathrm{s}^\beta$	0	0	$-^1/_2$
			$2\mathrm{s}^\alpha$	1-4	$\lvert B\rvert$	$-^1/_2$
⋮	⋮	⋮	⋮	⋮	⋮	⋮

$\vdots$	$\vdots$	$\vdots$	$\vdots$	$\vdots$	$\vdots$	$\vdots$
	≥ 0.106		$2\mathrm{p}^{\beta}_{-1}$	1-0	0	-1
			$2\mathrm{p}^{\beta}_{+1}$	$5/6$-$6/7^{\mathrm{a}}$	$\lvert B\rvert$	-1
			$2\mathrm{p}^{\alpha}_{-1}$	$5/6$-$6/7^{\mathrm{a}}$	$\lvert B\rvert$	-1
			$2\mathrm{p}^{\alpha}_{+1}$	10-20	$2\lvert B\rvert$	-1
Li	≤ 0.175	$^{2}\mathrm{S}_g/{}^{2}\Sigma_g\ (1\mathrm{s}^2\ 2\mathrm{s}^{\beta})$				
	≤ 0.090		$2\mathrm{s}^{\alpha}$	0-13	$\lvert B\rvert$	$-1/2$
	≥ 0.090		$2\mathrm{p}^{\beta}_{-1}$	0	0	-1
			$2\mathrm{p}^{\beta}_{+1}$	9-12	$\lvert B\rvert$	-1
	≥ 0.175	$^{2}\mathrm{P}_u/{}^{2}\Pi_{-1,u}\ (1\mathrm{s}^2\ 2\mathrm{p}^{\beta}_{-1})$				
	≤ 0.210		$2\mathrm{s}^{\beta}$	0	0	$-1/2$
	≥ 0.210		$2\mathrm{p}^{\alpha}_{-1}$	17	$\lvert B\rvert$	-1
Be	≤ 0.067	$^{1}\mathrm{S}_g/{}^{1}\Sigma_g\ (1\mathrm{s}^2\ 2\mathrm{s}^2)$				
			$2\mathrm{p}^{\beta}_{-1}$	0	0	-1
			$2\mathrm{p}^{\beta}_{+1}$	$2/3$-$8/9^{\mathrm{a}}$	$\lvert B\rvert$	-1
			$2\mathrm{p}^{\alpha}_{-1}$	$2/3$-$8/9^{\mathrm{a}}$	$\lvert B\rvert$	-1
			$2\mathrm{p}^{\alpha}_{+1}$	5-26	$2\lvert B\rvert$	-1
	≥ 0.067	$^{3}\mathrm{P}_u/{}^{3}\Pi_{-1,u}\ (1\mathrm{s}^2\ 2\mathrm{s}^{\beta}\ 2\mathrm{p}^{\beta}_{-1})$				
	≤ 0.149		$2\mathrm{s}^{\alpha}$	8-10	$\lvert B\rvert$	$-1/2$
	≥ 0.149		$2\mathrm{p}^{\beta}_{+1}$	8-10	$\lvert B\rvert$	-1
B	≤ 0.126	$^{2}\mathrm{P}_u/{}^{2}\Pi_{-1,u}\ (1\mathrm{s}^2\ 2\mathrm{s}^2\ 2\mathrm{p}^{\beta}_{-1})$				
			$2\mathrm{p}^{\beta}_{+1}$	3-7^{b}	$\lvert B\rvert$	-1
	≥ 0.126	$^{4}\mathrm{P}_g/{}^{4}\Pi_{-1,g}\ (1\mathrm{s}^2\ 2\mathrm{s}^{\beta}\ 2\mathrm{p}^{\beta}_{-1}\ 2\mathrm{p}^{\beta}_{0})$				
	≤ 0.193		$2\mathrm{s}^{\alpha}$	7-8	$\lvert B\rvert$	$-1/2$
	≥ 0.193		$2\mathrm{p}^{\beta}_{+1}$	6	$\lvert B\rvert$	-1
C		$^{3}\mathrm{P}_g/{}^{3}\Pi_{-1,g}\ (1\mathrm{s}^2\ 2\mathrm{s}^2\ 2\mathrm{p}^{\beta}_{-1}\ 2\mathrm{p}^{\beta}_{0})$				
	≤ 0.216		$2\mathrm{p}^{\beta}_{+1}$	0-4	$\lvert B\rvert$	-1
	≥ 0.216		$2\mathrm{p}^{\alpha}_{-1}$	8	$\lvert B\rvert$	-1
N		$^{4}\mathrm{S}_u/{}^{4}\Sigma_u\ (1\mathrm{s}^2\ 2\mathrm{s}^2\ 2\mathrm{p}^{\beta}_{-1}\ 2\mathrm{p}^{\beta}_{0}\ 2\mathrm{p}^{\beta}_{+1})$	$2\mathrm{p}^{\alpha}_{-1}$	0-7	$\lvert B\rvert$	-1
			$2\mathrm{p}^{\alpha}_{+1}$	2-26	$2\lvert B\rvert$	-1
O		$^{3}\mathrm{P}_g/{}^{3}\Pi_{-1,g}\ (1\mathrm{s}^2\ 2\mathrm{s}^2\ 2\mathrm{p}^{2}_{-1}\ 2\mathrm{p}^{\beta}_{0}\ 2\mathrm{p}^{\beta}_{+1})$	$2\mathrm{p}^{\alpha}_{+1}$	1-22	$2\lvert B\rvert$	-1
F		$^{2}\mathrm{P}_u/{}^{2}\Pi_{-1,u}\ (1\mathrm{s}^2\ 2\mathrm{s}^2\ 2\mathrm{p}^{2}_{-1}\ 2\mathrm{p}^{2}_{0}\ 2\mathrm{p}^{\beta}_{+1})$	$2\mathrm{p}^{\alpha}_{+1}$	0-7	$2\lvert B\rvert$	-1
$\vdots$	$\vdots$	$\vdots$	$\vdots$	$\vdots$	$\vdots$	$\vdots$

⋮	⋮	⋮	⋮	⋮	⋮	⋮
Ne		${}^2\mathrm{S}_g/{}^2\Sigma_g$ ($1\mathrm{s}^2$ $2\mathrm{s}^2$ $2\mathrm{p}_{-1}^2$ $2\mathrm{p}_0^2$ $2\mathrm{p}_{+1}^2$)				
	≤ 0.045		$3\mathrm{s}^\beta$	0-1	0	$-1/2$
			$3\mathrm{s}^\alpha$	1-5	$\vert B\vert$	$-1/2$
	≥ 0.045		$3\mathrm{p}_{-1}^\beta$	0	0	-1
			$3\mathrm{p}_{+1}^\beta$	3/4-7/8[a]	$\vert B\vert$	-1
			$3\mathrm{p}_{-1}^\alpha$	3/4-7/8[a]	$\vert B\vert$	-1
			$3\mathrm{p}_{+1}^\alpha$	7-18	$2\vert B\vert$	-1

[a] The $2\mathrm{p}_{+1}^\beta$ and $2\mathrm{p}_{-1}^\alpha$ spin orbitals are degenerate. They are, therefore, assigned with two order numbers n seperated by a slash.

[b] For very small field strengths, the $2p_0^\beta$ spin orbital should be the LUMO and the LUMO+1 the $2\mathrm{p}_{+1}^\beta$ spin orbital. However, for these field strengths, the HF-SCF calculations give a smaller orbital energy for the $3s$ spin orbitals, which is unphysical.

[c] Spin orbitals are numbered with integers n (order number) in ascending order with respect to their orbital energy. The energetically lowest virtual spin orbital defines $n = 0$. If the order number changes within a given range of magnetic field strengths (see second column), the range of order numbers of that spin orbital is listed.

In contrast to the *IE*s, the diamagnetic contribution of the actual system $\Delta E_{\mathrm{dia}}^{S2-S1}$ has a larger influence in the considered range of field strength for the *EA*s. This becomes most apparent for the noble gases He and Ne for which the additional electron has to occupy an orbital in a higher shell making it even more diffuse. Except for hydrogen, nitrogen, oxygen and fluorine, all *EA* curves exhibit at least one kink and, as for the *IE*s, discontinuities appear for lithium, beryllium, and boron due to changes of the ground states. The kinks appear when another electron attachment process becomes energetically favorable at a certain field strength. For the chosen set of atoms, two different kinds of such *EA* crossings can be observed. These can be traced back to the contributions with different orders in B given in Eq. (5.4). First, one attachment process with an initially higher *EA* can become energetically more favorable for stronger field strengths due to a steeper slope in *EA*(B). This can be observed for the ${}^3\mathrm{P}_u/{}^3\Pi_{-1,u}$ state ($1\mathrm{s}^2$ $2\mathrm{s}^\beta$ $2\mathrm{p}_{-1}^\beta$) of the beryllium atom. In the field-free case, capturing a $2\mathrm{s}^\alpha$ rather than a $2\mathrm{p}_{+1}^\beta$ electron is favored. In a magnetic field, however, the initial slope of the *EA* curve for the former process is only $m = -E_\mathrm{h}/2B_0$ while it is $m = -E_\mathrm{h}/B_0$ for the latter. Hence, the difference of the two corresponding *EA*s as a function of the magnetic field strength should be linear as can be seen in Fig. 5.7a. For the carbon atom in the ${}^3\mathrm{P}_g/{}^3\Pi_{-1,g}$ state ($1\mathrm{s}^2$ $2\mathrm{s}^2$ $2\mathrm{p}_{-1}^\beta$ $2\mathrm{p}_0^\beta$), a different behavior can be observed. An electron is attached in the $2\mathrm{p}_{+1}^\beta$ orbital for $B \leq 0.216$ B_0 and in the $2\mathrm{p}_{-1}^\alpha$ orbital for higher field strengths. Since both *EA*(B) curves exhibit the same slope, it must be the $\Delta E_{\mathrm{dia}}^{S2-S1}$ term which is

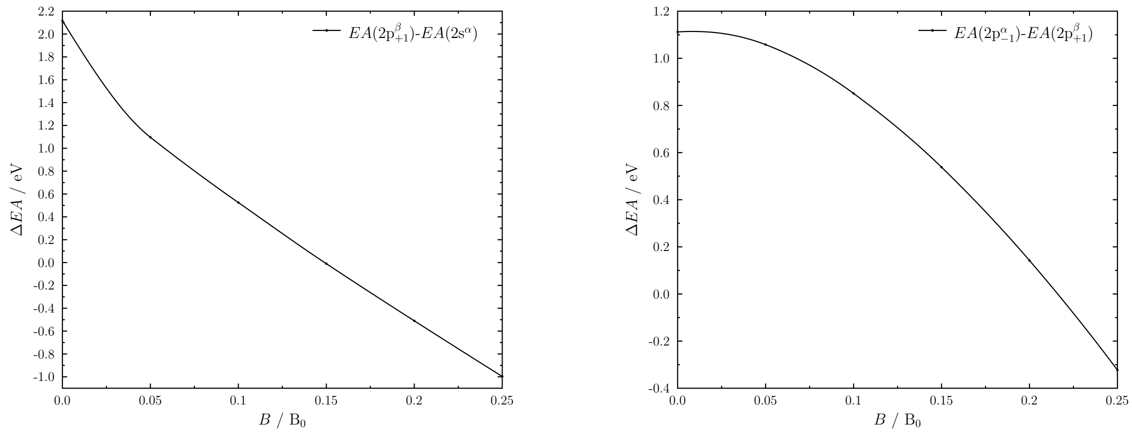

(a) Be

(b) C

Figure 5.7: Difference between two electron affinities which for certain field strengths are lowest: (a) beryllium and (b) carbon.

responsible for the crossing. This is plausible since $E_{\text{dia}}(S2(2p^{\beta}_{+1}))$ should be larger than $E_{\text{dia}}(S2(2p^{\alpha}_{-1}))$ since in the former case, all $2p^{\beta}$ orbitals are singly occupied. Hence, the Fermi correlation is larger than for the latter case leading to a larger spatial extent. In Fig. 5.7b, the resulting quadratic dependence is clearly visible in the difference of the two *EA*s.

As for the *IE*s, the evolution of *EA*s for the first and second row elements with an increasing magnetic field is strongly dictated by the Landau correction leading to decreasing *EA*s. For small field strengths, attaching an electron to yield the corresponding anions is more favorable as compared to the field-free case. However, the situation becomes more complex as the system's diamagnetic contribution $\Delta E^{S2-S1}_{\text{dia}}$ has a greater influence especially when orbitals with a larger main quantum number n are to be occupied.

5.2 Molecules in strong magnetic fields

5.2.1 Simple molecules made complicated: H_2 and LiH

After the previous discussion on atoms, the focus is now turned toward molecules. In addition, the discussion is extended to also include excited states. A key task in predicting spectra is to give the correct positions of transitions which are to be expected. Consequently, the accurate description of the electronic landscape of excited states in order to obtain sound excitation energies is indispensable. This chapter focuses on the total energy of molecules in strong magnetic fields. In contrast to atoms, the orientation of the magnetic field vector with respect to the molecule is of importance. The implications of this orientation dependence are core aspects of the subsequent analysis. First, the presumably simple hydrogen molecule is investigated before the electronic states of LiH are examined. Parts of the results presented here have been published in Refs. [85, 86].

For the H_2 molecule, the energies of the lowest singlet and triplet states have been calculated as a function of the magnetic field strength at the EOM-EE/SF-CCSD/aCQ levels of theory using the $1^1\Sigma_g^+$ state as the CC reference wave function.[25] As can clearly be seen in Fig. 5.8, the evolution of electronic energies obtained differs substantially depending on the orientation of the molecular axis with respect to the magnetic field vector. The situation is far more involved for the perpendicular case than it is for a parallel orientation.

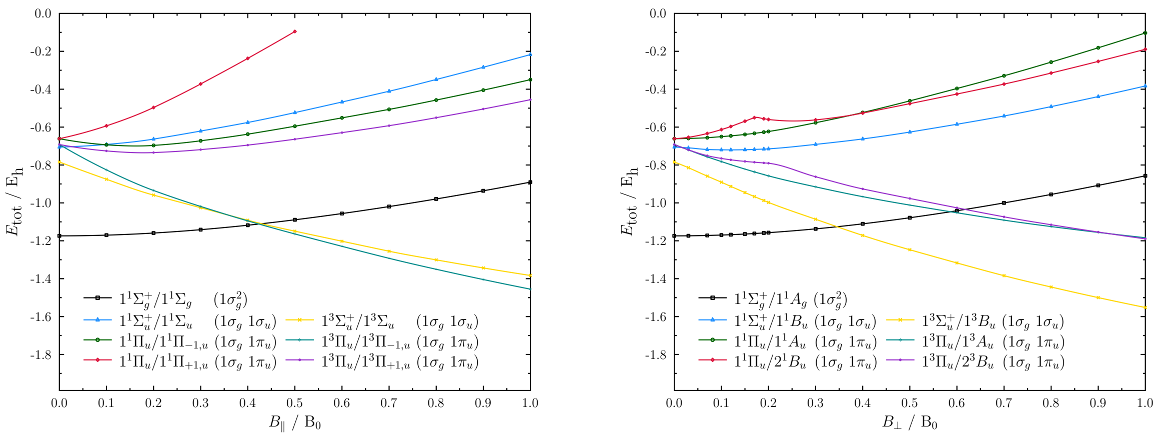

(a) ∥ (b) ⊥

Figure 5.8: Total energies of low-lying singlet and triplet states of the hydrogen molecule in a magnetic field between 0-1 B_0 with (a) parallel and (b) perpendicular orientation to the molecular axis, respectively.

---

[25] Equilibrium geometries for the $1^1\Sigma_g^+/1^1\Sigma_g$ state in a parallel magnetic field have been used. They are listed in the Electronic Supplement together with all other acquired data.

As the magnetic field vector $\boldsymbol{B}$ is an axial vector, compared to the field-free case, only rotation axes parallel as well as mirror planes perpendicular to $\boldsymbol{B}$ constitute symmetry operations when a magnetic field is applied (see Chpt. 2.1). Hence, the point-group symmetry of a hydrogen molecule in a parallel magnetic field is lowered from $D_{\infty h}$ to $C_{\infty h}$, thereby losing the symmetry of all σ_v planes. As shown in Fig. 5.8a, the $1^1\Sigma_g^+/1^1\Sigma_g$ and $1^1\Sigma_u^+/1^1\Sigma_u$ states (black and blue) are both merely energetically destabilized by the diamagnetic term as $M_S = M_L = 0$. Its triplet counterpart ($1^3\Sigma_u^+/1^3\Sigma_u$ state, yellow), hence, is only stabilized by the spin-Zeeman term. The Π states split into a Π_{-1} and Π_{+1} state. This is the typical Zeeman splitting with the Π_{-1} component being energetically lowered and its complement being destabilized. The splitting is nearly linear only for field strengths around $B \approx 0 - 0.02$ B_0. For the singlet, the states are shown in green and red while the triplet states are shown in turquoise and lilac. As discussed in Ref. [123], the fully spin-polarized $1^3\Pi_u/1^3\Pi_{-1,u}$ state (turquoise) eventually becomes the ground state for higher field strengths.[26]

Fig. 5.8b shows the total energies of the corresponding states in a perpendicular magnetic field. Here, the point-group symmetry is lowered to C_{2h} and, hence, M_L is no longer a good quantum number. The $1^1\Sigma_g^+/1^1A_g$ state (black) does not evolve very differently from the parallel case. However, the energy at $B = 1$ B_0 is 33 $\mathrm{mE_h}$ higher as compared to the parallel configuration. This can be rationalized by the diamagnetic term: It has to yield a larger contribution in the perpendicular case since the spatial extent in the plane perpendicular to the field is largest. All other states show pronounced differences in their evolution with the magnetic field. The $1^1\Sigma_u^+/1^1B_u$ state (blue) is stabilized up to a field strength of about $B \approx 0.1$ B_0. No such stabilization can be observed in the parallel field. It occurs due to the lowered symmetry that allows for orbitals of the same symmetry (here: b_u) to mix with the former σ_u orbital and, thus, introduce angular momentum. The same effect can be observed for the $1^3\Sigma_u^+/1^3B_u$ state (yellow) which thereby becomes the ground state for higher field strengths in a perpendicular magnetic field. Even though formally a bonding and an antibonding orbital are occupied, i.e., the formal bond order is zero, the state becomes bound by the paramagnetic bonding mechanism first described in Ref. [32]. This mechanism is described in more detail in Chpt. 5.2.3 using the example of the helium dimer. The states of former Π symmetry split into an A_u and a B_u state, respectively. The $1^1\Pi_u/1^1A_u$ state (green) does not exhibit any paramagnetic stabilization and its triplet counterpart is also less stabilized compared to the parallel configuration. The corresponding B_u states

---

[26] In contrast to the treatment of atoms, the crossing field strength for a change of ground states cannot be determined by one set of EOM calculations. Total energies are obtained by the determination of vertical excitation energies. For an exact crossing field strength, hence, total energies for the respective excited states' equilibrium geometries would need to be calculated.

(red and lilac) are more strongly destabilized than their A_u counterparts. This can be understood as an avoided crossing with the lower-lying B_u states of the respective multiplicity. Contrary to the parallel case, these states are no longer allowed to cross.[27] While the $1^1\Sigma_u^+/1^1B_u$ and $1^3\Sigma_u^+/1^3B_u$ states (blue and yellow) become stabilized as described above, the B_u states emerging from the former Π_u states are destabilized in return. The appearance of avoided crossings becomes more apparent for these states for $B \approx 0.17$ B$_0$ and $B \approx 0.22$ B$_0$, respectively. Each curve exhibits a prominent bulge where the slope is drastically altered. At these points, higher-lying electronic states of the same symmetry are prevented from crossing and the involved states interchange their characters.

The increased occurrence of avoided crossings between electronic states in magnetic fields is a general phenomenon that can also be observed for the LiH molecule. The total energies of its four lowest singlet states in a parallel and perpendicular magnetic field are depicted in Fig. 5.9. In the parallel case where the point-group symmetry is C_∞, the two lowest $^1\Sigma^+/^1\Sigma$ states (black and blue) are destabilized solely diamagnetically while the typical orbital-Zeeman induced splitting can be observed for the $1^1\Pi/1^1\Pi_{\pm1}$ states (green and red). In a perpendicular magnetic field, the point-group symmetry is merely C_s. In contrast to the case of H$_2$, even the $1^1\Sigma^+/1^1A'$ state[28] (black) is sta-

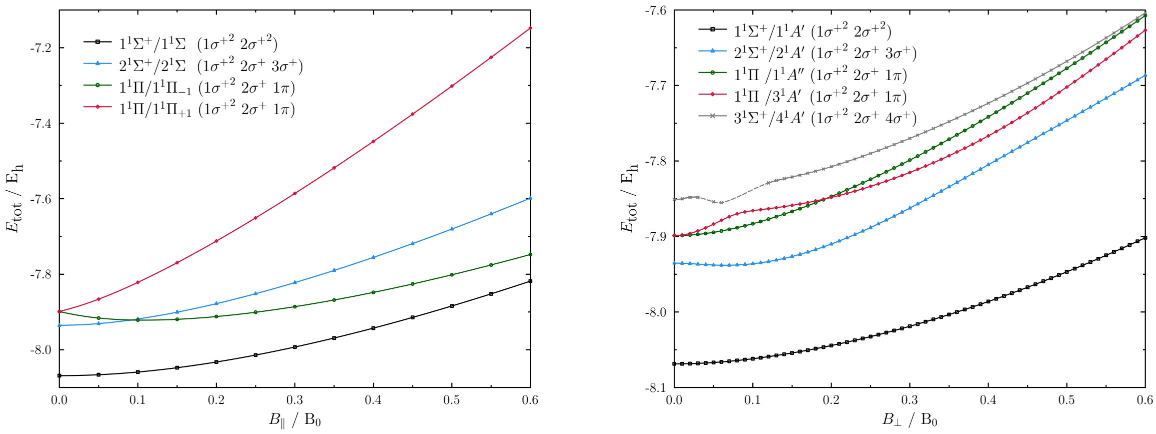

(a) ∥ (b) ⊥

Figure 5.9: Total energies of low-lying singlet states of the LiH molecule in a magnetic field between 0-0.6 B$_0$ with (a) parallel and (b) perpendicular orientation to the molecular axis, respectively.

---

[27] As remarked in Ref. [86], the prohibition for two states of the same symmetry to cross for a diatomic molecule is no longer strictly valid. For a fixed direction of the magnetic field, the bond length and the field strength now represent two degrees of freedom. The cases for which crossing may occur, however, can be ignored here due to their rare appearance.

[28] Note that this state does not remain the ground state throughout the considered range of field strengths.

bilized compared to the parallel case. At $B = 0.6$ B_0, the total energy is lower by 83 $\mathrm{mE_h}$. This suggests a slight interaction with higher-lying states of the same symmetry. Indeed, for the $2^1\Sigma^+/2^1A'$ state (blue), the same paramagnetic stabilization is found as for the $1^1\Sigma_u^+/1^1B_u$ state (blue) in H_2. For LiH, the $1^1\Pi$ state splits into the $3^1A'$ and $1^1A''$ states (red and green). While the latter increases smoothly in energy with higher field strengths, the $3^1A'$ state interacts with the lower-lying $2^1A'$ state (blue). In this interaction, the $2^1\Sigma^+/2^1A'$ state is stabilized while the $1^1\Pi/3^1A'$ state is destabilized. In fact, a whole cascade of avoided crossings can be observed. States even avoid each other multiple times as the field strength increases: Besides the interaction at the onset of the magnetic field, the $2^1\Sigma^+/2^1A'$ state (blue) and the $1^1\Pi/3^1A'$ state (red) exhibit a second avoided crossing at $B \approx 0.45$ B_0. The interplay of paramagnetic and diamagnetic contributions from the Hamiltonian introduces a complicated behavior in the total energies as a function of the magnetic field strength. Therefore, with lower point-group symmetry, the likelihood of encountering avoided crossings strongly increases.

$\boldsymbol{B-\lambda}$ diagrams

For spectra, the influence of a molecule's orientation on the evolution of its electronic states becomes most obvious when inspecting a $B-\lambda$ diagram. The latter can be used to assign observed spectra from magnetic stellar objects and determine their average field strength. In Fig. 5.10, the $B-\lambda$ diagrams including dipole-allowed transitions between the above introduced four lowest singlet states of LiH are shown. Energy differences

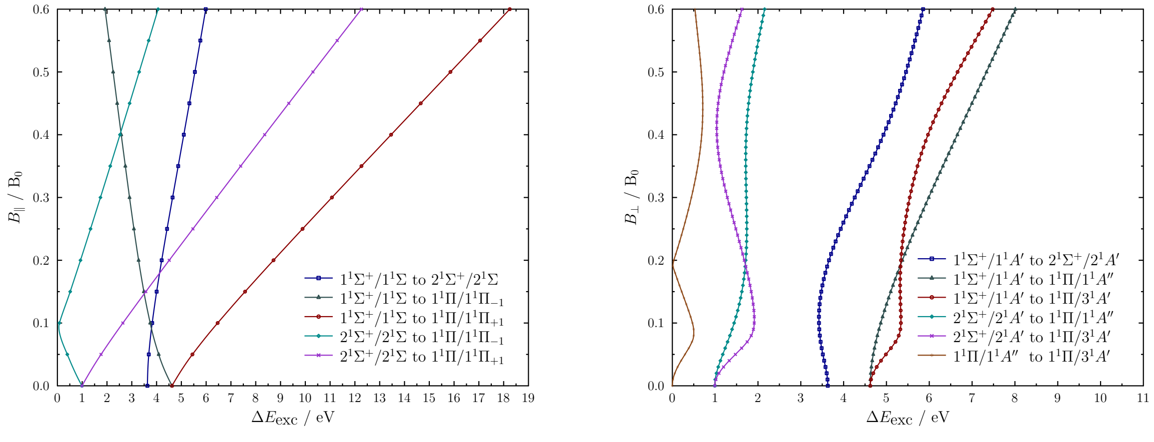

(a) ‖

(b) ⊥

Figure 5.10: $B-\lambda$ diagram for dipole-allowed transitions between low-lying singlet states of the LiH molecule in a magnetic field between 0-0.6 B_0 (a) parallel and (b) perpendicular to the molecular axis, respectively.

between two electronic states correspond to the wavelengths for which absorption bands may appear in observable spectra. Such diagrams figuratively show how the positions of potential bands change with increasing magnetic field strength. Comparing the two diagrams, their differences immediately become obvious. With less symmetry present, more electronic transitions become dipole-allowed and more bands can be observed for the perpendicular than for the parallel orientation because former $\Pi \rightarrow \Pi$ transitions become possible. As to be expected regarding the total energies, the positions of potential transitions for a given magnetic field strength vary tremendously for the different orientations. For spectra, this certainly has to result in broadened bands as one orientation of the molecule with respect to the magnetic field vector is generally favored but a distribution of orientations is to be expected. The bends that have been observed for the total energies are also reflected in the $B - \lambda$ diagram for the perpendicular case. Hence, for a certain excitation, the same excitation energy might occur several times for different field strengths making the assignment of additional transitions even more important. In any case, there is no way to even qualitatively predict the position of bands in observable spectra of magnetic stellar objects for a certain system by deducing them from respective positions in the field-free case. Hence, quantum-chemical calculations are essential for the assignment of such spectra.

5.2.2 Paramagnetism in closed-shell molecules

The plethora of avoided crossings occuring between electronic states of a system exposed to a magnetic field leads, among other things, to the existence of paramagnetic closed-shell molecules. Usually, molecules with a closed-shell ground state in the field-free case behave diamagnetically which can easily be explained by looking at the Hamiltonian. With all the electrons paired, molecules typically exhibit a fully symmetric singlet ground state. Therefore, all Zeeman contributions vanish making the diamagnetic term the leading B-dependent contribution to the energy. Thus, the energy rises as a function of the magnetic field and the system is repelled. It was shown in Refs. [118, 124] that closed-shell paramagnetic molecules can exist. Indeed, closed-shell systems as BH, [30, 118, 125–127] CH^+, [125–127] MnO_4^-, [128, 129] as well as antiaromatic polycycles [130, 131] have been found to be paramagnetic both in experiment and *ab-initio* studies. In Ref. [132], the effect is explained using an analytical two-state model involving the ground and a HOMO-LUMO excited state within a high-field HF-SCF study. However, the excited state is not explicitly calculated. With the advent of the EOM-CC methods developed in the course of this thesis, it is now possible to accurately investigate all involved states in detail. Fig. 5.11 shows the total energies of the four lowest singlet states of the CH^+ cation exposed to a magnetic field with either a parallel, 5°-bent, or perpendicular orientation with respect to the molecular axis. All energies have been

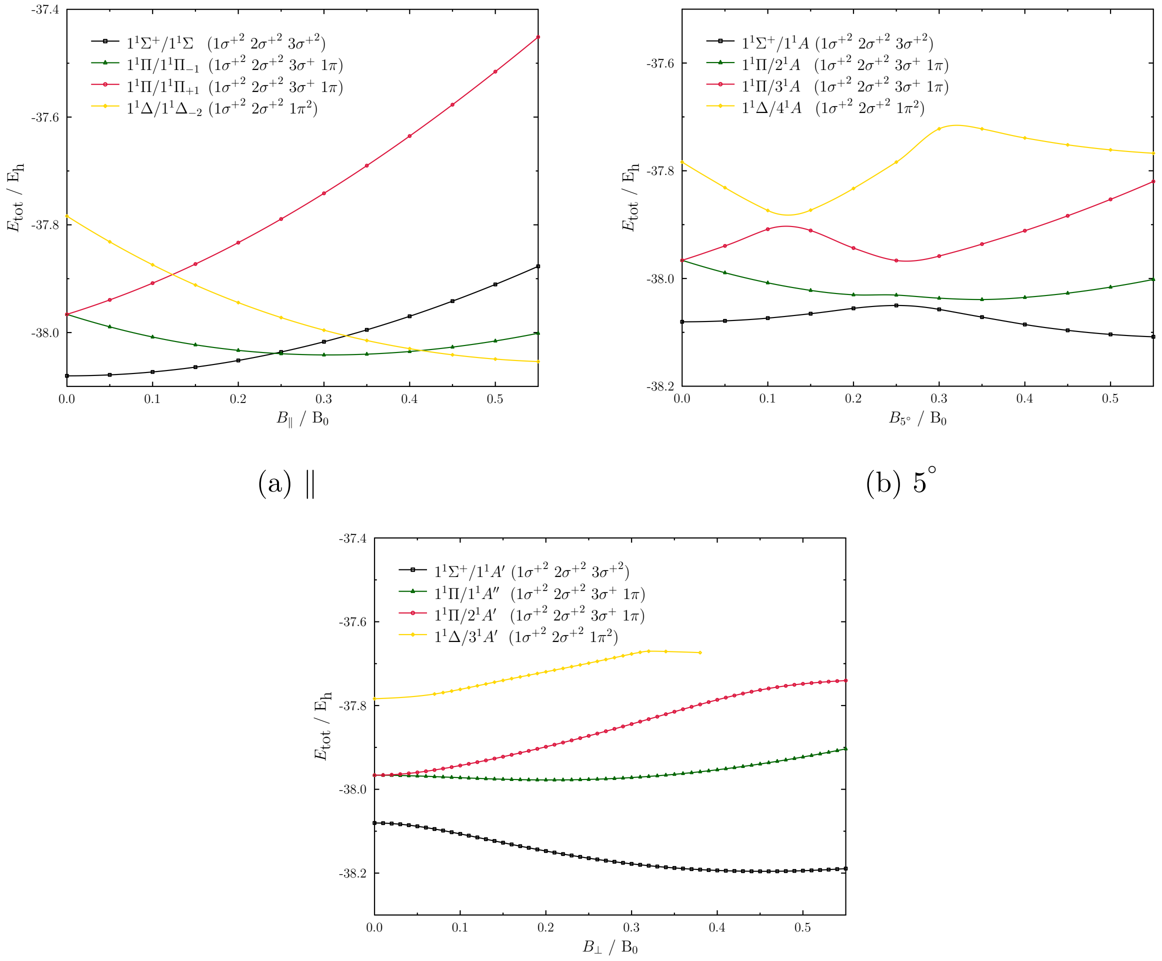

(a) ∥

(b) 5°

(c) ⊥

Figure 5.11: Total energies of low-lying singlet states of the methylidinium cation in a magnetic field between 0-0.55 B$_0$ with (a) parallel, (b) 5°-bent, and (c) perpendicular orientation to the molecular axis, respectively.

calculated at the EOM-EE-CCSD/aCQ level of theory using the $1^1\Sigma^+$ state ($1\sigma^{+2}$ $2\sigma^{+2}$ $3\sigma^{+2}$, black) as a reference. In the field-free case, it can be described in the HF picture by doubly occupying the 1s orbital of the carbon atom ($1\sigma^+$), the bonding orbital constituted from an sp-hybrid orbital of the carbon atom and the 1s orbital of the hydrogen atom ($2\sigma^+$), and the lone pair orbital. As described in Ref. [132], the LUMO is doubly degenerate and these π orbitals can be thought of as the two p orbitals at the carbon atom perpendicular to the bond axis. For the parallel orientation depicted in Fig. 5.11a, a diamagnetic response for the cation in its ground state is observed. The $1^1\Sigma^+/1^1\Sigma$ state (black) is merely energetically destabilized while only the $1^1\Pi/1^1\Pi_{-1}$ and $1^1\Delta/1^1\Delta_{-2}$ states (green and yellow) show paramagnetic stabilization. For these states, the 3σ orbital has been depopulated in favor of the paramagnetically stabilized π_{-1} orbital. If the magnetic field vector, however, is slightly bent with respect to the molecular axis, the situation is changed drastically. The point-group symmetry is lowered to C_1. Now, any state crossing is prohibited as is shown in Fig. 5.11b. This means that an avoided crossing occurs at each crossing point from the parallel orientation. For the $1^1\Sigma^+/1^1A$ state (black), paramagnetic stabilization can be observed for field strengths of $B \approx 0.25$ B$_0$ after the initial rise in energy. This is induced first by a crossing with the $1^1\Pi/2^1A$ state (green) and then intensified by a cascade of avoided crossings. Thereby, the $1^1\Delta/4^1A$ state (yellow) character is being transferred to the $1^1\Sigma^+/1^1A$ state (black) with the two former Π states (green and red) mediating. The interaction becomes stronger with increasing angle and is strongest at a perpendicular orientation. The point-group symmetry changes to C_{2h} and the $1^1\Pi/1^1A''$ state (green) appears to be merely a spectator state. As can be seen in Fig. 5.11c, the interaction between the states is so strong that the energies of the $1^1\Sigma^+/1^1A$ and the $1^1\Delta/3^1A'$ states (black and yellow) move apart with the onset of a magnetic field. The paramagnetic stabilization of the $1^1\Pi/2^1A'$ state (red) first and the $1^1\Delta/3^1A'$ state (yellow) leads to the overall stabilization and, hence, paramagnetic response of the $1^1\Sigma^+/1^1A$ ground state[29] (black). The molecule, hence, lowers its energy when orientating itself perpendicular to an applied magnetic field. The avoided crossings occuring at high field strengths can, hence, be regarded as the initiators of the paramagnetic response which is observable in terrestrial magnetic fields. [133]

For field strengths of $B \gtrapprox 0.45$ B$_0$, the molecular cation behaves diamagnetically again as the diamagnetic contribution of the Hamiltonian always starts to dominate at a certain field strengths. Interestingly, this is the same field strength that is also found for the HF calculations in Ref. [132]. This implies that, in this case, electron correlation merely leads to a shift of the total energy to lower energies. Finally, the following may be noted: It has been observed in Chpt. 4.2 that the inclusion of triple excitations leads to lower field strengths for which the singly excited states cross the $1^1\Delta/1^1\Delta_{-2}$ state in the parallel case. As explained before, each crossing can be viewed as the origin of what becomes an avoided crossing in the non-parallel case. As those affect the singly excited states, an insufficient description of the doubly excited state also has consequences on the excitation energies between two states not including the $1^1\Delta/1^1\Delta_{-2}$ state. For a quantitatively impeccable evaluation, triple excitations are also necessary in the perpendicular scenario.

5.2.3 Noble gas dimers and melting of neon

So far, the total energies of a variety of electronic states have been the subject of interest. In a next step, the bonding energy and its dependence on the magnetic field

---

[29] Note that for higher field strengths the $1^3\Pi$ state becomes the ground state of the methylidinium cation.

is investigated. In general, molecules become more strongly bound when subjected to a strong magnetic field. [134, 135] However, this chapter focuses on the situation for molecules for which the perpendicular paramagnetic bonding mechanism [32] mentioned earlier leads to bound states with a formal bond order of zero. This applies, e.g., to the $1^3\Sigma_u^+/1^3B_u$ state of the hydrogen molecule which becomes the ground state for larger field strengths. [32] In the following, perpendicular paramagnetic bonding is explained using the example of the helium dimer and its influence on the binding energy is discussed.

Perpendicular paramagnetic bonding mechanism

In the field-free case, the two energetically lowest orbitals of the helium dimer are formed as the positive and negative linear combination of the 1s orbitals resulting in the nearly symmetrically split bonding $1\sigma_g^+$ and antibonding $1\sigma_u^+$ orbitals. Both orbitals are doubly occupied yielding no net energy gain with a bond order of zero. However, due to the Van der Waals interaction, the electrostatic interaction between induced dipoles, the potential energy surface of the helium dimer exhibits a shallow minimum. The same holds for a helium dimer in a magnetic field parallel to the molecular axis. Its molecular orbital (MO) scheme is shown on the left side in Fig. 5.12. When the magnetic field vector is turned by 90°, the point-group symmetry is reduced from $C_{\infty h}$ to C_{2h}. The middle panel shows how the corresponding symmetry labels change. The two former σ_u^+ orbitals as well as one of the former π orbitals are of b_u symmetry and

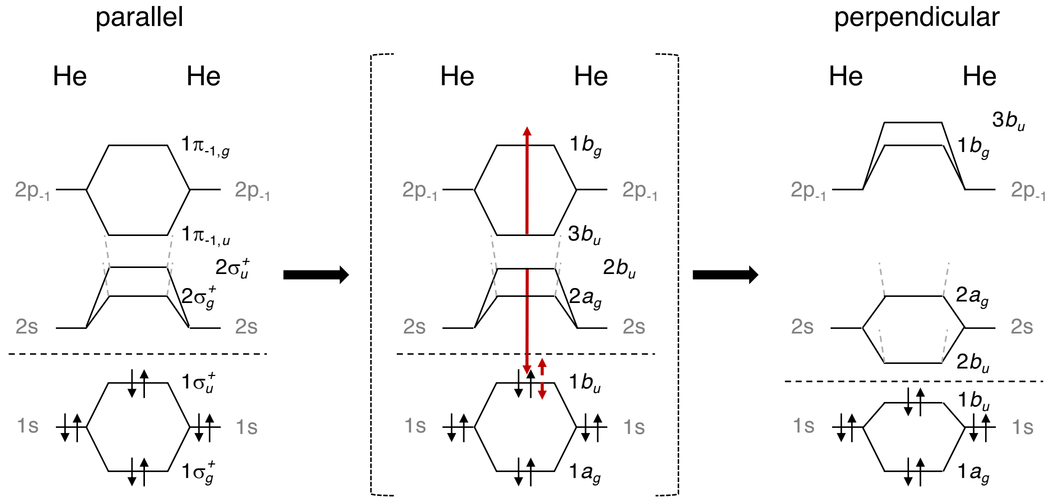

Figure 5.12: Molecular orbital scheme of the helium dimer in a magnetic field with parallel and perpendicular orientation to the molecular axis illustrating the mechanism of perpendicular paramagnetic bonding for the $1^1\Sigma_g^+/1^1A_g$ state. The energetic order of the molecular orbitals has been obtained at $R = 3$ Å and $B = 0.2$ B_0 at the HF/aQ level of theory. The scheme is not true to scale.

are, hence, allowed to mix. As a result, the $3b_u$ orbital is destabilized while the two energetically lower orbitals become stabilized. Consequently, the splitting of the former σ_g^+ and σ_u^+ orbitals is not symmetric and the $1^1\Sigma_g^+/1^1A_g$ state of the helium dimer becomes bound in a perpendicular magnetic field even though the formal bond order is zero. This corresponds to the description given in Ref. [9] that the magnetic field introduces angular momentum to the antibonding orbital by rotation. The interaction between the $1b_u$ and $3b_u$ orbitals is mediated by the $2b_u$ orbital.

Binding energies

Fig. 5.13a shows the binding energy of the helium dimer as a function of the magnetic field strength obtained at the CCSD(T)/aQ level of theory including the counterpoise correction.[30] The dotted grey line shows the interaction energy ΔE_{int} for the field-free

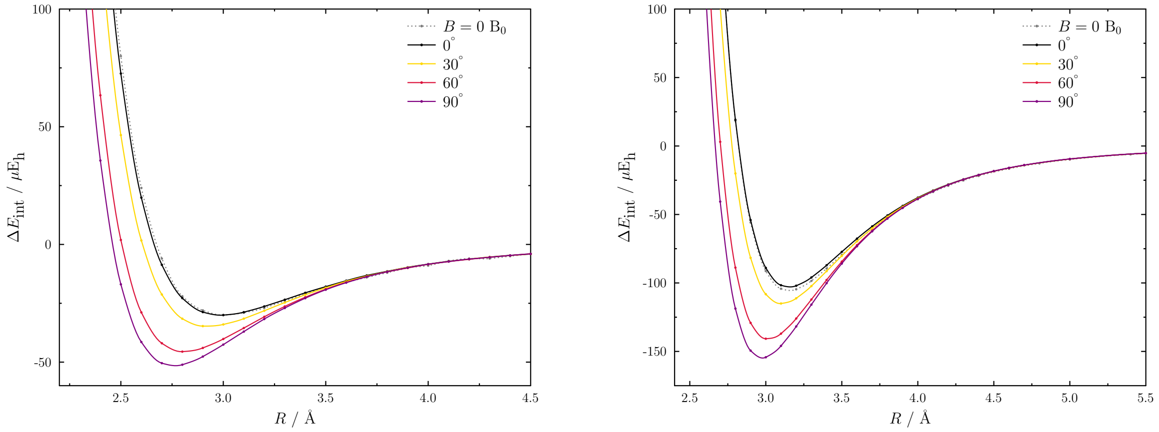

(a) He_2

(b) Ne_2

Figure 5.13: Comparison of the interaction energies for the (a) helium and (b) neon dimer, respectively, in the field-free case as well as in a magnetic field of $B = 0.2$ B$_0$ with different orientation toward the molecular axis.

case exhibiting a minimum at $R = 2.993$ Å with $\Delta E_{\text{int}} = -30$ μE$_\text{h}$. In a parallel magnetic field of $B = 0.2$ B$_0$, the potential curve (solid black) is very similar to the field-free case with a minimum at $R = 2.974$ Å and the interaction energy is essentially unchanged. The field increases the electron density slightly toward the molecular bond axis leading to the smaller equilibrium distance. When the magnetic field vector is gradually rotated from 0°-90°, the corresponding binding energy curves each exhibit a minimum at smaller bond lengths and larger interaction energies with increasing angle. For a perpendicular field, the minimum is at $R = 2.758$ Å with $\Delta E_{\text{int}} = -52$ μE$_\text{h}$. As

---

[30] To account for the basis set superposition error when calculating the binding energy, the energy of the single helium atom is calculated by adding a set of basis functions at the position of the second helium atom in the dimer.

the former $1\sigma_u^+$ orbital acquires more bonding character, the electron density between the helium nuclei increases and the equilibrium bond distance is shortend by 21.6 pm. The stabilizing effect by perpendicular paramagnetic bonding reaches its maximum for a perpendicular magnetic field.

A similar analysis has been carried out[31] in Ref. [136] for the neon dimer at the fc-CCSD(T)[32]/aQ level of theory. The corresponding results are depicted in Fig. 5.13b. Here, applying a parallel field of $B = 0.2\ \mathrm{B}_0$ actually leads to a decrease in the binding energy of 2 $\mu\mathrm{E_h}$ to $\Delta E_{\mathrm{int}} = -103\ \mu\mathrm{E_h}$ and the equilibrium bond length is increased by 0.9 pm to $R = 3.153$ Å. The spatial extent of neon is larger than for helium and, thus, its diamagnetic contribution is larger. However, in a perpendicular field, the interaction energy is increased to $\Delta E_{\mathrm{int}} = -156\ \mu\mathrm{E_h}$ and the bond length shortened by 17.6 pm to $R = 2.977$ Å due to the paramagnetic bonding. Compared to the interaction energy in the parallel case, the effect of paramagnetic bonding is stronger in the helium dimer with a factor of 1.73 than it is in the neon dimer with a factor of only 1.51. Yet, the overall increase in the bonding energy is larger for the neon dimer. The complication in quantifying the effect of paramagnetic bonding on the stabilization is the fact that it is not possible to completely untangle it from the evolution of the pure Van der Waals interaction with the magnetic field strength. However, the latter can at least be expected to oppose the stabilization in a magnetic field as Fig. 5.14 suggests. The figures show the evolution of the diagonal elements of the polarizability tensor for the two noble gas dimers as a function of the magnetic field strength both for a parallel and perpendicular orientation.[33] Independent of the orientation of the magnetic field vector with respect to the molecular bond axis, the dimers become harder to polarize which hampers the corresponding electrostatic interaction. It can be noticed that the decrease in the polarizability is more severe in the directions perpendicular to the magnetic field due to the diamagnetic confinement. In the perpendicular case, polarization is additionally hindered in the direction along the molecular axis. Again, this has to be attributed to the diamagnetic term having a stronger effect on the orbital compression in the direction of the largest spatial extent, thus, reducing the polarizability. Notably, this means that effects like dispersion interactions which depend on polarization should lessen within magnetic fields while regular bonds are strengthened.

The melting temperature of neon determined from calculated potential energy surfaces

So far, the strengthening effect of perpendicular paramagnetic bonding on the binding

---

[31] The corresponding calculations have been performed by S. Blaschke under my guidance.

[32] fc = frozen core, with the lowest four spin orbitals as core.

[33] The respective calculations have been conducted by S. Blaschke at the CCSD/aT level of theory. The polarizability tensor has been determined using numerical derivatives of dipole moments.

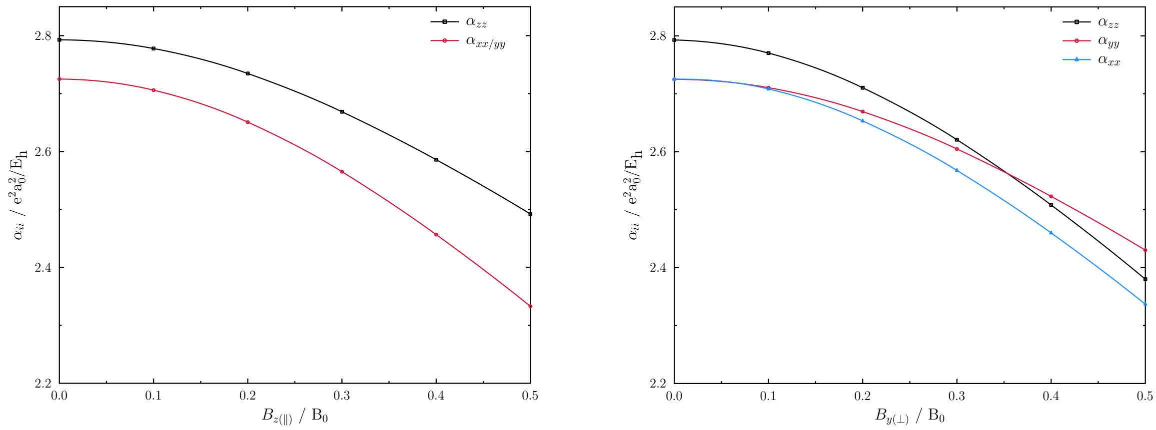

(a) He$_2$, $B_{\parallel}$ (b) He$_2$, $B_{\perp}$

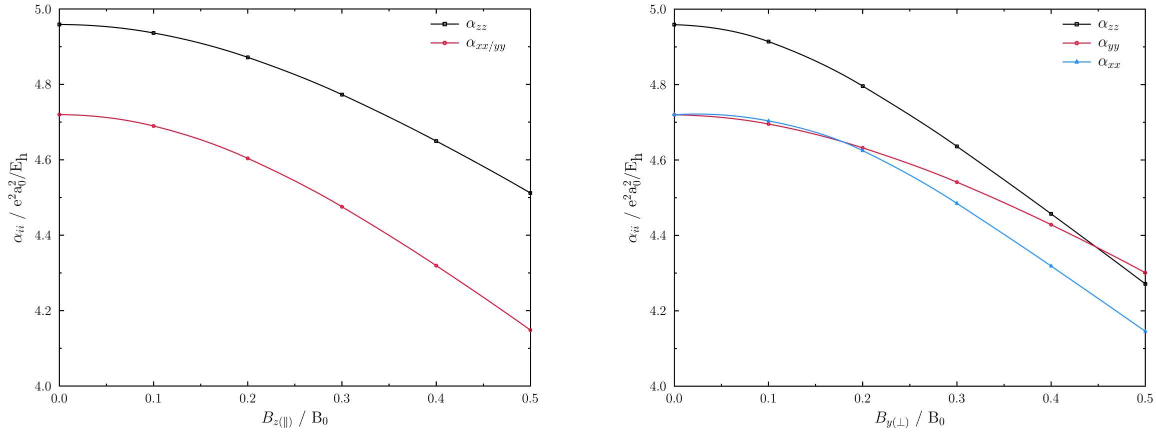

(c) Ne$_2$, $B_{\parallel}$ (d) Ne$_2$, $B_{\perp}$

Figure 5.14: Diagonal elements of the polarizability tensor of the (a,b) helium and (c,d) neon dimer, respectively, as a function of the magnetic field. The (a,c) parallel and (b,d) perpendicular orientations with respect to the molecular axis (z-direction) are depicted.

energy has been shown for a single noble gas dimer. However, if the binding energy increases for two atoms, it can be assumed that the interactions also become stronger in the corresponding solids. This would lead to an increase of the melting temperature T_m of noble gas solids in strong magnetic fields. In order to validate this assumption, investigations using Monte Carlo (MC) simulations [137] have been performed in a collaboration with E. Pahl and coworkers as described in the following.

In a statistical approach, properties of a macroscopic system are connected to the properties of its microscopic subsystems. The internal energy U of a system can be defined by the ensemble average of the energy

$$U = \langle E \rangle = \int \mathrm{d}\boldsymbol{r} \int \mathrm{d}\boldsymbol{p}\ E(\boldsymbol{r},\boldsymbol{p}) \cdot \omega(\boldsymbol{r},\boldsymbol{p}). \tag{5.5}$$

E is the energy for a given set of coordinates $\boldsymbol{r}$ and momenta $\boldsymbol{p}$. ω is the probability to find specific values of $\boldsymbol{r}$ and $\boldsymbol{p}$ for the system. As the integral in general cannot be solved analytically nor numerically, random sets of coordinates and momenta are generated and the ensemble average is determined as a statistical average. Melting temperatures can be deduced from the heat capacity C_V with

$$C_\mathrm{V} = \left(\frac{\partial U}{\partial T}\right)_V . \tag{5.6}$$

As the internal energy increases drastically for $T = T_\mathrm{m}$, C_V as a function of T exhibits a maximum at the respective melting temperature.
MC simulations have been successfully applied in the context of determining melting temperatures in the field-free case. [138, 139] The quality of the MC predictions depends strongly on the accuracy of the energies that are used in Eq. (5.5). In general, the energy can be expanded in many-body contributions:

$$E = \sum_{n}^{N} E^{(n)}. \tag{5.7}$$

The determination of the electronic part of these contributions is where quantum-chemical program packages come into play. Accurate and extensive calculations have to be performed in order to generate the required potential energy surfaces. For the application in strong magnetic fields, respective calculations have been performed using the QCUMBRE program and *ab-initio* two-body interaction energy surfaces ($\Delta E_\mathrm{int} = \Delta E_\mathrm{int}^{(2)}(B, \theta, r_{ij})$) have been generated for helium and neon. In the field-free case, the two-body interaction depends only on the internuclear distance r_{ij}. The appearance of the magnetic field introduces additional dependencies of the potential energy surface on the magnetic field strength B as well as the angle θ between the field vector and the principal axis of the dimer. Fig. 5.15 shows the complete potential energy surfaces for both the helium and the neon dimers for $B = 0.2\ \mathrm{B}_0$. The data on the neon dimer generated in Ref. [136] has been used in MC simulations[34] meant to predict the melting temperature of neon in strong magnetic fields. [140] The general procedure is as follows: MC calculations are performed on the so-called Mackay icosahedra [141] with N ($N = 13,\ 55,\ 147,\ \dots$) neon atoms (see Fig. 5.16). The melting temperature is determined for each icosahedron. To account for finite-size effects, the melting temperature for neon bulk can then be extrapolated by [142]

$$T_\mathrm{m}^\mathrm{bulk} - T_\mathrm{m}^{\mathrm{ico}(N)} = aN^{-1/3}. \tag{5.8}$$

---

[34] Corresponding simulations have been conducted by E. Pahl and coworkers (Massey University, Auckland).

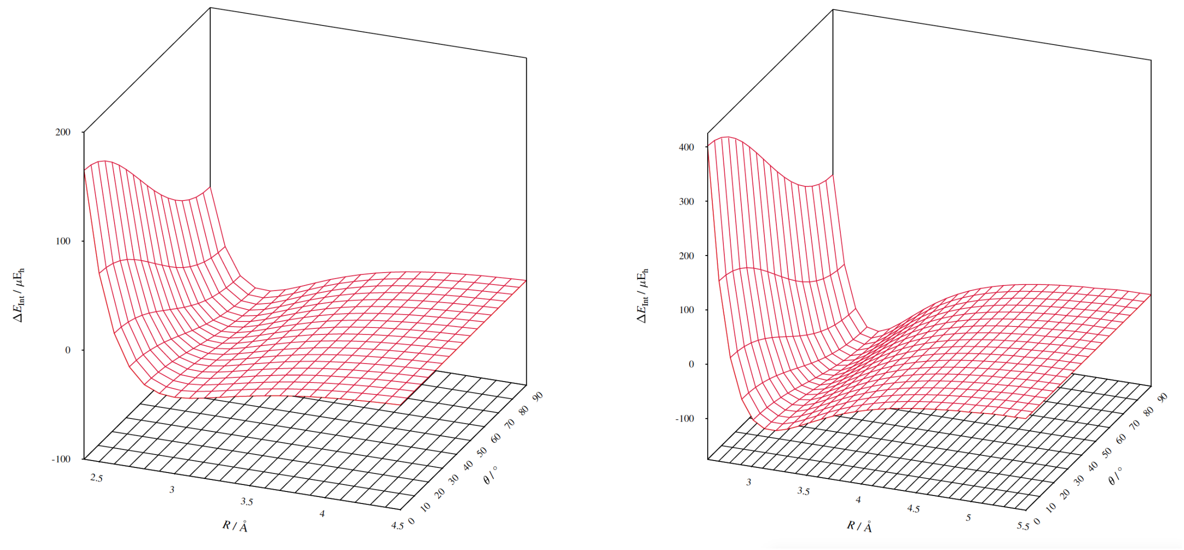

(a) He_2 (b) Ne_2

Figure 5.15: Interaction-energy surface for the (a) helium and (b) neon dimer, respectively, as a function of the interatomic distance and the angle between the dimer and the magnetic field vector at a field strength of $B = 0.2$ B_0.

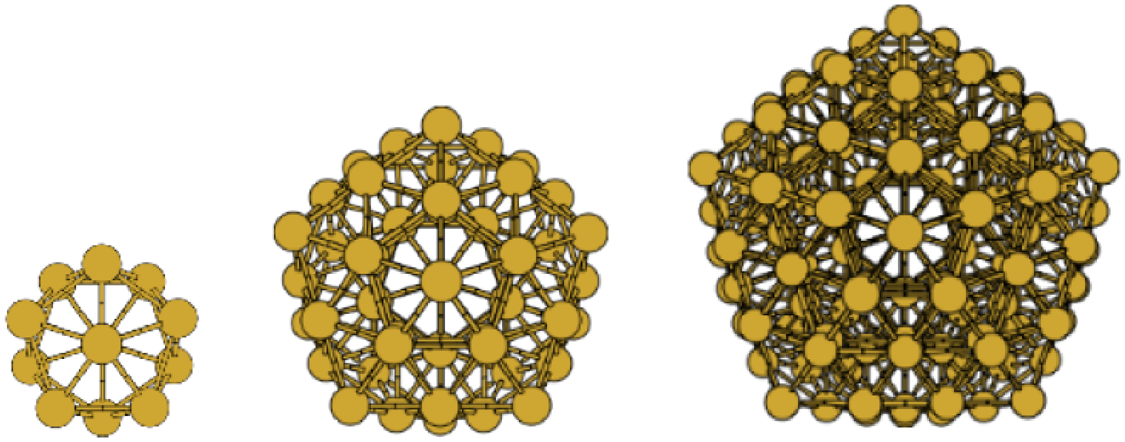

(a) $N = 13$ (b) $N = 55$ (c) $N = 147$

Figure 5.16: Structure of the three smallest Mackay icosahedra consituted of N atoms (Figure by E. Florez and E. Pahl, obtained via personal correspondence).

So far, results for the three smallest Mackay icosahedra are available. Several calculations relying on *ab-initio* potential energy surfaces obtained at the MP2,[35] CCSD, and CCSD(T) levels of theory have been performed. Fig. 5.17 shows the obtained heat capacities as a function of the temperature. The deduced melting temperatures are listed in Tab. 5.4. Three major observations can be made. The melting temperature increases with

---

[35] Corresponding calculations have been performed by A. M. Teale (University of Nottingham).

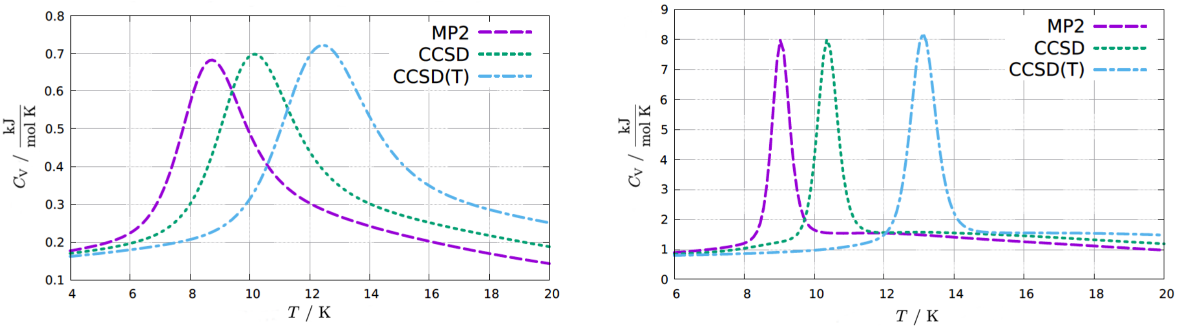

(a) Ne$_{13}$ (b) Ne$_{55}$

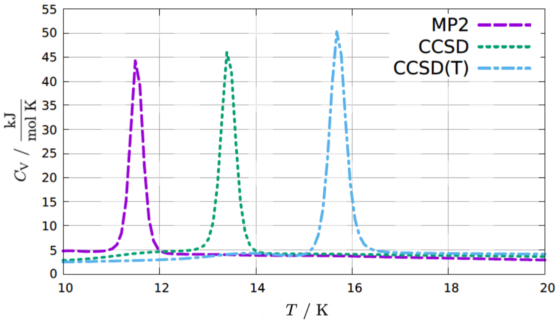

(c) Ne$_{147}$

Figure 5.17: Heat capacities obtained by MC simulations for differently sized neon icosahedra as a function of the temperature using *ab-initio* two-body interaction energies obtained at the MP2, CCSD, and CCSD(T) levels of theory at $B = 0.2\ \mathrm{B}_0$ (created by E. Florez and E. Pahl, obtained via personal correspondence).

1. increasing size of the icosahedra.
2. increasing magnetic field strength.
3. increasing accuracy of the quantum-chemical method that has been used for the generation of the energy surface.

The first effect can be explained by decreasing surface effects for larger icosahedra. In the field-free case, an exact method would converge to the melting temperature for Ne-bulk of $T_\mathrm{m} = 24.56$ K.[143] The second observation confirms the inital assumption that the increased interaction energy in a magnetic field should increase the melting temperature. When comparing the obtained melting temperatures for the Ne$_{13}$-cluster based on the MP2 results to their field-free counterparts, it can be observed that the melting temperature is increased by 2.00 K. For the Ne$_{147}$-cluster, the difference amounts to 2.66 K implying an even larger increase for larger systems. However, the melting temperature is much higher when the simulations are based on the more accurate CC

Table 5.4: Melting temperatures obtained by MC simulations for differently sized neon icosahedra as a function of the temperature using *ab-initio* two-body interaction energies obtained at the MP2, CCSD, and CCSD(T) levels of theory at $B = 0.2$ B$_0$ and in the field-free case (MP2). [140]

		T_m / K		
B / B$_0$	Method	Ne$_{13}$	Ne$_{55}$	Ne$_{147}$
0.0	MP2	6.75	6.84	8.84
0.2	MP2	8.75	9.03	11.50
0.2	CCSD	10.17	10.36	13.40
0.2	CCSD(T)	12.45	13.12	15.68

surfaces. For CCSD, the difference is 3.47 K for Ne$_{13}$ and 4.56 K for Ne$_{147}$. The deviation between CCSD and MP2 is, thereby, almost as large as the increase in the melting temperature induced by the magnetic field calculated at the MP2 level. For CCSD(T), even higher melting temperatures are obtained. Here, the deviation with respect to the MP2 results amounts to 3.70-4.18 K.

5.2.4 Varying intensities of electronic transitions

Apart from the accurate determination of excitation energies, also the intensities of the respective transitions need to be known for the prediction of spectra. The following chapter focuses on this second key aspect. The intensity of a band is proportional to the oscillator strength and, thus, to the STM (see Chpt. 2.6.2). Therefore, the STMs for transitions between the excited states previously presented for the systems H_2, LiH, and CH^+ have been calculated as EOM expectation values. They are analyzed with special focus on the appearance of avoided crossings. The aCQ basis set was used for all calculations. Parts of the results presented have been published in Ref. [86]. Fig. 5.18 shows the STMs for all dipole-allowed transitions occuring for the previously presented four singlet states of the H_2 molecule in a parallel and perpendicular magnetic field. In the first case, two different STM curves can be observed: one for the transition between the $1^1\Sigma_g^+/1^1\Sigma_g$ and the $1^1\Sigma_u^+/1^1\Sigma_u$ states (dark-blue) and another one for the transition between the $1^1\Sigma_g^+/1^1\Sigma_g$ state and the $1^1\Pi_u/1^1\Pi_{\pm1,u}$ states (maroon). For the first transition, the STM increases with the field strength. This can be related to an increased overlap between the σ_g and σ_u orbital as they are both stretched along the magnetic field vector. For the second transition, the STMs decrease for higher field strengths which, in contrast, mirrors the reduced overlap between the σ_g and the $\pi_{\pm1}$ orbitals. The latter may be thought of as donut-shaped rings encasing the molecular bond axis. The situation is remarkably different for a magnetic field with

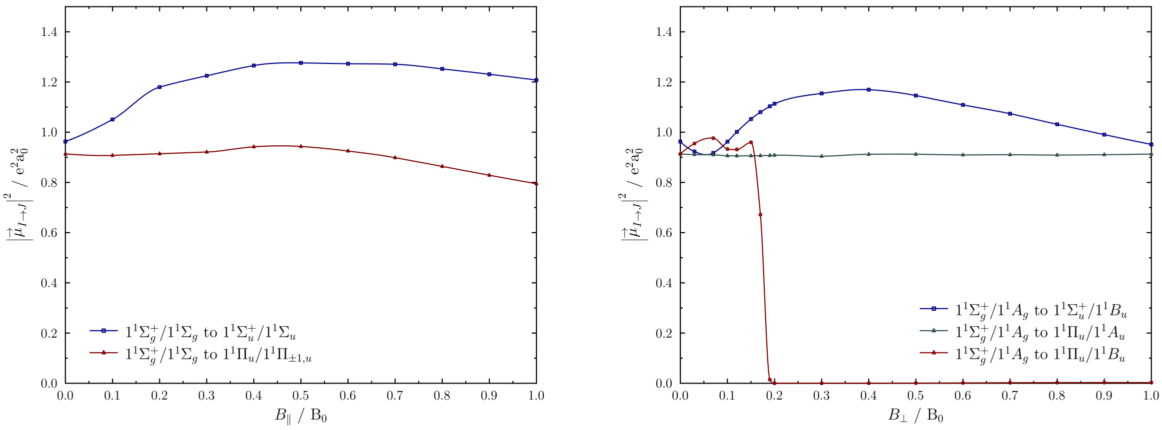

(a) ∥ (b) ⊥

Figure 5.18: EOM-EE-CCSD STMs for dipole-allowed electronic transitions between low-lying singlet states of the hydrogen molecule in a magnetic field between 0-1 B$_0$ with (a) parallel and (b) perpendicular orientation to the molecular axis, respectively.

perpendicular orientation. The symmetry of the $\pi_{\pm1}$ orbitals is lifted such that the STMs for the transitions between the $1^1\Sigma_g^+/1^1A_g$ and the $1^1\Pi_u/1_u^A$ / $1^1\Pi_u/1_u^B$ states (darkgreen and darkred) are now different. The curve for the former transition is rather smooth, while for the latter, it drops to nearly zero for $B \geq 0.2$ B$_0$. The turning at $B \approx 0.17$ B$_0$ coincides with the avoided crossing observed earlier in Chpt. 5.2.1 for the $1^1\Pi_u/1^1B_u$ state. For smaller field strengths, the unsteady course seems to stem from interaction between the $1^1\Sigma_u^+/1^1B_u$ and $1^1\Pi_u/1^1B_u$ states. Both STM curves for transitions involving these states show distinct changes in curvature in the respective range of field strengths for which avoided crossings occur. This suggests that avoided crossings in the energy of the respective states involved in the transition are reflected by drastic changes in curvature of the STMs. The fact that the states' characters are interchanged is, hence, also reflected in the respective properties.

This explanation is further supported by the behavior of the STMs between the lowest four singlet states of the LiH molecule as a function of the magnetic field strength as shown in Fig. 5.19. In the parallel case, there are five dipole-allowed transitions with three different STMs.[36] All of them decrease smoothly with increasing field strength. This behavior can be related to the effect of the orbital distortion which diminishes the overlap between the involved orbitals. Due to the breaking of the Π symmetry in the perpendicular case, different STMs for the respective transitions from the two $^1\Sigma^+/^1\Sigma$ states into the $1^1\Pi/1^1A''$ and the $1^1\Pi/3^1A'$ states can be observed. Additionally, the transition between the two states emerging from the former $1^1\Pi$ state becomes

---

[36] STMs for transitions into the Π_{-1} and Π_{+1} components of the Π state are equivalent by symmetry.

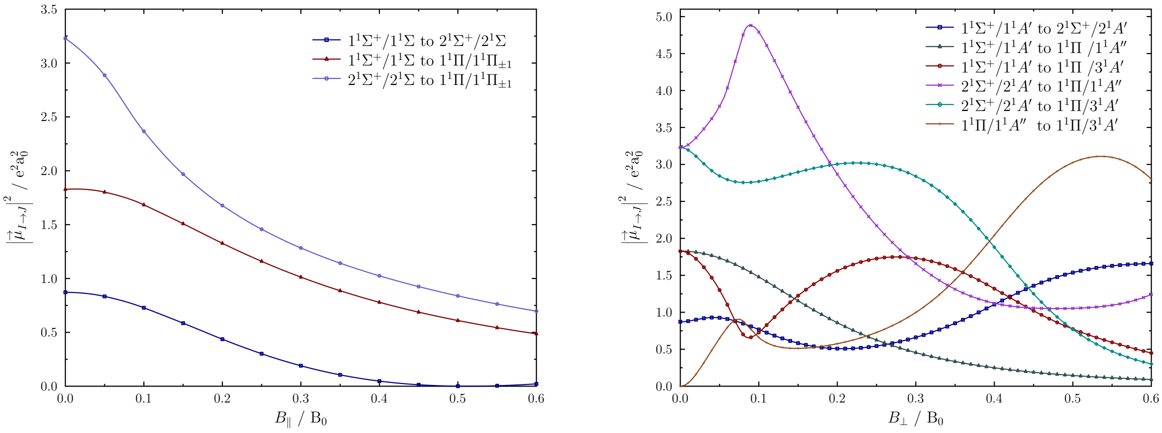

(a) ∥

(b) ⊥

Figure 5.19: EOM STMs for dipole-allowed electronic transitions between low-lying singlet states of the LiH molecule in a magnetic field between 0-0.6 B$_0$ with (a) parallel and (b) perpendicular orientation to the molecular axis, respectively.

dipole-allowed. Only the STM for the electronic transition between the $1^1\Sigma^+/1^1A'$ and the $1^1\Pi/1^1A''$ state shows a smooth decrease. This is due to the fact that none of the involved states encounters an avoided crossing in the considered magnetic field range. All other STMs exhibit profound changes concerning slope and curvature as the respective transitions all involve either the $2^1\Sigma^+/2^1A'$ state or the $1^1\Pi/3^1A'$ state. Those undergo multiple avoided crossings with the most pronounced ones at around $B \approx 0.09$ B$_0$ and $B \approx 0.40$ B$_0$ (see again Fig. 5.10b).

For the methylidinium cation, Fig. 5.20 shows a similar situation. With a magnetic field applied in a parallel manner, the three dipole-allowed transitions between the four lowest singlet states exhibit two different STMs with an almost parallel evolution with increasing field strength. Both transitions involve the excitation of an electron from the 3σ orbital into the $1\pi_{-1}$ orbital. The STMs rise slightly for higher field strengths. This suggests that the overlap between the 3σ lone pair orbital and the $1\pi_{-1}$ orbital rises indicating that the compression of the latter outweighs the stretching of the former. In the perpendicular case depicted in Fig. 5.20c, the expected sudden changes for the STMs involving the $1^1\Delta/3^1A'$ state (gold, green, and orange) occur around $B \approx 0.28$ B$_0$. No further values could be obtained due to the avoided crossing with the energetically higher $4^1A'$ state causing convergence problems. With a magnetic field vector at an angle of 5° with respect to the molecular bond axis, the evolution of the STMs as a function of the magnetic field strength becomes even more turbulent because all states are involved in avoided crossings.

In summary, it can be noted that all examples emphasize that STMs for spectra of

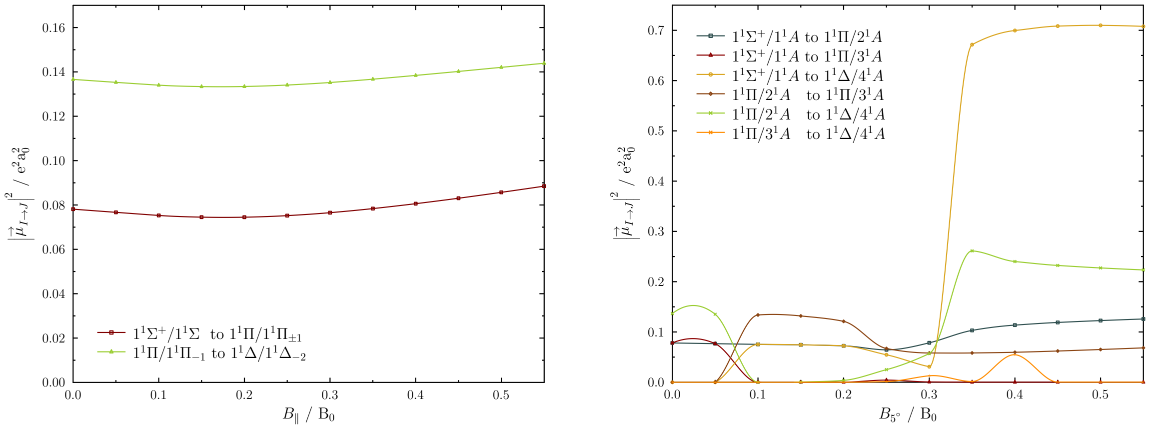

(a) ∥ (b) 5°

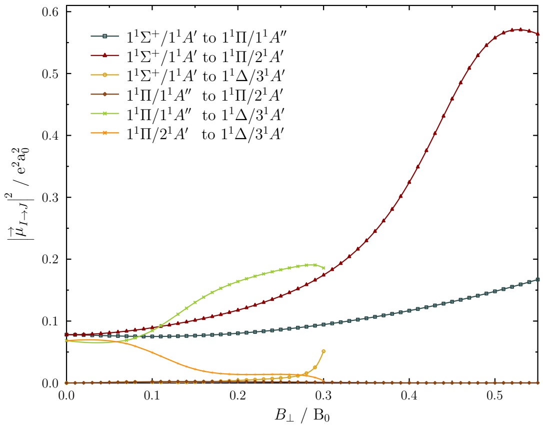

(c) ⊥

Figure 5.20: EOM STMs for dipole-allowed electronic transitions between low-lying singlet states of the methylidinium cation in a magnetic field between 0-0.55 B$_0$ with (a) parallel, (b) 5°-bent, and (c) perpendicular orientation to the molecular axis, respectively.

magnetic white dwarfs can by no means be deduced from the field-free case. Due to the abundance of avoided crossings resulting from a lowering in symmetry, not even a qualitative prediction can be made concerning whether a certain transition is observable or vanishes for a given magnetic field strength. Therefore, the presented finite-field calculations are vital when attempting to model observational spectra of atoms and molecules in strong magnetic fields.

5.3 Reaching for the stars - Excited states of the sodium atom

The last chapter of this thesis is dedicated to a concrete astrophysical application. Fig. 5.21 shows a compilation of observable spectra of several magnetic white dwarfs.[37] The red arrows mark bands that have not yet been assigned and do not fit any known transition. However, they exhibit a similar shape yet varying transition wavelengths. If the bands stem from the same atom or molecule, this indicates different magnetic field strengths for the white dwarfs. One educated guess by astrophysicists is that the transition may stem from the 3s ↔ 3p transition in the sodium atom which in the field-free case is known as the sodium D-lines. For strong magnetic fields, no predictions of electronic transition energies for the sodium atom are available. Therefore, an extensive investigation on the electronic transitions occuring between the manifold of doublet

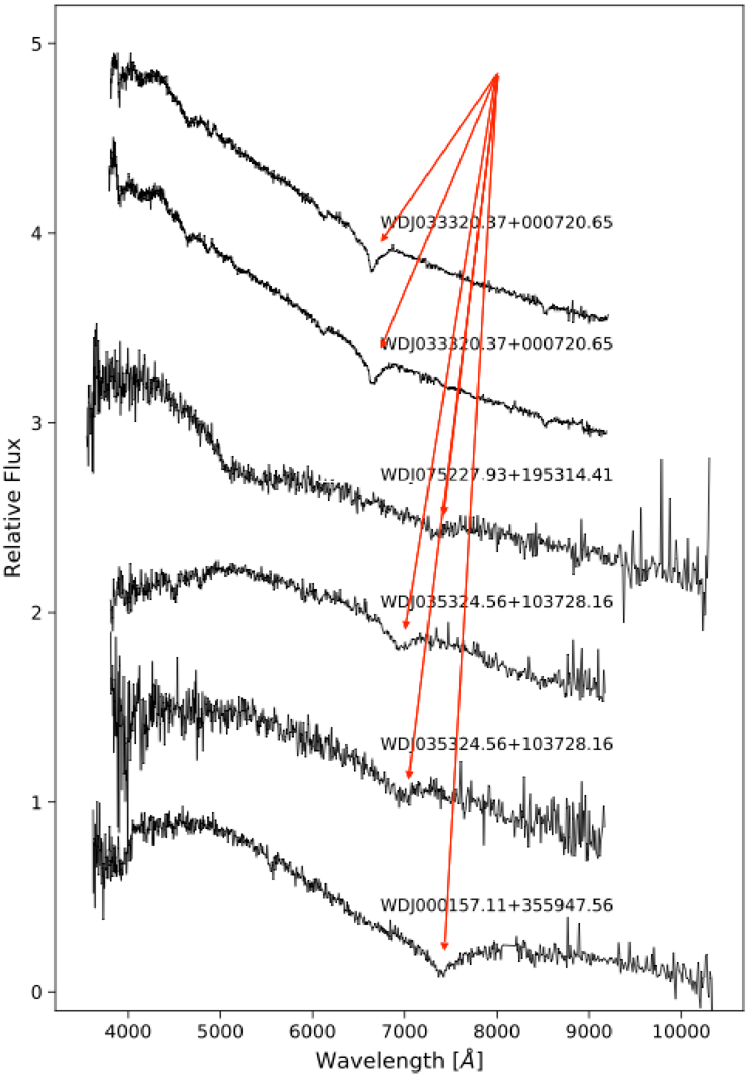

Figure 5.21: Observable white dwarf spectra with non-assigned features.

---

[37] Obtained via personal correspondence with P. Dufour (University of Montreal).

states of the sodium atom has been undertaken using the EOM machinery in QCUMBRE. Promising candidate lines have been isolated and subjected to a composite-extrapolation scheme to obtain highly accurate results.

5.3.1 Manifold of doublet states

Based on EOM-EA-CCSD/aCQ calculations using the closed-shell sodium cation ([Ne]) as a reference to ensure spin-purity, the total energies for many of the lowest doublet states of the sodium atom have been determined as a function of the magnetic field strength varying between 0-0.5 B_0. The states for which convergence could be reached for (almost) the complete considered range are compiled in Fig. 5.22a. The color code is the same for all states that are degenerate in the field-free case. Within the field, the state with the lowest M_L is the lowest in energy due to the orbital-Zeeman contribution. It may be noted that already for a supposedly simple system like the sodium atom the energetic landscape exhibits complexities. In a magnetic field, the point-group symmetry is lowered from SO_3 to $C_{\infty h}$. As a consequence, ${}^2L$ and ${}^2(L+2)$ states with the same M_L are then of the same symmetry. Therefore, they are no longer allowed to cross. This can be observed for $B \approx 0.05\ \mathrm{B}_0$ between the $2^2\mathrm{S}_g/2^2\Sigma_g$ (occupied 4s orbital, orange) and the $1^2\mathrm{D}_g/3^2\Sigma_g$ states (occupied $3\mathrm{d}_0$ orbital, second dark-green counting downward). This feature is also observed for states with occupied 4d orbitals (dark-blue). Obeying the selection rules for electronic transitions, Fig. 5.22b contains the $B-\lambda$ diagram showing all excitation energies for dipole-allowed transitions between the given doublet states in a range from $0 \leq \Delta E_{\mathrm{exc}} \leq 15000$ Å. For the subsequent study, promising transitions are to be selected. It should be noted that only such

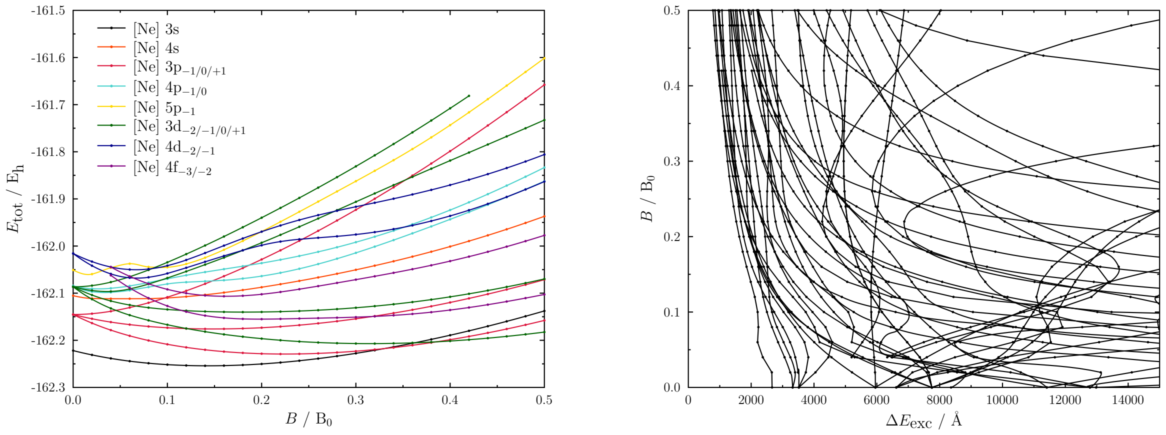

(a) E_{tot}

(b) ΔE_{exc}

Figure 5.22: (a) Total energies for as well as (b) electronic excitation energies between low-lying doublet states of the sodium atom.

transitions that exhibit a stationarity in the $B - \lambda$ plot are visible. As magnetic fields on white dwarfs are not static, transitions that change strongly with the magnetic field strength are smeared out. [14] Additionally, in the present investigation, the selection is limited to transitions involving the third shell ($n = 3$) as the quality of the basis set deteriorates for higher shell orbitals[38] since diffuse orbitals become more deformed with increasing magnetic field strength. Fig. 5.23a shows the $B - \lambda$ diagram for the selected transitions again indicating the interesting range of ΔE_{exc} by red dotted lines. Most promising with respect to stationarity are the transitions 3s ↔ $3p_0$ (orange), $3p_{\pm1}$ ↔ $3d_{\pm1}$ (bright-green), and $3p_0$ ↔ $3d_0$ (blue). The other 3s ↔ 3p and 3p ↔ 3d transitions are included for consistency. In Fig. 5.23b, the corresponding oscillator strengths are plotted as a function of the magnetic field strength. While the 3s ↔ $3p_0$ (orange) and $3p_{\pm1}$ ↔ $3d_{\pm1}$ (bright-green) transitions are supposed to be well-observable for all field strengths, the oscillator strength for the $3p_0$ ↔ $3d_0$ (blue) transition drops rapidly but the range where it is still comparably large ($B < 0.025$ B$_0$) overlaps entirely with the range where the slope is rather steep. It may be noted that the rapid decrease is a result of the before mentioned avoided crossing of the $1^2\text{D}_g/3^2\Sigma_g$ state (occupied $3d_0$ orbital). Therefore, the oscillator strengths of all 3p ↔ $3d_0$ transitions exhibit drastic changes for small field strengths.

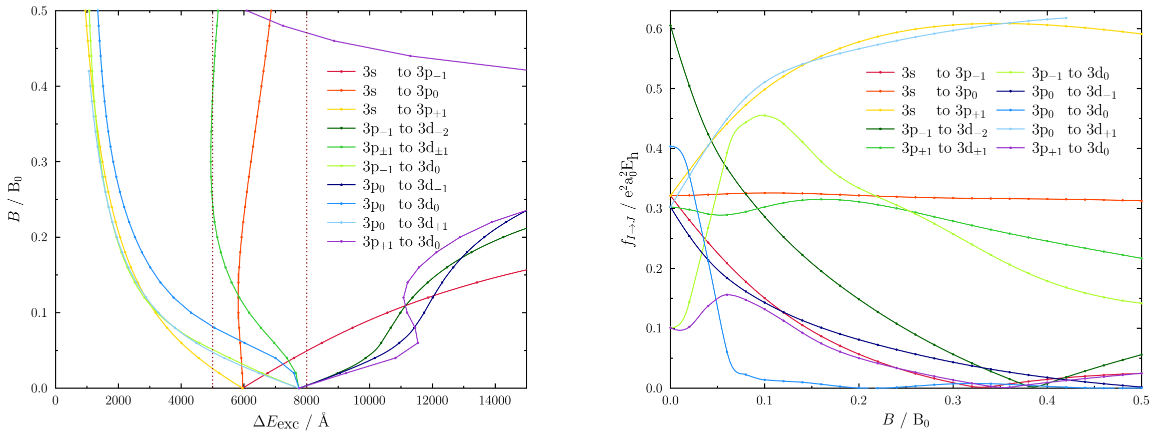

(a) ΔE_{exc}

(b) $f_{I \to J}$

Figure 5.23: (a) Excitation energies and (b) oscillator strengths for selected electronic transitions between low-lying doublet states of the sodium atom in a magnetic field between 0-0.5 B$_0$ that might cause the features in the observed spectra. The area for which the bands from the observable spectra occur are marked by dashed red lines.

---

[38] The only transitions with $n > 3$ that exhibit a stationarity point within the given range of field strengths are 4s ↔ $5p_{-1}$, $4p_{-1}$ ↔ $4d_{-2}$, and $4p_0$ ↔ $4d_{-1}$

5.3.2 A composite-extrapolation scheme for a thorough investigation of selected excitations

The accuracy of EOM-CCSD methods for excitation energies is usually estimated to be 0.1-0.3 eV for a well-behaved reference wave function. [37,43]. This means that for an excitation energy of, say, $\Delta E_{\mathrm{exc}} = 7000$ Å ≈ 1.771 eV with an error of $\Delta\Delta E_{\mathrm{exc}} = 0.1$ eV the error in angstrom is

$$\Delta\Delta E_{\mathrm{exc}} = \pm\sqrt{\left(-\frac{1\ \mathrm{eV}}{1.771^2\ \mathrm{eV}^2} \cdot 12398\ \text{Å} \cdot 0.1\ \mathrm{eV}\right)^2} \approx \pm 395\ \text{Å}. \tag{5.9}$$

However, accuracies of 10-50 Å are required for sound assignments. Therefore, highly accurate methods, large basis sets, as well as extrapolation techniques have to be used. The EOM-EA-CCSD results that have been obtained before are a good starting point for the investigation because spin-purity of the wave function is ensured. However, since EOM-EA-CCSDT is not yet available, currently, the only feasible option to go beyond EOM-CCSD is EOM-EE-CCSDT. For the time being, calculations using large basis sets at this level of theory are computationally too demanding. Therefore, a stepwise procedure is undertaken based on the EOM-EA energies which are refined by corrections that are calculated within the EOM-EE framework.

The excitation energies obtained at the EOM-EA-CCSD/aCQ level of theory are corrected individually for each state by a basis set extrapolation term $\Delta E_{\mathrm{basis}}$ and a correction accounting for triple excitations $\Delta E_{\mathrm{triples}}$. Additionally, a systematic correction $\Delta E_{\mathrm{offset}}$ is added in order to consider deviations from highly accurate experimental [144] field-free excitation energies:

$$\Delta E_{\mathrm{exc}}^{\mathrm{corrected}} = \Delta E_{\text{EOM-EA,exc}}^{\mathrm{QZ}} + \Delta E_{\mathrm{basis}} + \Delta E_{\mathrm{triples}} + \Delta E_{\mathrm{offset}}. \tag{5.10}$$

First, EOM-EE-CCSD and EOM-EA-CCSD results for total and excitation energies are compared to each other at the aCQ level of theory to define a confidence accuracy for the EOM-EA energies. Fig. 5.24 shows the differences between these two methods in total energies, excitation energies and transition moments between the two EOM variants. The deviations in total energies are largest for states with occupied 3p orbitals with up to 200 $\mu\mathrm{E_h}$ while the differences in excitation energies are similar albeit of opposite sign for the two different types of transitions (3s ↔ 3p and 3p ↔ 3d) ranging between 50-150 $\mu\mathrm{E_h}$. Therefore, all subsequent corrections larger than these energy differences will be included in the predictions. For the sake of completeness, the STMs have been compared as well yielding differences between the methods of less than 0.01 $\mathrm{e^2 a_0^2}$ which is at least two orders of magnitude smaller than the average oscillator strength that

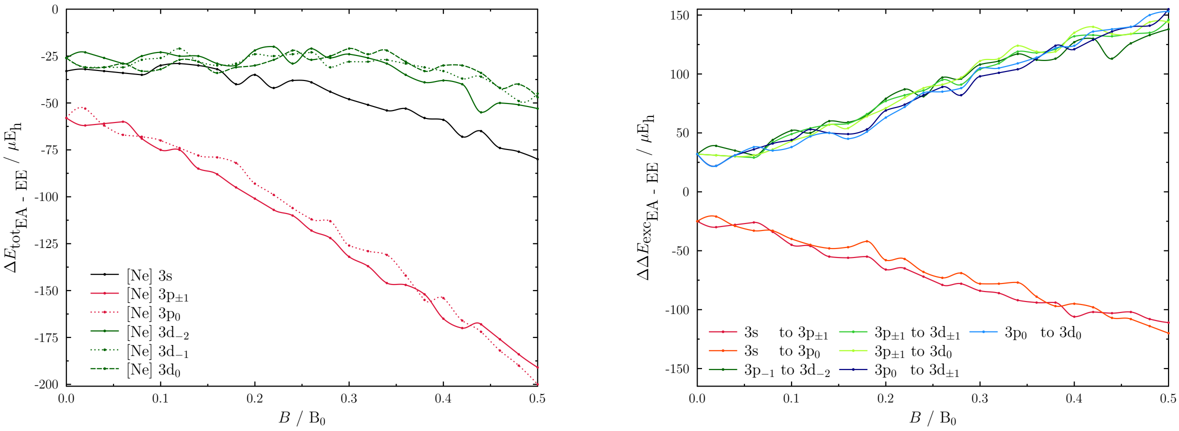

(a) ΔE_{tot} (b) $\Delta\Delta E_{\text{exc}}$

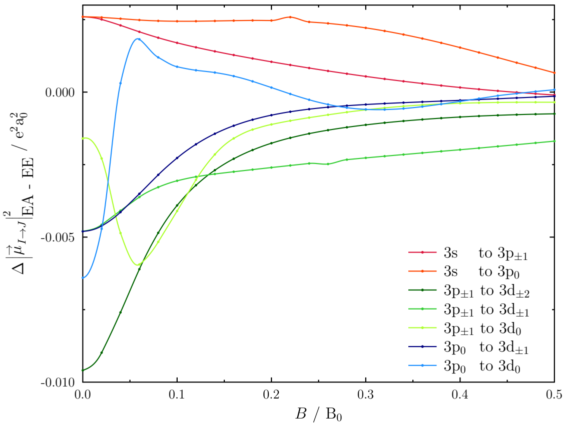

(c) $\Delta|\boldsymbol{\mu}_{I\to J}|^2$

Figure 5.24: Differences in the (a) total energies of low-lying doublet states of the sodium atom as well as (b) excitation energies and (c) STMs between them calculated at the EOM-EE-/ and EOM-EA-CCSD/aCQ levels of theory, respectively.

has been determined for the transitions of interest. Hence, no corrections will be made regarding the STMs.

Next, the basis set convergence is examined in order to determine the basis set error ΔE_{basis}. EOM-EE-CCSD/aCX (X=D,T,Q) results are compared between vicinal cardinal numbers as well as with the basis set limit. The basis set limit has been determined in the following way: Two-point fits of the excitation energies via

$$\Delta E_{\text{exc}}^{\infty} = \frac{\Delta E_{\text{exc}}^{\text{X}}\text{X}^3 - \Delta E_{\text{exc}}^{Y}\text{Y}^3}{\text{X}^3 - \text{Y}^3} \tag{5.11}$$

have been carried out as introduced in Ref. [145] and adapted to EOM-CC in Ref. [146]. The results for X=T and Y=Q have been used, thus, leaving out the energies for X=D as suggested in Ref. [145]. Several assumptions are implicitly made by proceeding in this manner. First, extrapolating excitation energies is equal to extrapolating the total energies of the respective states individually. Eq. (5.11), however, is defined for the extrapolation of correlation energies as they show significantly slower convergence with the size of the basis set than the HF energy. [107] Thereby, the HF energy is presumed to have converged already for the triple zeta basis defining the energy difference between the results for X=T and X=Q as a sole difference in the description of correlation effects. Second, energies obtained by EOM methods cannot be split in a HF fraction and a correlation contribution. Hence, the assumption is made that Eq. (5.11) holds for the total EOM energy subtracted by the HF energy. Fig. 5.25a shows the total energy differences between energies obtained by using the different basis sets. Switching from double- to triple-zeta yields deviations ranging from 50-150 $\mathrm{mE_h}$ and an oscillatory behavior for the $1^2D_g/3^2\Sigma_g$ state (occupied $3\mathrm{d}_0$ orbital, light-green). This clearly disqualifies the double-zeta basis set as reliable and justifies its exclusion from the extrapolation data set. Going from T to Q gives a nearly constant improvement in the quality of all energies of about 30 $\mathrm{mE_h}$ up to a field strength of $B \approx 0.2\ \mathrm{B_0}$ before all states with an occupied 3d orbital exhibit differences of more than 50 and up to 80 $\mathrm{mE_h}$. A similar trend is observed for the comparison of the Q results and the basis set limit. The deviations still amount to 21-25 $\mathrm{mE_h}$ for $B < 0.25\ \mathrm{B_0}$ and up to 60 $\mathrm{mE_h}$ for higher field strengths for states with an occupied 3d orbital. For the excitation energies given in Fig. 5.25b, less severe deviations are observed. In fact, the improvements for going from T to Q are of similar magnitude as the difference between the results for Q and the basis set limit. Both amount to less than 10 $\mathrm{mE_h}$ for $B < 0.25\ \mathrm{B_0}$ and do not exceed 30 $\mathrm{mE_h}$ for higher

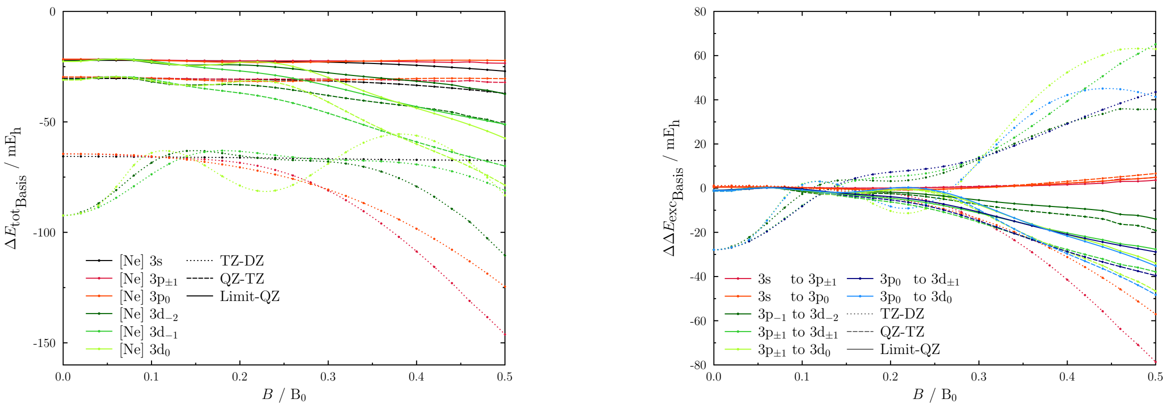

(a) $\Delta E_{\mathrm{tot,\ basis}}$ (EOM-CCSD)

(b) $\Delta\Delta E_{\mathrm{exc,\ basis}}$ (EOM-CCSD)

Figure 5.25: Differences in (a) total as well as (b) excitation energies for low-lying doublet states of the sodium atom calculated at the EOM-EE-CCSD/aCX (X=D,T,Q) levels of theory.

field strengths for the states with an occupied 3d orbital. The basis set correction is, therefore, calculated as

$$\Delta E_{\text{basis}} = \Delta E^{\infty}_{\text{EE,exc}} - \Delta E^{\text{QZ}}_{\text{EE,exc}}.$$

In the next step, $\Delta E_{\text{triples}}$ is determined to account for triple excitations within $\hat{\mathcal{R}}$ and $\hat{T}$. Corresponding calculations at the EOM-EE-CCSDT/aCX levels of theory have been performed with X limited to D and T due to the high demand on computational resources. This also prevents the calculation of a meaningful basis set limit for EOM-EE-CCSDT as the double-zeta basis set should not be included in such an extrapolation. Furthermore, the range of B has been confined to 0-0.4 B_0. Additionally, the number of considered states has been reduced leaving out the $1^2D_g/3^2\Sigma_g$ state. Figs. 5.26a-5.26b show the same behavior for total and excitation energies calculated at the EOM-EE-CCSDT level of theory as has been observed for EOM-EE-CCSD in Figs. 5.25a-5.25b. This allows for an adequate correction on top of the basis set correction. The nearly constant shift in energy by including triple excitations becomes more evident when consulting Fig. 5.27a where the total energies obtained for EOM-CCSD and EOM-CCSDT are directly compared for a given basis set. The energy differences are nearly constant with increasing field strength and amount to 1.5-2.0 mE_h for the double-zeta and 3.3-3.8 mE_h for the triple-zeta basis set. As shown in Fig. 5.27b, the effect on the excitation energies is one order of magnitude smaller and amounts to 33-173 μE_h for 3s ↔ 3p transitions and 85-195 μE_h for 3p ↔ 3s transitions for the triple-zeta basis set. The difference at the aCT level of theory is, hence, used to approximate the triples correction

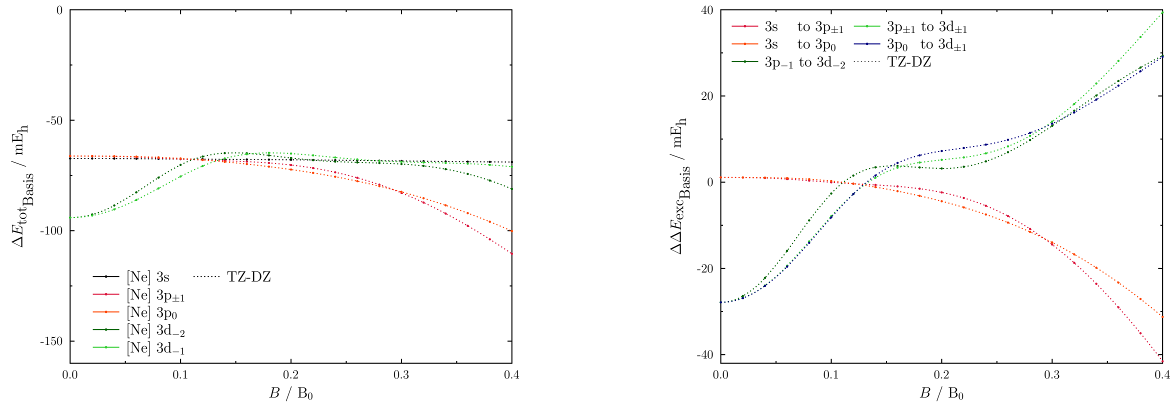

(a) $\Delta E_{\text{tot, basis}}$ (EOM-CCSDT)

(b) $\Delta\Delta E_{\text{exc, basis}}$ (EOM-CCSDT)

Figure 5.26: Differences in (a) total as well as (b) excitation energies for low-lying doublet states of the sodium atom calculated at the EOM-EE-CCSDT/aCX (X=D,T) levels of theory.

$$\Delta E_{\text{triples}} = \Delta E^{\text{TZ}}_{\text{CCSDT,exc}} - \Delta E^{\text{TZ}}_{\text{CCSD,exc}}.$$

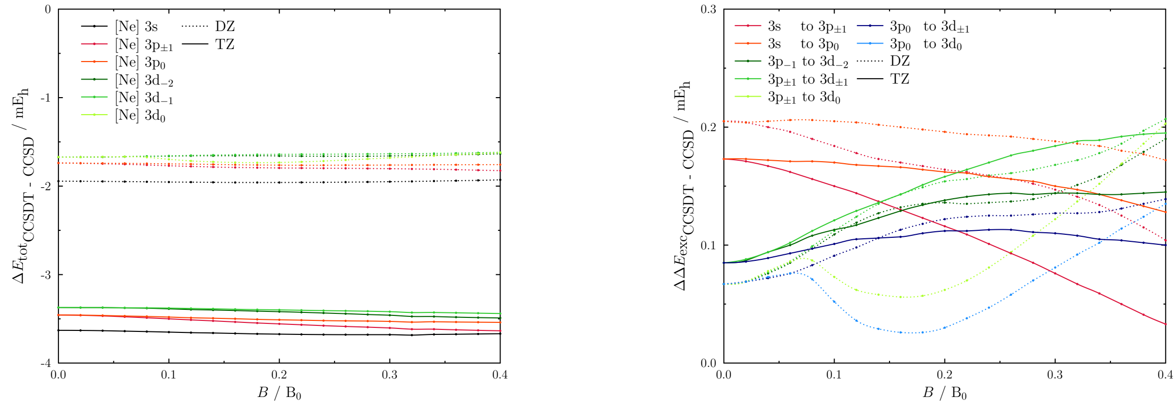

(a) $\Delta E_{\text{tot, method}}$

(b) $\Delta\Delta E_{\text{exc, method}}$

Figure 5.27: Differences in (a) total as well as (b) excitation energies for low-lying doublet states of the sodium atom calculated at the EOM-EE-CCSD/ and -CCSDT/aCX (X=D,T) levels of theory.

Admittedly, the $1^2D_g/3^2\Sigma_g$ state (occupied $3d_0$ orbital) has not been calculated at the EOM-EE-CCSDT level of theory. However, the EOM-CCSD calculations suggest that excitation energies that involve the $3d_0$ or the $3d_{\pm1}$ orbital, respectively, behave in a similar manner as a function of the magnetic field strength (see Fig. 5.25b). Therefore, the correction for the states with an occupied $3d_{\pm1}$ orbital has also been used for the state with an occupied $3d_0$ orbital. Note that the basis set correction ΔE_{basis} is two orders of magnitude larger than the correction for triple excitations $\Delta E_{\text{triples}}$.

In a last step, ΔE_{offset} is determined by comparing the field-free excitation energies to highly accurate experimental values. [144] The latter have been averaged in order to remove the effect from spin-orbit coupling which is not considered in this work.[39] The numbers are shown in Tab. 5.5. For transitions involving states with occupied 3s or 3p orbitals, the theoretical predictions are in excellent agreement with the experimental values exhibiting a deviation of less than 10 Å. For the 3p ↔ 3d transitions, however, the error is larger by a factor of 30 hinting at an insufficient modeling of states with an occupied 3d orbital even for the field-free case. Additionally, for smaller excitation energies and, hence, larger transition wavelengths, the error increases (see Eq. (5.9)). Treating both deviations as systematic errors of the method, all excitation energies are shifted by the deviation from the experimental zero-field values leading to the corrected $B - \lambda$ diagram shown in Fig. 5.28. The positions where the observed transitions from Fig. 5.21 occur are indicated by dashed red lines. For the 3s ↔ 3p transitions, only the 3s ↔ $3p_0$ transition shows stationarity. However, the calculated transition is by

---

[39] The effect of spin-orbit coupling is negligible in the presence of a strong magnetic field compared to the individual coupling of these quantities with the magnetic field itself.

Table 5.5: Experimental excitation energies for the sodium atom including spin-orbit coupling[a] $\Delta E_{\text{exc}}^{\text{exp}}$ and their averaged values neglecting spin-orbit coupling $\Delta E_{\text{exc}}^{\text{exp, no SO}}$ compared to the corresponding field-free excitation energies[b] $\Delta E_{\text{exc}}^{\text{EOM}}$ from the composite-extrapolation approach as well as the corresponding deviation ΔE_{offset}.

Transition	$\Delta E_{\text{exc}}^{\text{exp}}$ / Å	J	$\Delta E_{\text{exc}}^{\text{exp, no SO}}$ / Å	$\Delta E_{\text{exc}}^{\text{EOM}}$ / Å	ΔE_{offset} / Å
$3s \rightarrow 3p$	5889.95 5895.92	$^3/_2$ $^1/_2$	5892.94	5902.6	-9.7
$3p \rightarrow 3d$	8183.26 8194.79 8194.82	$^1/_2 \rightarrow {}^3/_2$ $^3/_2 \rightarrow {}^3/_2$ $^3/_2 \rightarrow {}^5/_2$	8189.04	7871.8	317.2

[a] See Ref. [144].

[b] $\Delta E_{\text{exc}}^{\text{EOM}} = \Delta E_{\text{EOM-EA,exc}}^{\text{QZ}} + \Delta E_{\text{basis}} + \Delta E_{\text{triples}}$.

400-1000 Å outside the range of the observed features. Since the remaining error is estimated to be well below 100 Å, this transition can be excluded. Additionally, the feature of the 3s ↔ 3p transition is nearly stationary for the whole range of magnetic field strengths considered here. Hence, it should be visible in the observed spectra at around 6000 Å if sodium was present. For the 3p ↔ 3d transitions, however, the error could indeed be large enough to shift the transition into the window of interest. Nevertheless, with the steep slope only present for field strengths of $B \lessapprox 0.025$ B_0, the $3\mathrm{p}_0 \leftrightarrow 3\mathrm{d}_0$ and $3\mathrm{p}_{\pm1} \leftrightarrow 3\mathrm{d}_{\pm1}$ transitions are also likely not the source for the observed features.

With these results at hand, sodium is most likely not the source for the features in the spectra in Fig. 5.21. However, as the EOM toolbox within QCUMBRE for the first time allows to tackle astrophysical questions like the one discussed, other candidate species such as Ca^+ may be investigated using the presented composite-extrapolation scheme.

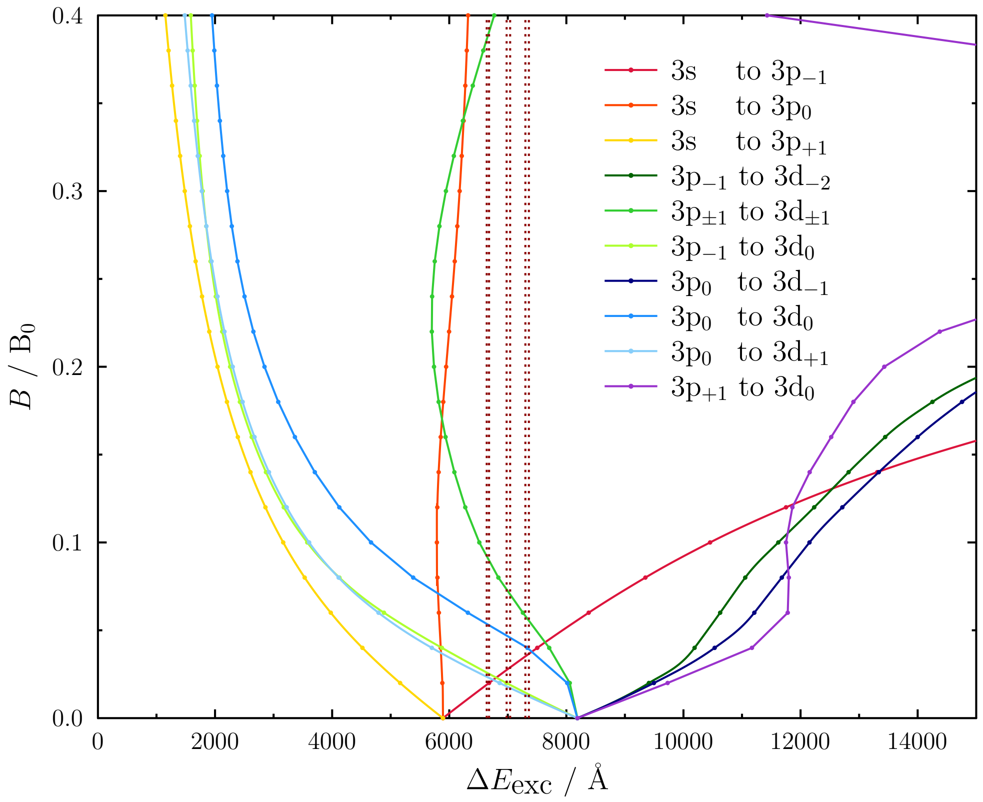

Figure 5.28: Excitation energies for selected electronic transitions between low-lying doublet states of the sodium atom in a magnetic field between 0-0.5 B$_0$ extrapolated toward the complete basis set limit and corrected by an approximate triples contribution as well as the error compared to experimental field-free values. The bands' peaks in the observational spectra are marked by dashed red lines.

6 Conclusion and outlook

In this thesis, a toolbox of methods for the accurate determination of the electronic structure of atoms and molecules in strong magnetic fields has been introduced. To this end, the quantum-chemical program package QCUMBRE has been developed. It comprises the first complex-valued EOM-CC implementation allowing for highly accurate calculations to investigate ground and especially excited states of systems in finite magnetic fields. Besides a complex-valued CCSD, CCSD(T), and CCSDT implementation, QCUMBRE features the EOM-EE, -SF, -IP, and -EA variants at the CCSD level and can provide one-electron properties for each method. Additionally, a CCSD-LR implementation for one-electron properties has been implemented. Furthermore, excitation energies are also available at the EOM-EE-CCSDT level. The program package provides a data-type infrastructure that is easily adjustable and features a 'black-box' contraction routine allowing for the efficient evaluation of working equations and the simple implementation of new code. Therefore, new features and general performance upgrades may be added in the future. For example, the applicability can be extended to larger systems by introducing memory saving options such as I/O to and from the hard disk and by the exploitation of symmetry. For both options, the existing data-type infrastructure allows for changes on the lowest level that will not affect existing code.

Assessment of EOM methods applied in the context of strong magnetic fields

EOM-CC methods have been rendered a suitable and accurate tool to study excited states in strong magnetic fields of up to at least $B = 1\ \mathrm{B}_0$. The implemented EOM methods enable investigations of (even complicated) excited states of interest in strong magnetic fields. The obtained accuracy for respective truncations of $\hat{T}$ and $\hat{\mathcal{R}}$ are comparable to the field-free case. Additionally, the influence of the lack of size-intensivity for EOM properties on single small molecules has been quantified and found to be negligible.

Change of the electronic landscape in strong magnetic fields

The change in the energetical landscape induced by a magnetic field in general and by its symmetry-lowering effect in particular has been investigated for both atoms and molecules. The less symmetry a system exhibits the larger the number of avoided crossings that can be observed. For this reason, absorption spectra in strong magnetic fields can, hence, by no means be inferred from their field-free analogs. The application of EOM methods allows to study in detail how high-lying electronic states may influence the electronic ground state of systems subdue to magnetic fields through a cascade of avoided crossings. In this context, the paramagnetism in the closed-shell methylidinium cation (CH^+) has been analyzed. Here, four electronic states have been found to be involved in the paramagnetic stabilization of the ground state. Due to the same mechanism, perpendicular paramagnetic bonding can be observed in noble gas dimers whose singlet ground states become more strongly bound in a perpendicular magnetic field. The involved orbitals have been identified and it has been observed that the paramagnetic stabilization even counteracts a decrease in the Van der Waals interaction. *Ab-initio* data generated with QCUMBRE has been used in Monte Carlo simulations within a collaboration with E. Pahl and coworkers to show that the paramagnetic stabilization leads to an increase of the melting temperature of neon in a strong magnetic field.

Access to correlated transition dipole moments

In order to be able to predict the intensity of bands in observable spectra, the squared transition dipole moments for selected excitations in several molecules have been calculated. Their general evolution with the magnetic field strength coincides with the expected field-induced change in the overlap between the involved orbitals. However, severe changes in slope and curvature are observed in the region of all field strengths for which one of the involved states undergoes an avoided crossing. Therefore, theoretical predictions are essential to even qualitatively predict whether a transition is visible for a given range of magnetic field strengths.

The influence of strong magnetic fields on ionization and electron-attachment processes

Applying the low-scaling EOM-IP and -EA methods, the *IE*s and *EA*s for the first and second row elements have been analyzed as functions of the magnetic field strength. For small field strengths, their evolution has been found to be dominated by the diamagnetic term of the Landau energy of the free electron. Many ionizations do not occur for the HOMO and electron attachment rarely is to be expected for the LUMO. In general, *IE*s increase while *EA*s decrease for field strengths in the range of $B \leq 0.25\ \mathrm{B}_0$.

Astrophysical application: Prediction of spectra

An extensive study on the manifold of doublet states of the sodium atom and dipole allowed electronic transitions between them has been undertaken in order to assign features of observed spectra of potentially magnetic white dwarfs. The implemented EOM-CC methods allowed for setting up a composite-extrapolation scheme for the accurate determination of excitation energies of selected transitions. The results have been compared to unassigned bands appearing in the observational spectra of several white dwarfs. Results suggest that contrary to the initial assumption, sodium is likely not responsible for the observed features.

This thesis shows how the various EOM-CC methods provide a powerful methodological arsenal to model ground as well as excited states in strong magnetic fields. For nearly any state to be modeled, a well-behaved reference state can be combined with a suited EOM-CC method. Thereby, effects on the electronic structure of excited states in strong magnetic fields can be investigated. The accuracy of the methods can systematically be improved by going to higher excitations within the EOM-CC hierarchy. As the impact of strong magnetic fields on the electronic structure of atoms and molecules is still a growing field of research, [35,87,88,122,133,140,147–149] EOM-CC will also play an important role in providing benchmark data for other methods. [122,150] Furthermore, EOM-CC methods are the ideal choice for astrophysical applications involving strong magnetic fields that require highly accurate results such as the prediction of spectra. As has been shown in this thesis, the EOM toolbox already constitutes an excellent equipment for performing calculations for atomic absorption spectra. For molecular spectra, assignments are more involved necessitating further work concerning, for example, the orientation-dependence and the determination of equilibrium geometries for excited states. These challenges will be tackled within the ongoing advance in the research on the electronic structure of atoms and molecules in strong magnetic fields.

References

[1] Koester, D.; Chanmugam, G. *Rep. Prog. Phys.* **1990**, *53*, 837–915.

[2] Barstow, M. A.; Barstow, J. K.; Casewell, S. L.; Holberg, L. B.; Hubeny, I. *Not. R. Astron. Soc.* **2014**, *440*, 1607–1625.

[3] Kepler, S. O.; Koester, D.; Ourique, G. *Science* **2016**, *352*, 67–69.

[4] Dufour, P.; Liebert, J.; Fontaine, G.; Behara, N. *Nature* **2007**, *450*, 522–524.

[5] Dufour, P.; Jordan, S.; Blouin, S.; Tardif, F.; Groulx, J.; Kilic, M.; Gianninas, A.; Barber, S. D.; Gilligan, C. *Astron. Soc. Pac. Conf. Ser.* **2015**, *493*, 37–39.

[6] Xu, S.; Jura, M.; Koester, D.; Klein, B.; Zuckerman, B. *Astrophys. J. Lett.* **2013**, *766*, L18.

[7] Kepler, S. O.; Pelisoli, I.; Jordan, S.; Kleinman, S. J.; Koester, D.; Külebi, B.; Peçanha, V.; Castanheira, B. G.; Nitta, A.; Costa, J. E. S.; Winget, D. E.; Kanaan, A.; Fraga, L. *Mon. Not. R. Astron. Soc.* **2013**, *429*, 2934–2944.

[8] Liebert, J.; Ferrario, L.; Wickramasinghe, D. T.; Smith, P. S. *Astrophys. J.* **2015**, *804*, 93.

[9] Stopkowicz, S. *Int. J. Quantum Chem.* **2018**, *118*, e25391.

[10] Greenstein, J. L. *Astrophys. J.* **1984**, *281*, L47.

[11] Greenstein, J. L.; Henry, R. J. W.; O'Connell, R. F. *Astrophys. J.* **1985**, *289*, L25.

[12] Schmidt, G. D.; Allen, R. G.; Smith, P. S.; Liebert, J. *Astrophys. J.* **1996**, *463*, 320–325.

[13] Schmidt, G. D.; Allen, R. G.; Smith, P. S.; Liebert, J. *Astrophys. J.* **1996**, *473*, 569.

[14] Jordan, S.; Schmelcher, P.; Becken, W.; Schweizer, W. *Astron. Astrophys.* **1998**, *336*, L33.

[15] Henry, R. J. W.; O'Connell, R. F. *Astrophys. J.* **1984**, *282*, L97.

[16] Henry, R. J. W.; O'Connell, R. F. *Publ. Astron. Soc. Pac.* **1985**, *97*, 333–338.

[17] Rösner, W.; Wunner, G.; Herold, H.; Ruder, H. *J. Phys. B: At. Mol. Phys.* **1984**, *17*, 29–52.

[18] Forster, H.; Strupat, W.; Rösner, W.; Wunner, G.; Ruder, H.; Herold, H. *J. Phys. B: At. Mol. Phys.* **1984**, *17*, 1301–1319.

[19] Becken, W.; Schmelcher, P.; Diakonos, F. K. *J. Phys. B: At. Mol. Opt. Phys.* **1999**, *32*, 1557–1584.

[20] Becken, W.; Schmelcher, P. *J. Phys. B: At. Mol. Opt. Phys.* **2000**, *33*, 545–568.

[21] Becken, W.; Schmelcher, P. *Phys. Rev. A* **2001**, *63*, 053412.

[22] Ivanov, M. V.; Schmelcher, P. *J. Phys. B: At. Mol. Opt. Phys.* **2001**, *34*, 2031–2044.

[23] Ivanov, M. V.; Schmelcher, P. *Phys. Rev. A* **1999**, *60*, 3558–3568.

[24] González-Férez, R.; Schmelcher, P. *Eur. Phys. J. D* **2003**, *23*, 189–199.

[25] de Melo, L. C.; Das, T. K.; Ferreira, R. C.; Miranda, L. C. M.; Brandi, H. S. *Phys. Rev. A* **1978**, *18*, 12–14.

[26] Schmelcher, P.; Cederbaum, L. S. *Phys. Rev. A* **1988**, *37*, 672–681.

[27] Pagola, G. I.; Pelloni, S.; Caputo, M. C.; Ferraro, M. B.; Lazzeretti, P. *Phys. Rev. A* **2005**, *72*, 033401.

[28] Pagola, G. I.; Caputo, M. C.; Ferraro, M. B.; Lazzeretti, P. *J. Chem. Phys.* **2007**, *126*, 154103.

[29] Tellgren, E. I.; Helgaker, T.; Soncini, A.; Lange, K. K.; Teale, A. M.; Ekström, U. E.; Stopkowicz, S.; Austad, J. H.; Sen, S. LONDON*:* A quantum chemistry program for plane-wave/GTO hybrid basis sets and finite magnetic field calculations (see londonprogram.org for more information).

[30] Tellgren, E. I.; Soncini, A.; Helgaker, T. *J. Chem. Phys.* **2008**, *129*, 154114.

[31] Tellgren, E. I.; Reine, S. S.; Helgaker, T. *Phys. Chem. Chem. Phys.* **2012**, *14*, 9492–9499.

[32] Lange, K. K.; Tellgren, E. I.; Hoffmann, M. R.; Helgaker, T. *Science* **2012**, *337*, 327–331.

[33] Tellgren, E. I.; Teale, A. M.; Furness, J. W.; Lange, K. K.; Ekström, U.; Helgaker, T. *J. Chem. Phys.* **2014**, *140*, 034101.

[34] Reynolds, R. D.; Shiozaki, T. *Phys. Chem. Chem. Phys.* **2015**, *17*, 14280–14283.

[35] Reynolds, R. D.; Yanai, T.; Shiozaki, T. *J. Chem. Phys.* **2018**, *149*, 014106.

[36] Stopkowicz, S.; Gauss, J.; Lange, K. K.; Tellgren, E. I.; Helgaker, T. *J. Chem. Phys.* **2015**, *143*, 074110.

[37] Krylov, A. I. *Annu. Rev. Phys. Chem.* **2008**, *59*, 433–462.

[38] Geertsen, J.; Rittby, M.; Bartlett, R. J. *Chem. Phys. Lett.* **1989**, *164*, 57–62.

[39] Levchenko, S. V.; Krylov, A. I. *J. Chem. Phys.* **2004**, *120*, 175–185.

[40] Krylov, A. I. *Acc. Chem. Res.* **2006**, *39*, 83–91.

[41] Krylov, A. I. *Chem. Phys. Lett.* **2001**, *338*, 375–384.

[42] Stanton, J. F.; Gauss, J. *J. Chem. Phys.* **1994**, *101*, 8938–8944.

[43] Nooijen, M.; Bartlett, R. J. *J. Chem. Phys.* **1995**, *102*, 3629–3647.

[44] Bartlett, R. J.; Stanton, J. F. *Rev. Comput. Chem.* **1994**, *5*, 65–169.

[45] Helgaker, T.; Jørgensen, P.; Olsen, J. *Molecular Electronic-Structure Theory;* Wiley: West Sussex, 1st ed., 2000.

[46] Atkins, P.; Friedman, R. *Molecular Quantum Mechanics;* Oxford University Press: Oxford, 5th ed., 2011.

[47] Szabo, A.; Ostlund, N. S. *Modern Quantum Chemistry;* Dover Publications: Mineola, New York, 1st ed., 1996.

[48] Jackson, J. D. *Klassische Elektrodynamik;* de Gruyter: Berlin/Boston, 5th ed., 2014.

[49] Dyall, K. G.; Fægri, Jr., K. *Introduction to Relativistic Quantum Chemistry;* Oxford University Press: New York, 1st ed., 2007.

[50] Lévy-Leblond, J. M. *Commun. Math. Phys.* **1967**, *6*, 286–311.

[51] Landau, L. D.; Lifschitz, E. M. *Lehrbuch der theoretischen Physik III - Quantenmechanik;* Wissenschaftlicher Verlag Harri Deutsch: Frankfurt a. Main, 9th ed., 2012.

[52] Helgaker, T.; Jaszuński, M.; Ruud, K. *Chem. Rev.* **1999**, *99*, 293–352.

[53] London, F. *J. Phys. Radium* **1937**, *8*, 397–409.

[54] P. Pulay, J. F. Hinton, K. Wolinski *Efficient Implementation of the GIAO Method for Magnetic Properties: Theory and Application* In: J. A. Tossell J.A. (ed.) *Nuclear Magnetic Shieldings and Molecular Structure* NATO ASI Series C (Kluwer, Dordrecht, 1993), Vol 386., 243-262.

[55] Schmelcher, P.; Cederbaum, L. S. *Phys. Rev. A* **1990**, *41*, 4936–4943.

[56] Crawford, T. D.; Schaefer III, H. F. *Rev. Comput. Chem.* **2007**, *14*, 33–136.

[57] Davidson, E. R. *J. Comput. Phys.* **1975**, *17*, 87–94.

[58] Bene, J. E. D.; Ditchfield, R.; Pople, J. A. *J. Chem. Phys.* **1971**, *55*, 2236–2241.

[59] Shavitt, I.; Bartlett, R. J. *Many-Body Methods in Chemistry and Physics;* Cambridge University Press: New York, 1st ed., 2009.

[60] Čížek, J. *J. Chem. Phys.* **1966**, *45*, 4256–4266.

[61] Bartlett, R. J.; Musiał, M. *Rev. Mod. Phys.* **2007**, *79*, 291–352.

[62] Taylor, P. R.; Bacskay, G. B.; Hush, N. S.; Hurley, A. C. *Chem. Phys. Lett.* **1976**, *41*, 444–449.

[63] Bartlett, R. J.; Purvis, G. D. *Int. J. Quantum Chem.* **1978**, *14*, 561–581.

[64] Purvis III., G. D.; Bartlett, R. J. *J. Chem. Phys.* **1982**, *76*, 1910–1918.

[65] Noga, J.; Bartlett, R. J. *J. Chem. Phys.* **1987**, *86*, 7041–7050.

[66] Noga, J.; Bartlett, R. J. *J. Chem. Phys.* **1988**, *89*, 3401.

[67] Scuseria, G. E.; Schaefer III, H. F. *Chem. Phys. Lett.* **1988**, *152*, 382–386.

[68] Raghavachari, K.; Trucks, G. W.; Pople, J. A.; Head-Gordon, M. *Chem. Phys. Lett.* **1989**, *157*, 479–483.

[69] Bak, K. L.; Jørgensen, P.; Olsen, J.; Helgaker, T.; Gauss, J. *Chem. Phys. Lett.* **2000**, *317*, 116–122.

[70] Brandow, B. H. *Rev. Mod. Phys.* **1967**, *39*, 771–828.

[71] Kállay, M.; Gauss, J. *J. Chem. Phys.* **2004**, *121*, 9257–9269.

[72] Rowe, D. J. *Rev. Mod. Phys.* **1968**, *40*, 153–166.

[73] Bartlett, R. J. *Wiley Interdiscip. Rev.: Comput. Mol. Sci.* **2012**, *2*, 126–138.

[74] Sneskov, K.; Christiansen, O. *Wiley Interdiscip. Rev.: Comput. Mol. Sci.* **2012**, *2*, 566–584.

[75] Caricato, M.; Trucks, G. W.; Frisch, M. J. *J. Chem. Theory Comput.* **2010**, *6*, 1966–1970.

[76] Stanton, J. F.; Bartlett, R. J. *J. Chem. Phys.* **1993**, *98*, 7029–7039.

[77] Koch, H.; Aa. Jensen, H. J.; Jørgensen, P.; Helgaker, T. *J. Chem. Phys.* **1990**, *93*, 3345–3350.

[78] Slipchenko, L. V.; Krylov, A. I. *J. Chem. Phys.* **2005**, *123*, 084107.

[79] Gauss, J. New Developments in Coupled-Cluster Theory Workshop, Telluride, USA, 2015.

[80] Gauss, J.; Krylov, A. I. *in preparation* **2019**.

[81] A Whirlwind Introduction to Coupled Cluster Response Theory, T. D. Crawford, Virginia Tech, Blacksburg, Private Notes.

[82] Koch, H.; Kobayashi, R.; de Merás, A. S.; Jørgensen, P. *J. Chem. Phys.* **1994**, *100*, 4393–4400.

[83] Hättig, C.; Christiansen, O.; Jørgensen, P. *J. Chem. Phys.* **1998**, *108*, 8331–8354.

[84] Stroustrup, B. *The C++ Programming Language;* Addison-Wesley: Boston, special ed., 2000.

[85] Hampe, F.; Stopkowicz, S. *J. Chem. Phys.* **2017**, *146*, 154105.

[86] Hampe, F.; Stopkowicz, S. *J. Chem. Theory Comput.* **2019**, *15*, 4036–4043.

[87] Hampe, F.; Stopkowicz, S. *in preparation* **2019**.

[88] Hampe, F.; Gross, N.; Stopkowicz, S. *in preparation* **2019**.

[89] Gross, N. (2018). *Dreifachanregungen in der Coupled-Cluster- und Equation-of-Motion Coupled-Cluster-Theorie für Atome und Moleküle in starken Magnetfeldern* (Unpublished Master's thesis). Johannes Gutenberg-Universität Mainz, Mainz, Germany.

[90] Hirata, S. *J. Phys. Chem. A* **2003**, *107*, 9887–9897.

[91] Datta, D.; Gauss, J. *J. Chem. Theory Comput.* **2013**, *9*, 2639–2653.

[92] Epifanovsky, E.; Wormit, M.; Kuś, T.; Landau, A.; Zuev, D.; Khistyaev, K.; Manohar, P.; Kaliman, I.; Dreuw, A.; Krylov, A. I. *J. Comput. Chem.* **2013**, *34*, 2293–2309.

[93] Dongarra, J. J.; Croz, J. D.; Hammarling, S.; Duff, I. S. *ACM Trans. Math. Softw.* **1990**, *16*, 1–17.

[94] Intel® Math Kernel Library Developer Reference, *https://software.intel.com/sites/default/files/mkl-2019-developer-reference-c_1.pdf*, Last checked: Apr 15th, 2019.

[95] Pulay, P. *Chem. Phys. Lett.* **1980**, *73*, 393–398.

[96] Anderson, E.; Bai, Z.; Bischof, C.; Blackford, S.; Demmel, J.; Dongarra, J.; Du Croz, J.; Greenbaum, A.; Hammarling, S.; McKenney, A.; Sorensen, D. *LAPACK Users' Guide;* Society for Industrial and Applied Mathematics: Philadelphia, PA, 3rd ed., 1999.

[97] Purvis III., G. D.; Bartlett, R. J. *J. Chem. Phys.* **1981**, *75*, 1284–1292.

[98] Cfour, Coupled-Cluster techniques for Computational Chemistry, a quantum-chemical program package. Stanton, J. F.; Gauss, J.; Cheng, L.; Harding, M. E.; Matthews, D. A.; Szalay, P. G. With contributions from A.A. Auer, R.J. Bartlett, U. Benedikt, C. Berger, D.E. Bernholdt, Y.J. Bomble, O. Christiansen, F. Engel, R. Faber, M. Heckert, O. Heun, M. Hilgenberg, C. Huber, T.-C. Jagau, D. Jonsson, J. Jusélius, T. Kirsch, K. Klein, W.J. Lauderdale, F. Lipparini, T. Metzroth, L.A. Mück, D.P. O'Neill, D.R. Price, E. Prochnow, C. Puzzarini, K. Ruud, F. Schiffmann, W. Schwalbach, C. Simmons, S. Stopkowicz, A. Tajti, J. Vázquez, F. Wang, J.D. Watts and the integral packages MOLECULE (J. Almlöf and P.R. Taylor), PROPS (P.R. Taylor), ABACUS (T. Helgaker, H.J. Aa. Jensen, P. Jørgensen, and J. Olsen), and ECP routines by A. V. Mitin and C. van Wüllen. For the current version, see http://www.cfour.de.

[99] Dunning, T. H. *J. Chem. Phys.* **1989**, *90*, 1007–1023.

[100] Kendall, R. A.; Dunning, T. H.; Harrison, R. J. *J. Chem. Phys.* **1992**, *96*, 6796–6806.

[101] Woon, D. E.; Dunning, T. H. *J. Chem. Phys.* **1995**, *103*, 4572–4585.

[102] Gross, N. (2016). *Quantenchemische Untersuchung der elektronischen Zustände des Kohlenstoffatoms in starken Magnetfeldern* (Unpublished Bachelor's thesis). Johannes Gutenberg-Universität Mainz, Mainz, Germany.

[103] Wickramasinghe, D. T.; Ferrario, L. *Publ. Astron. Soc. Pac.* **2000**, *112*, 873–924.

[104] Cao, Z.; Li, Z.; Wang, F.; Liu, W. *Phys. Chem. Chem. Phys.* **2017**, *19*, 3713–3721.

[105] Epifanovsky, E.; Klein, K.; Stopkowicz, S.; Krylov, A. I. *J. Chem. Phys.* **2015**, *143*, 064102.

[106] Rittby, M.; Bartlett, R. J. *J. Phys. Chem.* **1988**, *92*, 3033–3036.

[107] Halkier, A.; Helgaker, T.; Jørgensen, P.; Klopper, W.; Olsen, J. *Chem. Phys. Lett.* **1999**, *302*, 437–446.

[108] Prengel, M. (2016). *Quantenchemische Untersuchung der elektronischen Zustände des Sauerstoffatoms in starken Magnetfeldern* (Unpublished Bachelor's thesis). Johannes Gutenberg-Universität Mainz, Mainz, Germany.

[109] Hättig, C. *Adv. Quantum Chem.* **2005**, *50*, 37–60.

[110] Köhn, A.; Tajti, A. *J. Chem. Phys.* **2007**, *127*, 044105.

[111] Kjønstad, E. F.; Koch, H. *J. Phys. Chem. Lett.* **2017**, *8*, 4801–4807.

[112] Kjønstad, E. F.; Myhre, R. H.; Martínez, T. J.; Koch, H. *J. Chem. Phys.* **2017**, *147*, 164105.

[113] Thomas, S. (2018). *Komplexe Eigenwerte in der Equation-of-Motion Coupled-Cluster-Theorie* (Unpublished Master's thesis). Johannes Gutenberg-Universität Mainz, Mainz, Germany.

[114] Bartlett, R. J.; Kucharski, S. A.; Noga, J. *Chem. Phys. Lett.* **1988**, *155*, 133–140.

[115] Szalay, P. G.; Nooijen, M.; Bartlett, R. J. *J. Chem. Phys.* **1994**, *103*, 281–298.

[116] Watts, J. D.; Trucks, G. W.; Bartlett, R. J. *Chem. Phys. Lett.* **1989**, *157*, 359–366.

[117] Caricato, M.; Trucks, G. W.; Frisch, M. J. *J. Chem. Phys.* **2009**, *131*, 174104.

[118] Hegstrom, R. A.; Lipscomb, W. N. *Rev. Mod. Phys.* **1968**, *40*, 354–358.

[119] Schmidt, G. D.; Bergeron, P.; Bruce Fegley, J. *Astrophys. J.* **1995**, *443*, 274–280.

[120] McCook, G. P.; Sion, E. M. *Astrophys. J. Suppl. Ser.* **1999**, *121*, 1–130.

[121] Hodgkin, S. T.; Oppenheimer, B. R.; Hambly, N. C.; Jameson, R. F.; Smartt, S. J.; Steele, I. A. *Nature* **2000**, *403*, 57–59.

[122] Holzer, C.; Teale, A. M.; Hampe, F.; Stopkowicz, S.; Helgaker, T.; Klopper, W. *J. Chem. Phys.* **2019**, *150*, 214112.

[123] Detmer, T.; Schmelcher, P.; Cederbaum, L. S. *Phys. Rev. A* **1998**, *57*, 1767–1777.

[124] Rebane, T. K. *Sov. Phys. JETP* **1960**, *11*, 694.

[125] Fowler, P. W.; Steiner, E. *Mol. Phys.* **1991**, *74*, 1147–1158.

[126] Sauer, S. P. A.; Enevoldsen, T.; Oddershede, J. *J. Chem. Phys.* **1993**, *98*, 9748–9757.

[127] Ruud, K.; Helgaker, T.; Bak, K. L.; Jørgensen, P.; Olsen, J. *Chem. Phys.* **1995**, *195*, 157–169.

[128] Ishiwara, T. *Sci. Rept. Tohoku Imp. Univ.* **1914**, *3*, 303.

[129] Fowler, P. W.; Steiner, E. *J. Chem. Phys.* **1992**, *97*, 4215–4222.

[130] Fowler, P. W.; Steiner, E.; Cadioli, B.; Zanasi, R. *J. Phys. Chem. A* **1998**, *102*, 7297–7302.

[131] Monaco, G.; Scott, L. T.; Zanasi, R. *J. Phys. Chem. A* **2008**, *112*, 8136–8147.

[132] Tellgren, E. I.; Helgaker, T.; Soncini, A. *Phys. Chem. Chem. Phys.* **2009**, *11*, 5489–5498.

[133] Stopkowicz, S.; Borgoo, A.; Hampe, F.; Teale, A. M.; Klopper, W.; Gauss, J.; Helgaker, T. *in preparation* **2019**.

[134] Schmelcher, P.; Cederbaum, L. S. *Int. J. Quantum Chem.* **1997**, *64*, 501–511.

[135] Schmelcher, P. *Science* **2012**, *337*, 302–303.

[136] Blaschke, S. (2018). *Schmelzen von Edelgasen im starken Magnetfeld: Berechnung genauer Potentialhyperflächen* (Unpublished Bachelor's thesis). Johannes Gutenberg-Universität Mainz, Mainz, Germany.

[137] Binder, K. *Rep. Prog. Phys.* **1997**, *60*, 487–559.

[138] Pahl, E.; Calvo, F.; Koci, L.; Schwerdtfeger, P. *Angew. Chem.* **2008**, *47*, 8207–8210.

[139] Cybulski, S. M.; Toczyłowski, R. R. *J. Chem. Phys.* **1999**, *111*, 10520–10528.

[140] Florez, E.; Blaschke, S.; Hampe, F.; Helgaker, T.; Klopper, W.; Schwerdtfeger, P.; Teale, A. M.; Stopkowicz, S.; Pahl, E. *in preparation* **2019**.

[141] Mackay, A. L. *Acta Cryst.* **1962**, *15*, 916–918.

[142] Pawlow, P. *Z. Phys. Chem.* **1909**, *65U*, 1–35.

[143] Lide, D. R., Ed. *CRC Handbook of Chemistry and Physics;* CRC Press: Boca Raton, FL, 84th ed., 2004.

[144] Kramida, A.; Yu. Ralchenko.; Reader, J.; and NIST ASD Team. NIST Atomic Spectra Database (ver. 5.6.1), [Online]. Available: `https://physics.nist.gov/asd` [2019, June 9]. National Institute of Standards and Technology, Gaithersburg, MD., **2018**.

[145] Halkier, A.; Helgaker, T.; Jørgensen, P.; Klopper, W.; Koch, H.; Olsen, J.; Wilson, A. K. *Chem. Phys. Lett.* **1998**, *286*, 243–252.

[146] Musiał, M.; Bartlett, R. J. *Chem. Phys. Lett.* **2004**, *384*, 210–214.

[147] Reimann, S.; Borgoo, A.; Austad, J.; Tellgren, E. I.; Teale, A. M.; Helgaker, T.; Stopkowicz, S. *Mol. Phys.* **2018**, *117*, 97–109.

[148] Knecht, S. *in preparation* **2019**.

[149] Pausch, A.; Klopper, W. *in preparation* **2019**.

[150] Furness, J. W.; Verbeke, J.; Tellgren, E. I.; Stopkowicz, S.; Ekström, U.; Helgaker, T.; Teale, A. M. *J. Chem. Theory Comput.* **2015**, *11*, 4169–4181.

[151] Stanton, J. F.; Gauss, J.; Watts, J. D.; Bartlett, R. J. *J. Chem. Phys.* **1991**, *94*, 4334–4345.

[152] Gauss, J.; Stanton, J. F. *Phys. Chem. Chem. Phys.* **2000**, *2*, 2047–2060.

[153] Gauss, J.; Stanton, J. F. *J. Chem. Phys.* **2002**, *116*, 1773–1782.

[154] Pieniazek, P. A.; Arnstein, S. A.; Bradforth, S. E.; Krylov, A. I.; Sherrill, C. D. *J. Chem. Phys.* **2007**, *127*, 164110.

A Coupled-cluster amplitude equations

In the following, the singles, doubles, and triples amplitude equations for CCSD and CCSDT are presented in terms of diagrams and corresponding algebraic expressions.

$\hat{T}_1$-equations for CCSDT

$0 =$

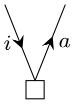

$\mathcal{F}_{ai}$

$=$

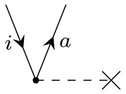

f_{ai}

$+$

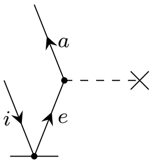

$\sum_{e} f_{ae}\; t_i^e$

$+$

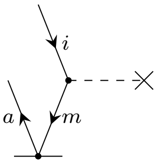

$-\sum_{m} f_{mi}\; t_m^a$

$+$

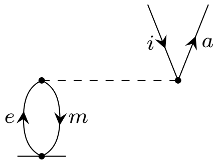

$\sum_{e}\sum_{m} \langle ma||ei\rangle\; t_m^e$

$+$

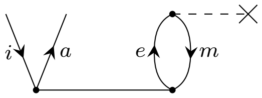

$\sum_{e}\sum_{m} f_{me}\; t_{im}^{ae}$

$+$

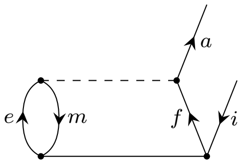

$\frac{1}{2}\sum_{e,f}\sum_{m} \langle am||fe\rangle\; t_{mi}^{ef}$

$+$

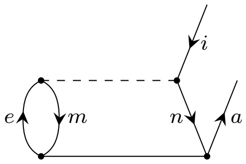

$-\frac{1}{2}\sum_{e}\sum_{m,n} \langle nm||ie\rangle\; t_{mn}^{ea}$

$+$

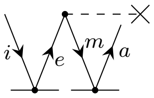

$-\sum_{e}\sum_{m} f_{me}\; t_i^e\; t_m^a$

$+$

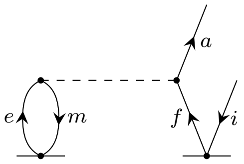

$\sum_{e,f}\sum_{m} \langle am||fe\rangle\; t_m^e\; t_i^f$

$+$

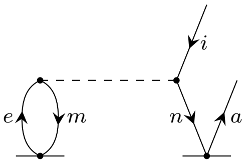

$-\sum_{e}\sum_{m,n} \langle nm||ie\rangle\; t_m^e\; t_n^a$

$+$

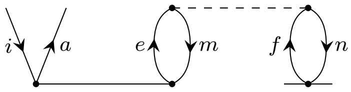

$\sum_{e,f}\sum_{m,n} \langle mn||ef\rangle\; t_{im}^{ae}\; t_n^f$

$+$

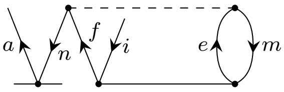

$-\frac{1}{2}\sum_{e,f}\sum_{m,n} \langle mn||ef\rangle\; t_n^a\; t_{mi}^{ef}$

$+$

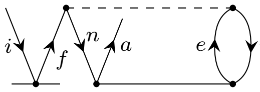

$-\frac{1}{2}\sum_{e,f}\sum_{m,n} \langle mn||ef\rangle\; t_i^f\; t_{mn}^{ea}$

$+$

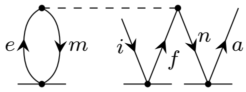

$-\sum_{e,f}\sum_{m,n} \langle mn||ef\rangle\; t_m^e\; t_i^f\; t_n^a$

$+$

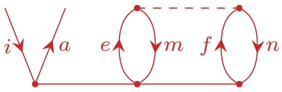

$\frac{1}{4}\sum_{e,f}\sum_{m,n} \langle mn||ef\rangle\; t_{imn}^{aef}$

$\hat{T}_2$-equations for CCSDT

$0 \quad = $

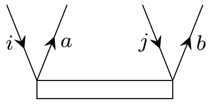

$\mathcal{W}_{abij} \quad =$

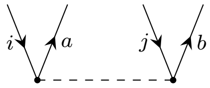

$\langle ab||ij\rangle$ $+$

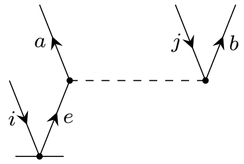

$P_-(ij)\sum_e \langle ab||ej\rangle\ t_i^e$ $+$

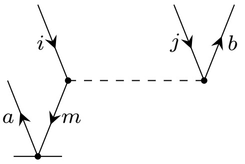

$-P_-(ab)\sum_m \langle mb||ij\rangle\ t_m^a$ $+$

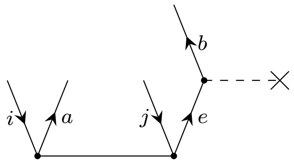

$P_-(ab)\sum_e f_{be}\ t_{ij}^{ae}$ $+$

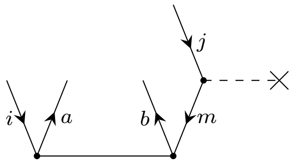

$-P_-(ij)\sum_m f_{mj}\ t_{im}^{ab}$ $+$

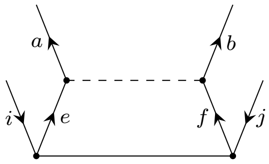

$\frac{1}{2}\sum_{e,f}\langle ab||ef\rangle\ t_{ij}^{ef}$ $+$

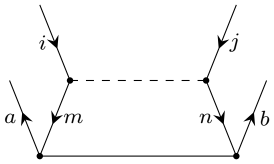

$\frac{1}{2}\sum_{m,n}\langle mn||ij\rangle\ t_{mn}^{ab}$ $+$

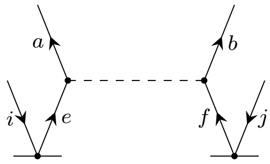

$\frac{1}{2}P_-(ij)\sum_{e,f}\langle ab||ef\rangle\ t_i^e\ t_j^f$ $+$

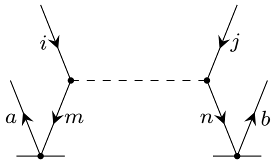

$\frac{1}{2}P_-(ab)\sum_{m,n}\langle mn||ij\rangle\ t_m^a\ t_n^b$ $+$

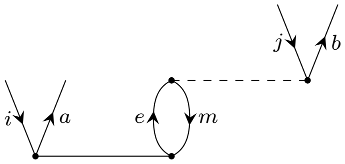

$P_-(ab)P_-(ij)\sum_e\sum_m\langle mb||ej\rangle\ t_{im}^{ae}$ $+$

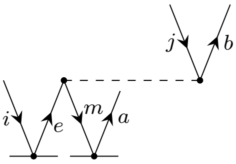

$-P_-(ab)P_-(ij)\sum_e\sum_m\langle mb||ej\rangle\ t_i^e\ t_m^a$ $+$

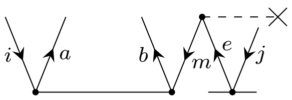

$-P_-(ij)\sum_e\sum_m f_{me}\ t_{im}^{ab}\ t_j^e$ $+$

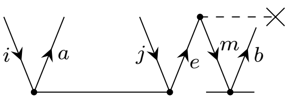

$-P_-(ab)\sum_e\sum_m f_{me}\ t_{ij}^{ae}\ t_m^b$ $+$

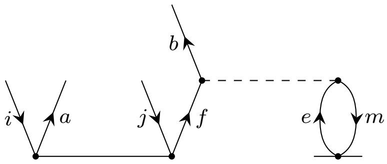

$P_-(ab)\sum_{e,f}\sum_m\langle bm||fe\rangle\ t_{ij}^{af}\ t_m^e$ $+$

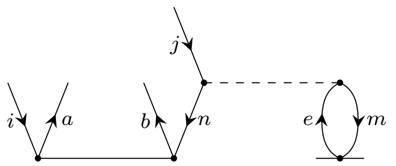

$$-P_-(ij)\sum_{e}\sum_{m,n}\langle nm||je\rangle\ t_{in}^{ab}$$

+

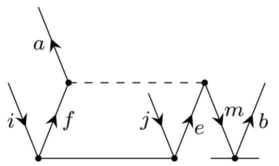

$$-\tfrac{1}{2}P_-(ab)\sum_{e,f}\sum_{m}\langle am||fe\rangle\ t_{ij}^{fe}\ t_{m}^{b}$$

+

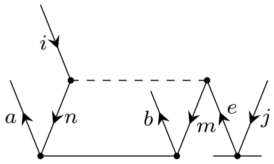

$$\tfrac{1}{2}P_-(ij)\sum_{e}\sum_{m,n}\langle nm||ie\rangle\ t_{nm}^{ab}\ t_{j}^{e}$$

+

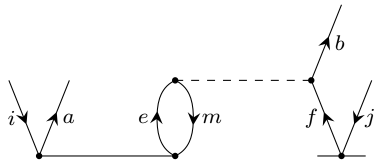

$$P_-(ab)P_-(ij)\sum_{e,f}\sum_{m}\langle bm||fe\rangle\ t_{im}^{ae}\ t_{j}^{f}$$

+

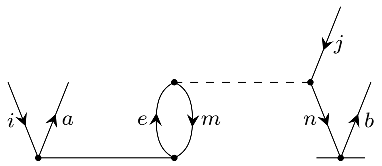

$$-P_-(ab)P_-(ij)\sum_{e}\sum_{m,n}\langle nm||je\rangle\ t_{im}^{ae}\ t_{n}^{b}$$

+

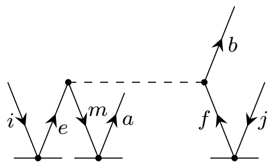

$$-\tfrac{1}{2}P_-(ab)P_-(ij)\sum_{e,f}\sum_{m}\langle bm||fe\rangle\ t_{i}^{e}\ t_{m}^{a}\ t_{j}^{f}$$

+

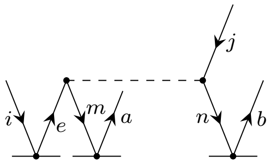

$$\tfrac{1}{2}P_-(ab)P_-(ij)\sum_{e}\sum_{m,n}\langle nm||je\rangle\ t_{i}^{e}\ t_{m}^{a}\ t_{n}^{b}$$

+

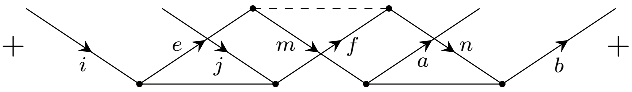

$$\tfrac{1}{4}\sum_{e,f}\sum_{m,n}\langle mn||ef\rangle\ t_{ij}^{ef}\ t_{mn}^{ab}$$

+

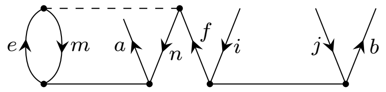

$$-\tfrac{1}{2}P_-(ab)\sum_{e,f}\sum_{m,n}\langle mn||ef\rangle\ t_{mn}^{ea}\ t_{ij}^{fb}$$

+

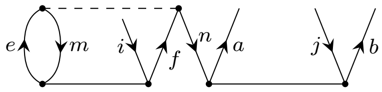

$$-\tfrac{1}{2}P_-(ij)\sum_{e,f}\sum_{m,n}\langle mn||ef\rangle\ t_{mi}^{ef}\ t_{nj}^{ab}$$

+

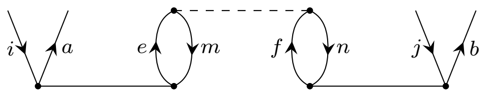

$$\tfrac{1}{2}P_-(ab)P_-(ij)\sum_{e,f}\sum_{m,n}\langle mn||ef\rangle\ t_{im}^{ae}\ t_{jn}^{bf}$$

+

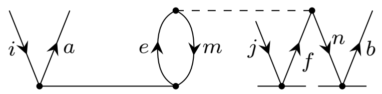

$$-P_-(ab)P_-(ij)\sum_{e,f}\sum_{m,n}\langle mn||ef\rangle\ t_{im}^{ae}\ t_{j}^{f}\ t_{n}^{b}$$

+

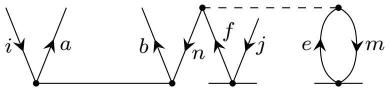

$$-P_-(ij)\sum_{e,f}\sum_{m,n}\langle mn||ef\rangle\ t_{in}^{ab}\ t_{j}^{f}\ t_{m}^{e}$$

+

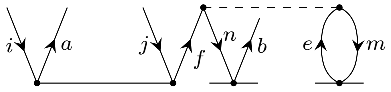

$$-P_-(ab)\sum_{e,f}\sum_{m,n}\langle mn||ef\rangle\ t_{ij}^{af}\ t_{n}^{b}\ t_{m}^{e}$$

+

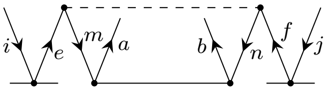

$$\tfrac{1}{4}P_-(ij)\sum_{e,f}\sum_{m,n}\langle mn|\,|ef\rangle\;t_i^e\;t_{mn}^{ab}\;t_j^f \qquad +$$

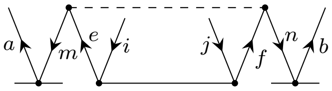

$$\tfrac{1}{4}P_-(ab)\sum_{e,f}\sum_{m,n}\langle mn|\,|ef\rangle\;t_m^a\;t_{ij}^{ef}\;t_n^b \qquad +$$

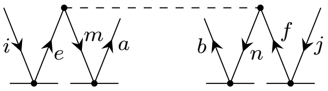

$$\tfrac{1}{4}P_-(ab)P_-(ij)\sum_{e}\sum_{m,n}\langle mn|\,|ef\rangle\;t_i^e\;t_m^a\;t_n^b\;t_j^f \qquad +$$

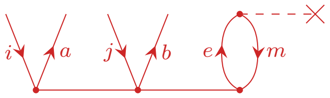

$$\sum_{e}\sum_{m} f_{me}\;t_{ijm}^{abe} \qquad +$$

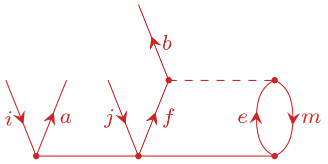

$$\tfrac{1}{2}P_-(ab)\sum_{e,f}\sum_{m}\langle bm|\,|fe\rangle\;t_{ijm}^{afe} \qquad +$$

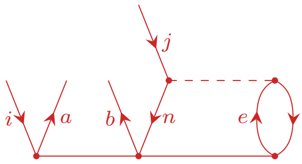

$$-\tfrac{1}{2}P_-(ij)\sum_{e}\sum_{m,n}\langle nm|\,|je\rangle\;t_{inm}^{abe} \qquad +$$

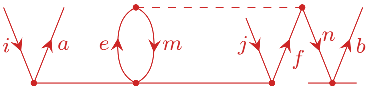

$$-\tfrac{1}{2}P_-(ab)\sum_{e,f}\sum_{m,n}\langle mn|\,|ef\rangle\;t_{ijm}^{afe}\;t_n^b \qquad +$$

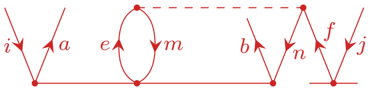

$$-\tfrac{1}{2}P_-(ij)\sum_{e,f}\sum_{m,n}\langle mn|\,|ef\rangle\;t_{inm}^{abe}\;t_j^f \qquad +$$

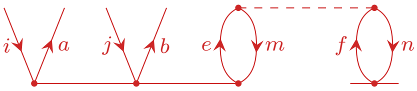

$$\sum_{e,f}\sum_{m,n}\langle mn|\,|ef\rangle\;t_{ijm}^{abe}\;t_n^f$$

$\hat{T}_3$-equations for CCSDT

$0 \quad = $

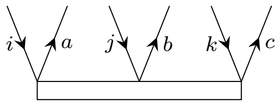

$\mathcal{X}_{abcijk}$

$=$

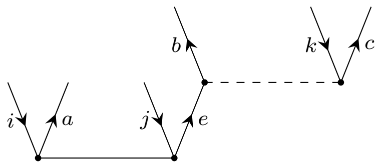

$P_-(a|bc)P_-(k|ij)\sum_e \langle bc|\,|ek\rangle\ \ t_{ij}^{ae}$ $+$

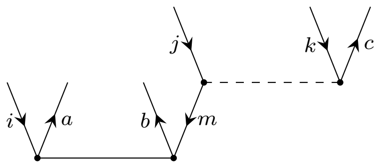

$-P_-(c|ab)P_-(i|jk)\sum_m \langle mc|\,|jk\rangle\ \ t_{im}^{ab}$ $+$

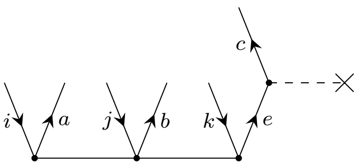

$P_-(c|ab)\sum_e f_{ce}\ t_{ijk}^{abe}$ $+$

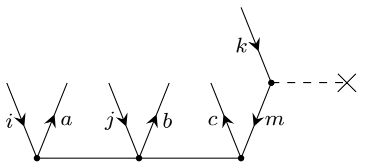

$-P_-(k|ij)\sum_m f_{mk}\ t_{ijm}^{abc}$ $+$

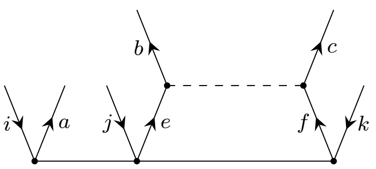

$\frac{1}{2}P_-(a|bc)\sum_{e,f}\langle bc|\,|ef\rangle\ \ t_{ijk}^{aef}$ $+$

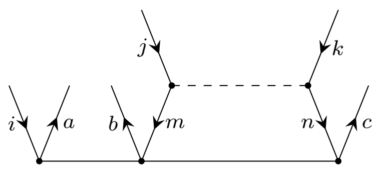

$\frac{1}{2}P_-(i|jk)\sum_{m,n}\langle mn|\,|jk\rangle\ \ t_{imn}^{abc}$ $+$

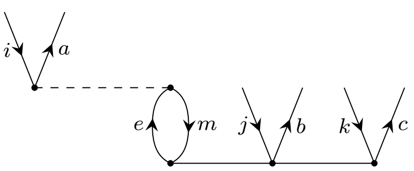

$P_-(a|bc)P_-(i|jk)\sum_e\sum_m \langle ma|\,|ei\rangle\ \ t_{jkm}^{bce}$ $+$

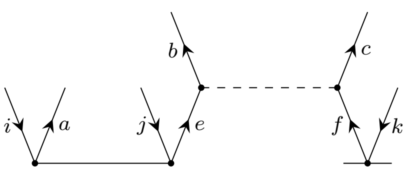

$P_-(a|bc)P_-(k|ij)\sum_{e,f}\langle bc|\,|ef\rangle\ \ t_{ij}^{ae}\ t_k^f$ $+$

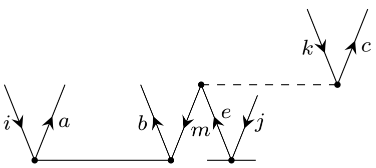

$-P_-(c|ab)P_-(ijk)\sum_e\sum_m \langle mc|\,|ek\rangle\ \ t_{im}^{ab}\ t_j^e$ $+$

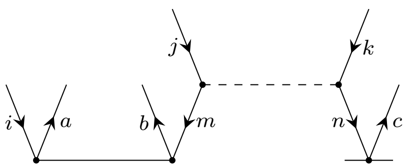

$P_-(c|ab)P_-(i|jk)\sum_{m,n}\langle mn|\,|jk\rangle\ \ t_{im}^{ab}\ t_n^c$ $+$

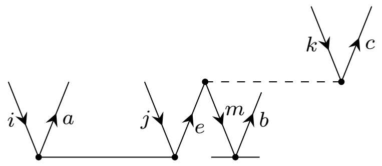

$$-P_-(abc)P_-(k|ij)\sum_{e}\sum_{m}\langle mc|\,|ek\rangle\;t_{ij}^{ae}\;t_{m}^{b}\qquad+$$

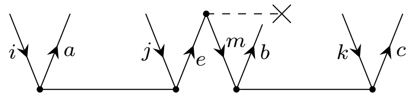

$$-P_-(a|bc)P_-(k|ij)\sum_{e}\sum_{m}f_{me}\;t_{ij}^{ae}\;t_{mk}^{bc}\qquad+$$

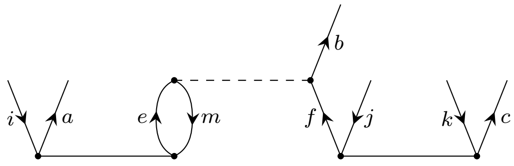

$$P_-(abc)P_-(i|jk)\sum_{e,f}\sum_{m}\langle bm|\,|fe\rangle\;t_{im}^{ae}\;t_{jk}^{fc}\qquad+$$

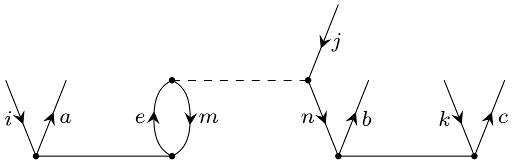

$$-P_-(a|bc)P_-(ijk)\sum_{e}\sum_{m,n}\langle nm|\,|je\rangle\;t_{im}^{ae}\;t_{nk}^{bc}\qquad+$$

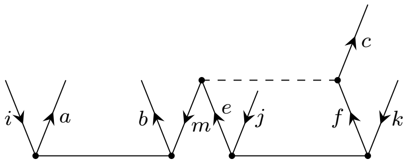

$$-\frac{1}{2}P_-(c|ab)P_-(i|jk)\sum_{e,f}\sum_{m}\langle mc|\,|ef\rangle\;t_{im}^{ab}\;t_{jk}^{ef}\qquad+$$

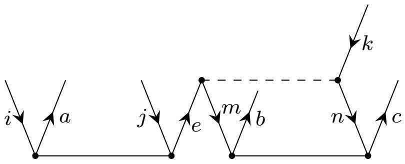

$$\frac{1}{2}P_-(a|bc)P_-(k|ij)\sum_{e}\sum_{m,n}\langle nm|\,|ke\rangle\;t_{ij}^{ae}\;t_{mn}^{bc}\qquad+$$

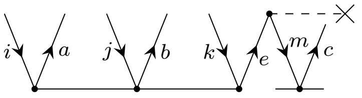

$$-P_-(c|ab)\sum_{e}\sum_{m}f_{me}\;t_{ijk}^{abe}\;t_{m}^{c}\qquad+$$

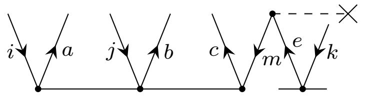

$$-P_-(k|ij)\sum_{e}\sum_{m}f_{me}\;t_{ijm}^{abc}\;t_{k}^{e}\qquad+$$

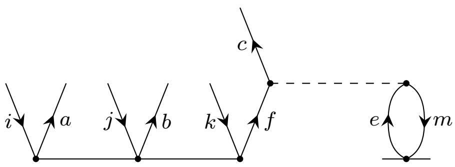

$$P_-(c|ab)\sum_{e,f}\sum_{m}\langle cm|\,|fe\rangle\;t_{ijk}^{abf}\;t_{m}^{e}\qquad+$$

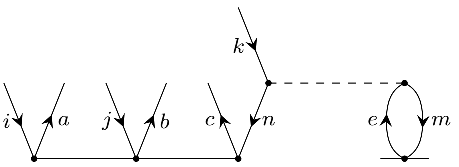

$$-P_-(k|ij)\sum_{e}\sum_{m,n}\langle nm|\,|ke\rangle\;t_{ijm}^{abc}\;t_{m}^{e}\qquad+$$

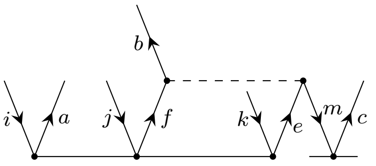

$$-\frac{1}{2}P_-(abc)\sum_{e,f}\sum_{m}\langle bm|\,|fe\rangle\;t_{ijk}^{afe}\;t_{m}^{c}\qquad+$$

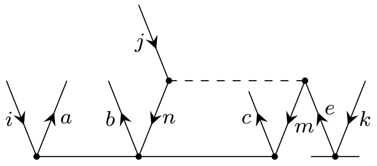

$$\frac{1}{2}P_-(ijk)\sum_{e}\sum_{m,n}\langle nm|\,|je\rangle\;t_{inm}^{abc}\;t_{k}^{e}\qquad+$$

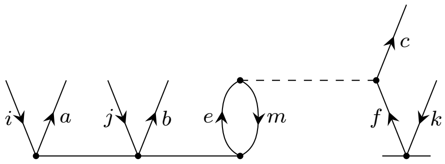

$$P_-(c|ab)P_-(k|ij)\sum_{e,f}\sum_{m}\langle cm|\,|fe\rangle\;\; t_{ijm}^{abe}\;\, t_k^{f}$$

+

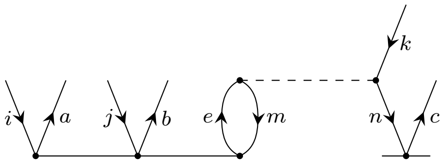

$$-P_-(c|ab)P_-(k|ij)\sum_{e,f}\sum_{m}\langle nm|\,|ke\rangle\;\; t_{ijm}^{abe}\;\, t_n^{c}$$

+

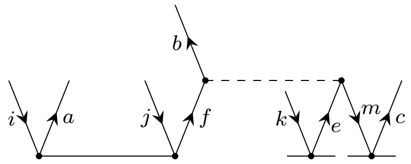

$$-P_-(abc)P_-(k|ij)\sum_{e,f}\sum_{m}\langle bm|\,|fe\rangle\;\; t_{ij}^{af}\;\, t_k^{e}\;\, t_m^{c}$$

+

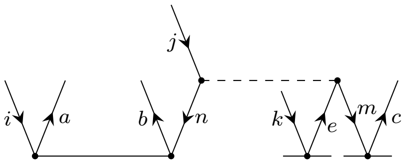

$$P_-(c|ab)P_-(ijk)\sum_{e}\sum_{m,n}\langle nm|\,|je\rangle\;\; t_{in}^{ab}\;\, t_k^{e}\;\, t_m^{c}$$

+

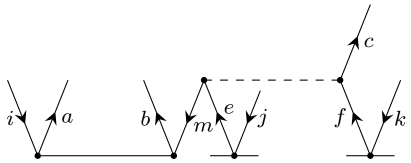

$$-\frac{1}{2}P_-(c|ab)P_-(ijk)\sum_{e,f}\sum_{m}\langle mc|\,|ef\rangle\;\; t_{im}^{ab}\;\, t_j^{e}\;\, t_k^{f}$$

+

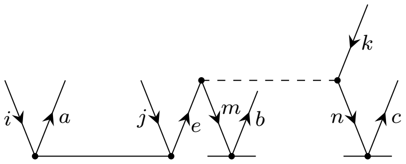

$$\frac{1}{2}P_-(abc)P_-(k|ij)\sum_{e}\sum_{m,n}\langle nm|\,|ke\rangle\;\; t_{ij}^{ae}\;\, t_m^{b}\;\, t_n^{c}$$

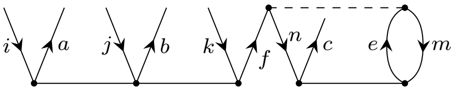

$$-\frac{1}{2}P_-(c|ab)\sum_{e,f}\sum_{m,n}\langle mn|\,|ef\rangle\;\; t_{ijk}^{abf}\;\, t_{mn}^{ec}$$

+

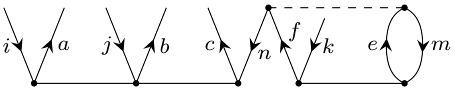

$$-\frac{1}{2}P_-(k|ij)\sum_{e,f}\sum_{m,n}\langle mn|\,|ef\rangle\;\; t_{ijn}^{abc}\;\, t_{mk}^{ef}$$

+

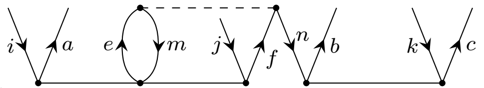

$$-\frac{1}{2}P_-(a|bc)P_-(k|ij)\sum_{e,f}\sum_{m,n}\langle mn|\,|ef\rangle\;\; t_{ijm}^{afe}\;\, t_{nk}^{bc}$$

+

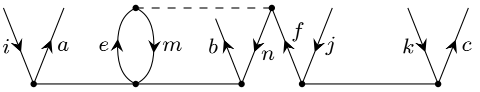

$$-\frac{1}{2}P_-(c|ab)P_-(i|jk)\sum_{e,f}\sum_{m,n}\langle mn|\,|ef\rangle\;\; t_{inm}^{abe}\;\, t_{jk}^{fc}$$

+

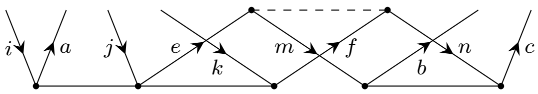

$$\frac{1}{4}P_-(a|bc)\sum_{e,f}\sum_{m,n}\langle mn|\,|ef\rangle\;\; t_{ijk}^{aef}\;\, t_{mn}^{bc}$$

+

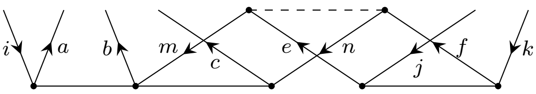

$$\frac{1}{4}P_-(i|jk)\sum_{e,f}\sum_{m,n}\langle mn|\,|ef\rangle\;\; t_{imn}^{abc}\;\, t_{jk}^{ef}$$

+

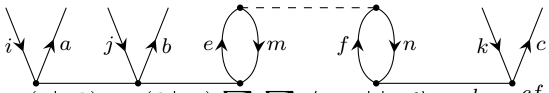

$$P_-(c|ab)P_-(k|ij)\sum_{e,f}\sum_{m,n}\langle mn|\,|ef\rangle\;\; t_{ijm}^{abe}\;\, t_{kn}^{cf}$$

+

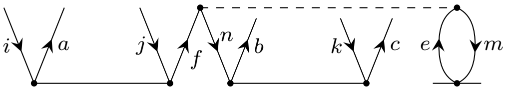

$$-P_-(a|bc)P_-(k|ij)\sum_{e,f}\sum_{m,n}\langle mn|\,|ef\rangle\;\; t_{ij}^{af}\;\, t_{nk}^{bc}\;\, t_m^{e}$$

+

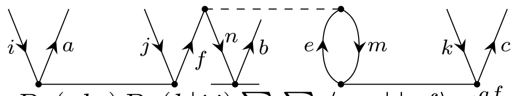

$+$

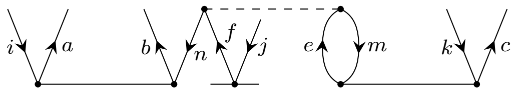

$+$

$$-P_-(abc)P_-(k|ij)\sum_{e,f}\sum_{m,n}\langle mn||ef\rangle\ t_{ij}^{af}\ t_n^{b}\ t_{km}^{ce}$$

$$-P_-(c|ab)P_-(ijk)\sum_{e,f}\sum_{m,n}\langle mn||ef\rangle\ t_{in}^{ab}\ t_j^{f}\ t_{km}^{ce}$$

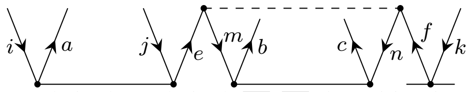

$+$

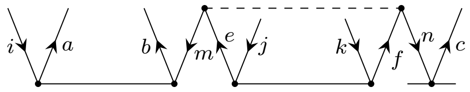

$+$

$$\frac{1}{2}P_-(a|bc)P_-(k|ij)\sum_{e,f}\sum_{m}\langle mn||ef\rangle\ t_{ij}^{ae}\ t_{mn}^{bc}\ t_k^{f}$$

$$\frac{1}{2}P_-(c|ab)P_-(i|jk)\sum_{e,f}\sum_{m}\langle mn||ef\rangle\ t_{im}^{ab}\ t_{jk}^{ef}\ t_n^{c}$$

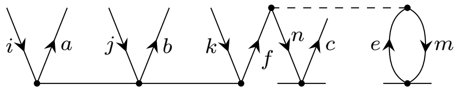

$+$

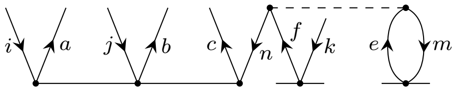

$+$

$$-P_-(c|ab)\sum_{e,f}\sum_{m}\langle mn||ef\rangle\ t_{ijk}^{abf}\ t_n^{c}\ t_m^{e}$$

$$-P_-(k|ij)\sum_{e,f}\sum_{m}\langle mn||ef\rangle\ t_{ijn}^{abc}\ t_k^{f}\ t_m^{e}$$

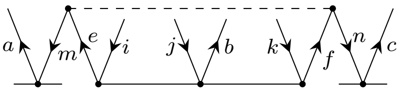

$+$

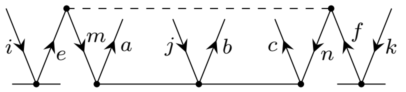

$+$

$$\frac{1}{4}P_-(abc)\sum_{e,f}\sum_{m,n}\langle mn||ef\rangle\ t_m^{a}\ t_{ijk}^{ebf}\ t_n^{c}$$

$$\frac{1}{4}P_-(ijk)\sum_{e,f}\sum_{m,n}\langle mn||ef\rangle\ t_i^{e}\ t_{mjn}^{abc}\ t_k^{f}$$

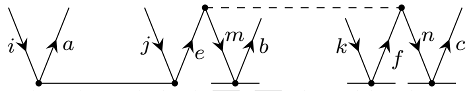

$+$

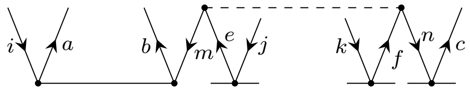

$+$

$$\frac{1}{2}P_-(abc)P_-(k|ij)\sum_{e,f}\sum_{m,n}\langle mn||ef\rangle\ t_{ij}^{ae}\ t_m^{b}\ t_k^{f}\ t_n^{c}$$

$$\frac{1}{2}P_-(c|ab)P_-(ijk)\sum_{e,f}\sum_{m,n}\langle mn||ef\rangle\ t_{im}^{ab}\ t_j^{e}\ t_k^{f}\ t_n^{c}$$

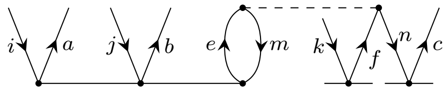

$$-P_-(c|ab)P_-(k|ij)\sum_{e,f}\sum_{m,n}\langle mn||ef\rangle\ t_{ijm}^{abe}\ t_k^{f}\ t_n^{c}$$

Equations for the perturbative CCSD(T) correction

For CCSD(T), E_{CCSD} is corrected by a fourth- and fifth-order energy term:

$$E_{\mathrm{CCSD(T)}} = E_{\mathrm{CCSD}} + \Delta E^{[4]} + \Delta E^{[5]}. \tag{A.1}$$

It is:

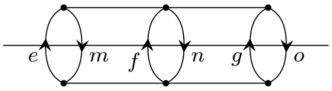

$$\Delta E^{[4]} = \frac{1}{36} \sum_{e,f,g} \sum_{m,n,o} t_{mno}^{efg\ [2]*}\ t_{mno}^{efg\ [2]}\ (\varepsilon_m + \varepsilon_n + \varepsilon_o - \varepsilon_e - \varepsilon_f - \varepsilon_g), \tag{A.2}$$

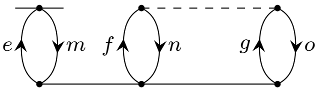

$$\Delta E^{[5]} = \frac{1}{4} \sum_{e,f,g} \sum_{m,n,o} t_m^{e*}\ \langle no|\,|fg\rangle\ t_{mno}^{efg\ [2]}. \tag{A.3}$$

The second-order $\hat{T}_3$-amplitudes are obtained via:

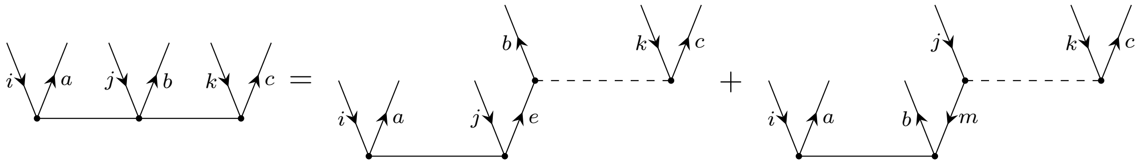

$$t_{ijk}^{abc\ [2]} = \frac{P_-(a|bc)P_-(k|ij) \sum_e \langle bc|\,|ek\rangle\ t_{ij}^{ae} - P_-(c|ab)P_-(i|jk) \sum_m \langle mc|\,|jk\rangle\ t_{im}^{ab}}{\varepsilon_i + \varepsilon_j + \varepsilon_k - \varepsilon_a - \varepsilon_b - \varepsilon_c}. \tag{A.4}$$

The $\hat{T}_3$-amplitudes as well as the energy correction terms are calculated using the converged $\hat{T}_1$- and $\hat{T}_2$-amplitudes.

Implementational details on the CCSD and CCSDT equations

The CCSD equations have been implemented following the intermediate formalism presented by Stanton *et al.* in Ref. [151]. Analogous to the implementations in CFOUR [98] and LONDON, [29] setting up the intermediate $\mathcal{W}_{abef}$ with a dimension of n_{virt}^4 is avoided in order to save memory. This is accomplished in the following way:[40]

---

[40] Note that the definition of τ_{ij}^{ab} is found in Ref. [151] as $\tau_{ij}^{ab} = t_{ij}^{ab} + t_i^a\ t_j^b - t_i^b\ t_j^a$.

1. $\mathcal{W}_{mnij}$ is replaced by

$$\mathcal{W}'_{mnij} = \langle mn|\,|ij\rangle + P_{-}(ij)\sum_{e}\langle mn|\,|ie\rangle\, t_j^e + \frac{\mathbf{1}}{\mathbf{2}}\sum_{e,f}\langle mn|\,|ef\rangle\;\; \tau_{ij}^{ef}.$$

2. An additional intermediate $\mathcal{W}_{kaij}$ is calculated with

$$\mathcal{W}_{kaij} = \frac{1}{2}\sum_{e,f}\langle ak|\,|ef\rangle\;\; \tau_{ij}^{fe}.$$

3. In the $\hat{T}_2$-amplitude equations, the term $\frac{1}{2}\sum_{e,f}\mathcal{W}_{bcef}\;\tau_{ij}^{ef}$ is replaced by

$$\frac{1}{2}\sum_{e,f}\langle bc|\,|ef\rangle\;\; \tau_{ij}^{ef} - P_{-}(ab)\sum_{m}\mathcal{W}_{maji}\; t_m^b.$$

The CCSDT equations have been implemented following the intermediate formalism presented by Gauss *et al.* in Refs. [152, 153]. As suggested in Ref. [89], setting up and saving the intermediate $\mathcal{W}_{abef}$ is not necessary and can optionally be avoided in the QCUMBRE implementation. However, saving the memory for an additional n_{virt}^4-dimensional quantity comes at the cost of additional N^8-steps in order to solve the $\hat{T}_3$-amplitude equations:

- In contrast to the usual procedure of performing multi-step contractions such that intermediates with the lowest possible dimensionality are generated, additional six-index intermediates $\mathcal{X}_{ablijk}$ and $\mathcal{X}_{almijk}$ are calculated with

$$\mathcal{X}_{ablijk} = \frac{1}{2}P_{-}(ab)\sum_{e,f}\langle bl|\,|ef\rangle\;\; t_{ijk}^{aef},$$

$$\mathcal{X}_{almijk} = \frac{1}{2}\sum_{e,f}\langle lm|\,|ef\rangle\;\; t_{ijk}^{aef}.$$

- In the $\hat{T}_3$-amplitude equations, the term $\frac{1}{2}P_{-}(a|bc)\sum_{e,f}\mathcal{W}_{abef}\;t_{ijk}^{aef}$ is replaced by

$$\frac{1}{2}P_{-}(a|bc)\sum_{e,f}\langle ab|\,|ef\rangle\;\; t_{ijk}^{aef} - P_{-}(c|ab)\sum_{m}\mathcal{X}_{abmijk}\; t_m^c + \frac{1}{2}P_{-}(a|bc)\sum_{m,n}\mathcal{X}_{amnijk}\;\tau_{mn}^{bc}.$$

B Equation-of-motion working equations

B.1 Many-particle elements of $\bar{\boldsymbol{H}}$ for CCSDT

In the following, the many-particle elements of $\bar{\boldsymbol{H}}$ are presented in terms of diagrams and corresponding algebraic expressions.

One-particle elements of $\bar{\boldsymbol{H}}$

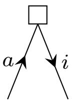

$\mathcal{F}_{ia}$

=

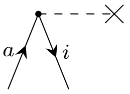

f_{ia}

+

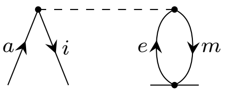

$\sum_{e}\sum_{m}\langle im||ae\rangle\ t_m^e$

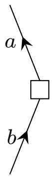

$\mathcal{F}_{ab}$

=

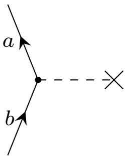

f_{ab}

+

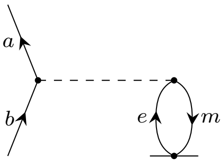

$\sum_{e}\sum_{m}\langle am||be\rangle\ t_m^e$

+

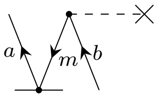

$-\sum_{m} f_{mb}\ t_m^a$

+

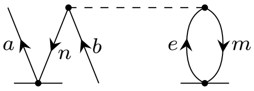

$-\sum_{e}\sum_{m,n}\langle nm||be\rangle\ t_n^a\ t_m^e$

+

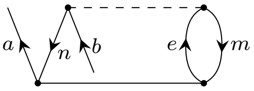

$-\frac{1}{2}\sum_{e}\sum_{m,n}\langle nm||be\rangle\ t_{nm}^{ae}$

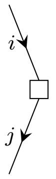

$\mathcal{F}_{ij}$

=

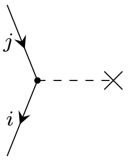

f_{ij}

+

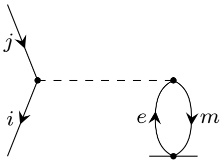

$\sum_{e}\sum_{m}\langle im||je\rangle\ t_m^e$

+

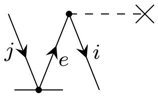

$\sum_{e} f_{ie}\ t_j^e$

+

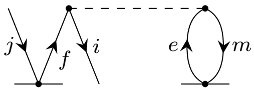

$\sum_{e,f}\sum_{m}\langle im||fe\rangle\ t_j^f\ t_m^e$

+

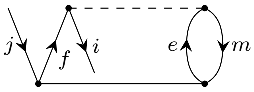

$\frac{1}{2}\sum_{e,f}\sum_{m}\langle im||fe\rangle\ t_{jm}^{fe}$

Two-particle elements of $\bar{H}$

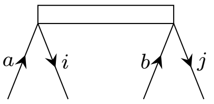

$$\mathcal{W}_{ijab}$$

=

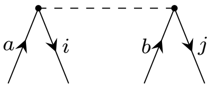

$$\langle ij|\,|ab\rangle$$

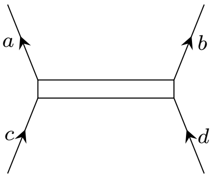

$$\mathcal{W}_{abcd}$$

=

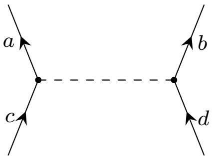

$$\langle ab|\,|cd\rangle$$

+

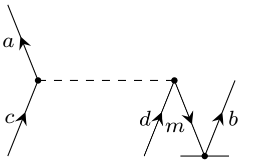

$$-P_{-}(ab)\sum_{m}\langle am|\,|cd\rangle\ t_{m}^{b}$$

+

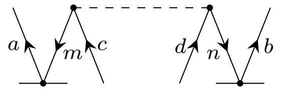

$$\tfrac{1}{2}P_{-}(ab)\sum_{m,n}\langle mn|\,|cd\rangle\ t_{m}^{a}\ t_{n}^{b}$$

+

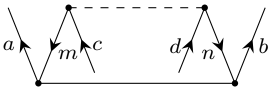

$$\tfrac{1}{2}\sum_{m,n}\langle mn|\,|cd\rangle\ t_{mn}^{ab}$$

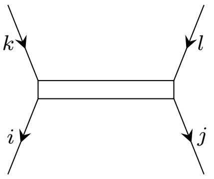

$$\mathcal{W}_{ijkl}$$

=

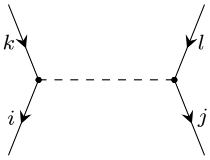

$$\langle ij|\,|kl\rangle$$

+

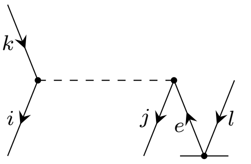

$$P_{-}(kl)\sum_{e}\langle ij|\,|ke\rangle\ t_{l}^{e}$$

+

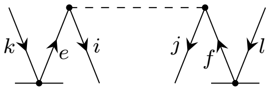

$$\tfrac{1}{2}P_{-}(kl)\sum_{e,f}\langle ij|\,|ef\rangle\ t_{k}^{e}\ t_{l}^{f}$$

+

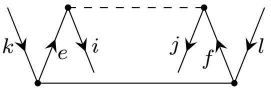

$$\tfrac{1}{2}\sum_{e,f}\langle ij|\,|ef\rangle\ t_{kl}^{ef}$$

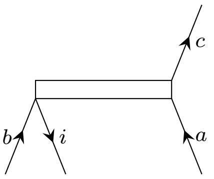

$$\mathcal{W}_{ciab}$$

=

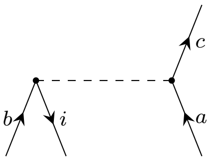

$$\langle ci|\,|ab\rangle$$

+

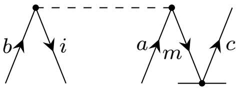

$$-\sum_{m}\langle im|\,|ba\rangle\ t_{m}^{c}$$

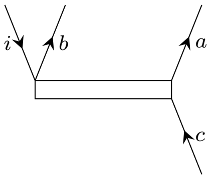

$\mathcal{W}_{abci}$

=

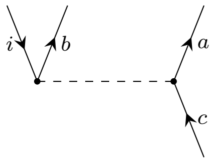

$\langle ab|\,|ci\rangle$

+

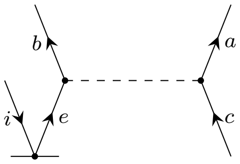

$\sum_{e} \langle ab|\,|ce\rangle \;\; t_i^e$

+

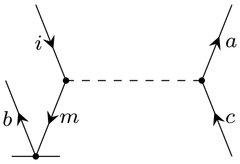

$P_{-}(ab) \sum_{m} \langle ma|\,|ci\rangle \;\; t_m^b$

+

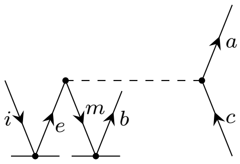

$-P_{-}(ab) \sum_{e} \sum_{m} \langle am|\,|ce\rangle \;\; t_i^e \; t_m^b$

+

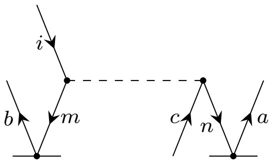

$\frac{1}{2} P_{-}(ab) \sum_{m,n} \langle mn|\,|ic\rangle \;\; t_m^b \; t_n^a$

+

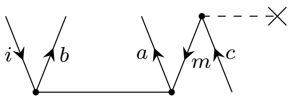

$-\sum_{m} f_{mc} \; t_{mi}^{ab}$

+

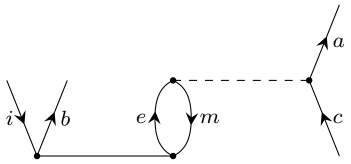

$P_{-}(ab) \sum_{e} \sum_{m} \langle am|\,|ce\rangle \;\; t_{im}^{be}$

+

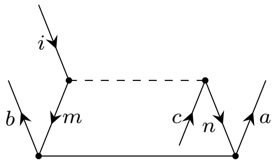

$\frac{1}{2} \sum_{m,n} \langle mn|\,|ic\rangle \;\; t_{mn}^{ba}$

+

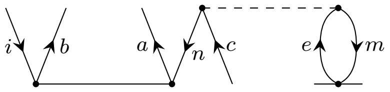

$-\sum_{e} \sum_{m,n} \langle mn|\,|ec\rangle \;\; t_{ni}^{ab} \; t_m^e$

+

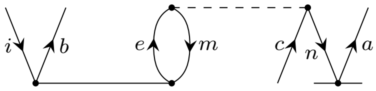

$-P_{-}(ab) \sum_{e} \sum_{m,n} \langle mn|\,|ec\rangle \;\; t_{im}^{be} \;\; t_n^a$

+

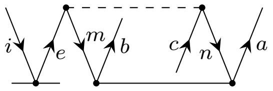

$\frac{1}{2} \sum_{e} \sum_{m,n} \langle mn|\,|ec\rangle \;\; t_{mn}^{ba} \;\; t_i^e$

+

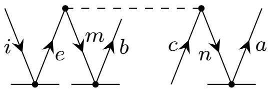

$\frac{1}{2} P_{-}(ab) \sum_{e} \sum_{m,n} \langle mn|\,|ec\rangle \;\; t_i^e \; t_m^b \; t_n^a$

+

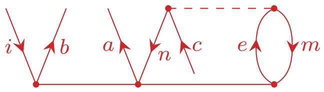

$-\frac{1}{2} \sum_{e} \sum_{m,n} \langle mn|\,|ec\rangle \;\; t_{inm}^{bae}$

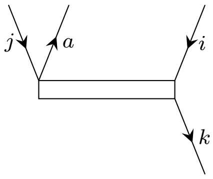

$$\mathcal{W}_{kaij}$$

=

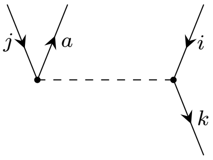

$$\langle ka|\,|ij\rangle$$

+

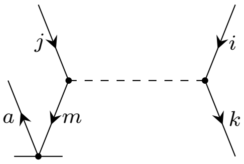

$$-\sum_{e}\langle km|\,|ij\rangle\; t_{m}^{a}$$

+

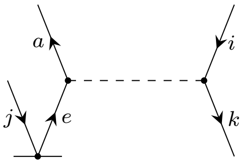

$$-P_{-}(ij)\sum_{e}\langle ka|\,|ei\rangle\; t_{j}^{e}$$

+

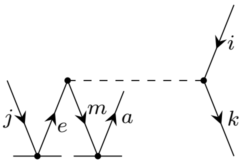

$$-P_{-}(ij)\sum_{e}\sum_{m}\langle km|\,|ie\rangle\; t_{j}^{e}\, t_{m}^{a}$$

+

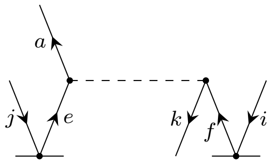

$$\tfrac{1}{2}P_{-}(ij)\sum_{e,f}\langle ak|\,|ef\rangle\; t_{j}^{e}\, t_{i}^{f}$$

+

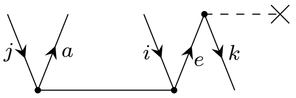

$$\sum_{e} f_{ke}\; t_{ij}^{ea}$$

+

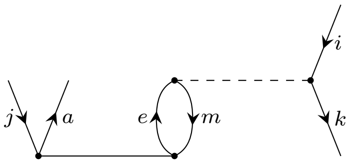

$$P_{-}(ij)\sum_{e}\sum_{m}\langle km|\,|ie\rangle\; t_{jm}^{ae}$$

+

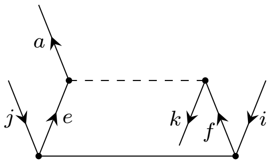

$$\tfrac{1}{2}\sum_{e,f}\langle ak|\,|ef\rangle\; t_{ji}^{ef}$$

+

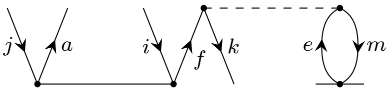

$$\sum_{e,f}\sum_{m}\langle mk|\,|ef\rangle\; t_{ij}^{fa}\; t_{m}^{e}$$

+

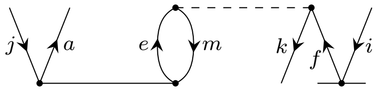

$$P_{-}(ij)\sum_{e,f}\sum_{m}\langle mk|\,|ef\rangle\; t_{jm}^{ae}\; t_{i}^{f}$$

+

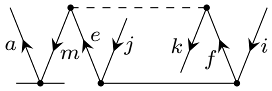

$$-\tfrac{1}{2}\sum_{e,f}\sum_{m}\langle mk|\,|ef\rangle\; t_{ji}^{ef}\; t_{m}^{a}$$

+

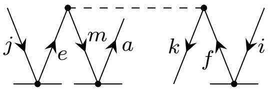

$$-\tfrac{1}{2}P_{-}(ij)\sum_{e,f}\sum_{m}\langle mk|\,|ef\rangle\; t_{j}^{e}\; t_{m}^{a}\; t_{i}^{f}$$

+

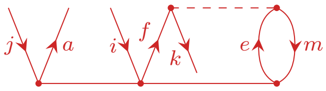

$$\tfrac{1}{2}\sum_{e,f}\sum_{m}\langle mk|\,|ef\rangle\; t_{jim}^{afe}$$

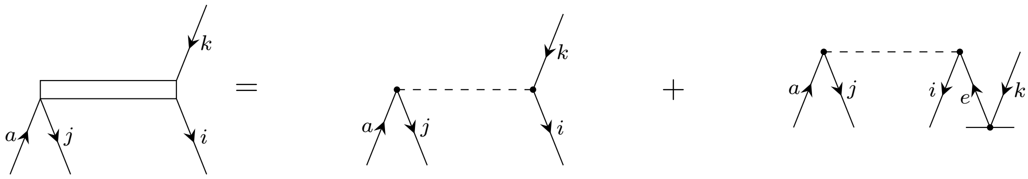

$\mathcal{W}_{ijka}$ $\quad \langle ij||ka\rangle \quad \sum_{e} \langle ij||ea\rangle\ t_{k}^{e}$

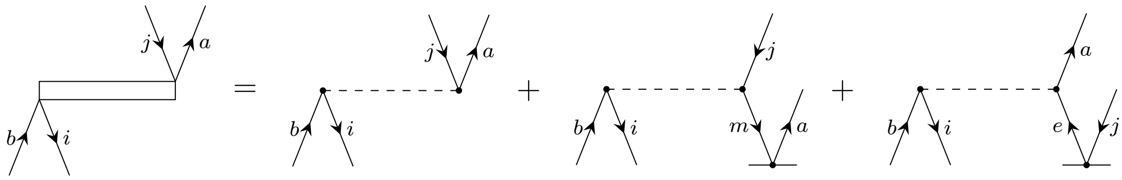

$\mathcal{W}_{iabj}$ $\quad \langle ia||bj\rangle \quad -\sum_{m} \langle mi||jb\rangle\ t_{m}^{a} \quad \sum_{e} \langle ai||eb\rangle\ t_{j}^{e}$

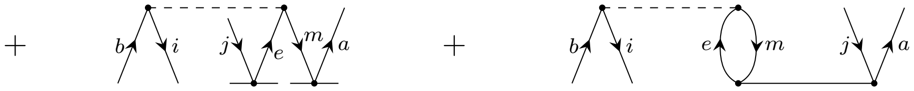

$-\sum_{e}\sum_{m} \langle im||be\rangle\ t_{j}^{e}\ t_{m}^{a} \quad \sum_{e}\sum_{m} \langle im||be\rangle\ t_{mj}^{ea}$

Three-particle elements of $\bar{\boldsymbol{H}}$

The three-particle elements of $\bar{\boldsymbol{H}}$ are never calculated and stored in the Qcumbre program package. Terms within the EOM equations containing these elements are calculated stepwise using one- and two-body elements, thus, avoiding higher memory usage and method scaling.

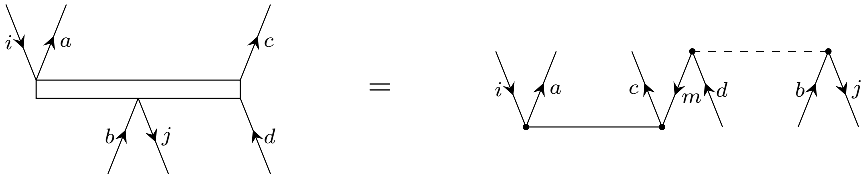

$\mathcal{X}_{ajcibd}$ $\quad -\sum_{m} \langle jm||bd\rangle\ t_{im}^{ac}$

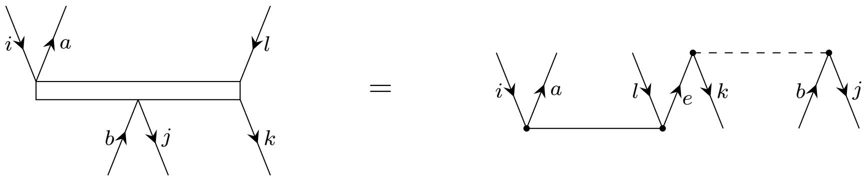

$\mathcal{X}_{ajkibl}$ $\quad \sum_{e} \langle jk||be\rangle\ t_{il}^{ae}$

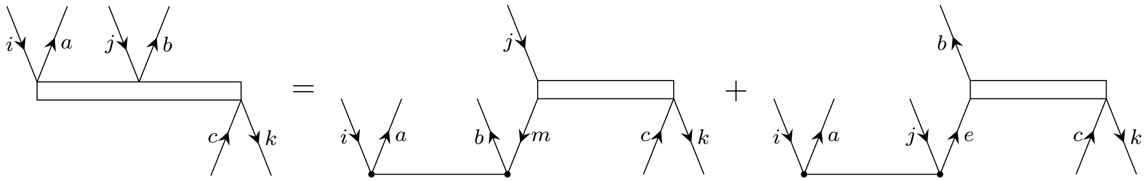

$\mathcal{X}_{abkijc}$ $\quad -P_-(ij)\sum_m \mathcal{W}_{mkjc}\ t^{ab}_{im}$ $\quad P_-(ab)\sum_e \mathcal{W}_{bkec}\ t^{ae}_{ij}$

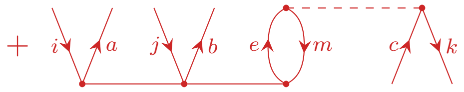

$\sum_e\sum_m \langle mk||ec\rangle\ t^{abe}_{ijm}$

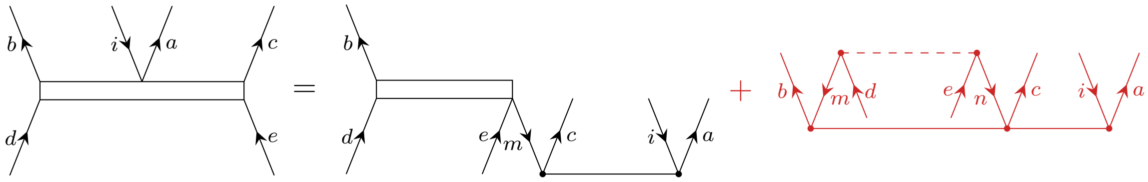

$\mathcal{X}_{abcide}$ $\quad -P_-(b|ac)\sum_m \mathcal{W}_{bmde}\ t^{ac}_{im}$ $\quad \frac{1}{2}\sum_{m,n} \langle mn||de\rangle\ t^{abc}_{imn}$

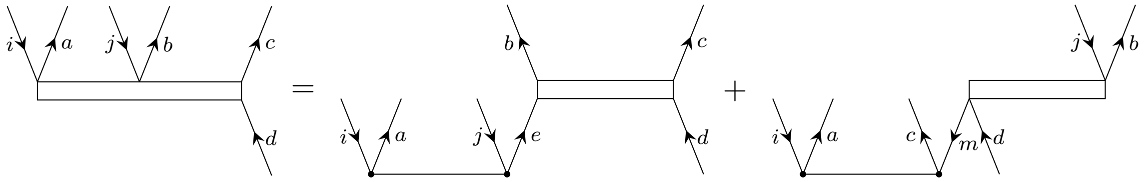

$\mathcal{X}_{abcijd}$ $\quad P_-(a|bc)\sum_e \mathcal{W}_{bced}\ t^{ae}_{ij}$ $\quad -P_-(b|ac)P_-(ij)\sum_m \mathcal{W}_{mbdj}\ t^{ac}_{im}$

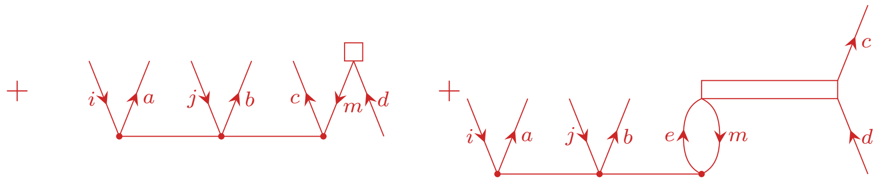

$-\sum_m \mathcal{F}_{md}\ t^{abc}_{ijm}$ $\quad P_-(c|ab)\sum_e\sum_m \mathcal{W}_{cmde}\ t^{abe}_{ijm}$

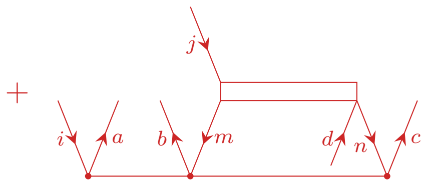

$\frac{1}{2}P_-(ij)\sum_{m,n} \mathcal{W}_{mnjd}\ t^{abc}_{imn}$

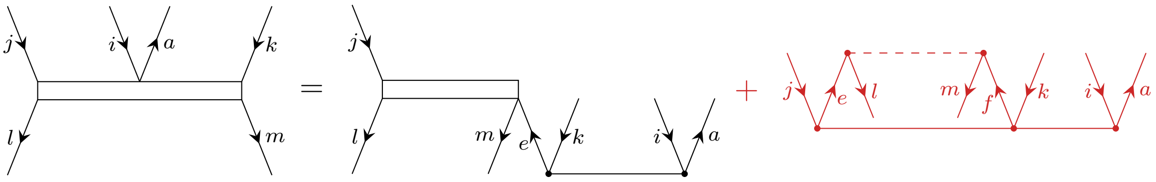

$$\mathcal{X}_{almijk} = P_-(j|ik)\sum_e \mathcal{W}_{lmje}\; t_{ik}^{ae} + \frac{1}{2}\sum_{e,f}\langle lm||ef\rangle\; t_{ijk}^{aef}$$

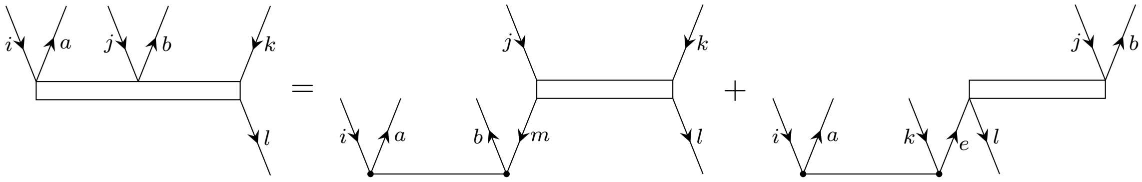

$$\mathcal{X}_{ablijk} = -P_-(i|jk)\sum_m \mathcal{W}_{mljk}\; t_{im}^{ab} + P_-(ab)P_-(j|ik)\sum_e \mathcal{W}_{lbej}\; t_{ik}^{ae}$$

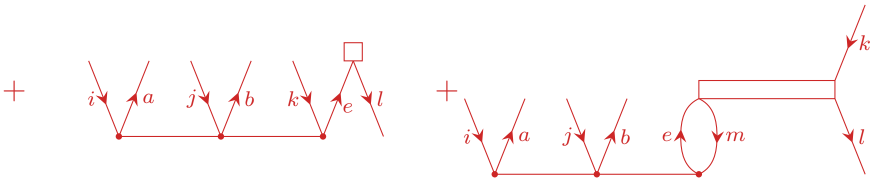

$$+\sum_e \mathcal{F}_{le}\; t_{ijk}^{abe} + P_-(k|ij)\sum_e\sum_m \mathcal{W}_{lmke}\; t_{ijm}^{abe}$$

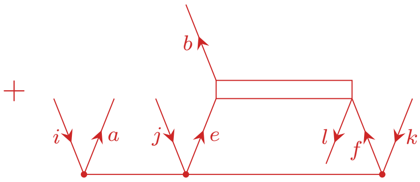

$$+\frac{1}{2}P_-(ab)\sum_{e,f}\mathcal{W}_{blef}\; t_{ijk}^{aef}$$

Four-particle elements of $\bar{H}$

The four-particle elements of $\bar{H}$ are never calculated and stored in the Qcumbre program package. Terms within the EOM equations containing these elements are calculated stepwise using two-body elements, thus, avoiding higher memory usage and method scaling.

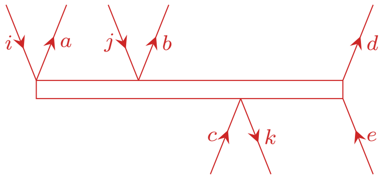

$\mathcal{K}_{abkdijce}$

$=$

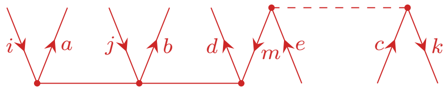

$$-\sum_m \langle km||ce\rangle\ t_{ijm}^{abd}$$

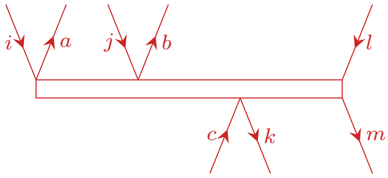

$\mathcal{K}_{abkmijcl}$

$=$

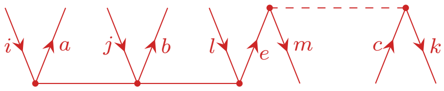

$$\sum_e \langle km||ce\rangle\ t_{ijl}^{abe}$$

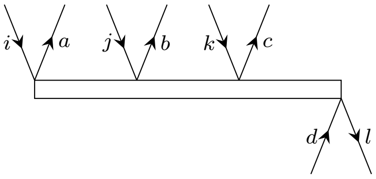

$\mathcal{K}_{abclijkd}$

$=$

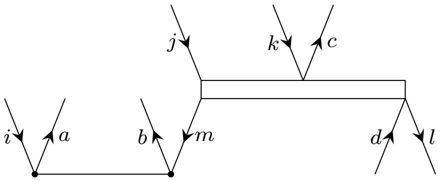

$$-P_-(c|ab)P_-(i|jk)\sum_m \mathcal{X}_{clmkdj}\ t_{im}^{ab}$$

$+$

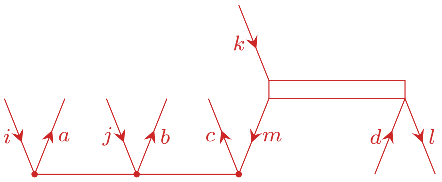

$$-P_-(k|ij)\sum_m \mathcal{W}_{mlkd}\ t_{ijm}^{abc}$$

$+$

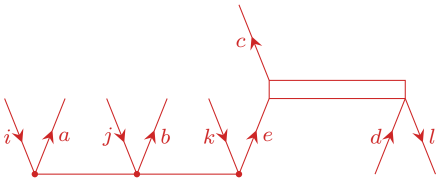

$$P_-(c|ab)\sum_e \mathcal{W}_{cled}\ t_{ijk}^{abe}$$

B.2 EOM-EE and EOM-SF working equations

All EOM working equations are presented in the following. They are formulated by using the many-body elements of $\bar{\boldsymbol{H}}$. As mentioned before, only the one- and two-body elements are stored making multi-step contractions necessary for the remaining terms. All multi-step contractions in Qcumbre are performed by first eliminating as many summation indices as possible and, such, generating a new intermediate with as few indices as possible. For a given number of indices, the intermediate with the fewest virtual indices is composed. In the diagrams, the symbols for the $\hat{\mathcal{R}}$- and $\hat{\mathcal{L}}$-operators are chosen to be bold lines.

Right-hand side $\boldsymbol{\sigma_i^a}$-equations for CCSDT

$\Delta E_{\text{exc}}\; r_i^a \quad =$

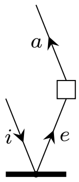

$\sum_e \mathcal{F}_{ae}\; r_i^e$ +

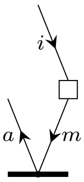

$-\sum_m \mathcal{F}_{mi}\; r_m^a$ +

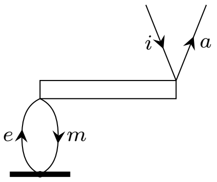

$\sum_e \sum_m \mathcal{W}_{maei}\; r_m^e$ +

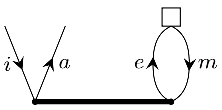

$\sum_e \sum_m \mathcal{F}_{me}\; r_{im}^{ae}$ +

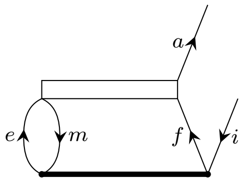

$\frac{1}{2} \sum_{e,f} \sum_m \mathcal{W}_{amfe}\; r_{mi}^{ef}$ +

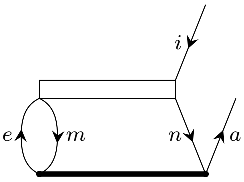

$-\frac{1}{2} \sum_e \sum_{m,n} \mathcal{W}_{nmie}\; r_{mn}^{ea}$ +

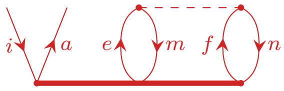

$\frac{1}{4} \sum_{e,f} \sum_{m,n} \langle mn||ef\rangle\; r_{imn}^{aef}$

Right-hand side $\boldsymbol{\sigma_{ij}^{ab}}$-equations for CCSDT

$\Delta E_{\text{exc}}\; r_{ij}^{ab} \quad =$

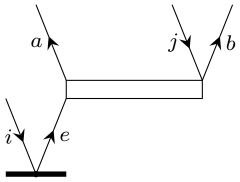

$P_-(ij) \sum_e \mathcal{W}_{abej}\; r_i^e$ +

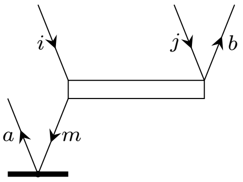

$-P_-(ab) \sum_m \mathcal{W}_{mbij}\; r_m^a$ +

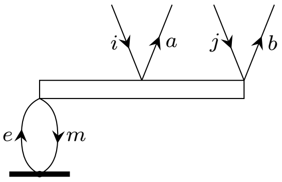

$\sum_e \sum_m \mathcal{X}_{abmije}\; r_m^e$ +

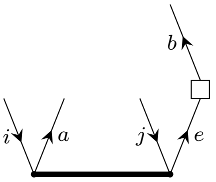

$$P_-(ab)\sum_e \mathcal{F}_{be}\ r^{ae}_{ij}$$

+

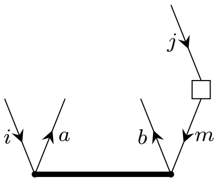

$$-P_-(ij)\sum_m \mathcal{F}_{mj}\ r^{ab}_{im}$$

+

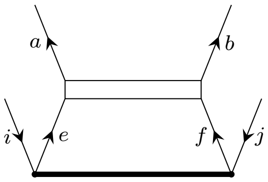

$$\frac{1}{2}\sum_{e,f}\mathcal{W}_{abef}\ r^{ef}_{ij}$$

+

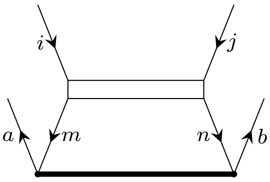

$$\frac{1}{2}\sum_{m,n}\mathcal{W}_{mnij}\ r^{ab}_{mn}$$

+

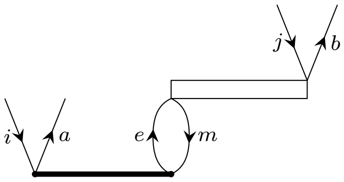

$$P_-(ab)P_-(ij)\sum_e\sum_m \mathcal{W}_{mbej}\ r^{ae}_{im}$$

+

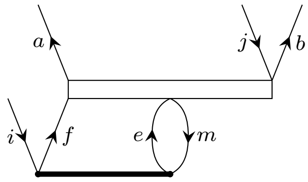

$$\frac{1}{2}P_-(ij)\sum_{e,f}\sum_m \mathcal{X}_{bmajef}\ r^{fe}_{im}$$

+

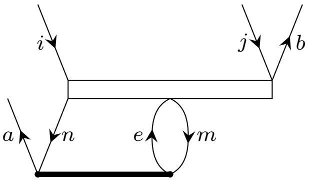

$$-\frac{1}{2}P_-(ab)\sum_e\sum_{m,n}\mathcal{X}_{bmnjei}\ r^{ae}_{nm}$$

+

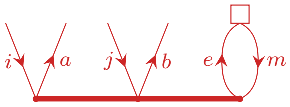

$$\sum_e\sum_m \mathcal{F}_{me}\ r^{abe}_{ijm}$$

+

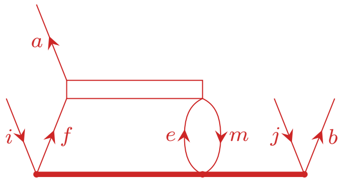

$$\frac{1}{2}P_-(ab)\sum_{e,f}\sum_m \mathcal{W}_{amfe}\ r^{fbe}_{ijm}$$

+

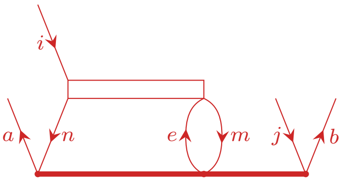

$$-\frac{1}{2}P_-(ij)\sum_e\sum_{m,n}\mathcal{W}_{nmie}\ r^{abe}_{njm}$$

Right-hand side $\boldsymbol{\sigma^{abc}_{ijk}}$-equations for CCSDT

$$\Delta E_{\text{exc}}\ r^{abc}_{ijk} \quad =$$

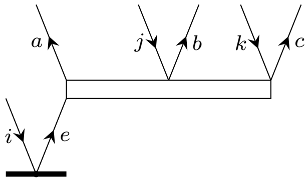

$$P_-(i|jk)\sum_e \mathcal{X}_{bcajke}\ r^{e}_{i}$$

+

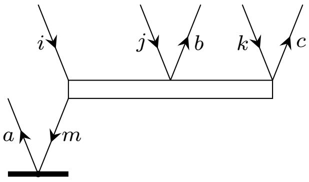

$$-P_-(a|bc)\sum_m \mathcal{X}_{bcmjki}\ r^{a}_{m}$$

+

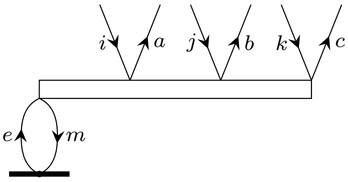

$$\sum_e\sum_m \mathcal{K}_{abcmijke}\ r^{e}_{m}$$

+

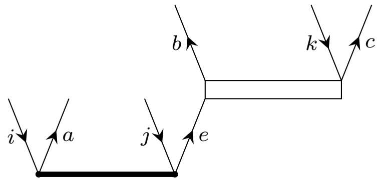

$$P_-(a|bc)P_-(k|ij)\sum_{e}\mathcal{W}_{bcek}\ r_{ij}^{ae}$$

$+$

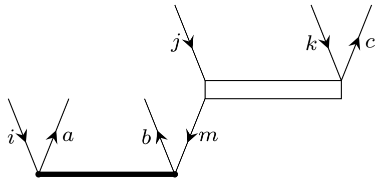

$$-P_-(c|ab)P_-(i|jk)\sum_{m}\mathcal{W}_{mcjk}\ r_{im}^{ab}$$

$+$

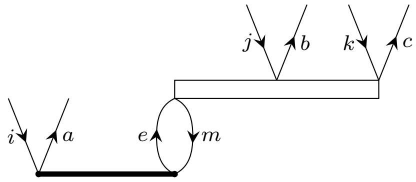

$$P_-(a|bc)P_-(i|jk)\sum_{e}\sum_{m}\mathcal{X}_{bcmjke}\ r_{im}^{ae}$$

$+$

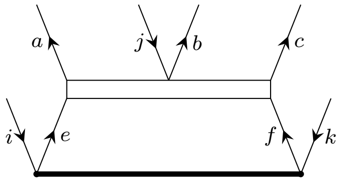

$$\tfrac{1}{2}P_-(j|ik)\sum_{e,f}\mathcal{X}_{bacjef}\ r_{ik}^{ef}$$

$+$

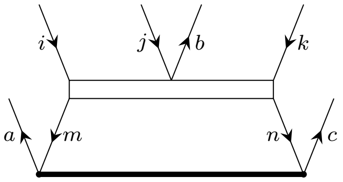

$$\tfrac{1}{2}P_-(b|ac)\sum_{m,n}\mathcal{X}_{bmnjik}\ r_{mn}^{ac}$$

$+$

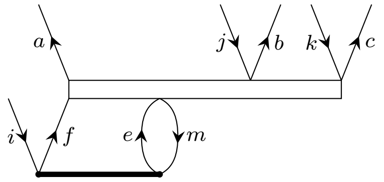

$$\tfrac{1}{2}P_-(i|jk)\sum_{e,f}\sum_{m}\mathcal{K}_{cbmakjef}\ r_{im}^{fe}$$

$+$

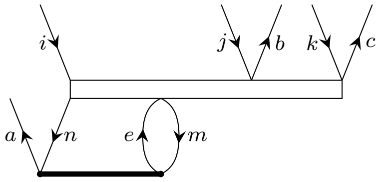

$$-\tfrac{1}{2}P_-(a|bc)\sum_{e}\sum_{m,n}\mathcal{K}_{cbmnkjei}\ r_{nm}^{ae}$$

$+$

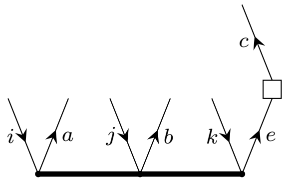

$$P_-(a|bc)\sum_{e}\mathcal{F}_{ce}\ r_{ijk}^{abe}$$

$+$

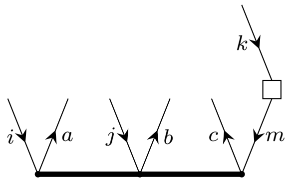

$$-P_-(k|ij)\sum_{m}\mathcal{F}_{mk}\ r_{ijm}^{abc}$$

$+$

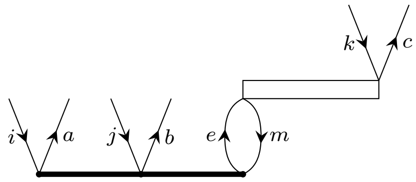

$$P_-(c|ab)P_-(k|ij)\sum_{e}\sum_{m}\mathcal{W}_{mcek}\ r_{ijm}^{abe}$$

$+$

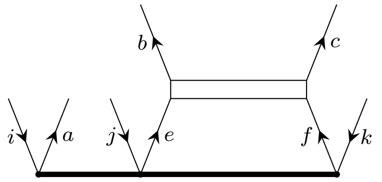

$$\tfrac{1}{2}P_-(a|bc)\sum_{e,f}\mathcal{W}_{bcef}\ r_{ijk}^{aef}$$

$+$

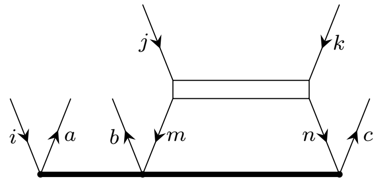

$$\tfrac{1}{2}P_-(i|jk)\sum_{m,n}\mathcal{W}_{mnjk}\ r_{imn}^{abc}$$

$+$

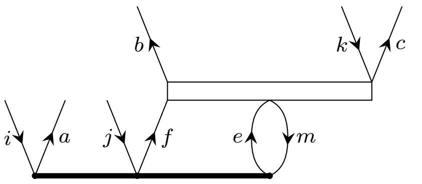

$$\tfrac{1}{2}P_-(a|bc)P_-(k|ij)\sum_{e,f}\sum_{m}\mathcal{X}_{cmbkef}\; r^{afe}_{ijm}$$

$+$

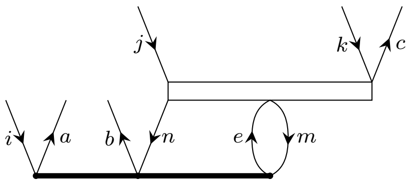

$$-\tfrac{1}{2}P_-(c|ab)P_-(i|jk)\sum_{e}\sum_{m,n}\mathcal{X}_{cmnkej}\; r^{abe}_{inm}$$

Left-hand side $\boldsymbol{\sigma^i_a}$-equations for CCSD

$$\Delta E_{\text{exc}}\; l^i_a \quad =$$

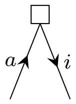

$$l_0\;\mathcal{F}_{ia}$$

$+$

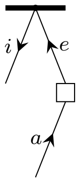

$$\sum_{e}\mathcal{F}_{ea}\; l^i_e$$

$+$

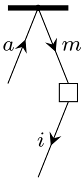

$$-\sum_{m}\mathcal{F}_{im}\; l^m_a$$

$+$

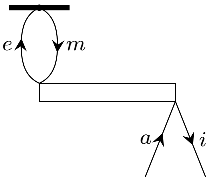

$$\sum_{e}\sum_{m}\mathcal{W}_{ieam}\; l^m_e$$

$+$

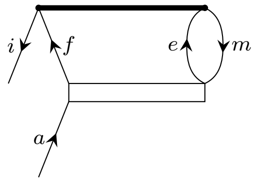

$$\tfrac{1}{2}\sum_{e,f}\sum_{m}\mathcal{W}_{feam}\; l^{im}_{fe}$$

$+$

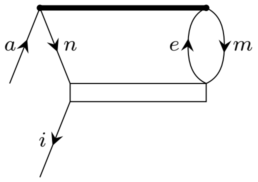

$$-\tfrac{1}{2}\sum_{e}\sum_{m,n}\mathcal{W}_{ienm}\; l^{nm}_{ae}$$

$+$

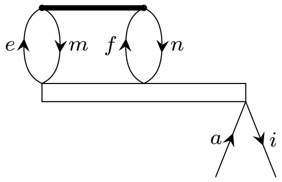

$$\tfrac{1}{4}\sum_{e,f}\sum_{m,n}\mathcal{X}_{efimna}\; l^{mn}_{ef}$$

Left-hand side $\boldsymbol{\sigma^{ij}_{ab}}$-equations for CCSD

$$\Delta E_{\text{exc}}\; l^{ij}_{ab} \;=$$

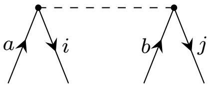

$$l_0\;\langle ij||ab\rangle$$

$+$

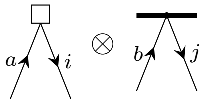

$$P_-(ab)P_-(ij)\;\mathcal{F}_{ia}\; l^j_b$$

$+$

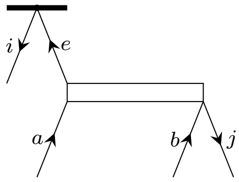

$$P_-(ij)\sum_{e}\mathcal{W}_{ejab}\; l^i_e$$

$+$

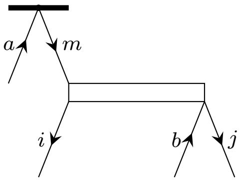

$$-P_-(ab)\sum_{m}\mathcal{W}_{ijmb}\; l^m_a$$

$+$

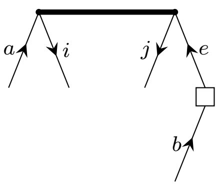

$$P_-(ab)\sum_e \mathcal{F}_{eb}\; l^{ij}_{ae}$$

+

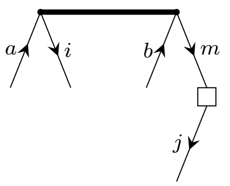

$$-P_-(ij)\sum_m \mathcal{F}_{jm}\; l^{im}_{ab}$$

+

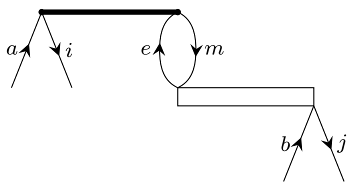

$$P_-(ab)P_-(ij)\sum_e\sum_m \mathcal{W}_{jebm}\; l^{im}_{ae}$$

+

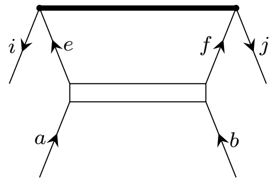

$$\tfrac{1}{2}\sum_{e,f} \mathcal{W}_{efab}\; l^{ij}_{ef}$$

+

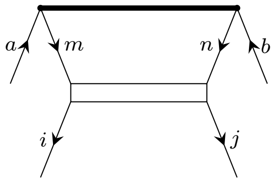

$$\tfrac{1}{2}\sum_{m,n} \mathcal{W}_{ijmn}\; l^{mn}_{ab}$$

+

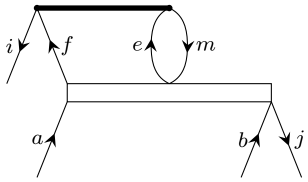

$$\tfrac{1}{2}P_-(ij)\sum_{e,f}\sum_m \mathcal{X}_{ejfmba}\; l^{im}_{fe}$$

+

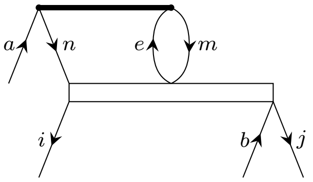

$$-\tfrac{1}{2}P_-(ab)\sum_e\sum_{m,n} \mathcal{X}_{ejimbn}\; l^{nm}_{ae}$$

Implementational details on the EOM-CCSD and EOM-CCSDT equations

The EOM-CCSD equations have been implemented in a straightforward manner by implementing the one- and two-body terms of $\bar{\boldsymbol{H}}$ and performing the respective contractions by using the least costly factorizations in multi-step contractions. The same has been done for the EOM-CCSDT equations using the intermediate formalism proposed in Ref. [89] involving the following steps. The existing $\mathcal{W}$-intermediates are extended by the contributions of the $\hat{T}_3$-operator. Contractions between an $\hat{\mathcal{R}}_n$-operator and $\mathcal{F}$- as well as $\mathcal{W}$-intermediates are directly performed. For all contributions from three- and four-body terms of $\bar{\boldsymbol{H}}$, additional intermediates involving $\hat{\mathcal{R}}_n$-operators are set up and defined in the following.[41]

---

[41] The original definitions can be found in Ref. [89] but are listed here to correct for notational falsities.

Triples contributions to $\boldsymbol{\sigma_{ij}^{ab}}$ from the three-body term

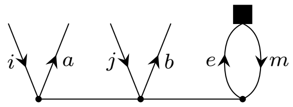

$\sum_e \sum_m \widetilde{\mathcal{F}}_{me}\ t_{ijm}^{abe}$

with

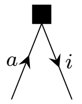

$\widetilde{\mathcal{F}}_{ia}$

=

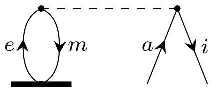

$\sum_e \sum_m \langle im|\,|ae\rangle\ r_m^e$

Triples contributions to $\boldsymbol{\sigma_{ijk}^{abc}}$ from the three- and four-body terms

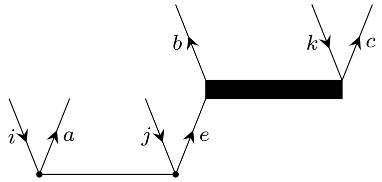

$P_-(a|bc)P_-(k|ij)\sum_e \widetilde{\mathcal{W}}_{bcek}\ t_{ij}^{ae}$

with

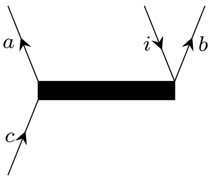

$\widetilde{\mathcal{W}}_{abci}$

=

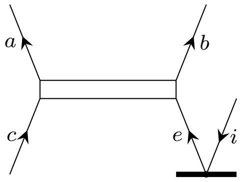

$\sum_e \mathcal{W}_{abce}\ r_i^e$

+

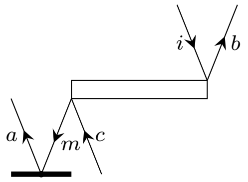

$-P_-(ab)\sum_m \mathcal{W}_{mbci}\ r_m^a$

+

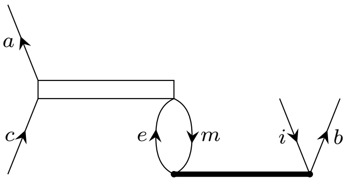

$P_-(ab)\sum_e \sum_m \mathcal{W}_{amce}\ r_{im}^{be}$

+

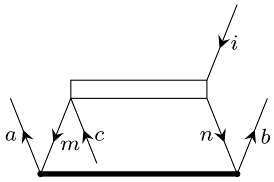

$\frac{1}{2}\sum_{m,n} \mathcal{W}_{nmic}\ r_{mn}^{ab}$

+

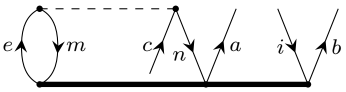

$-\frac{1}{2}\sum_e \sum_{m,n} \langle mn|\,|ec\rangle\ r_{mni}^{eab}$

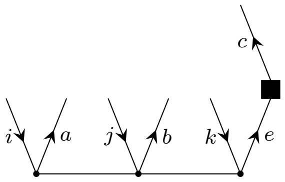

$P_-(c|ab)\sum_e \widetilde{\mathcal{F}}_{ce}\; t_{ijk}^{abe}$

with

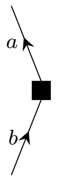

$\widetilde{\mathcal{F}}_{ab}$

=

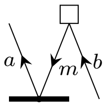

$-\sum_m \mathcal{F}_{mb}\; r_m^a$

+

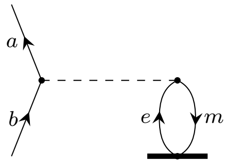

$\sum_e \sum_m \langle am||be\rangle \; r_m^e$

+

$-\frac{1}{2}\sum_e \sum_{m,n} \langle mn||eb\rangle \; r_{mn}^{ea}$

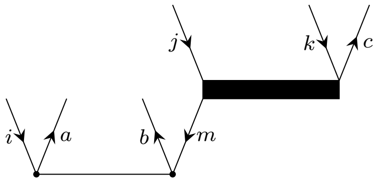

$-P_-(c|ab)P_-(i|jk)\sum_m \widetilde{\mathcal{W}}_{mcjk}\; t_{im}^{ab}$

with

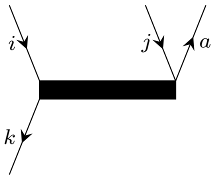

$\widetilde{\mathcal{W}}_{kaij}$

=

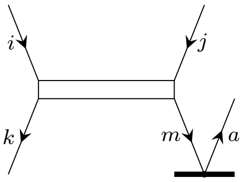

$-\sum_m \mathcal{W}_{kmij}\; r_m^a$

+

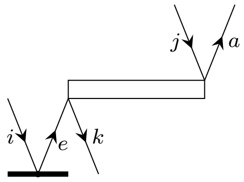

$P_-(ij)\sum_e \mathcal{W}_{kaej}\; r_i^e$

+

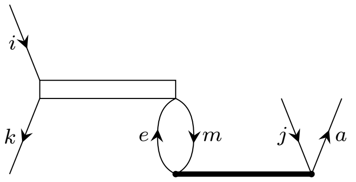

$P_-(ij)\sum_e \sum_m \mathcal{W}_{kmie}\; r_{jm}^{ae}$

+

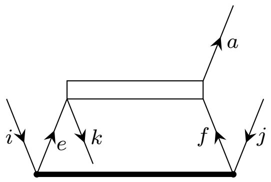

$\frac{1}{2}\sum_{e,f} \mathcal{W}_{akfe}\; r_{ij}^{ef}$

+

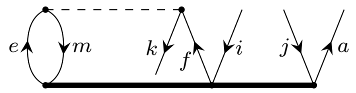

$\frac{1}{2}\sum_{e,f} \sum_m \langle mk||ef\rangle \; r_{mij}^{efa}$

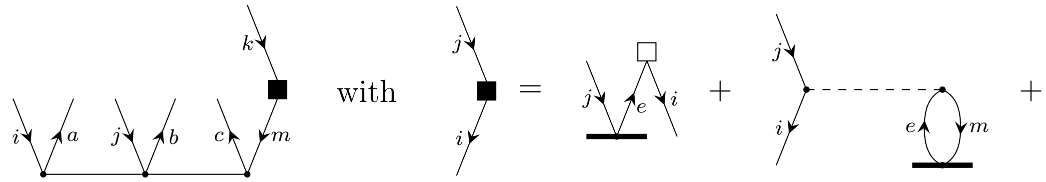

$$-P_{-}(k|ij)\sum_{m}\widetilde{\mathcal{F}}_{mk}\,t^{abc}_{ijm} \qquad \widetilde{\mathcal{F}}_{ij} \qquad \sum_{e}\mathcal{F}_{ie}\,r^{e}_{j} \qquad \sum_{e}\sum_{m}\langle im|\,|je\rangle\;r^{e}_{m}$$

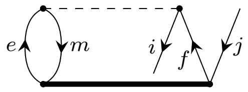

$$\frac{1}{2}\sum_{e,f}\sum_{m}\langle mi|\,|ef\rangle\;r^{ef}_{mj}$$

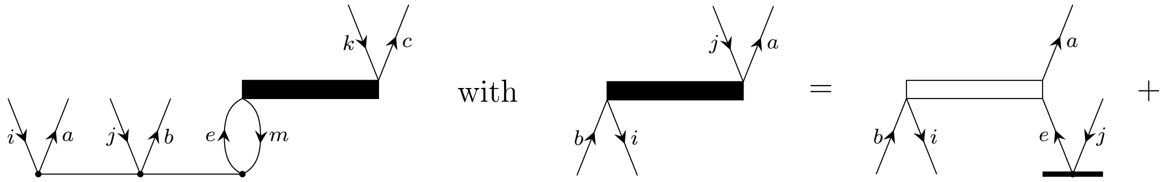

$$P_{-}(c|ab)P_{-}(k|ij)\sum_{e}\sum_{m}\widetilde{\mathcal{W}}_{mcek}\,t^{abe}_{ijm} \qquad \widetilde{\mathcal{W}}_{iabj} \qquad \sum_{e}\mathcal{W}_{aieb}\,r^{e}_{j}$$

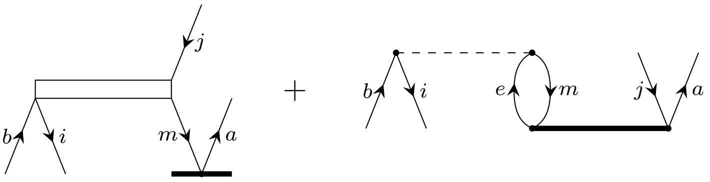

$$-\sum_{m}\mathcal{W}_{mijb}\,r^{a}_{m} \qquad \sum_{e}\sum_{m}\langle im|\,|be\rangle\;r^{ae}_{jm}$$

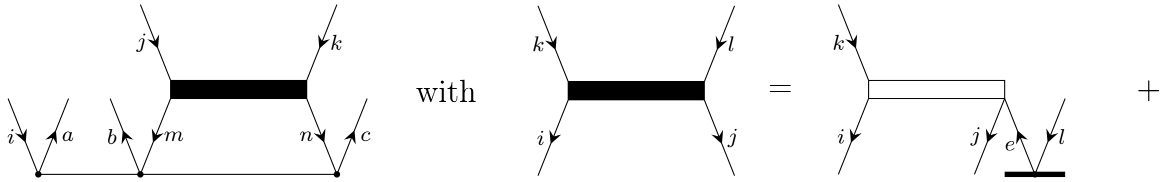

$$\frac{1}{2}\sum_{m,n}\widetilde{\mathcal{W}}_{mnjk}\,t^{abc}_{imn} \qquad \widetilde{\mathcal{W}}_{ijkl} \qquad P_{-}(kl)\sum_{e}\mathcal{W}_{ijke}\,r^{e}_{l}$$

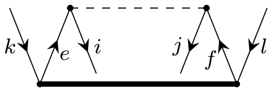

$$\frac{1}{2}\sum_{e,f}\langle ij|\,|ef\rangle\;r^{ef}_{kl}$$

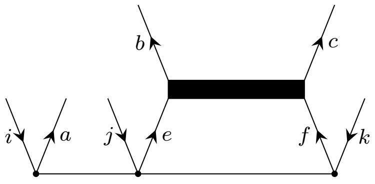

$\frac{1}{2}\sum_{e,f}\widetilde{\mathcal{W}}_{bcef}\; t_{ijk}^{aef}$

with

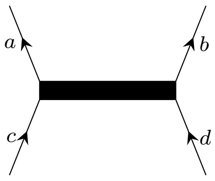

$\widetilde{\mathcal{W}}_{abcd}$

=

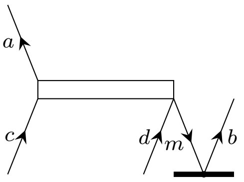

$-P_{-}(ab)\sum_{m}\mathcal{W}_{amcd}\; r_{m}^{b}$

+

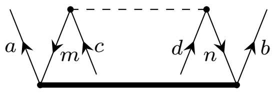

$\frac{1}{2}\sum_{m,n}\langle mn|\,|cd\rangle\; r_{mn}^{ab}$

As for the $\mathcal{W}_{abcd}$-intermediate within CCSDT, the setup of the additional n_{virt}^{4}-dimensional intermediate $\widetilde{\mathcal{W}}_{abcd}$ can optionally be avoided by first contracting the respective integral or two-body term with the $\hat{T}_3$-amplitude to a six-index intermediate.

B.3 EOM-IP working equations

Right-hand side $\boldsymbol{\sigma_i}$-equations for CCSD

$\Delta E_{\text{exc}}\; r_i \quad =$

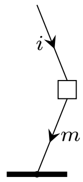

$-\sum_{m}\mathcal{F}_{mi}\; r_m$

+

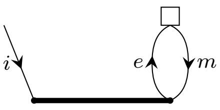

$\sum_{e}\sum_{m}\mathcal{F}_{me}\; r_{mi}^{e}$

+

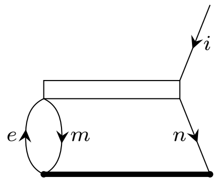

$-\frac{1}{2}\sum_{e}\sum_{m,n}\mathcal{W}_{nmie}\; r_{mn}^{e}$

Right-hand side $\boldsymbol{\sigma_{ji}^{b}}$-equations for CCSD

$\Delta E_{\text{exc}}\; r_{ji}^{b} \quad =$

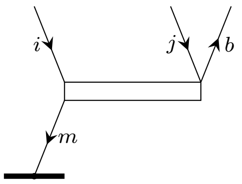

$-\sum_{m}\mathcal{W}_{mbij}\; r_m$

+

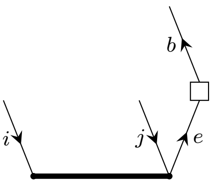

$\sum_{e}\mathcal{F}_{be}\; r_{ji}^{e}$

+

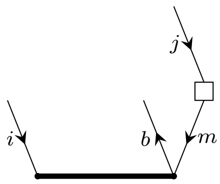

$-P_{-}(ij)\sum_{m}\mathcal{F}_{mj}\; r_{mi}^{b}$

+

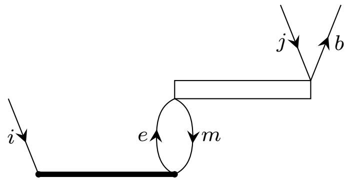

$$P_-(ij)\sum_e\sum_m \mathcal{W}_{mbej}\; r^e_{mi}$$

$+$

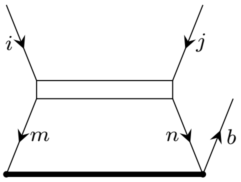

$$\tfrac{1}{2}\sum_{m,n}\mathcal{W}_{mnij}\; r^b_{nm}$$

$+$

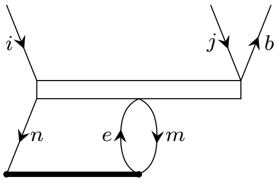

$$-\tfrac{1}{2}\sum_e\sum_{m,n}\mathcal{X}_{bmnjei}\; r^e_{mn}$$

Left-hand side $\boldsymbol{\sigma}^i$-equations for CCSD

$$\Delta E_{\text{exc}}\; l^i \quad =$$

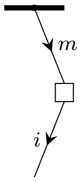

$$-\sum_m \mathcal{F}_{im}\; l^m$$

$+$

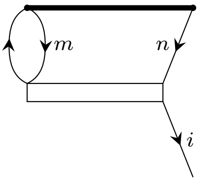

$$-\tfrac{1}{2}\sum_e\sum_{m,n}\mathcal{W}_{ienm}\; l^{mn}_e$$

Left-hand side $\boldsymbol{\sigma}^{ji}_b$-equations for CCSD

$$\Delta E_{\text{exc}}\; l^{ji}_b \quad =$$

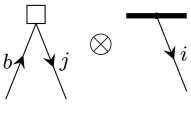

$$P_-(ij)\;\mathcal{F}_{jb}\; l^i$$

$+$

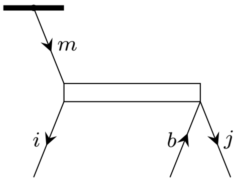

$$-\sum_m \mathcal{W}_{ijmb}\; l^m$$

$+$

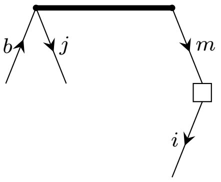

$$-P_-(ij)\sum_m \mathcal{F}_{im}\; l^{jm}_b$$

$+$

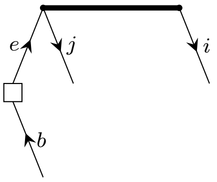

$$\sum_e \mathcal{F}_{eb}\; l^{ji}_e$$

$+$

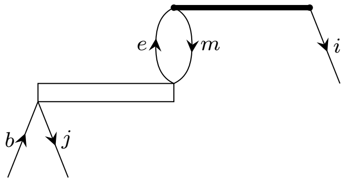

$$P_-(ij)\sum_e\sum_m \mathcal{W}_{jebm}\; l^{mi}_e$$

$+$

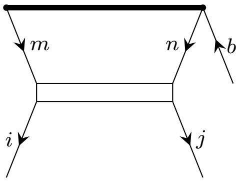

$$\tfrac{1}{2}\sum_{m,n}\mathcal{W}_{ijmn}\; l^{nm}_b$$

$+$

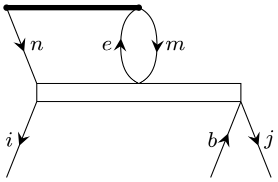

$$-\tfrac{1}{2}\sum_e\sum_{m,n}\mathcal{X}_{ejimbn}\; l^{mn}_e$$

B.4 EOM-EA working equations

Right-hand side $\boldsymbol{\sigma}^{a}$-equations for CCSD

$$\Delta E_{\text{exc}}\; r^{a} \quad =$$

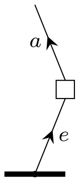

$$\sum_{e} \mathcal{F}_{ae}\; r^{e}$$

$+$

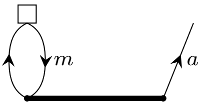

$$\sum_{e}\sum_{m} \mathcal{F}_{me}\; r^{ea}_{m}$$

$+$

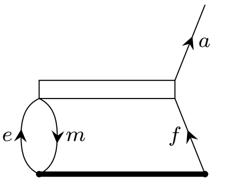

$$\tfrac{1}{2}\sum_{e,f}\sum_{m} \mathcal{W}_{amfe}\; r^{ef}_{m}$$

Right-hand side $\boldsymbol{\sigma}^{ba}_{j}$-equations for CCSD

$$\Delta E_{\text{exc}}\; r^{ba}_{j} \quad =$$

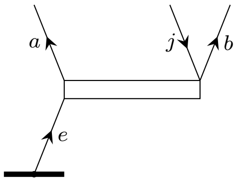

$$\sum_{e} \mathcal{W}_{abej}\; r^{e}$$

$+$

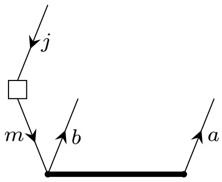

$$-\sum_{m} \mathcal{F}_{mj}\; r^{ba}_{m}$$

$+$

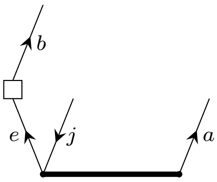

$$P_{-}(ab)\sum_{e} \mathcal{F}_{be}\; r^{ea}_{j}$$

$+$

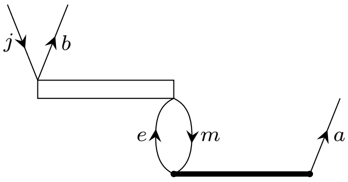

$$P_{-}(ab)\sum_{e}\sum_{m} \mathcal{W}_{mbej}\; r^{ea}_{m}$$

$+$

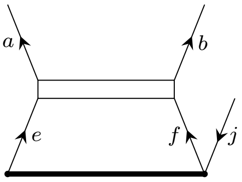

$$\tfrac{1}{2}\sum_{e,f} \mathcal{W}_{abef}\; r^{fe}_{j}$$

$+$

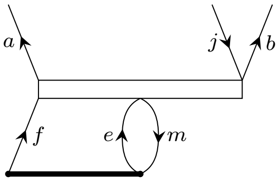

$$\tfrac{1}{2}\sum_{e,f}\sum_{m} \mathcal{X}_{bmajef}\; r^{ef}_{m}$$

Left-hand side $\boldsymbol{\sigma_a}$-equations for CCSD

$$\Delta E_{\text{exc}}\ l_a \quad =$$

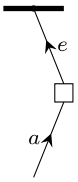

$\sum_e \mathcal{F}_{ea}\ l_e$

$+$

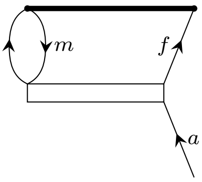

$\frac{1}{2}\sum_{e,f}\sum_m \mathcal{W}_{feam}\ l^m_{ef}$

Left-hand side $\boldsymbol{\sigma^j_{ba}}$-equations for CCSD

$$\Delta E_{\text{exc}}\ l^j_{ba} \quad =$$

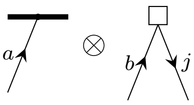

$P_-(ab)\ \mathcal{F}_{jb}\ l_a$

$+$

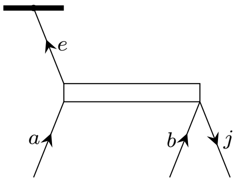

$\sum_e \mathcal{W}_{ejab}\ l_e$

$+$

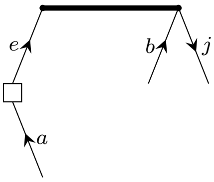

$P_-(ab)\sum_e \mathcal{F}_{ea}\ l^j_{eb}$

$+$

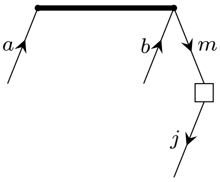

$-\sum_m \mathcal{F}_{jm}\ l^m_{ba}$

$+$

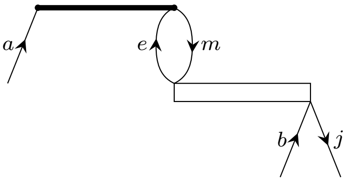

$P_-(ab)\sum_e\sum_m \mathcal{W}_{jebm}\ l^m_{ea}$

$+$

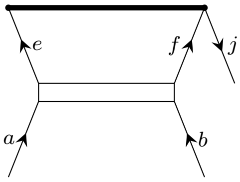

$\frac{1}{2}\sum_{e,f} \mathcal{W}_{efab}\ l^j_{fe}$

$+$

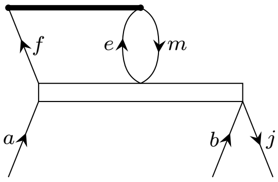

$\frac{1}{2}\sum_{e,f}\sum_m \mathcal{X}_{ejfmba}\ l^m_{ef}$

B.5 EOM properties: One-particle density matrices and $\hat{\mathcal{Z}}$-equations

B.5.1 One-particle density matrices

The contributing diagrams to the expectation value of an arbitrary one-electron operator[42] $\langle \hat{O}_1 \rangle$ are shown ordered by the appearance of the one-electron integrals $o_{1,pq}$. Below, the equations for the corresponding density matrix elements ρ_{pq} are given obtained by leaving out the summation over the internal lines connected to the one-electron operator and the integral itself. Therefore, it should be noted that the equations are not obtained by simply applying the corresponding rules to the diagrams without the one-electron operator.

EOM-EE and EOM-SF

$\boldsymbol{\rho_{ab}}$:

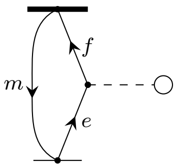

$r_0 \sum_{m} l_b^m \; t_m^a$

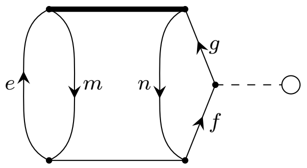

$\frac{1}{2} r_0 \sum_{e} \sum_{m,n} l_{be}^{nm} \; t_{nm}^{ae}$

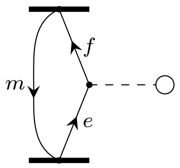

$\sum_{m} r_m^a \; l_b^m$

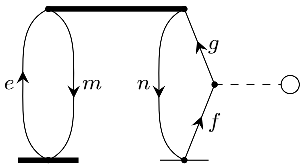

$\sum_{e} \sum_{m,n} r_m^e \; l_{be}^{nm} \; t_n^a$

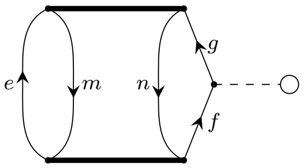

$\frac{1}{2} \sum_{e} \sum_{m,n} r_{nm}^{ae} \; l_{be}^{nm}$

$\boldsymbol{\rho_{ia}}$:

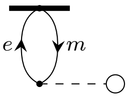

$r_0 \; l_a^i$

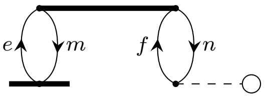

$\sum_{e} \sum_{m} r_m^e \; l_{ae}^{im}$

---

[42] The diagrammatic representation equals the one for the Fock operator with the × replaced by a ○.

$\boldsymbol{\rho_{ij}}$:

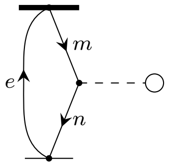

$-r_0 \sum_{e} l_e^i \; t_j^e$

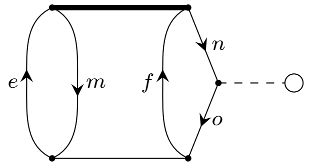

$-\frac{1}{2} r_0 \sum_{e,f} \sum_{m} l_{ef}^{mi} \; t_{jm}^{fe}$

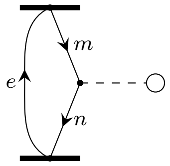

$-\sum_{e} r_j^e \; l_e^i$

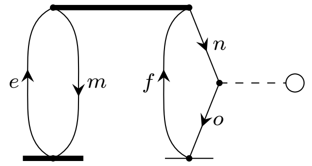

$-\sum_{e,f} \sum_{m} r_m^e \; l_{ef}^{mi} \; t_j^f$

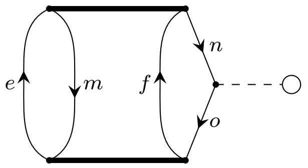

$-\frac{1}{2} \sum_{e,f} \sum_{m} r_{jm}^{fe} \; l_{ef}^{mi}$

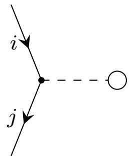

$\delta_{IJ} \; \delta_{ij}$ [43]

$\boldsymbol{\rho_{ai}}$:

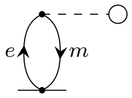

$\delta_{IJ} \; t_i^a$

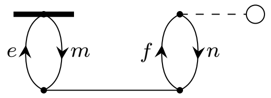

$r_0 \sum_{e} \sum_{m} l_e^m \; t_{im}^{ae}$

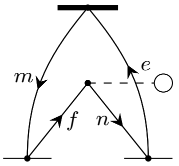

$-r_0 \sum_{e} \sum_{m} l_e^m \; t_m^a \; t_i^e$

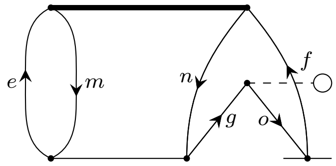

$-\frac{1}{2} r_0 \sum_{e,f} \sum_{m,n} l_{ef}^{mn} \; t_{nm}^{ae} \; t_i^f$

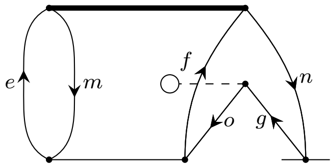

$-\frac{1}{2} r_0 \sum_{e,f} \sum_{m,n} l_{ef}^{mn} \; t_{im}^{fe} \; t_n^a$

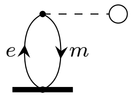

$l_0 \; r_i^a$

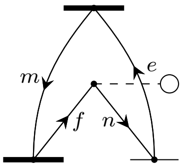

$-\sum_{e} \sum_{m} r_m^a \; l_e^m \; t_i^e$

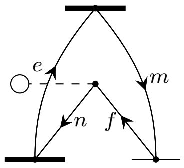

$-\sum_{e} \sum_{m} r_i^e \; l_e^m \; t_m^a$

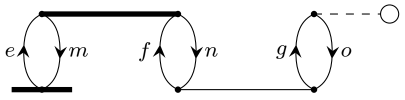

$\sum_{e,f} \sum_{m,n} r_m^e \; l_{ef}^{mn} \; t_{in}^{af}$

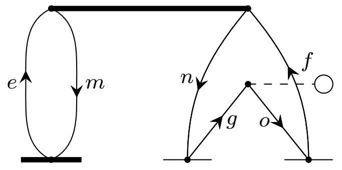

$-\sum_{e,f} \sum_{m,n} r_m^e \; l_{ef}^{mn} \; t_n^a \; t_i^f$

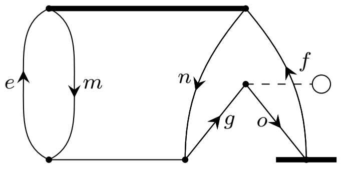

$-\frac{1}{2} \sum_{e,f} \sum_{m,n} r_i^f \; l_{ef}^{mn} \; t_{nm}^{ae}$

---

[43] This is the HF contribution and appears for all EOM methods.

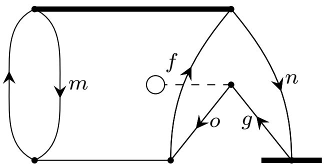

$-\frac{1}{2}\sum_{e,f}\sum_{m,n} r_n^a\ l_{ef}^{mn}\ t_{im}^{fe}$

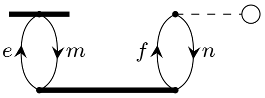

$\sum_e\sum_m r_{im}^{ae}\ l_e^m$

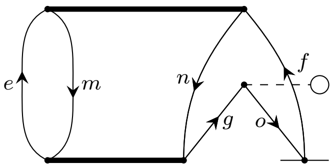

$-\frac{1}{2}\sum_{e,f}\sum_{m,n} r_{nm}^{ae}\ l_{ef}^{mn}\ t_i^f$

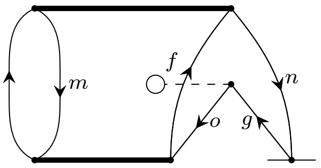

$-\frac{1}{2}\sum_{e,f}\sum_{m,n} r_{im}^{fe}\ l_{ef}^{mn}\ t_n^a$

EOM-IP

Note that the sign rules for deducing algebraic expressions from diagrams with both $\hat{\mathcal{R}}$- and $\hat{\mathcal{L}}$-operator with an odd number of quasiparticle operators appearing only apply if the missing lines are treated as an internal connection between the two operators.

$\boldsymbol{\rho_{ab}}$:

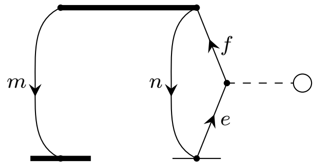

$\sum_{m,n} r_m\ l_b^{nm}\ t_n^a$

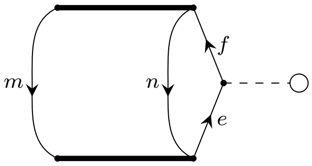

$\frac{1}{2}\sum_{m,n} r_{nm}^a\ l_b^{nm}$

$\boldsymbol{\rho_{ia}}$:

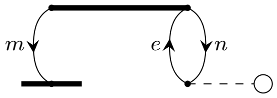

$\sum_m r_m\ l_a^{im}$

$\boldsymbol{\rho_{ij}}$:

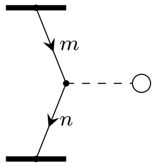

$-r_j\ l^i$

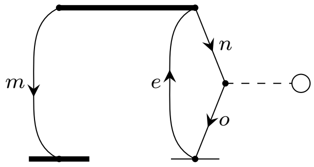

$-\sum_e\sum_m r_m\ l_e^{im}\ t_j^e$

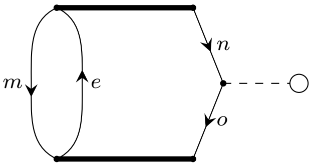

$-\sum_e\sum_m r_{mj}^e\ l_e^{mi}$

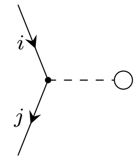

$\delta_{IJ}\ \delta_{ij}$

$\boldsymbol{\rho_{ai}}$:

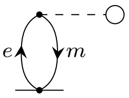

$\delta_{IJ}\ t_i^a$

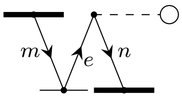

$-\sum_m r_i\ l^m\ t_m^a$

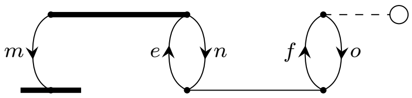

$\sum_e \sum_{m,n} r_m\ l_e^{nm}\ t_{in}^{ae}$

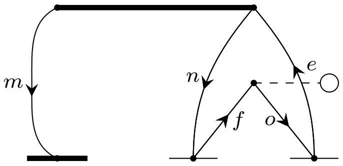

$-\sum_e \sum_{m,n} r_m\ l_e^{nm}\ t_n^a\ t_i^e$

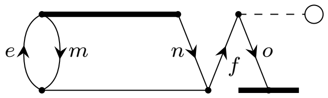

$-\frac{1}{2}\sum_e \sum_{m,n} r_i\ l_e^{mn}\ t_{mn}^{ea}$

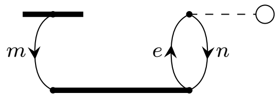

$\sum_m r_{im}^a\ l^m$

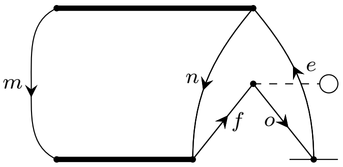

$-\frac{1}{2}\sum_e \sum_{m,n} r_{nm}^a\ l_e^{nm}\ t_i^e$

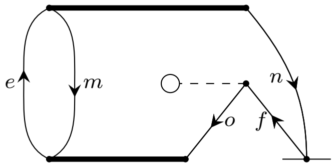

$-\sum_e \sum_{m,n} r_{mi}^e\ l_e^{mn}\ t_n^a$

EOM-EA

$\boldsymbol{\rho_{ab}}$:

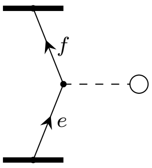

$r^a\ l_b$

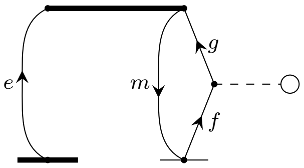

$\sum_e \sum_m r^e\ l_{be}^m\ t_m^a$

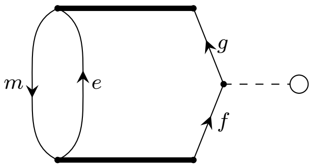

$\sum_e \sum_m r_m^{ea}\ l_{eb}^m$

$\boldsymbol{\rho_{ia}}$:

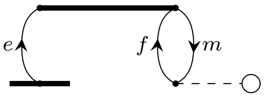

$\sum_e r^e\ l_{ae}^i$

$\boldsymbol{\rho_{ij}}$:

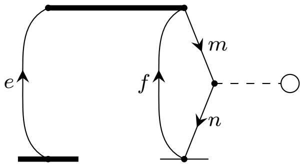

$-\sum_{e,f} r^e\ l_{fe}^i\ t_j^f$

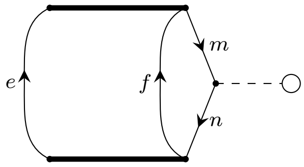

$-\frac{1}{2}\sum_{e,f} r_j^{fe}\ l_{fe}^i$

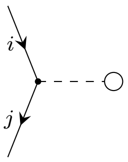

$\delta_{IJ}\ \delta_{ij}$

$\boldsymbol{\rho_{ai}}$:

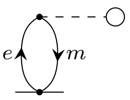

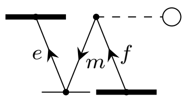

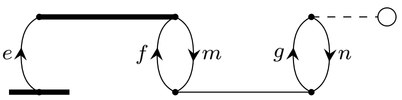

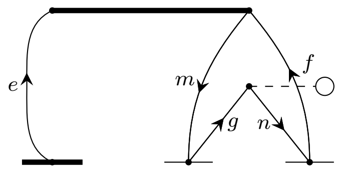

$\delta_{IJ}\; t_i^a$ $\quad -\sum_e r^a\; l_e\; t_i^e$ $\quad \sum_{e,f}\sum_m r^e\; l^m_{fe}\; t^{af}_{im}$ $\quad -\sum_{e,f}\sum_m r^e\; l^m_{fe}\; t^a_m\; t^f_i$

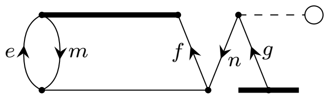

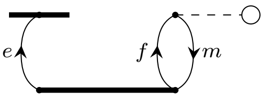

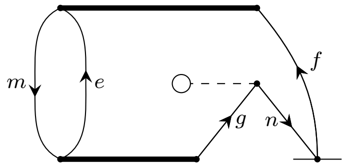

$-\frac{1}{2}\sum_{e,f}\sum_m r^a\; l^m_{ef}\; t^{ef}_{mi}$ $\quad \sum_e r^{ae}_i\; l_e$ $\quad -\sum_{e,f}\sum_m r^{ea}_m\; l^m_{ef}\; t^f_i$

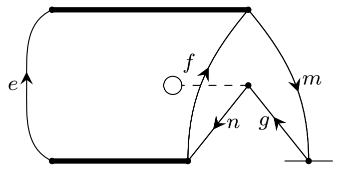

$-\frac{1}{2}\sum_{e,f}\sum_m r^{fe}_i\; l^m_{fe}\; t^a_m$

B.5.2 $\hat{\mathcal{Z}}$-equations for EOM-EE-CCSD

Inhomogeneity vector $\boldsymbol{\Xi = \langle\Phi_0|\,\hat{\mathcal{L}}^{(I)}\left[\left[\bar{H},\hat{\tau}_p\right],\hat{\mathcal{R}}^{(J)}\right]|\Phi_0\rangle}$

$\boldsymbol{\xi^i_a}$:

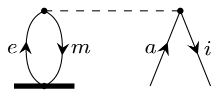

$+$

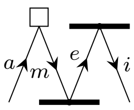

$+$

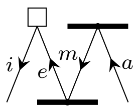

$+$

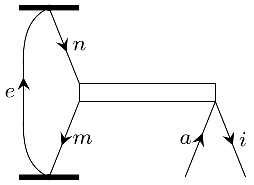

$+$

$\sum_e\sum_m \langle im|\,|ae\rangle\; r^e_m$ $\quad -\sum_e\sum_m \mathcal{F}_{ma}\; r^e_m\; l^i_e - \sum_e\sum_m \mathcal{F}_{ie}\; r^e_m\; l^m_a$ $\quad -\sum_e\sum_{m,n}\mathcal{W}_{mina}\; r^e_m\; l^n_e$

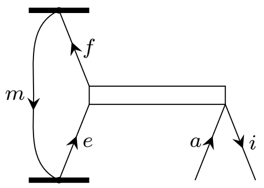

$+$

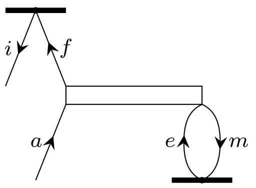

$+$

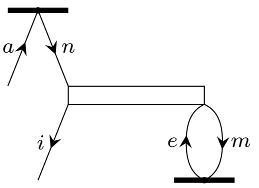

$+$

$\sum_{e,f}\sum_m \mathcal{W}_{fiea}\; r^e_m\; l^m_f$ $\quad \sum_{e,f}\sum_m \mathcal{W}_{fmae}\; r^e_m\; l^i_f$ $\quad -\sum_e\sum_{m,n}\mathcal{W}_{imne}\; r^e_m\; l^n_a$

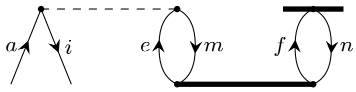

$$\sum_{e,f}\sum_{m,n}\langle im||ae\rangle\ r^{ef}_{mn}\ l^{n}_{f} +$$

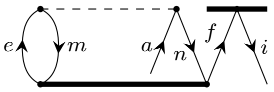

$$-\frac{1}{2}\sum_{e,f}\sum_{m,n}\langle mn||ea\rangle\ r^{ef}_{mn}\ l^{i}_{f} +$$

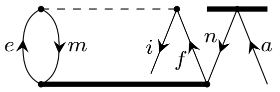

$$-\frac{1}{2}\sum_{e,f}\sum_{m,n}\langle mi||ef\rangle\ r^{ef}_{mn}\ l^{n}_{a} +$$

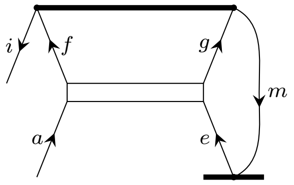

$$\frac{1}{2}\sum_{e,f,g}\sum_{m}\mathcal{W}_{fgae}\ r^{e}_{m}\ l^{im}_{fg} +$$

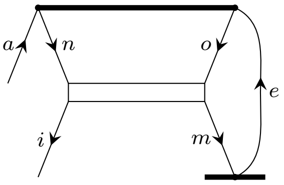

$$\frac{1}{2}\sum_{e}\sum_{m,n,o}\mathcal{W}_{imno}\ r^{e}_{m}\ l^{no}_{ae} +$$

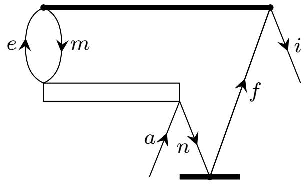

$$-\sum_{e,f}\sum_{m,n}\mathcal{W}_{neam}\ r^{f}_{n}\ l^{mi}_{ef} +$$

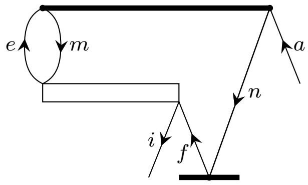

$$-\sum_{e,f}\sum_{m,n}\mathcal{W}_{iefm}\ r^{f}_{n}\ l^{mn}_{ea} +$$

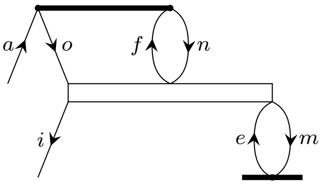

$$-\frac{1}{2}\sum_{e,f}\sum_{m,n,o}\mathcal{X}_{fmineo}\ r^{e}_{m}\ l^{on}_{af} +$$

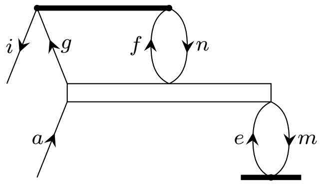

$$\frac{1}{2}\sum_{e,f,g}\sum_{m,n}\mathcal{X}_{fmgnea}\ r^{e}_{m}\ l^{ni}_{fg} +$$

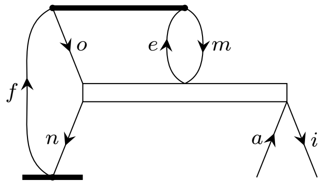

$$-\frac{1}{2}\sum_{e,f}\sum_{m,n,o}\mathcal{X}_{einmao}\ r^{f}_{n}\ l^{mo}_{ef} +$$

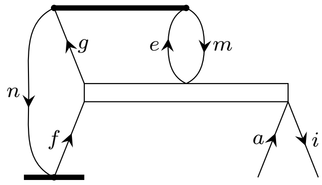

$$\frac{1}{2}\sum_{e,f,g}\sum_{m,n}\mathcal{X}_{eigmaf}\ r^{f}_{n}\ l^{mn}_{eg} +$$

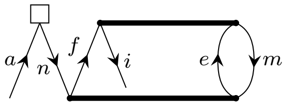

$$-\frac{1}{2}\sum_{e,f}\sum_{m,n}\mathcal{F}_{na}\ r^{ef}_{mn}\ l^{mi}_{ef} +$$

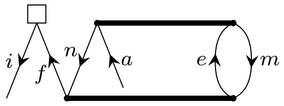

$$-\frac{1}{2}\sum_{e,f}\sum_{m,n}\mathcal{F}_{if}\ r^{ef}_{mn}\ l^{mn}_{ea} +$$

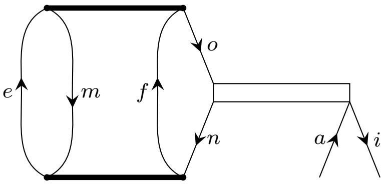

$$-\frac{1}{2}\sum_{e,f}\sum_{m,n,o}\mathcal{W}_{nioa}\ r^{ef}_{mn}\ l^{mo}_{ef} +$$

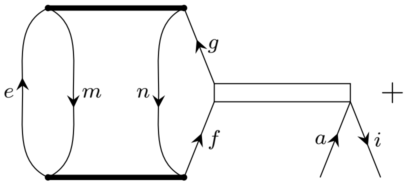

$$\frac{1}{2}\sum_{e,f,g}\sum_{m,n}\mathcal{W}_{gifa}\ r^{ef}_{mn}\ l^{mn}_{eg} +$$

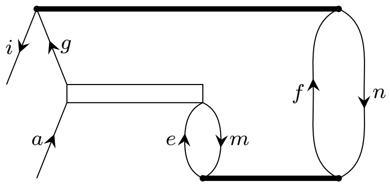

$$\sum_{e,f,g}\sum_{m,n}\mathcal{W}_{gmae}\ r^{ef}_{mn}\ l^{ni}_{fg} +$$

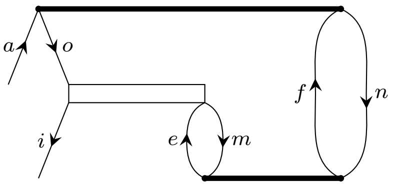

$$-\sum_{e,f}\sum_{m,n,o}\mathcal{W}_{imoe}\ r^{ef}_{mn}\ l^{on}_{af} +$$

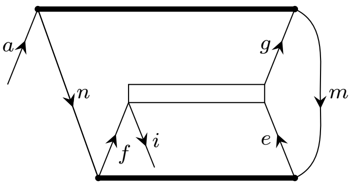

$-\frac{1}{2}\sum_{e,f,g}\sum_{m,n}\mathcal{W}_{gief}\ r^{ef}_{mn}\ l^{nm}_{ag}$ +

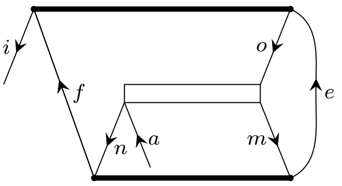

$\frac{1}{2}\sum_{e,f}\sum_{m,n,o}\mathcal{W}_{mnoa}\ r^{ef}_{mn}\ l^{oi}_{ef}$ +

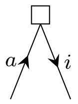

$\delta_{IJ}\ \mathcal{F}_{ia}$ [44]

$\boldsymbol{\xi^{ij}_{ab}}$:

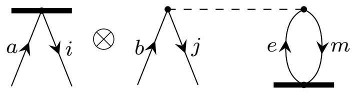

$P_{-}(ab)P_{-}(ij)\sum_{e}\sum_{m}\langle jm||be\rangle\ r^{e}_{m}\ l^{i}_{a}$ +

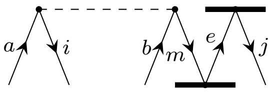

$-P_{-}(ij)\sum_{e}\sum_{m}\langle im||ab\rangle\ r^{e}_{m}\ l^{j}_{e}$ +

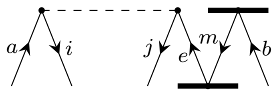

$-P_{-}(ab)\sum_{e}\sum_{m}\langle ij||ae\rangle\ r^{e}_{m}\ l^{m}_{b}$ +

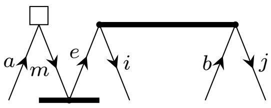

$-P_{-}(ab)\sum_{e}\sum_{m}\mathcal{F}_{ma}\ r^{e}_{m}\ l^{ij}_{eb}$ +

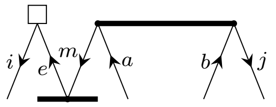

$-P_{-}(ij)\sum_{e}\sum_{m}\langle jm||ab\rangle\ r^{e}_{m}\ l^{i}_{e}$ +

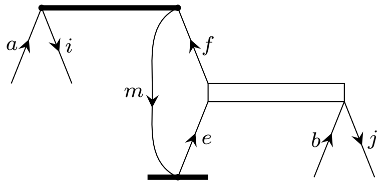

$P_{-}(ab)P_{-}(ij)\sum_{e,f}\sum_{m}\mathcal{W}_{fjeb}\ r^{e}_{m}\ l^{im}_{af}$ +

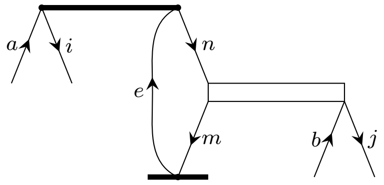

$-P_{-}(ab)P_{-}(ij)\sum_{e}\sum_{m,n}\mathcal{W}_{mjnb}\ r^{e}_{m}\ l^{in}_{ae}$ +

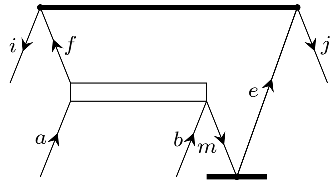

$-\sum_{e,f}\sum_{m}\mathcal{W}_{fmab}\ r^{e}_{m}\ l^{ji}_{ef}$ +

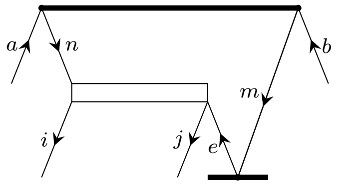

$\sum_{e}\sum_{m,n}\mathcal{W}_{ijne}\ r^{e}_{m}\ l^{nm}_{ab}$ +

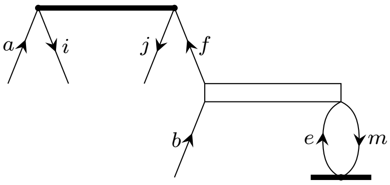

$P_{-}(ab)\sum_{e,f}\sum_{m}\mathcal{W}_{fmbe}\ r^{e}_{m}\ l^{ij}_{af}$ +

---

[44] This is the singles contribution from the CC reference state's energy that has been subtracted in the formulation of the theory and gives also a doubles contribution: $\frac{\partial E_{\mathrm{CC}}}{\partial t_p} = \langle\Phi_0|\,\bar{H}\,|\Phi_p\rangle$.

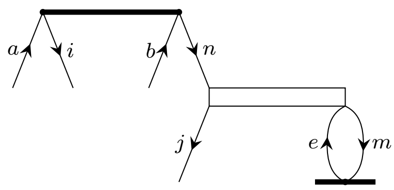

$$-P_-(ij)\sum_{e}\sum_{m,n}\mathcal{W}_{jmne}\; r^{e}_{m}\; l^{in}_{ab}$$

+

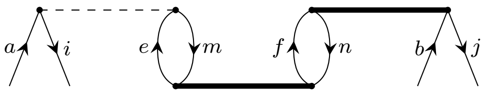

$$P_-(ab)P_-(ij)\sum_{e,f}\sum_{m,n}\langle im|\,|ae\rangle\; r^{ef}_{mn}\; l^{jn}_{bf}$$

+

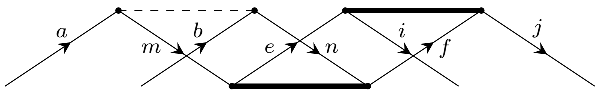

$$\frac{1}{4}\sum_{e,f}\sum_{m,n}\langle mn|\,|ab\rangle\; r^{ef}_{mn}\; l^{ij}_{ef}$$

+

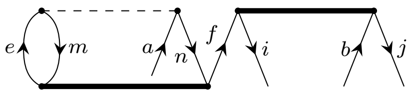

$$-\frac{1}{2}P_-(ab)\sum_{e,f}\sum_{m,n}\langle mn|\,|ea\rangle\; r^{ef}_{mn}\; l^{ij}_{fb}$$

+

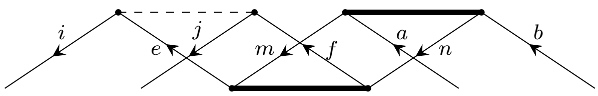

$$\frac{1}{4}\sum_{e,f}\sum_{m,n}\langle ij|\,|ef\rangle\; r^{ef}_{mn}\; l^{mn}_{ab}$$

+

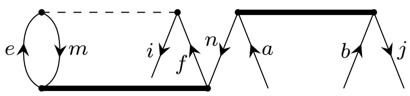

$$-\frac{1}{2}P_-(ij)\sum_{e,f}\sum_{m,n}\langle mi|\,|ef\rangle\; r^{ef}_{mn}\; l^{nj}_{ab}$$

+

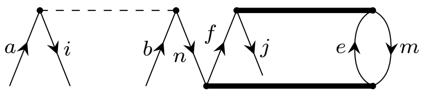

$$-\frac{1}{2}P_-(ij)\sum_{e,f}\sum_{m,n}\langle in|\,|ab\rangle\; r^{ef}_{mn}\; l^{mj}_{ef}$$

+

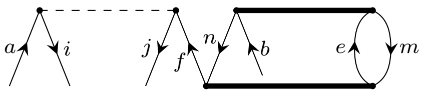

$$-\frac{1}{2}P_-(ab)\sum_{e,f}\sum_{m,n}\langle ij|\,|af\rangle\; r^{ef}_{mn}\; l^{mn}_{eb}$$

+

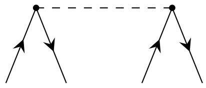

$$\delta_{IJ}\;\; \langle ij|\,|ab\rangle$$

Contributions to $Z = \langle\Phi_0|\,\hat{\mathcal{Z}}(\omega_{IJ})\,\left[\bar{H},\hat{\tau}_p\right]|\Phi_0\rangle$

The diagrammatic representation of the $\hat{\mathcal{Z}}$-operator is a solid line as is used for the $\hat{T}$-operator.

ζ^{i}_{a} :

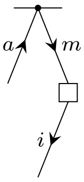

$$-\sum_{m}\mathcal{F}_{im}\;\zeta^{m}_{a}$$

+

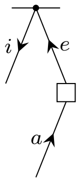

$$\sum_{e}\mathcal{F}_{ea}\;\zeta^{i}_{e}$$

+

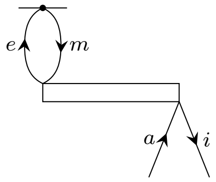

$$\sum_{e}\sum_{m}\mathcal{W}_{ieam}\;\zeta^{m}_{e}$$

+

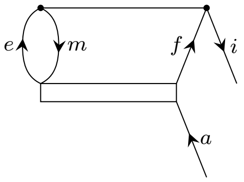

$$\frac{1}{2}\sum_{e,f}\sum_{m}\mathcal{W}_{feam}\;\zeta^{mi}_{ef}$$

+

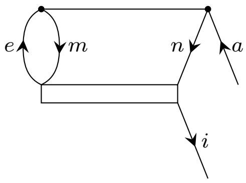

$-\frac{1}{2}\sum_{e}\sum_{m,n}\mathcal{W}_{ienm}\;\zeta^{mn}_{ea}$

+

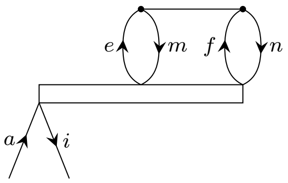

$\frac{1}{4}\sum_{e,f}\sum_{m,n}\mathcal{X}_{efimna}\;\zeta^{mn}_{ef}$

$\boldsymbol{\zeta^{ij}_{ab}}$:

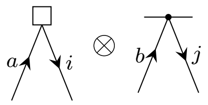

$P_{-}(ab)P_{-}(ij)\;\mathcal{F}_{ia}\;\zeta^{j}_{b}$

+

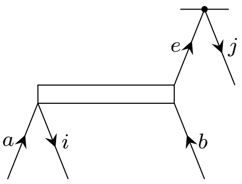

$P_{-}(ij)\sum_{e}\mathcal{W}_{eiba}\;\zeta^{j}_{e}$

+

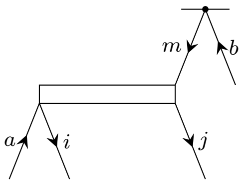

$-P_{-}(ab)\sum_{m}\mathcal{W}_{jima}\;\zeta^{m}_{b}$

+

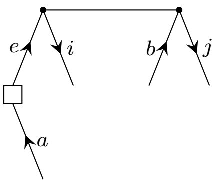

$P_{-}(ab)\sum_{e}\mathcal{F}_{ea}\;\zeta^{ij}_{eb}$

+

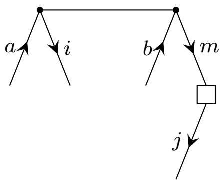

$-P_{-}(ij)\sum_{m}\mathcal{F}_{jm}\;\zeta^{im}_{ab}$

+

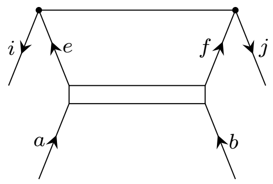

$\frac{1}{2}\sum_{e,f}\mathcal{W}_{efab}\;\zeta^{ij}_{ef}$

+

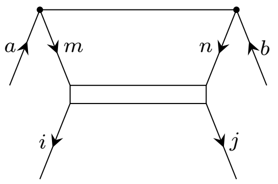

$\frac{1}{2}\sum_{m,n}\mathcal{W}_{ijmn}\;\zeta^{mn}_{ab}$

+

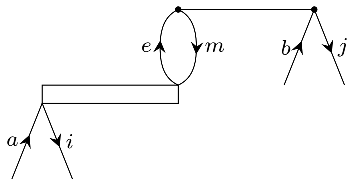

$P_{-}(ab)P_{-}(ij)\sum_{e}\sum_{m}\mathcal{W}_{ieam}\;\zeta^{jm}_{be}$

+

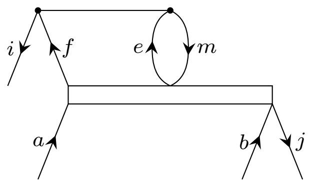

$\frac{1}{2}P_{-}(ij)\sum_{e,f}\sum_{m}\mathcal{X}_{ejfmba}\;\zeta^{mi}_{ef}$

+

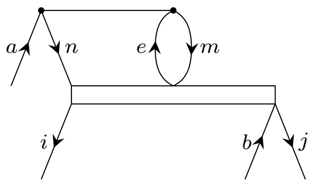

$-\frac{1}{2}P_{-}(ab)\sum_{e}\sum_{m,n}\mathcal{X}_{ejimbn}\;\zeta^{nm}_{ae}$

Calculation of size-intensive $\boldsymbol{\mu}^{\mathrm{c}}_{I\to J}$

1. $\langle\Phi_0|\,\hat{\mathcal{L}}^{(I)}\left(\bar{\boldsymbol{\mu}}\hat{\mathcal{R}}^{(J)}\right)_{\mathrm{c}}|\Phi_0\rangle$ is calculated by tracing the modified one-electron density matrix with the dipole integral matrix $\boldsymbol{\mu}$.

2. $\langle\Phi_0|\,\hat{\mathcal{L}}^{(I)}\left(\left[\bar{H},\hat{T}^{\varepsilon}(\omega_{IJ})\right]\hat{\mathcal{R}}^{(J)}\right)_{\mathrm{c}}|\Phi_0\rangle$ is calculated by tracing the converged $\hat{\mathcal{Z}}$-amplitudes with the similarity transformed dipole matrix $\bar{\boldsymbol{\mu}}$. The definitions of the elements of $\bar{\boldsymbol{\mu}}$ - $\bar{\mu}_{ai}$ and $\bar{\mu}_{abij}$ - equal the respective CC-amplitude equations which build up $\mathcal{F}_{ai}$ and $\mathcal{W}_{abij}$ when leaving out all contributions from two-electron integrals and replacing the Fock integrals by the dipole integrals.

3. To account for the contribution from the CC reference state's energy[45] that has been subtracted in the formulation of the theory,

$$\frac{\partial\Delta E_{\mathrm{corr}}}{\partial\boldsymbol{\varepsilon}} = \langle\Phi_0|\,\bar{\boldsymbol{\mu}}\,|\Phi_0\rangle$$

has to be added:

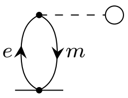

$$\sum_e\sum_m \mu_{me}\; t_m^e$$

---

[45] The perturbation is not considered at the HF level of theory and no orbital relaxation is included.

C Qcumbre input keywords

In the following, all keywords and their respective options for the Qcumbre input file are given in Tab. C.1. An exemplary input file is provided.

Table C.1: Keywords and their options for the Qcumbre program package.

Keyword & Default	Options	Effect
`coupled-cluster {...}`		
`truncation-level` `ccsd`	`none`	no CC calculation is performed, amplitudes are read from file, CCSD assumed for EOM
	`ccsd`	CCSD calculation is performed
	`ccsdt`	CCSDT calculation is performed
	`ccsd(t)`	CCSD(T) calculation is performed, CCSD assumed for EOM
	`ccsdt-none`	no CC calculation is performed, amplitudes are read from file, CCSDT assumed for EOM
`convergence-criterion` $1e^{-7}$	$1e^{-13} \leq x \leq 1e^{-3}$	sets the CC convergence criterion
`diis-max-subspace` 7	$x \in \mathbb{N}\backslash\{1\}$	0: no DIIS is used for CC, else, last x vectors used for DIIS
`maxccit` 50	$10 \leq x \leq 100$	maximum number of iterations
`write_amp` `false`	`false, no, 0`	converged amplitudes are saved if keyword is different from named ones
`build_abcd` `false`	`false, no, 0`	for CCSDT, $\mathcal{W}_{abcd}$ is built if keyword is different from named ones

`equation-of-motion {...}`		
`eom-method` `ee`	`none`	no EOM calculation is performed
	`ee`	EOM-EE calculation is performed
	`sf`	EOM-SF calculation is performed
	`ip`	EOM-IP calculation is performed
	`ea`	EOM-EA calculation is performed
	`cis`	only a CIS calculation is performed
`delta-m_s` -1	$x \in \{-1, 0, 1\}$	-1: $\Delta M_S = -1$ for EOM-SF, $\Delta M_S = -\frac{1}{2}$ for EOM-IP/EA
		1: $\Delta M_S = +1$ for EOM-SF, $\Delta M_S = +\frac{1}{2}$ for EOM-IP/EA
		$\Delta M_S = 0$ for EOM-EE independently
`number-of-roots` 1	$0 \leq x \leq 50$	number of roots calculated from CIS guesses
`skiproots` `""`	list of integers seperated by ,	numbers of CIS roots omitted
`convergence-criterion` $1\mathrm{e}^{-7}$	$1\mathrm{e}^{-13} \leq x \leq 1\mathrm{e}^{-3}$	sets the EOM convergence criterion
`maxeomit` 30	$10 \leq x \leq 100$	maximum number of iterations per root
`maxbasis` `maxeomit`	$3 \leq x \leq$ `maxeomit`	maximum number of basis vectors used for each root
⋮	⋮	⋮

⋮	⋮	⋮
`properties` 0	0	no properties are calculated
	1	properties are calculated via EOM expectation values
	2	size-intensive properties are calculated via $\hat{\mathcal{Z}}$-vector equations
	3	size-intensive properties are calculated explicitly solving the perturbed CC-amplitude equations
`moments` `none`	`d`	dipole moments are calculated
	`t`	transition dipole moments between the ground state and all excited states are calculated
	`et`	transition dipole moments between all states are calculated
	combinations of `d` and `t`/`et`	dipole and transition dipole moments are calculated
`diis-max-subspace` 7	$x \in \mathbb{N} \backslash \{1\}$	0: no DIIS is used for EOM, else, last x vectors used for DIIS
`guessval` `""`	list of floats seperated by ,	values for the manual guesses, both real and imaginary part
`guesspos` `""`	list of integers seperated by ,	occ. and virt. orbitals listed in turns for the manual guesses
`guessdouble` `""`	1	if set to 1, the corresponding double amplitudes are set to the guess values
`build_abcd` `false`	`false, no, 0`	for EOM-CCSDT, $\widetilde{\mathcal{W}}_{abcd}$ is built if keyword is different from named ones
`coupling` `false`	1	if set to 1, the couplings following Ref. [154] are calculated

Exemplary input file

```
coupled-cluster {
  truncation-level = ccsd
  convergence-criterion = 1e-7
  diis-max-subspace = 7
}
equation-of-motion {
  eom-method = ea
  delta_m-s = -1
  number-of-roots = 5
  convergence-criterion = 1e-7
  diis-max-subspace = 7
  properties = 1
  moments = et
}
```

All information concerning geometry, basis set, molecular charge, etc. is provided via the input file for the underlying program package (here: London [29]).

Logo design by F. Engel

List of publications

1. Hampe, F.; Stopkowicz, S. *J. Chem. Phys.* **2017**, *146*, 154105.

2. Holzer, C.; Teale, A. M.; Hampe, F.; Stopkowicz, S.; Helgaker, T.; Klopper, W. *J. Chem. Phys.* **2019**, *150*, 214112.

3. Hampe, F.; Stopkowicz, S. *J. Chem. Theory Comput.* **2019**, *15*, 4036-4043.